Ferrofluid Surface and Volume Flows in Uniform Rotating Magnetic Fields

by

Shihab Mahmoud Elborai

Submitted to the Department of Electrical Engineering and Computer Science
in partial fulfillment of the requirements for the degree of

Doctor of Philosophy

at the

MASSACHUSETTS INSTITUTE OF TECHNOLOGY

May 2006

Author . . . .
Department of Electrical Engineering and Computer Science
May 25, 2006

Certified by . . . .
Markus Zahn
Professor
Thesis Supervisor

Accepted by . . . .
Arthur C. Smith
Chairman, Department Committee on Graduate Students

Ferrofluid Surface and Volume Flows in Uniform Rotating Magnetic Fields

by

Shihab Mahmoud Elborai

Submitted to the Department of Electrical Engineering and Computer Science
on May 25, 2006, in partial fulfillment of the
requirements for the degree of
Doctor of Philosophy

Abstract

Ferrofluid surface and volume effects in uniform dc and rotating magnetic fields are studied. Theory and corroborating measurements are presented for meniscus shapes and resulting surface driven flows, spin-up flows, and Hele-Shaw cell flows and instabilities. To characterize the water-based and oil-based ferrofluids used in experiments, measurements were made of the magnetization curve, surface tension, viscosity, density, and the speed of sound.

Extensive measurements of the height and shape of ferrofluid menisci in applied uniform dc magnetic fields show that the height of the meniscus increases for vertical applied magnetic fields, whereas horizontal magnetic fields decrease meniscus height. An approximate energy minimization analysis agrees with the observed trends in ferrofluid meniscus height. The effects of ferrofluid meniscus curvature on spin-up flow were modeled under simplified assumptions. Analytical solutions were derived for two dimensional low Reynolds number flows and extended results were obtained numerically using COMSOL's Multiphysics finite element software package (FEMLAB) to solve for three dimensional recirculating flows at higher Reynolds numbers.

Familiar magnetostatic energy expressions in linear magnetic media were extended to non-linear magnetization relations. These energy expressions were applied to study the effects of linear and non-linear magnetization on flows and instabilities in Hele-Shaw cells with simultaneously applied in-plane rotating and dc axial magnetic fields.

Ultrasound velocimetry of the spin-up flow in the bulk region of water-based ferrofluids conclusively demonstrates the co-rotation of the bulk of the ferrofluid with the applied rotating magnetic field with and without a free surface. Careful ultrasound investigation of flow profiles at different heights in uncovered ferrofluid cylinders showed flow direction reversal between the counter-rotating top free surface and the co-rotating bulk region of the ferrofluid. A framework for a numerical solution of the coupled governing equations of conservation of linear and angular momentum in magnetic spin-up flows that considers all the terms in the first Shliomis magnetization relaxation equation was formulated and solved. Previous solutions in the literature which decouple the magnetic and fluid mechanical dynamics by neglecting the linear and spin velocities in the magnetization relaxation equations result in no spin-up flow in uniform magnetic fields in the absence of spin diffusion effects. Contrary to the commonly held view in the literature, spin-up flows develop in rotating uniform magnetic fields even in the absence of spin diffusion effects. Including the linear and spin velocity terms in the magnetization relaxation equation results in non-zero spin-up flow. Numerical solutions using FEMLAB software are shown for flow profiles with zero and non-zero spin viscosity. Fitting numerical simulations to velocity profile ultrasound measurements allows the estimation of the magnetization relaxation time and the spin viscosity for Ferrotec Corp.'s MSG W11 and EMG705 water-based ferrofluids.

Thesis Supervisor: Markus Zahn
Title: Professor

Acknowledgments

I would like to thank my advisor Prof. Markus Zahn for his kindness and inexhaustible patience. I am fortunate to have worked on a challenging technical problem with a knowledgeable teacher and role model. An equal measure of thanks is due to my thesis committee members: Dr. Rosensweig and Prof. Lang.

I would like to thank Mr. Thomas F. Peterson for his generosity in supporting my thesis research.

Special thanks are due to Chris Connaire for proof-reading an almost full draft of this thesis. I have finally renounced my carelessness and learned not to split infinitives.

Tony He, and Se-Hee Lee maintained a measure of sanity in the lab and were always generous with their friendship, encouragement and trust. They have earned my lasting gratitude in return. Special thanks are due to Chris Connaire for proof-reading an almost full draft of this thesis. I have finally learned to avoid splitting infinitives.

I would like to thank my parents, Suad and Mahmoud, for everything they have done for me. In the darkest days–when nothing seemed to work–my siblings, Ranim, Marwa and Hisham, were always ready with care, love and support. I am grateful to my grandfather, Mohammed Dakhil, for being a great man and role model.

This work is dedicated to the memory of my dear friend Joshua Ian Cates, in recognition of his true friendship and the joyous memories of our undergraduate life at MIT.

Contents

List of Figures

List of Tables

Chapter 1

Introduction to ferrofluid flow phenomena

The research for this doctoral thesis focuses on the effects of magnetic force and torque densities in ferrofluid as well as magnetic-surface-shear stress at a ferrofluid/air meniscus on the magnetic spin-up behavior of ferrofluids. Ferrofluids are stable colloidal-suspensions of permanently magnetized nanoparticles in a carrier liquid like water or oil. Each particle is typically made from magnetite (Fe_3O_4) coated with a monolayer of surfactant to prevent the particles from agglomerating under van der Waals attraction forces. Furthermore, the ~ 10 nanometer particle diameter is small enough to ensure that the particles remain dispersed by Brownian motion and do not agglomerate under gravity and magnetic interactions. Ferrofluids are therefore stable suspensions that exhibit superparamagnetic susceptibilities with suspended magnetic particles constituting typically up to 10% of the total fluid volume.

Spin-up flow of ferrofluids results from the coupling of uniform rotating magnetic fields to ferrofluid angular momentum. A rotating magnetic field acting on a ferrofluid in a stationary vessel entrains the ferrofluid into a steady circular motion. The study of the coupling of magnetic and mechanical forces in ferrofluids draws from the diverse fields of magnetism, fluid dynamics, electromechanics, colloidal chemistry and thermodynamics. There remains, however, a fundamental disagreement in the literature about the relative significance of surface and volume forces driving the observed flows in ferrofluids. Disagreements exist also on whether a uniform magnetic field can cause spin-up flow with some researchers contending that spin-up flows are in fact due to slight magnetic field non-uniformity. This thesis research combines the analysis of contending theories in the literature with careful experimental investigation to resolve the effects of the different physical models presented in the literature.

1.1 Background and motivation

Ferrofluids exhibit a rich set of flow patterns and instabilities in the presence of dc, ac, and rotating magnetic fields [40, 10]. Current applications of ferrofluid technology generally rely on dc magnetic fields and include liquid-rotary-shaft seals on disk drives, improved heat transfer in loud speakers, and sink-float systems for separation of materials. Ferrofluid spheres are also used to model and study gravitational dynamics in a controlled laboratory setting [41].

Magnetic-field-based micro-electromechanical (MEMS) and nano-electromechanical systems (NEMS) that use ferrofluids offer a potentially more reliable and compact alternative technology to existing electric-field-based devices. Zahn proposed a number of device concepts that use the magnetic particles of ferrofluid with or without a carrier liquid to make nanoscale electromechanical micro-power generators [49]. The ability to position a ferrofluid volume precisely in a flow channel presents many opportunities in the design of microfluidic systems. Various microfluidic devices using magnetic fluids such as micro-actuators, dampers, accelerometers and generators have been developed and reported in the literature. Koser and Mao built a pump for ferrofluids in filled pipes using spatially traveling sinusoidal magnetic fields [25] extending the analysis and results of Zahn and Greer [51]. Krauss *et al.* built a ferrofluid pump for open channels where a rotating magnetic field drives a flow on the ferrofluid/air interface [22]. They report an operating magnetic field rotational frequency range that extends from 300 Hz to 30 kHz with maximum volumetric flow rate near 3 kHz.

Numerous biomedical applications can benefit from this technology, including:

microfluidic medical devices, magnetically targeted drug delivery [19], targeted destruction of tumors [18], in-vivo monitoring of chemical activity in the brain [20], enhancement of existing medical imaging technology [1] and toxin removal from the body [21]. Often in the field of chemotherapy successful treatment depends as much upon the means of delivering the drug to its target as it does upon the efficacy of the drug itself. Biocompatible surfactant coatings have been designed for ferrofluid nanoparticles so that they selectively bond to specific molecules on cells and perform predetermined chemical functions (*e.g.*, deliver anti-cancer agents such as radionuclides, cancer-specific antibodies, genes, *etc.*) [2].

1.2 Force mechanisms in ferrofluid literature

Rosensweig pioneered the study of ferrofluids and with the help of his early coworkers laid down the first-principles of ferrohydrodynamics. He documented a broad overview of these early efforts in his book: Ferrohydrodynamics [40]–a term first coined by Rosensweig. When subjected to rotating or time varying magnetic fields, ferrofluid particles will rotate to align their magnetic axis with the instantaneous applied field. The magnetization relaxation equation, first proposed by Shliomis, governs the process by which the magnetization of the fluid bulk eventually settles into its steady state value. Two processes limit the rate of ferrofluid particle alignment with the applied magnetic field: rotational Brownian motion and Néel redistribution of sub-particle magnetic domains. These delays lead to a lag between the ferrofluid magnetization and the applied magnetic field so that magnetization $\mathbf{M}$ is not collinear with the magnetic field $\mathbf{H}$ which results in a body-torque density $\mu_0 \mathbf{M} \times \mathbf{H}$. This body-torque density drives fluid flow and spinning nanoparticles [43] as well as contributing to the shear stress at a free surface [39].

The phenomenon of magnetic fluid spin-up flow has been reported by many independent investigators. Experiments reported in the literature place a stationary cylindrical container of ferrofluid in rotating magnetic fields. Essentially rigid-body rotation of the ferrofluid is reported by most investigators based on observations of the top free surface. The reported direction of ferrofluid rotation depends on the amplitude and frequency of the applied magnetic field. The reports in the literature often conflict about the direction of magnetic fluid rotation with respect to the rotation direction of the applied magnetic field. Brown and Horsnell report that the sense of spin-up rotation for a magnetic oxide slurry switches from counter-rotation to co-rotation as the applied rotating magnetic field strength is increased beyond a threshold value [8]. Kagan, on the other hand, reports the opposite trend with co-rotation for low field strengths and counter rotation for high field strengths [16]. The mean size of the magnetic particles in Kagan's experiment was $\sim 0.2\ \mu$m and volume concentration of the solid phase was 10-20%. These experimental results are for slurries of micron sized particles and have yet unknown significance to ferrofluids. The opacity of the fluids limits these experimental observations to the velocity profile at the free surface of the ferrofluid. There are no reports in the literature of measured velocity profiles in the bulk of the ferrofluid. These measurements can provide the quantitative observations needed to resolve the current confusion in the literature.

In order to explain these experimental observations, the ferrofluid literature presents two main theories on the dominant mechanism in establishing spin-up flow: the spin-diffusion model and the surface-driven flow model. The spin-diffusion model for ferrofluid spin-up considers the non-equilibrium magnetization of ferrofluid particles to be the dominant mechanism for transfer of momentum from the rotating magnetic field to the ferrofluid. In this mechanism the magnetization relaxation time constant, due to Brownian and Néel relaxation of the fluid, prevents the magnetic nanoparticles from instantaneously aligning with the applied magnetic field. This relaxation time introduces a lag between the orientation of the magnetization of the ferrofluid and the rotating field. The resulting torque tries to align each particle with the applied magnetic field and is transferred to the bulk of the ferrofluid by viscous coupling [35, 38, 37]. Rinaldi, Zahn *et al.* report torque measurements on hollow spindles filled completely with ferrofluid so that there is no free surface [45]. They report that when the ferrofluid spindles are placed in a rotating magnetic field a non-zero torque is measured even in the absence of free surfaces. The issue of whether this observed torque necessarily implies an internal fluid flow remains open for debate.

Rosensweig's model for the spin-up flow of magnetic fluid in a uniform magnetic field considers the interfacial deformation of a free ferrofluid surface having contact angle θ_0 with a container wall [39]. The deformation of the ferrofluid results in a magnetic surface shear stress driven flow. The surface-driven flow is believed to be usually stronger than that produced by the spin diffusion model which was recently treated by Rinaldi [35]. The volume flow field resulting from the surface-driven model, however, remained unmeasured until recently [9]. Rosensweig conducted a careful set of experiments with concave, flat and convex free surface shapes by respectively under-filling, filling to the brim, and slightly over-filling a container with ferrofluid. He reports counter-rotation for concave surface shapes, no rotation for flat surface shapes, and co-rotation for convex surface shapes. Rosensweig concludes that this observed behavior constitutes evidence that surface stress rather than a volume torque density drives the spin-up flow [39]. Rosensweig, however, observed only the flow velocity at the top free surface of the ferrofluid, and the flow in the bulk of the ferrofluid was not known.

Shliomis and Zaitsev argued in their early work that macroscopic velocities were possible only if non-uniform spin velocities existed in the bulk of ferrofluid [53, 52]. The authors solved the ferrohydrodynamic equations, under a limiting set of assumptions, for the velocity and spin velocity profiles, taking into account the spin-diffusion term (i.e., they considered non-zero spin viscosity). More recently, Shliomis, Pshenichnikov *et. al* have reported that the early spin-diffusion model predicted velocities that fell short of experimentally observed values by three to four orders of magnitude [32, 31]. The authors conclude that spin diffusion leads to negligible rotational flows and propose two alternative mechanisms: tangential surface shear stress at the ferrofluid meniscus and magnetic field gradients induced by thermal gradients in the bulk of the ferrofluid.

Most researchers in the field espouse views that are more or less aligned with Shliomis' conclusions as evidenced by [31]. The statement that negligible spin-diffusion, *i.e.,* when $\eta' = 0$, cannot result in rotational flow in a uniform rotating magnetic field is, however, misleading. Shliomis' analysis [53, 32], as well as similar arguments by Pshenichnikov and Lebedev [31], decouple the magnetic and hydrodynamic equations by neglecting the linear and spin velocity terms in the magnetization relaxation equation. This means that while the magnetic fields drive the ferrofluid flow, the resulting flow does not affect the field. Rosensweig considers a spatially constant spin velocity but neglects the effect of linear velocity in the magnetization relaxation equation [40]. Chapter 8 continues the discussion of these issues and presents numerical solutions that take into account the nonlinear convective derivative terms in the magnetization relaxation equation as well as the spin diffusion term.

1.3 Overview of thesis

This thesis documents the investigation of the dominant force and torque mechanisms in ferrofluids in uniform, dc and rotating magnetic fields. As a result of our research effort, we succeeded in developing simple tractable analytical and numerical models to describe ferrofluid spin-up flow that agree with velocity profile measurements.

1.3.1 Research methodology

Interfacial force effects of uniform horizontal and vertical magnetic fields on the shape of a ferrofluid meniscus were studied. Hele-Shaw cell experiments demonstrated the role of magnetic forces and torques on ferrofluid flows and patterns in combined dc and rotating magnetic fields. Spin-up volume flows of ferrofluids were investigated in rotating uniform magnetic fields.

Finite element analysis was used to examine the basic assumptions of simple analytical models and to refine further theoretical predictions (*e.g.*, finite element analysis was used to extend the analytical low Reynolds number expressions for flow profiles at higher Reynolds numbers). This modeling effort was combined with careful experimental investigations to verify theoretical predictions.

The opacity of ferrofluid rules out laser Doppler or streak path techniques for measuring the bulk velocity flow profiles. Experimental measurements of the velocity in the bulk of the ferrofluid can help decide the debate in the ferrofluid spin-up literature. There have been no investigations of ferrofluid spin-up in the literature that report the flow velocities inside the bulk of the ferrofluid prior to our collaborative effort with the Rinaldi research group [9]. Experimental techniques thus far have been limited to studying the flow profile on the top surface of the ferrofluid by recording the motion of floating tracer particles. Pshenichnikov reports covering the surface of the ferrofluid with particles of aluminum powder and using photographs to examine the flow profiles [31]. Others have used similar techniques to measure spin-up flow [39, 8, 16].

The pulsed ultrasound velocimetry technique uses reflections off small tracer particles or air bubbles suspended in the fluid volume. The technique then uses the time of flight of the reflected ultrasound beams to estimate the velocity of the tracer particles. A clear advantage of this technique is that it allows non-disruptive measurement of the flow profile in opaque fluids since the ultrasound probes can be placed in the walls of the ferrofluid container without directly contacting ferrofluid. Investigators have reported using this technique to investigate the flow of various fluid flows including flow of liquid metals and ferrofluids [6, 7, 17, 46].

With this ultrasound velocimetry we have investigated the r and z dependence of bulk flows in a cylindrical container of ferrofluid driven by a rotating magnetic field. The measured flow profiles agreed well with theoretical analysis reported by Rinaldi in the literature [35] and with numerical simulations. Moreover, by fitting measured velocity profiles to theory, the magnetization relaxation time constant and the spin viscosity coefficient for were determined for MSG W11 and EMG705 water-based ferrofluids. Moreover, ultrasound measurements of ferrofluid spin-up flow confirm flow reversal in ferrofluid spin-up flow in an uncovered container. Measurements show that the volume flow velocity co-rotates with the applied rotating magnetic field, which agrees with spin-diffusion theory [35], while the free surface of the ferrofluid counter-rotated as predicted by Rosensweig *et al.* [39] for a concave free surface.

1.3.2 Thesis preview

Chapter 2 presents a summary of some useful magnetic, rheological and physical properties of the ferrofluids used in experiments and simulations as well as a brief description of the experimental techniques used to measure these properties.

Chapter 3 describes an optical system using reflections of a narrow laser beam to measure the height and shape of a ferrofluid meniscus in response to a uniform applied magnetic field. Characterization of the effect of an applied magnetic field on the ferrofluid interface is an important first step in understanding the surface-shear-stress-driven flows experimentally observed in ferrofluids.

Chapter 4 describes energy models for determining the height of the meniscus formed when a ferrofluid wets a wall in horizontal and vertical applied uniform magnetic fields. These models explain the trends observed in Chapter 3.

Chapter 5 presents preliminary analytical and numerical models for surface shear stress driven flows in cylindrical cavities. This chapter assumes a known surface shear stress drive due to the magnetic phenomena discussed in Chapters 3 and 4.

Chapter 6 presents observations of spiral pattern formation and abrupt phase-transformation like behavior of Hele-Shaw cells in combinations of vertical dc and in-plane rotating magnetic fields. The chapter applies the results of Appendix B to predict some features of the observed patterns.

Chapter 7 presents the results of the pulsed ultrasound velocimetry experimental investigation of ferrofluid spin-up flow phenomena by measuring bulk and free top surface interfacial velocities of the ferrofluid.

Chapter 8 uses FEMLAB software to compare the predictions of an iterative finite element numerical simulation with the experimentally observed bulk flows in Chapter

7, in order to determine best fit values of magnetization relaxation time and ferrofluid spin viscosity.

Chapter 2

Ferrofluid physical parameters

This chapter summarizes the measured physical properties of three commercial ferrofluid samples used extensively throughout the experiments and analyses reported in the following chapters of this thesis. We performed a wide array of experimental characterization techniques on Ferrotec Corp. oil-based ferrofluid EFH1, and water-based ferrofluids MSG W11 and EMG 705. Any physical properties for NBF-1677 fluorocarbon-based ferrofluid reported in this chapter were not measured by us and are taken directly from T. Franklin's thesis [13]. Some measurements were performed also on non-magnetic fluids like de-ionized (DI) water and Nytro—a commercial transformer oil—to test the operation of the experimental apparatus and build confidence in the measurements we report. For each of the fluid samples we measured the speed of sound in the fluid, the mass density, surface tension, and viscosity. Furthermore, for magnetic fluid samples, we measured the magnetization curve from which we determined the saturation magnetization, the low-field magnetic susceptibility, and volume fraction of magnetic material in order to obtain rough estimates for the range of nanoparticle diameters. Finally, Transmission Electron Microscopy (TEM) was used to measure the distribution of ferrofluid particle sizes more accurately.

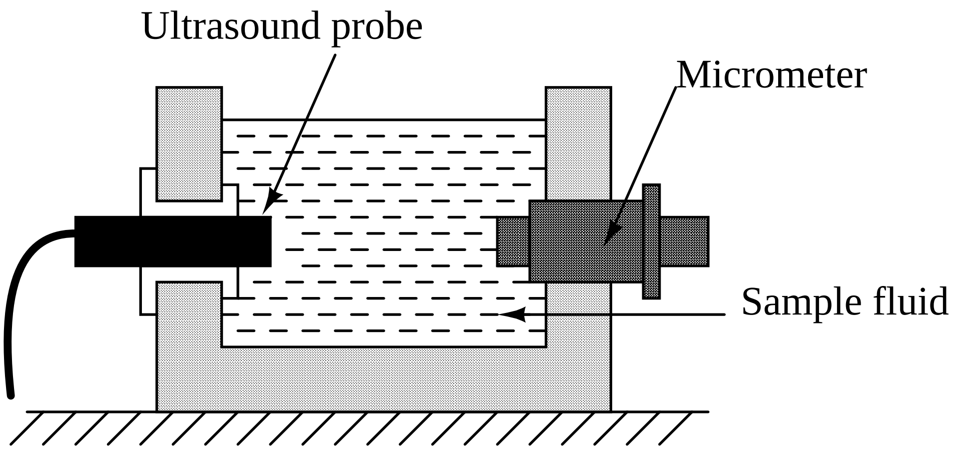

Figure 2-1: Schematic cross-section showing the container used to measure the speed of sound in the sample fluids.

2.1 Speed of sound measurement

The ultrasound velocimetry results presented in Chapter 7 require precise knowledge of speed of sound in the fluid sample to interpret the ultrasound reflections. Table 2.1 lists the results of two experimental techniques to measure the speed of sound in ferrofluids under investigation as well as DI water and Nytro, a commercial transformer oil, for reference. Both techniques adapt Signal Processing Corporation's DOP 2000 pulsed ultrasound velocimeter to measure the speed of sound in a fluid sample in a container provided by Signal Processing Corporation specifically for measuring the speed of sound in fluids. The cylindrical vessel houses a calibrated micrometer and an insertable ultrasound probe at diametrically opposite ends on the perimeter. Turning the micrometer changes the distance between the probe and the opposite reflecting surface in a controllable fashion. The first method–suggested by Signal Processing– measures the differential change in the ultrasonic echo correlation signal due to a known incremental change in the distance between the face of the ultrasound probe and the reflecting face of the micrometer. The ratio between the nominal change in round-trip distance and actual change in distance leads to an estimate of the speed of sound in the fluid sample.

The results of the first method (*i.e.*, Signal Processing's method) were not repeatable enough to inspire trust without corroboration from an independent experiment.

While the technique usually yields reasonable results, small errors or disturbances in turning the micrometer can lead to a string of unreasonably high measured sound speeds. The second method (MIT's relative method) uses the same experimental setup as the first differential method, but avoids the requirement of changing the reflection distance. Instead the micrometer is maintained at a known fixed position while recording the echo correlation signals for all the different fluid samples in sequence. The speed of sound for the various ferrofluid samples is determined relative to a reference fluid sample (*e.g.*, de-ionized water). Table 2.1 demonstrates that the results of the two techniques of measuring the speed of sound at 18° Celsius differ by less than 5%, which falls well within practical engineering margins. Moreover, Bilanuik *et al.* [5] quote a value of 1476 m/s for the speed of sound in water at a temperature of 18° Celsius, which again differs from our relatively simple measurement by less than 0.1%. The agreement between the two measurement techniques, as well as the close agreement with the accepted value for the speed of sound in water inspire confidence in the measured values of the speed of sound in the ferrofluid samples.

2.2 Mechanical properties

2.2.1 Mass density

The mass densities of each of the sample ferrofluids used in our research effort are summarized in Table 2.2. The mass density is needed in our magnetization measurements to convert measured fluid weight to volume accurately and subsequently convert the measured magnetization in emu (electromagnetic units) to gauss using the relationship $\mu_0 M[\text{gauss}] = 4\pi[\text{emu}]/\text{volume}[\text{cc}]$. The values for the mass densities were determined by filling a container of calibrated volume with the sample fluid. The difference in weight between the full and empty container divided by the volume of the container yields the mass density listed in Table 2.2. The values we report fall within the range given in Ferrotec Corporation's data sheets.

Fluid sample	Speed of sound [m/s] Signal Processing method	Speed of sound [m/s] MIT relative method	Diff. %
DI water	1459	1462	+0.21
Nytro (oil)	1456	1403	-3.64
EMG705 water-based	1487	1432	-3.70
MSG W11 water-based	1487	1439	-3.23
EFH1 oil-based	1143	1116	-2.36

Table 2.1: Speed of sound measurements for water-based ferrofluids, an oil-based ferrofluid, and non-magnetic fluids at a temperature of 18° Celsius. The results of two different techniques of measuring the speed of sound agree to within less than 4%. The value of the speed of sound in water at 20° Celsius reported in the literature is 1476 m/s which exceeds our measured value by about 0.1% only.

2.2.2 Viscosity

We obtained the viscosities summarized in Table 2.2 by using the CSL500 rheometer from TA instruments configured in a Couette cell geometry. The rheometer performed a controlled shear-rate sweep to determine the viscosity of the suspension. Because ferrofluids act like Newtonian fluids even with applied magnetic field, the resulting shear-strain to shear-rate profile is a straight line with constant slope. The ratio of the shear-strain to the shear-rate given by the slope of the measured profile is the viscosity of the fluid. Note that the EFH1 oil-based ferrofluid is about 3.6 times as viscous as MSG W11 water-based ferrofluid and 2.9 times as viscous as EMG705 water based ferrofluid.

2.2.3 Surface tension

The coefficient of surface tension is a measure of the force necessary to hold a fluid interface together. We estimated the surface tension by measuring the peak spacing and threshold magnetic field at the incipience of the Rosensweig peaking instability in perpendicular magnetic fields [3]. The surface tension results were verified using a Krüss Tensiometer (K10ST). This apparatus first dips a small metal plate slightly below the surface of the fluid sample and then records the force needed to pull the plate out. Table 2.2 shows that surface tension measurement techniques agree within 1.8% for MSG W11 and to within 5.2% for EFH1. Note that the standard accepted value for the surface tension of water in the literature is 72.8 mN/m [11], which exceeds the value we measured with the tensiometer by only 1.2%.

2.3 Magnetic properties

Magnetization curves for the sample ferrofluids were characterized using a vibrating sample magnetometer (VSM) model 880 Digital Measurement System (DMS) by ADE Technologies. Tests were performed on small samples of fluid placed in a standard DMS plastic container with a 6.0 mm internal diameter, and an internal height

Fluid sample	Mass density [kg/m^3]	Surface tension Fluid/air [mN/m] Peaking method	Surface tension Fluid/air [mN/m] Tensiometer method	Viscosity [cP]
DI Water	998	—	71.9	1.01
Nytro (oil)	890	—	23.4	10.26
EMG705 water-based	1194	—	42.1	2.48
MSG W11 water-based	1200	38.4	39.1	2.02
EFH1 oil-based	1221	23.5	24.8	7.27
NBF-1677 [13] fluorocarbon-based	1169	—	—	—

Table 2.2: Mass density, surface tension and viscosity of non-magnetic fluids, water-based and oil-based Ferrotec ferrofluids. The surface tension of the ferrofluid/air interface was estimated from observing the incipience of the Rosensweig peaking instability [3] as well as directly measured using a Krüss Tensiometer (K10ST). The viscosities were measured using a CSL500 rheometer from TA instruments configured in a Couette cell geometry. We performed a controlled shear-rate sweep to determine the viscosity of the fluid sample.

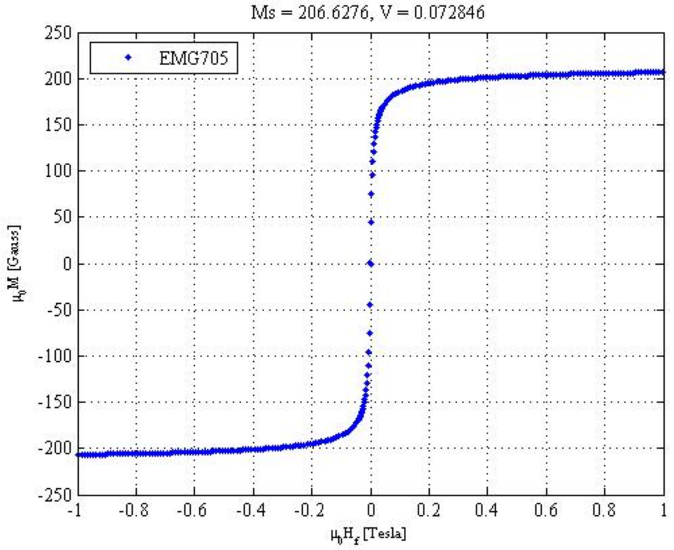

Figure 2-2: Measured magnetization relation curve for EMG705 water-based ferrofluid.

of 2.5 mm. The applied magnetic field was smoothly increased in small increments until magnetic saturation was reached. We also carefully investigated the magnetization in the linear regime with low applied magnetic fields to determine the magnetic susceptibility χ. The details of VSM measurement are discussed in detail in Chapter 2 of Thomas A. Franklin's master's thesis [13]. Franklin describes how to use the measured magnetization curves and a simple Langevin model to estimate the range of nanoparticle diameters in the sample ferrofluid. The magnetic parameters relevant to our research (*i.e.*, the saturation magnetization and the magnetic susceptibility) are summarized in Table 2.3. The reader should be aware that in this thesis measured values of the magnetization M and magnetic field intensity H, which have proper SI units of Amps/m, are generally reported as $\mu_0 M$ and and $\mu_0 H$ with units of gauss, a preference of the author. The volume fraction of magnetic particles listed in the table is based on a nominal magnetization ($\mu_0 M_d$) of 5600 gauss for magnetite.

Ferrofluid sample	Saturation magnetization [G] $\mu_0 M_s$	Magnetic susceptibility χ	Volume fraction % vol. $\phi = \frac{\mu_0 M_S}{\mu_0 M_d}$	Estimated particle diameter (VSM) [nm]	TEM particle diameter [nm]
EMG705 water-based	206.6	1.89	3.69	7.9-16.9	4.8-19.5 mean: 15.6 ± 5.3
MSG W11 water-based	153.9	0.56	2.75	5.5-12.4	6.3-27.6 mean: 9.4 ± 3.4
EFH1 oil-based	421.2	1.59	7.52	6.9-13.3	—
NBF-1677 [13] fluorocarbon-based	394.1	3.03	7.0	9.7-15.9	—

Table 2.3: Magnetic properties of oil-based and water-based ferrofluids. An ADE Technologies model 880 Digital Measurement System (DMS) vibrating sample magnetometer (VSM) was used to characterize the magnetization curve of a small sample of each ferrofluid. Particle sizes were estimated by fitting a Langevin curve to the magnetization data from the vibrating sample magnetometer (VSM) and was also observed directly with Transmission Electron Microscopy. We were unable to obtain clear uncontaminated TEM images of the EFH1 oil-based ferrofluid because the oil based ferrofluid does not evaporate completely.

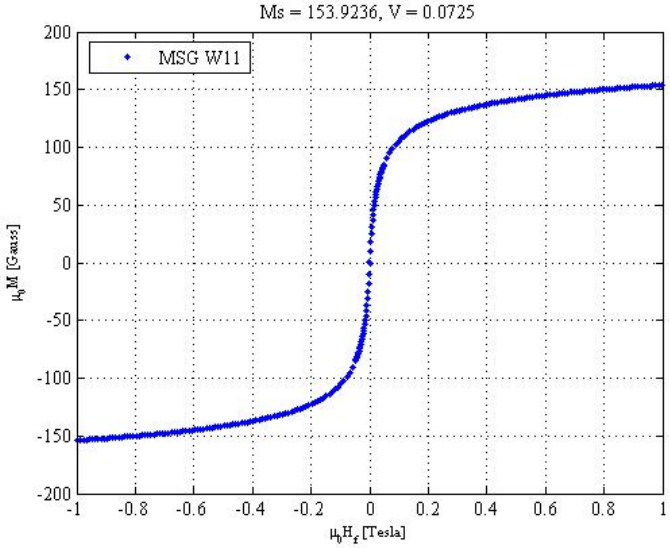

Figure 2-3: Magnetization curve for MSG W11 water-based ferrofluid.

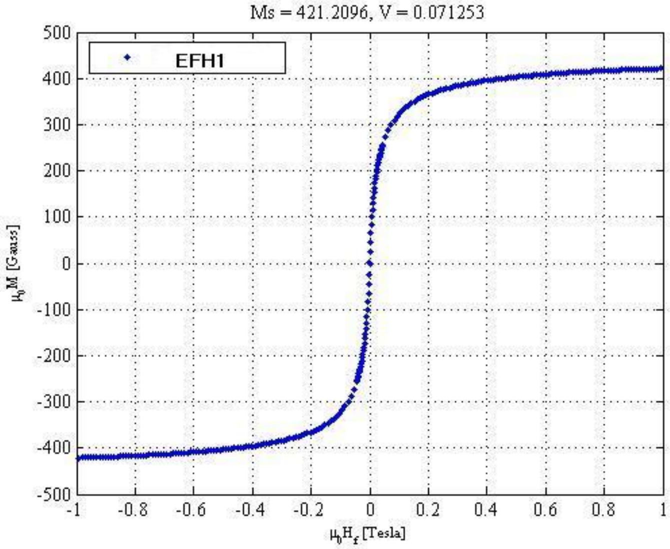

Figure 2-4: Magnetization curve for EFH1 water-based ferrofluid.

2.4 Particle size

The VSM data summarized in Table 2.3 allows us to estimate the range of ferrofluid particle sizes. The minimum and maximum particle sizes can be calculated from fitting VSM measurements to the high field and low field limits of the Langevin curve respectively. Table 2.3 compares the VSM estimates to Transmission Electron Microscopy results.

Note that the TEM particle diameter values in the second column of Table 2.3 represent the smallest and largest particles observed in the TEM images. TEM images show a distribution of MSG W11 particle sizes with a mean particle diameter of 15.6 nm and a standard deviation of ±5.3 nm (See Fig. 2-5). The particle size distribution for EMG705 had a mean of 9.4 nm and standard deviation of ±3.4 nm (See Fig. 2-6). We were unable to obtain clear uncontaminated TEM images of the EFH1 oil-based ferrofluid because the oil based ferrofluid does not evaporate completely and the residue hydrocarbons react with the electron beam.

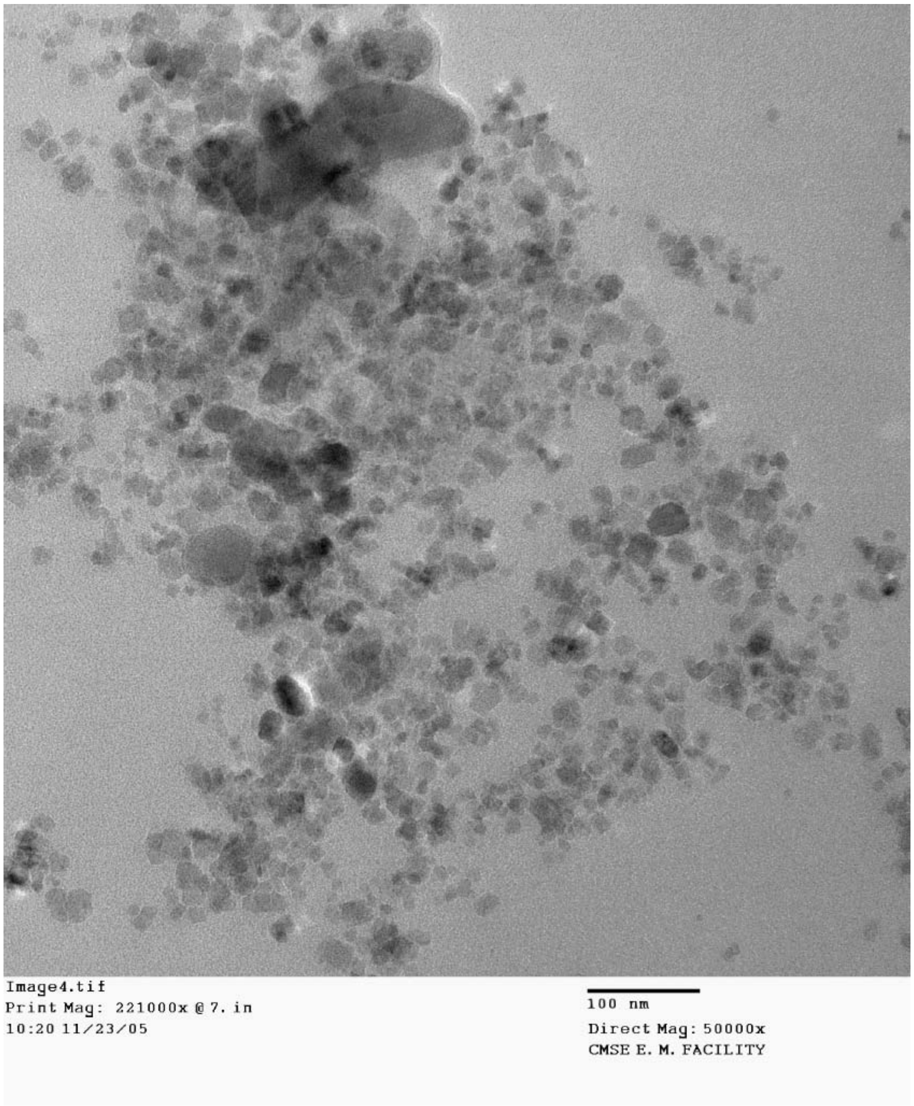

Figure 2-5: Transmission Electron Microscope image of EMG705 ferrofluid (50, 000× magnification). The magnetic nanoparticles have a mean diameter of 9.4 nm and a standard deviation of ±3.4 nm .

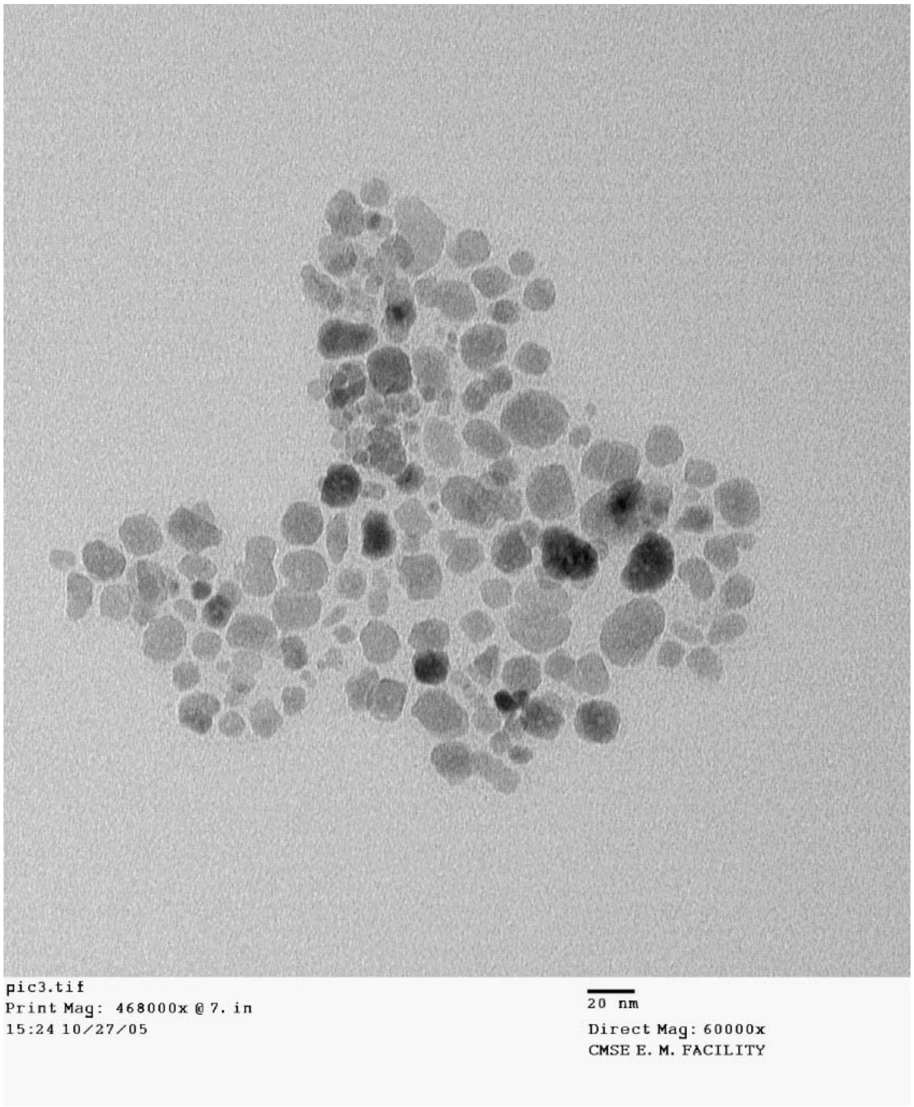

Figure 2-6: Transmission Electron Microscope image of MSG W11 ferrofluid particles ($60,000\times$ magnification). The magnetic nanoparticles have a mean diameter of 15.6 nm and a standard deviation of ±5.3 nm

Chapter 3

Laser measurement of ferrofluid meniscus shape in a uniform applied magnetic field

3.1 Introduction

This chapter documents an optical measurement technique of the equilibrium shape of the meniscus formed when a ferrofluid contacts a vertical glass surface. Initially, we investigated the shape of the meniscus for EFH1 oil-based and MSG W11 water-based ferrofluids by immersing a glass slide in a container of ferrofluid with no applied magnetic field. A uniform-dc-magnetic field was subsequently applied to a glass container of ferrofluid in the three configurations illustrated in Fig. 3-1. In the first configuration, the applied magnetic field is tangential to both the glass slide and the flat portion of the ferrofluid meniscus. In the second configuration the applied magnetic field is perpendicular to the glass slide and tangential to the flat portion of the ferrofluid meniscus. The applied magnetic field is tangential to the glass slide and perpendicular to the flat portion of the interface in the third configuration. We used a Helmholtz coil configuration to generate the applied magnetic fields in configurations a and b, resulting in a $\sim$ 30 gauss per ampere scaling between current and field strength. In configuration c we used a single coil with a core of highly permeable iron to generate fields that scaled as $\sim$ 20 gauss/ampere with current.

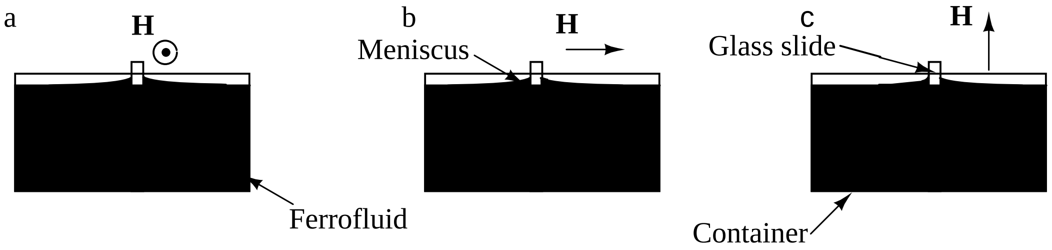

Figure 3-1: The three magnetic field configurations of the ferrofluid meniscus experimentally investigated.

3.2 Experimental setup

Fig. 3-2 illustrates the experimental setup for measurement of meniscus height and shape. A laser is mounted above a container of ferrofluid so that its position can be accurately controlled with a micrometer. The laser shines a narrow beam vertically through a transparent calibrated glass pane onto the ferrofluid surface. The laser beam gets reflected back onto the glass pane where the reflected beam's position on the glass pane is recorded. Far from the glass slide and the container walls, in the flat region of the ferrofluid meniscus, the reflected beam is vertical and it intersects the glass pane at the same position as the incident beam. As we translate the laser towards the glass slide, it enters the region where the meniscus begins to curve. Consequently the reflected beam deflects from the vertical and the distance between the two laser points on the glass pane increases.

The deflection of the reflected beam from the vertical incident beam is related to the slope of the ferrofluid by simple geometry, as illustrated in Fig. 3-3. From the figure we see that the angle θ_L between the incident and reflected beams is double the angle θ_F formed by the tangent to the ferrofluid meniscus at the point of incidence with the horizontal:

$$\theta_L = 2\theta_F \tag{3.1}$$

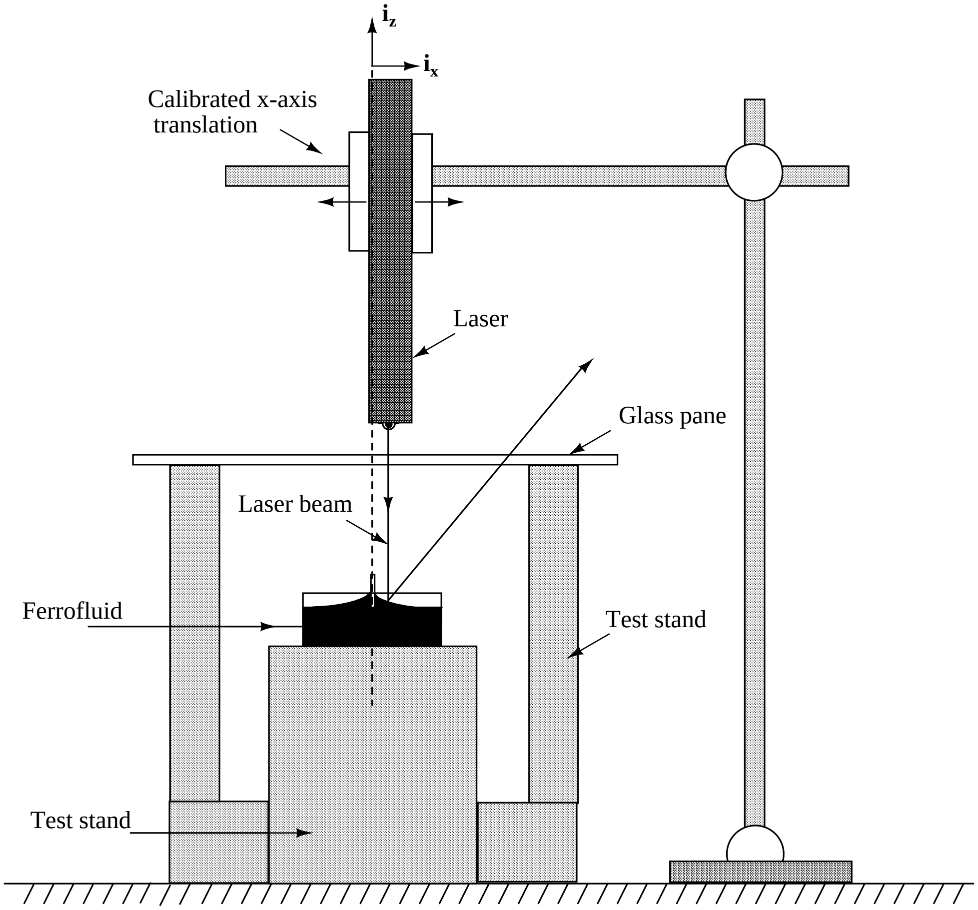

Figure 3-2: The experimental setup for optically measuring the shape of the ferrofluid meniscus with no applied magnetic field. The laser beam reflects off the surface of the ferrofluid to the observed point on the glass pane. The angle by which the beam is deflected from the vertical depends on the slope of the ferrofluid meniscus.

We also see from the figure that Δ, the distance between the two points where the laser intersects the glass pane is related to the angle θ_F by,

$$\theta_F = \frac{\theta_L}{2} = \frac{1}{2}\tan^{-1}(\frac{\Delta}{H-\xi}) \tag{3.2}$$

where H, the distance between the glass pane and the flat region of the ferrofluid meniscus, is much larger than the meniscus height ξ so that $H - \xi \approx H$. The slope of the meniscus is related to the angle θ_F by the expression,

$$\tan\theta_F = -\frac{d\xi}{dx} \tag{3.3}$$

Integration of the measured slope of the ferrofluid yields the height of the meniscus as a function of distance from the glass slide. The height of the ferrofluid far from the glass slide in the flat region of the meniscus is taken to be zero.

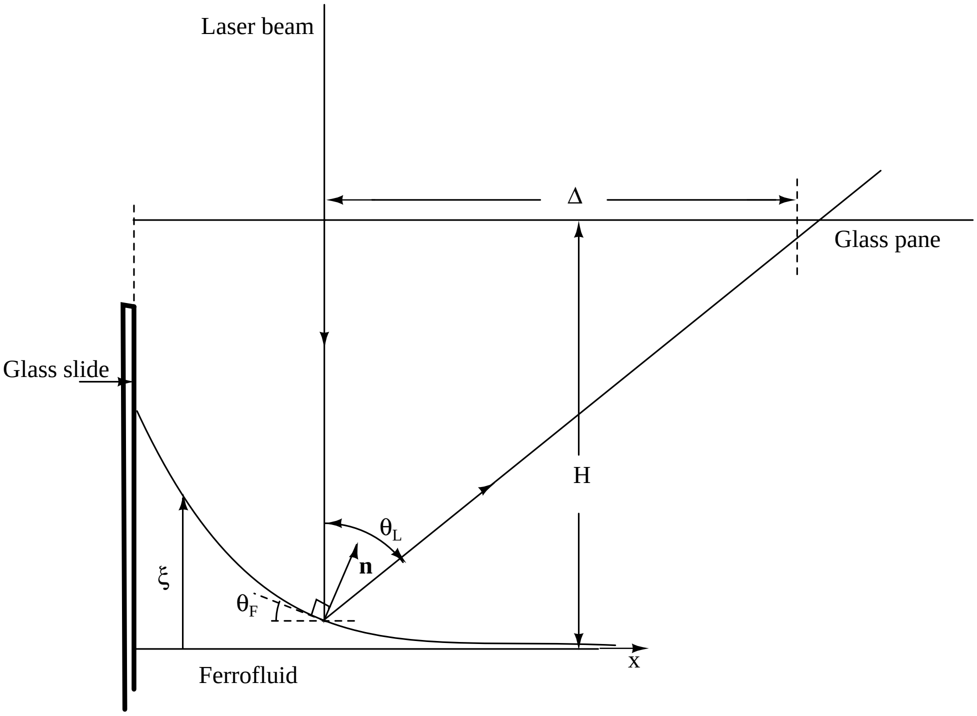

Figure 3-3: Geometric relationship of the laser beam's deflection from the vertical to the local slope of the ferrofluid meniscus. The shape of the meniscus is obtained from the integration of measured slope values. The height of the ferrofluid far away from the walls is taken to be zero.

The finite diameter of the laser beam (1.0 mm for our measurements) poses a serious challenge in this system of measurement. The curvature of the meniscus increases near the glass slide, deforming the reflected beam into a long thin ellipse because the slope of the ferrofluid interface changes significantly across the width of the laser beam. Fig. 3-4 illustrates how the ferrofluid meniscus acts like a concave mirror, first focusing then elongating the impression of the reflected laser beam on the glass pane. To overcome this difficulty the relative positions of the left-most and right-most edges of the two laser spots on the glass pane were recorded and processed as two independent sets of measurements. We can apply Eq. 3.2 twice to compute θ_{F1} and θ_{F2} using the displacements Δ_1 and Δ_2. Fig. 3-4 shows the case when the focal point is below the glass pane, but relationship for the case when the focal point is above the glass pane can be similarly derived. The elongation and blurriness of the reflected laser beam reduces the quality of our measurements near the glass slide where the slope of the meniscus is large. The accuracy of the measurement near the glass slide can, of course, be improved by reducing the diameter of the laser beam.

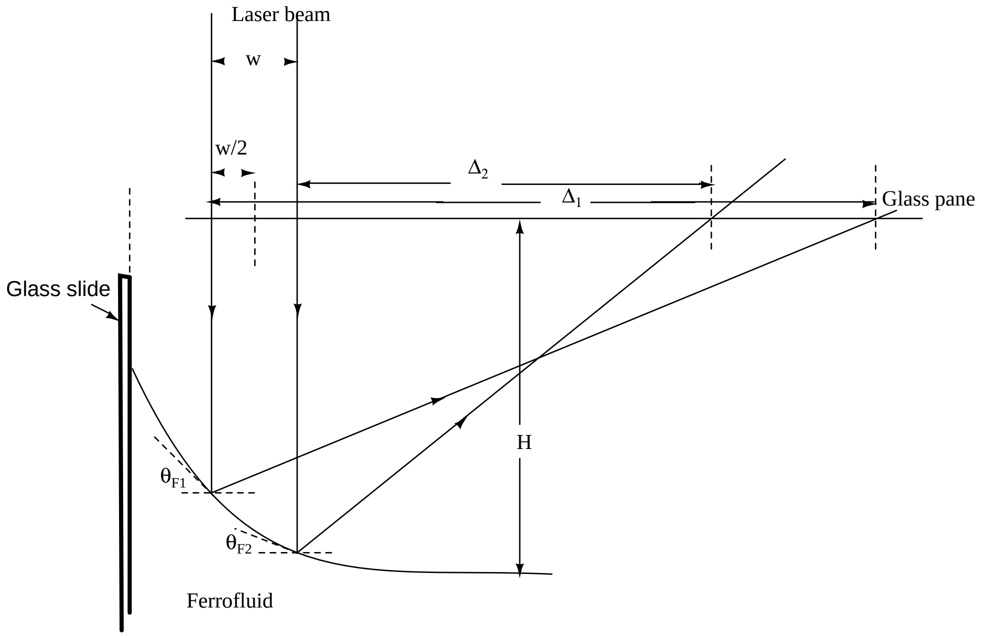

Figure 3-4: Geometrical optics of the laser beam reflection off the surface of the ferrofluid. The curvature of the ferrofluid meniscus first focuses and then disperses the reflected laser beam as the beam moves towards the glass slide.

3.3 Meniscus measurements in a large beaker

A pair of electromagnets in a Helmholtz coil configuration were used to excite the uniform field in configurations *a* and *b*. For configuration *c*, only one electromagnet was used because a Helmholtz coil in this configuration would have completely enclosed the experimental vessel making it difficult to investigate the shape of the meniscus with laser reflections. The electromagnets used were two identical cylindrical copper coils with a height of 13 cm, an inner radius of 18 cm and an outer radius of 27 cm. In a Helmholtz coil configuration the centers of the two circular coils are spaced by an axial distance equal to the average coil radius (22.5 cm) to generate a very uniform magnetic field on axis. The total number of turns in each coil is 235.

To form the meniscus a glass slide (7.5 cm × 2.5 cm) was immersed in a large 300 ml cylindrical beaker partially filled with ferrofluid. The long dimension of the glass slide was placed against the bottom of the beaker and we measured the meniscus shape at the midpoint of the slide to minimize the effects from the edges of the glass slide. The beaker had a diameter of 15 cm and a height of 6 cm and was filled with ferrofluid up to a 2 cm level. The beaker was positioned inside the Helmholtz coil setup so that the ferrofluid interface was near the magnetic axis of the electromagnets. Fig. 3-5 shows measurements of the highly uniform magnetic flux density, with magnetic field applied in configuration *b*, in the air right above the central region of a glass beaker filled with EFH1 oil-based ferrofluid. The location of the flat ferrofluid interface far away from the glass slide in the figure is at $z = 0$ and the location of the glass slide is at $x = 0$. The magnetic field in this setup remained relatively uniform near the glass slide.

3.3.1 No applied magnetic field

We first measured the shape of the ferrofluid meniscus without any magnetic field. Fig.s 3-6 and 3-7 document these measurements for water-based (MSG W11) and oil-based (EFH1) ferrofluids respectively. Each figure shows three sets of measurements that were performed just prior to the application of the magnetic field in each of the

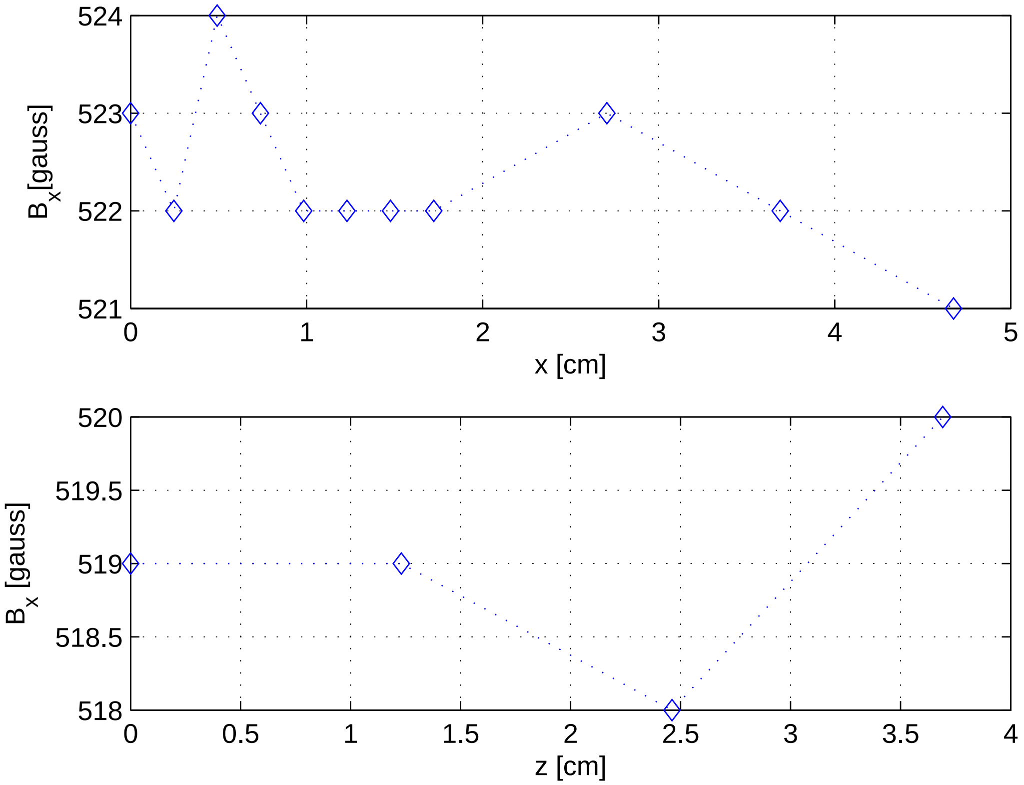

Figure 3-5: The variation of horizontal magnetic flux density $B_x(x, z)$ in the central region of a glass beaker filled with oil-based ferrofluid. Measurements on the air side just above the ferrofluid show horizontal (x) and vertical (z) variations in magnetic flux density.

configurations shown in Fig. 3-1 and were done on different days with the same batch of ferrofluid re-poured each time. The solid curves in the figures show the Landau and Lifschitz [23] theoretical expression for the shape of a fluid meniscus in the absence of magnetic forces,

$$\frac{x}{a} = \frac{1}{\sqrt{2}} \cosh^{-1} \frac{a\sqrt{2}}{\xi} - \sqrt{2 - \left(\frac{\xi}{a}\right)^2} - \frac{1}{\sqrt{2}} \cosh^{-1} \frac{a\sqrt{2}}{h} + \sqrt{2 - \left(\frac{h}{a}\right)^2} \tag{3.4}$$

where a is the capillary length and $h = \xi(x = 0)$ is related to the contact angle θ_0 by the expression,

$$h = a\sqrt{1 - \sin\theta_0} \tag{3.5}$$

These relationships are derived in Chapter 4, and extended to include magnetic forces. Note that our expression for the shape of the meniscus in Eq. 3.4 differs from the Landau and Lifschitz expression by a minus sign. This disagreement is due to a sign error in the derivation published by Landau and Lifschitz and is discussed in our theoretical investigation of ferrofluid interfacial behavior in Chapter. 4.

The parameters a and θ_0 are selected to minimize the least squares error between the theoretical curve and the experimental data. For MSG W11 water-based ferrofluid $a = 2.7$ mm and $\theta_0 = 40°$, whereas for EFH1 oil-based ferrofluid $a = 2.0$ mm and $\theta_0 = 50°$. Figs. 3-6 and 3-7 demonstrate that the theory and experimental data are in good agreement with no applied magnetic field.

The capillary length, a, can also be calculated from the ferrofluid properties given in Table 2.2 according to the expression,

$$a = \sqrt{\frac{2\sigma}{\rho g}} \tag{3.6}$$

where σ is the surface tension, ρ is the density, and g is the acceleration due to gravity. Representative parameter values for Ferrotec Corp. water-based ferrofluid (MSG W11) are $\rho = 1200$ kg/m^3 and $\sigma = 0.0384$ N/m yielding $a = 2.55$ mm. For EFH1 oil-based ferrofluid $\rho = 1221$ kg/m^3 and $\sigma = 0.0235$ N/m yields $a = 1.98$ mm. The calculated values of the capillary length agree with the values observed experimentally.

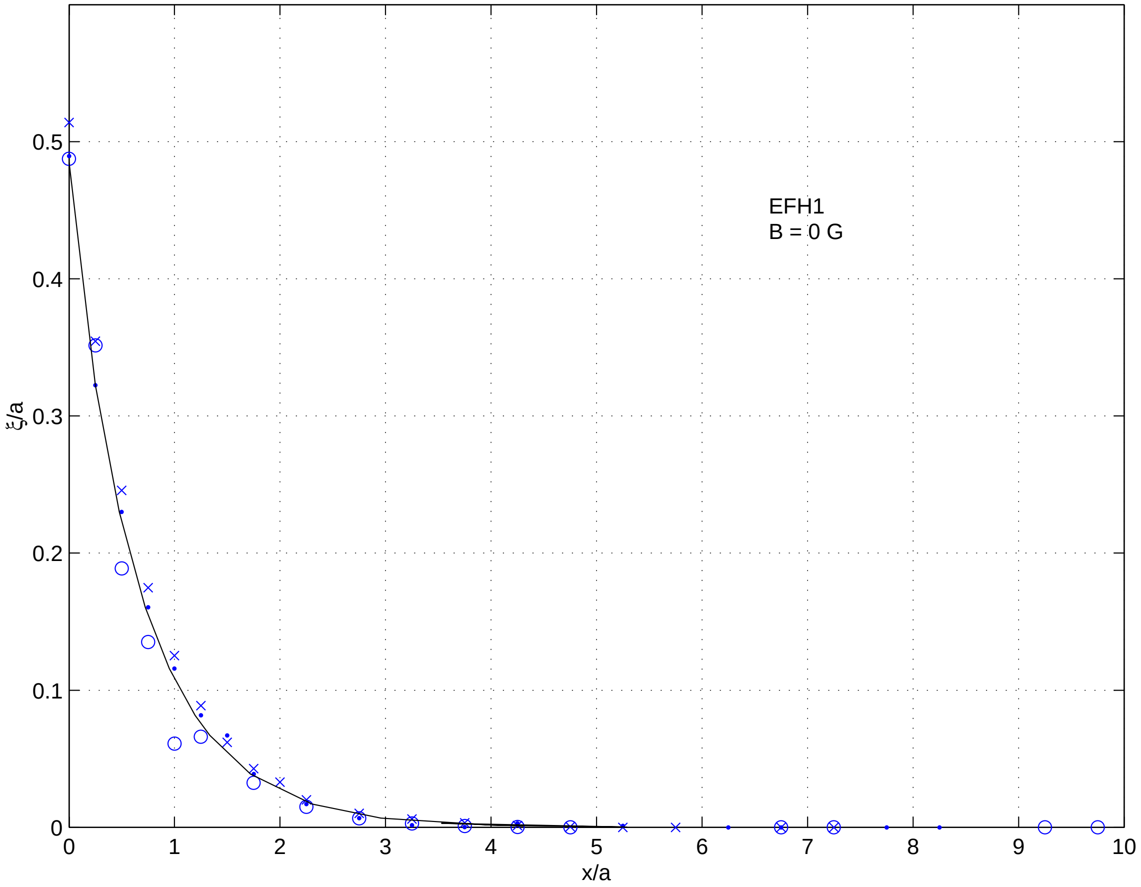

Figure 3-6: The shape of the meniscus formed when a water-based ferrofluid (MSG W11) wets a glass slide with no applied magnetic field. The solid curve shows the least-squares method best fit of the data to the theoretical expression of Landau and Lifschitz (Eq. 3.4), with best fit parameters $a = 2.7$ mm and $\theta_0 = 40°$. The figure shows three independent sets of repeated measurements under identical conditions with zero applied magnetic field denoted by $\times$, $\cdot$ and $\circ$.

3.3.2 Applied horizontal tangential magnetic field (configuration *a*)

Fig.s 3-8 and 3-9 show the effect of a horizontal magnetic field, as in configuration *a* in Fig. 3-1, on oil-based and water-based ferrofluids contacting a glass surface.

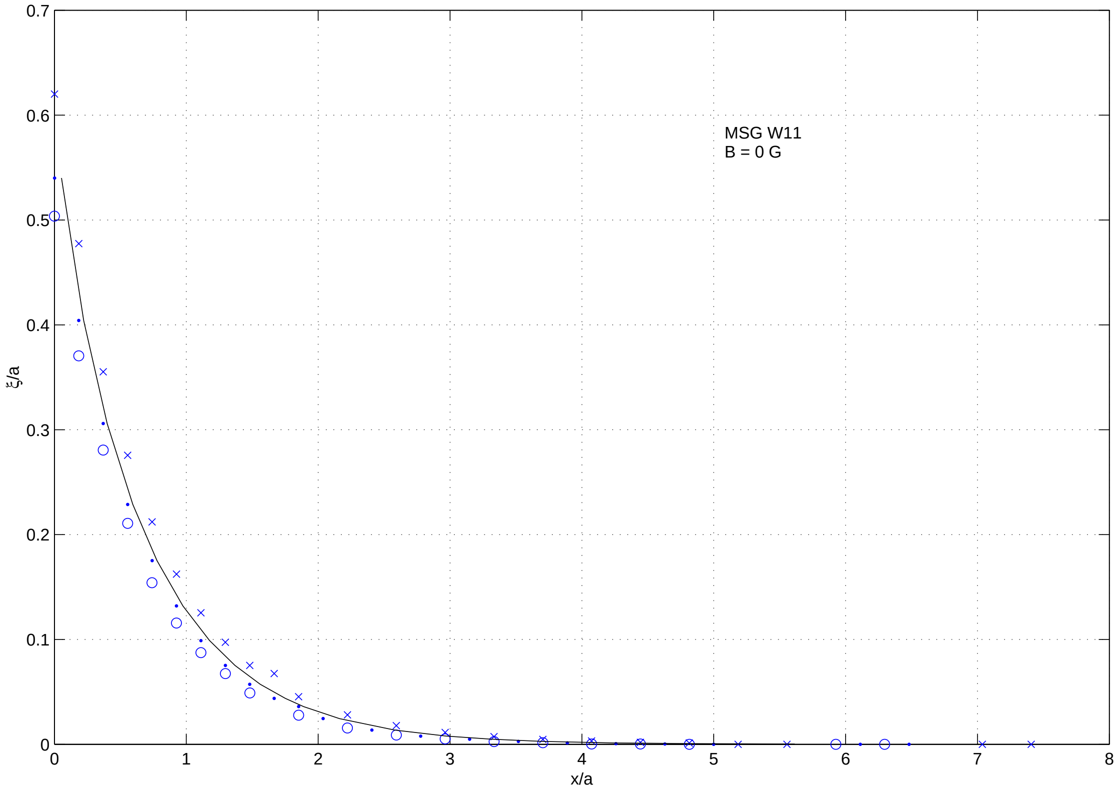

Figure 3-7: The shape of the meniscus formed when an oil-based ferrofluid (EFH1) wets a glass slide with no applied magnetic field. Best fit parameters for the solid curve are $a = 2.0$ mm and $\theta_0 = 50°$. The figure shows three independent sets of repeated measurements under identical conditions with zero applied magnetic field denoted by $\times$, $\cdot$ and $\circ$.

Experiments demonstrate that the effects of the magnetic field in this configuration are negligible, as expected from theory. These results provide further proof of the uniformity of the magnetic field at the ferrofluid interface in our experimental setup, since even a small gradient in the magnetic field can lead to significant forces and alter the shape of the ferrofluid meniscus.

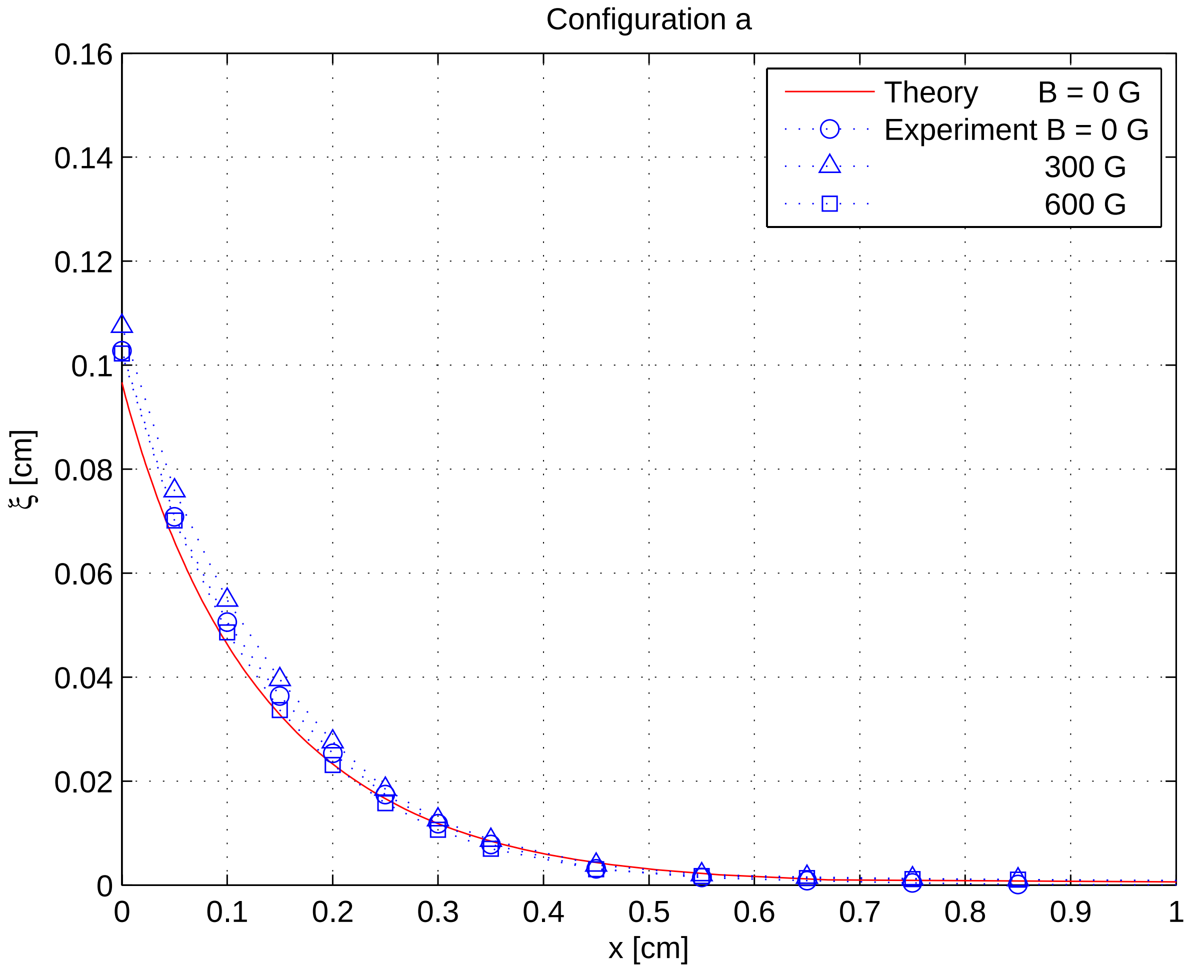

Figure 3-8: The shape of the meniscus formed when an oil-based ferrofluid (EFH1) wets a glass slide with an applied horizontal magnetic field in configuration *a* of Fig. 3-1. The meniscus shape at zero applied magnetic field (○) is essentially unaffected by configuration *a* applied magnetic field strengths of 300 G (□) and 600 G (△).

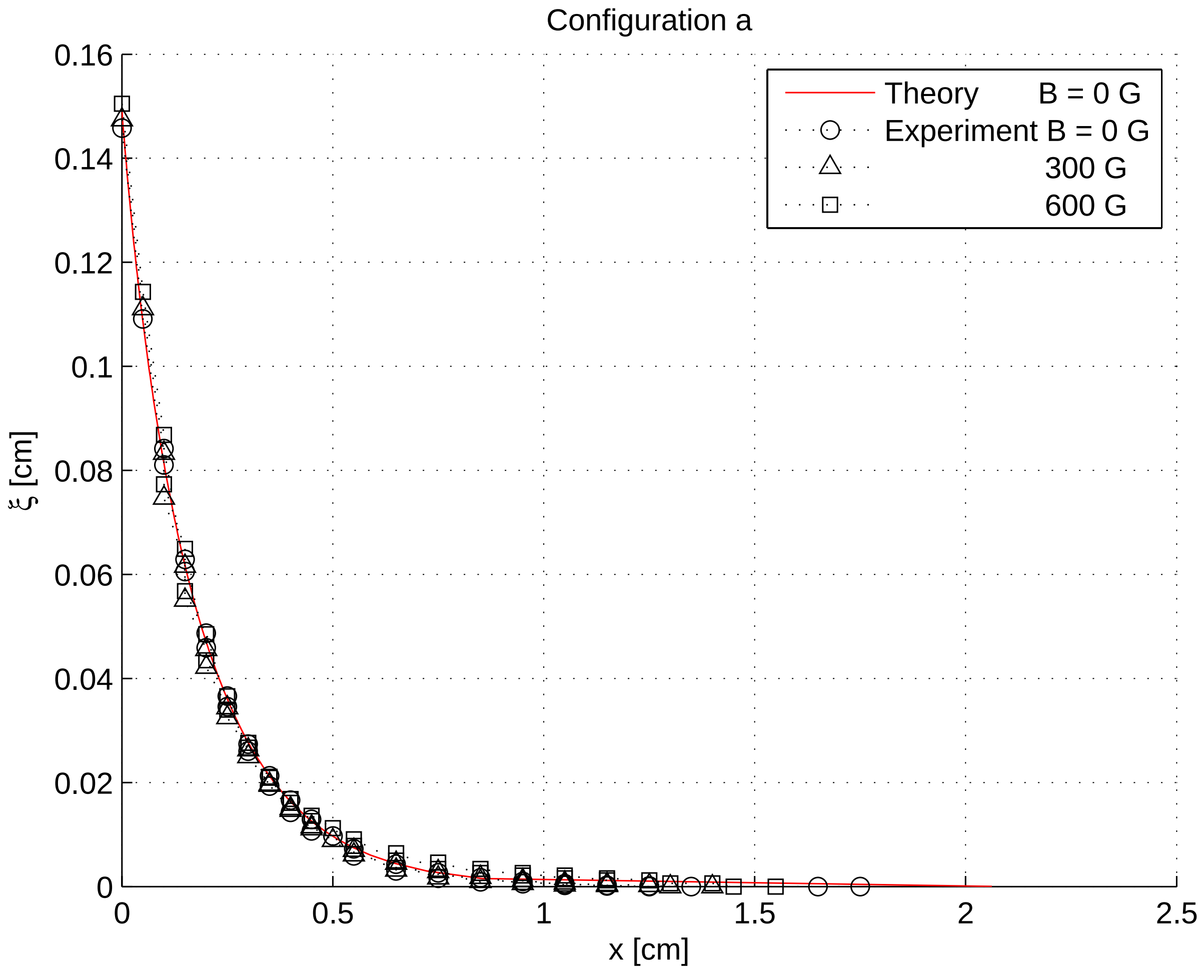

Figure 3-9: The shape of the meniscus formed when a water-based ferrofluid (MSG W11) wets a glass slide with an applied horizontal magnetic field in configuration *a* of Fig. 3-1. The meniscus at zero magnetic field (○) is essentially unaffected by the applied magnetic field strengths of 300 G (□) and 600 G (△).

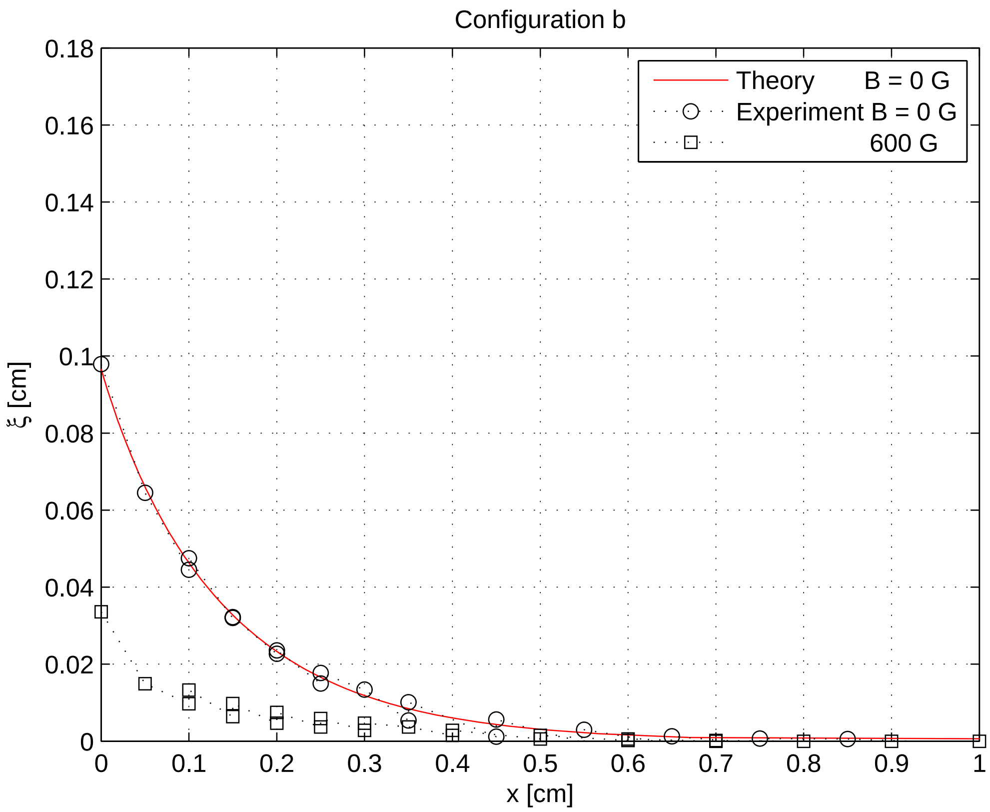

Figure 3-10: The shape of the meniscus formed when an oil-based ferrofluid wets a glass slide with an applied horizontal magnetic field (configuration *b* in Fig. 3-1). The meniscus height decreases with an increased applied field strength of 600 G (□).

3.3.3 Horizontal perpendicular applied magnetic field (configuration *b*)

Fig.s 3-10 and 3-11 show the effect of a horizontal magnetic field in configuration *b* of Fig. 3-1 on oil-based (EFH1) and water-based (MSG W11) ferrofluids contacting a glass surface. Experiments show that a horizontal magnetic field decreases the height of the ferrofluid meniscus. Increasing the magnetic field strength to the maximum available value leads to a steady depression of the ferrofluid interface. The strength of the generated magnetic fields was limited by the capabilities of the available equipment, which were less than ~ 20 amperes (corresponding to ~ 600 G).

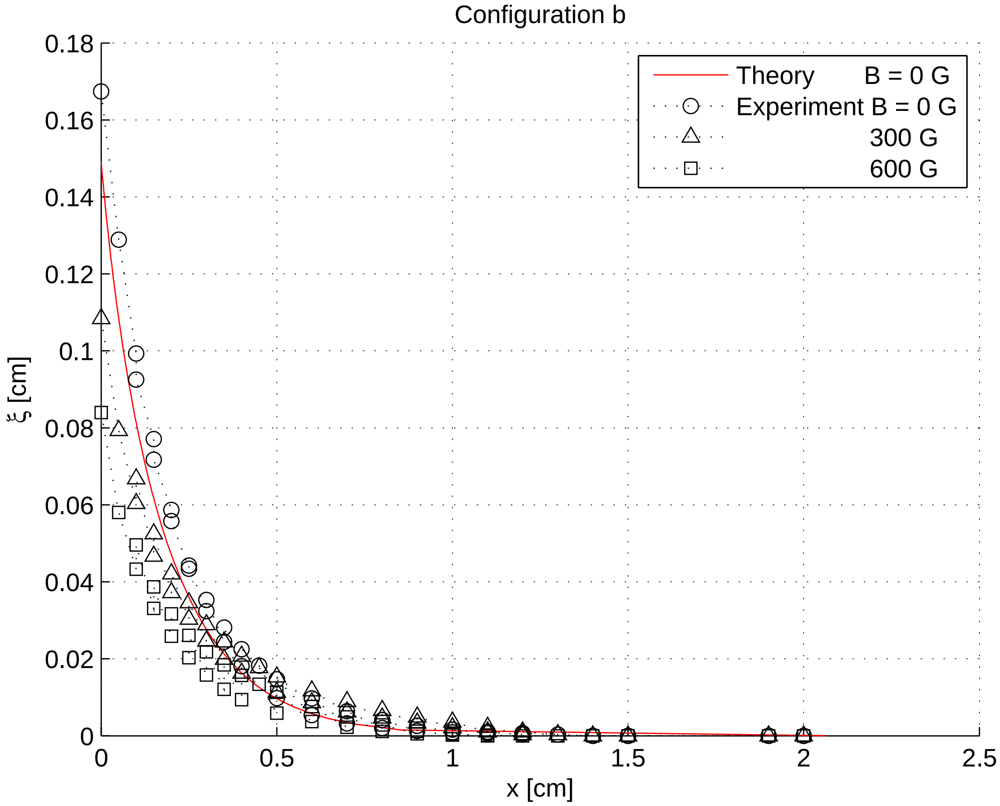

Figure 3-11: The shape of the meniscus formed when a water-based ferrofluid (MSG W11) wets a glass slide with an applied horizontal magnetic field (configuration *b* in Fig. 3-1). The meniscus height decreases with increased field strengths of 300 G (△) and 600 G (□).

3.3.4 Applied vertical magnetic field (configuration c)

Fig.s 3-12 and 3-13 show the effect of a vertical magnetic field on oil-based and water-based ferrofluids contacting a glass surface. Experiments show that a vertical magnetic field increases the height of the ferrofluid meniscus. This increase in meniscus height is limited by the critical value of vertical magnetic field at which the Cowley-Rosensweig instability [10] occurs and ferrofluid peaks begin to form. For magnetic field strengths greater than the threshold value for the instability, the ferrofluid interface does not remain smooth and hexagonally spaced peaks cover the surface of the ferrofluid. For MSG W11 water-based ferrofluid the critical value of the magnetic field was observed at ~ 642 gauss and whereas for EFH1 the critical value was observed to be as low as ~ 81.9 gauss, which is in agreement with the analysis presented by Amin and Elborai in [3].

3.4 Meniscus measurements in a small rectangular container

Experiments were also conducted in a small (10.2 cm ×5.1 cm ×5.1 cm) rectangular glass container, where instead of inserting a glass slide we observed the meniscus formed at the walls of the small container. We measured the magnetic field at the edges of the container. These measurements show that the ferrofluid significantly affects the uniformity of the magnetic field. The field non-uniformity becomes most significant at the edges of the container. Fig. 3-14 shows measurements of the horizontal magnetic field applied in configuration b in the air outside the wall of a small glass container filled with oil-based ferrofluid. The hall probe was moved along the outside wall of the glass container. The ferrofluid demagnetizing field tends to lower the magnetic field strength inside the ferrofluid. The ferrofluid feels a force that acts to move it towards regions of higher magnetic field strength. The effects of this magnetic field gradient force significantly alter the behavior of the ferrofluid meniscus in our experiments.

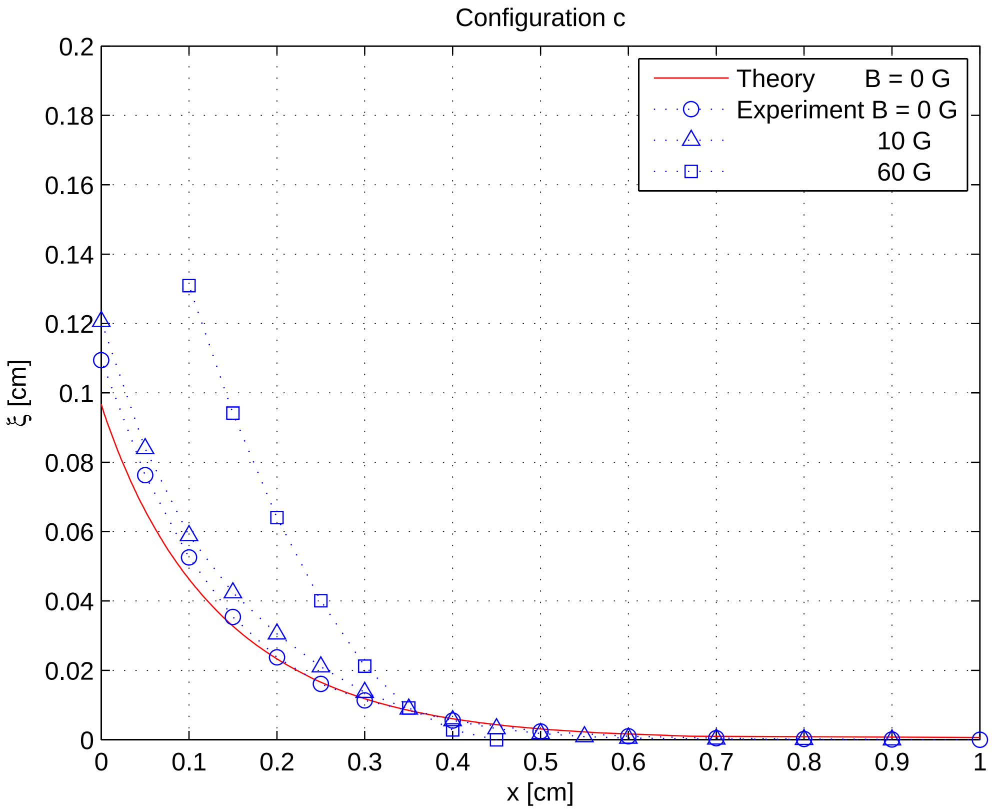

Figure 3-12: The shape of the meniscus formed when an oil-based ferrofluid (EFH1) wets a glass slide with an applied vertical magnetic field (configuration *c* in Fig. 3-1). The meniscus rises with increased field strength. The magnetic flux density scales with current as $\sim$ 20 gauss/ampere in this configuration.

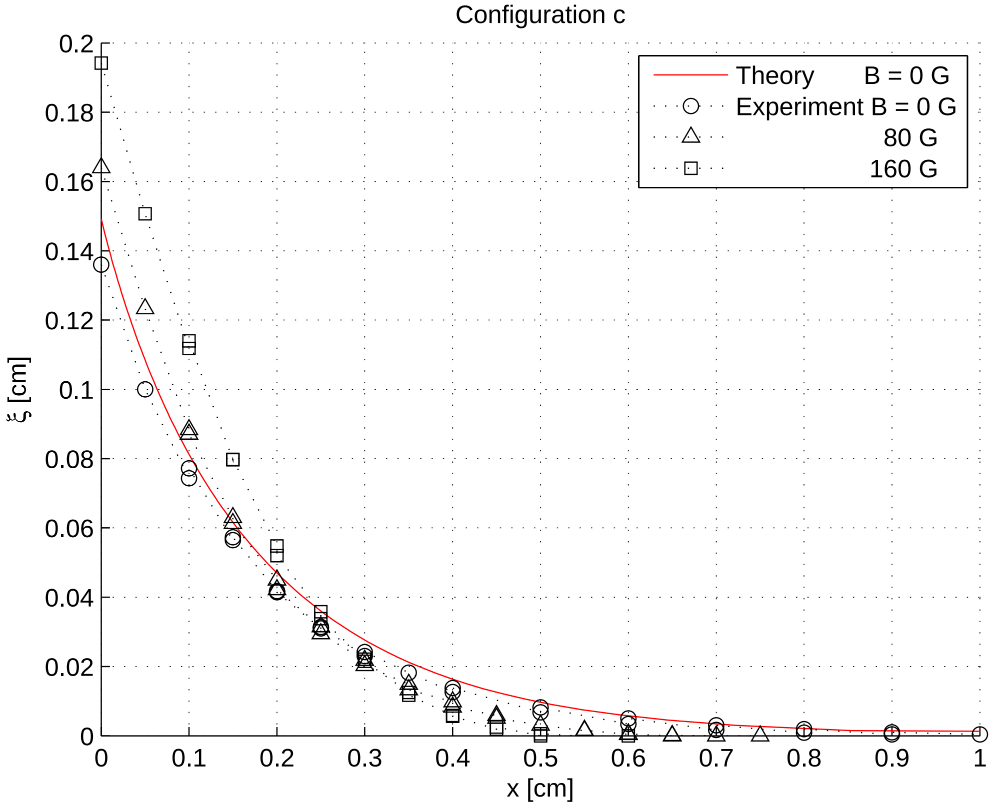

Figure 3-13: The shape of the meniscus formed when a water-based ferrofluid (MSG W11) wets a glass slide with an applied vertical magnetic field (configuration *c* in Fig. 3-1). The meniscus rises with increased field strength. The magnetic flux density scales with current as $\sim$ 20 gauss/ampere in this configuration.

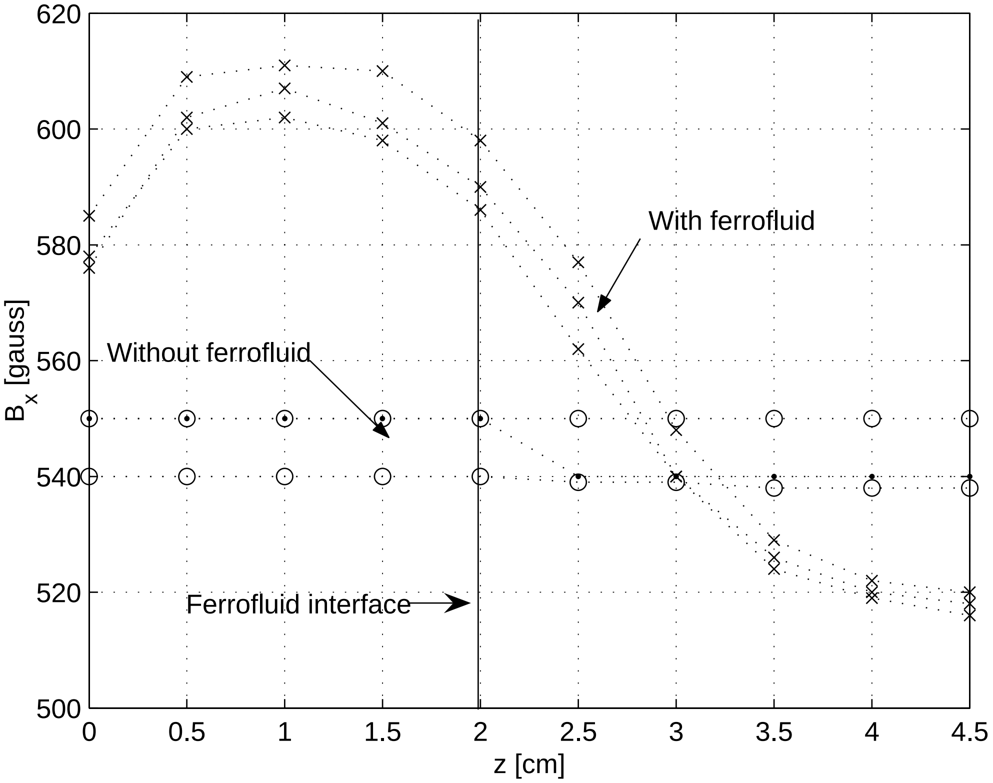

Figure 3-14: The variation of the horizontal magnetic flux density with vertical parameter z at the edge of the narrow side-wall of a small rectangular glass container partially filled with oil-based ferrofluid. Measurements are shown for the case without ferrofluid (◯) and for the case with ferrofluid (×). The ferrofluid interface is at $z = 0$. The transverse hall probe was tightly pressed against the outer edge of the container wall.

3.4.1 Applied horizontal tangential magnetic field (configuration a)

Fig. 3-15 shows the effects of the applied horizontal magnetic field on the meniscus formed by an oil-based ferrofluid on the walls of a small rectangular container. The height of the meniscus increases significantly with increasing magnetic field strength. The effects of the magnetic field are stronger than any of the measurements described in Section 3.3. At higher values of the magnetic field incremental increases of the applied field strength result in only small changes in the height and shape of the meniscus.

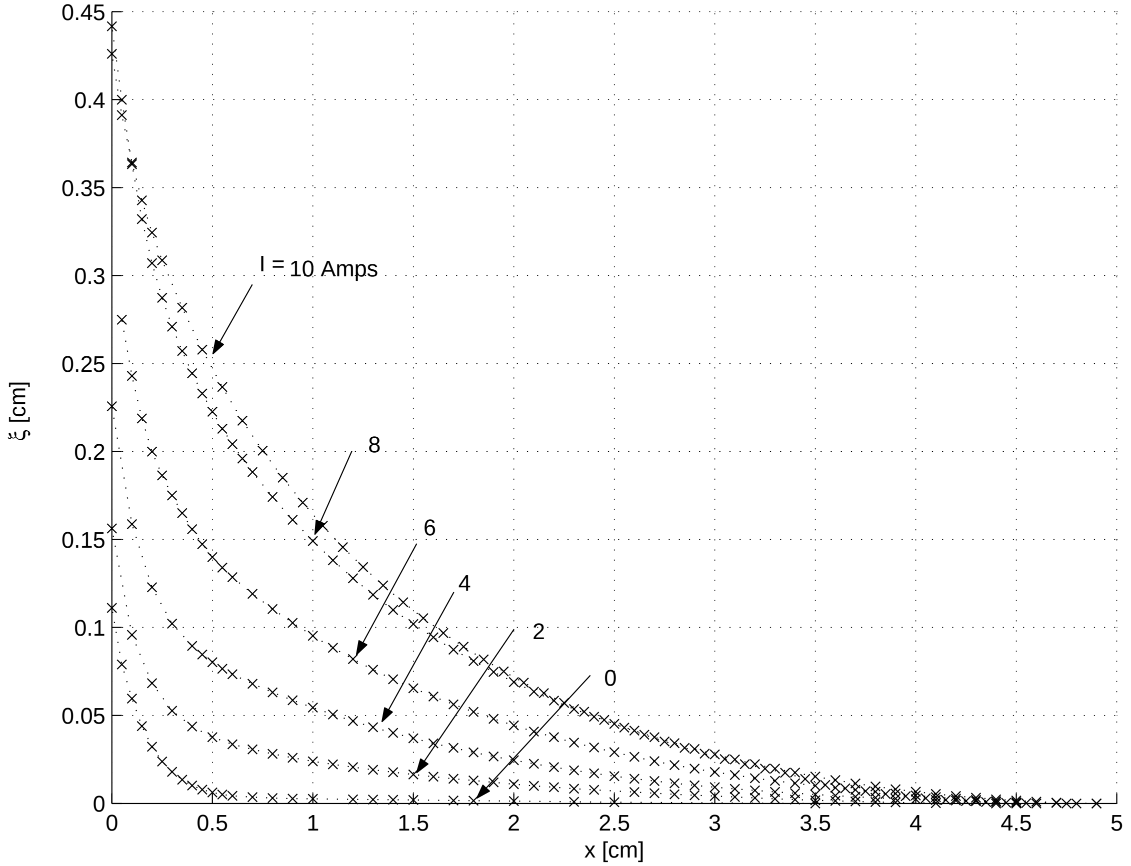

Figure 3-15: The shape of the meniscus formed when an oil-based ferrofluid (EFH1) wets the glass wall of a rectangular container with an applied tangential magnetic field (configuration a in Fig. 3-1). The meniscus rises with increased field strength. The magnetic flux density scales with current as ~ 30 gauss/ampere in this configuration.

3.4.2 Horizontal perpendicular applied magnetic field (configuration *b*)

Fig. 3-16 shows the effects of a horizontal magnetic field applied in configuration *b* on the shape of the ferrofluid meniscus in a small rectangular container. The ferrofluid height increases with increasing magnetic field strength. However, the effects of the magnetic field strength on the meniscus height are smaller for higher values of magnetic field strength.

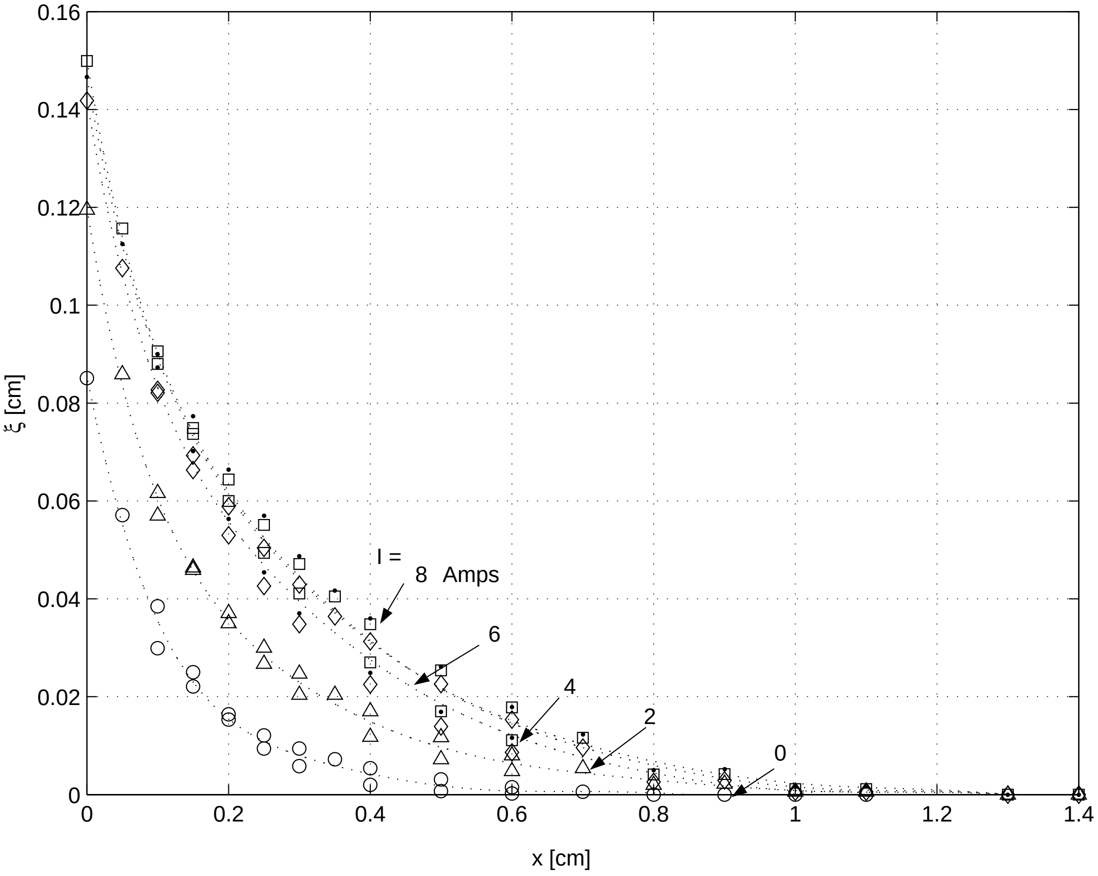

Figure 3-16: The shape of the meniscus formed when an oil-based ferrofluid (EFH1) wets the glass wall of a rectangular container with an applied horizontal magnetic field (configuration *b* in Fig. 3-1). The meniscus rises with increased field strength. The magnetic flux density scales with current as $\sim$ 30 gauss/ampere in this configuration.

3.4.3 Applied vertical magnetic field (configuration *c*)

Fig. 3-17 shows the effects of a vertical magnetic field on the shape of an oil-based ferrofluid meniscus formed in a small rectangular container. The ferrofluid meniscus rise exceeds that of the corresponding case in Section 3.3. The maximum magnetic field strength is limited by peak formation at the onset of the Cowley-Rosensweig surface instability [10].

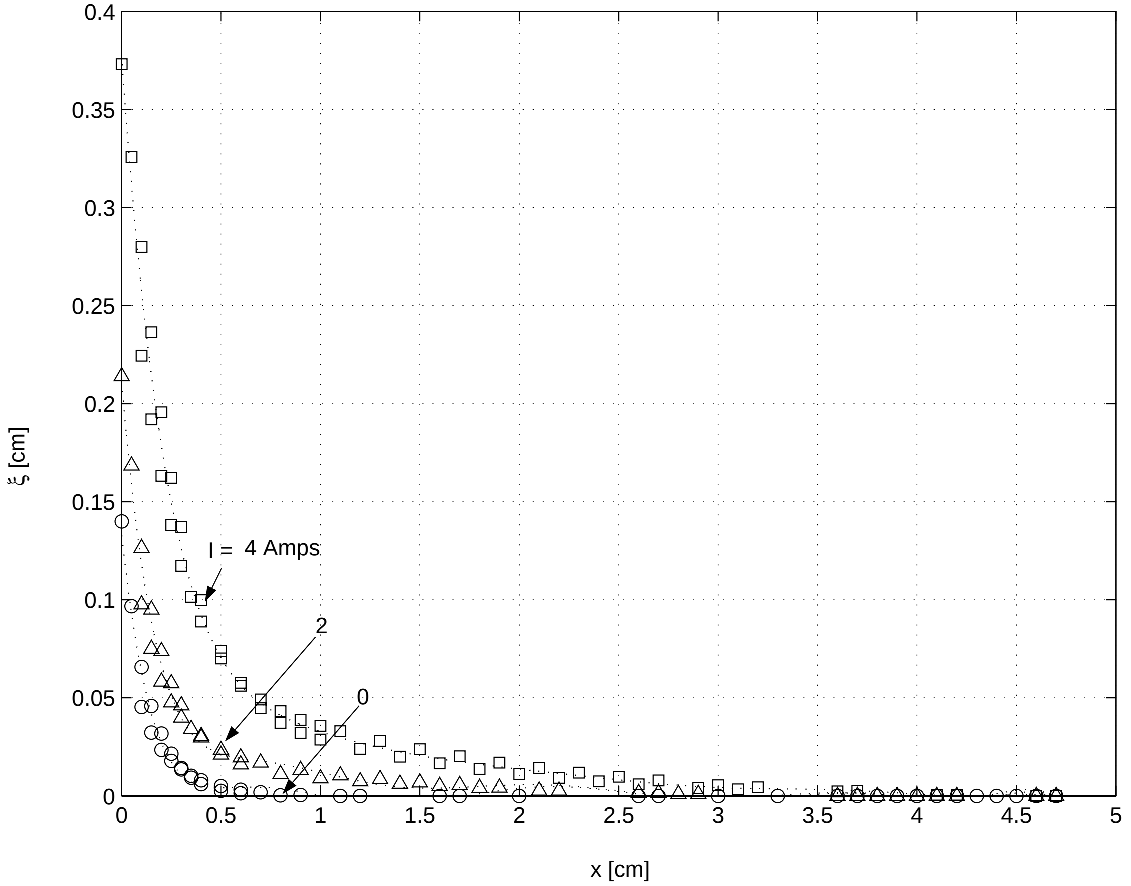

Figure 3-17: The shape of the meniscus formed when an oil-based ferrofluid wets the glass wall of a rectangular container with an applied vertical magnetic field (configuration *c* in Fig. 3-1). The meniscus rises with increased field strength. The magnetic flux density scales with current as $\sim$ 20 gauss/ampere in this configuration.

3.5 Summary of results

The experimental data presented in this chapter shows that for a glass slide partially immersed in a large cylindrical container of ferrofluid a horizontal field perpendicular to the wall reduces meniscus height, a vertical field increases the height, and a field parallel to the wall has no effect. At the side walls of a rectangular container strong effects were observed due to fringing field effects.

Chapter 4

Height of ferrofluid meniscus in applied magnetic field

4.1 Introduction

Chapter 3 of this thesis documents experiments measuring, with laser reflection, the height and shape of the meniscus formed by the partial immersion of a thin glass plate into ferrofluid contained in a large vessel. The meniscus curve formed on both sides of the immersed plate decreases in horizontal applied magnetic fields and increases in vertical applied fields. The approximate analysis presented in this chapter uses the calculus of energy minimization to determine the observed influence of an applied magnetic field on meniscus height h.

For a stationary, incompressible ferrofluid the ferrohydrodynamic form of Bernoulli's equation in the ferrofluid volume is [40],

$$p + \rho g z - \mu_0 \int_0^H M dH = constant \tag{4.1}$$

where the magnetostrictive force density is neglected because it has no effect for incompressible fluids [26].

In addition, there must be an interfacial force balance of pressure, magnetic, and surface tension forces. The i^{th} component of the interfacial surface force with interfacial normal $\mathbf{n}$ is,

$$(p_b - p_a)\, n_i + (T_{ija} - T_{ijb}) n_j + T_{si} = 0 \tag{4.2}$$

where a and b are the positions just above and just below the interface in Fig. 4-1 respectively, $p_b - p_a$ is the jump in interfacial pressure, $T_{ija} - T_{ijb}$ is the jump in magnetic stress tensor across the interface, and T_{si} is the surface tension stress.

For the interfacial deflection $\xi(x)$ shown in Fig. 4-1, the interfacial unit normal vector is

$$\mathbf{n} = \frac{\mathbf{i_z} - \frac{d\xi}{dx}\mathbf{i_x}}{\sqrt{1 + \left(\frac{d\xi}{dx}\right)^2}} \tag{4.3}$$

where there are no variations with the y coordinate as we take the wall at $x = 0$ to be flat and of infinite depth in the y direction. This one-dimensional treatment is justified for flat walls and for cylindrical vessels whose diameter is much larger than the interfacial radius of curvature.

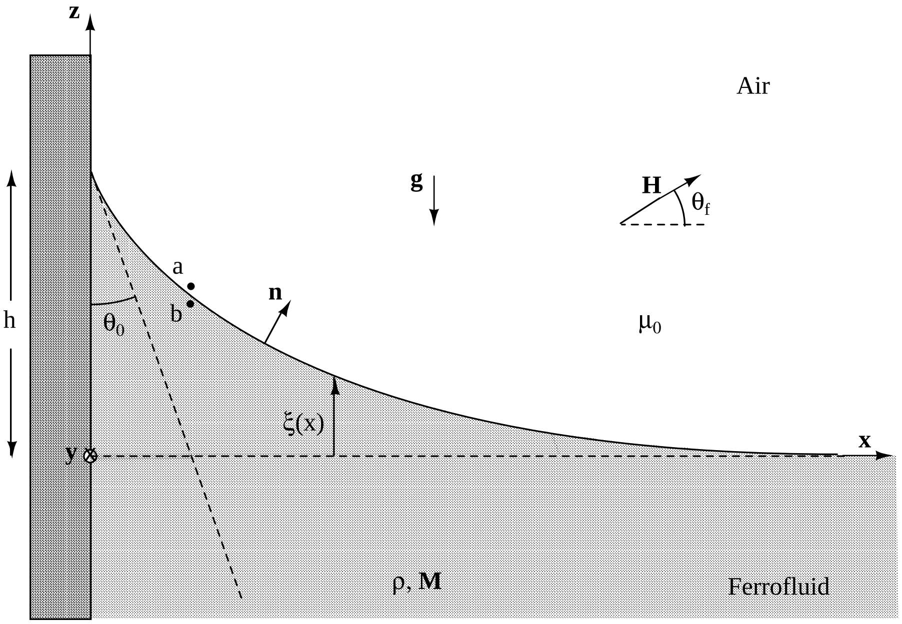

Figure 4-1: A ferrofluid in a uniform applied magnetic field at an angle θ_f to the x-axis. The ferrofluid contacts a vertical wall at $x = 0$ at an angle θ_0 rising to a height h. The shape of the meniscus is described by $\xi(x)$

The surface tension stress T_{si} depends on the radius of curvature R at the interface which is related to the unit normal vector as [26],

$$\mathbf{T}_s = -\frac{\sigma}{R}\mathbf{n} = -\sigma\left(\nabla \cdot \mathbf{n}\right)\mathbf{n} = \frac{\sigma\mathbf{n}\frac{d^2\xi}{dx^2}}{\left(1+\left(\frac{d\xi}{dx}\right)^2\right)^{\frac{3}{2}}} \tag{4.4}$$

where σ is the surface tension and the radius of curvature in the y direction is taken to be infinite.

Boundary conditions on **B** and **H** require that the normal component of **B** and tangential component of **H** be continuous across the interface.

$$\begin{aligned} B_{an} &= B_{bn} \\ H_{at} &= H_{bt} \end{aligned} \tag{4.5}$$

The magnetic stress tensor T_{ij}, where i denotes the component direction of force and j the normal to the plane on which the force acts, without magnetostriction is given by [40]

$$T_{ij} = H_i B_j - \frac{1}{2}\delta_{ij}\mu_0 H_k H_k \tag{4.6}$$

Let us take a coordinate system (t, n) which has unit vectors tangential (t) and normal (n) to the interface. Then the magnetic surface force tangential to the interface is

$$T_{tna} - T_{tnb} = H_{at}B_{an} - H_{bt}B_{bn} = 0 \tag{4.7}$$

where we used the continuity boundary conditions on tangential components of **H** and normal components of **B** (Eq. 4.5) to show that the net magnetic shear stress is zero.

Similarly, the magnetic surface force normal to the interface is

$$\begin{aligned} T_{nna} - T_{nnb} &= H_{an}B_{an} - \frac{1}{2}\mu_0\left(H_{an}^2 + H_{at}^2\right) - \left(H_{bn}B_{bn} - \frac{1}{2}\mu_0\left(H_{bn}^2 + H_{bt}^2\right)\right) \\ &= \frac{1}{2}\frac{B_{an}^2 - B_{bn}^2}{\mu_0} - \frac{1}{2}\mu_0(H_{at}^2 - H_{bt}^2) - \frac{1}{2}\mu_0(M_{an}^2 - M_{bn}^2) \\ &= \frac{1}{2}\mu_0 M_n^2 \end{aligned} \tag{4.8}$$

where $M_{an} = 0$ and $M_{bn} = M_n$ in Fig. 4-1. Both of the magnetic stress relationships in Equations 4.7 and 4.8 were derived by Rosensweig [40].

The normal component of magnetization is,

$$M_n = \mathbf{M} \cdot \mathbf{n} = M_x(x)n_x + M_z(x)n_z = \frac{M_z(x) - M_x(x)\frac{d\xi}{dx}}{\sqrt{1 + \left(\frac{d\xi}{dx}\right)^2}} \tag{4.9}$$

The normal magnetic stress is then given by the expression,

$$T_{nna} - T_{nnb} = \frac{1}{2}\mu_0 \frac{\left(M_z(x) - M_x(x)\frac{d\xi}{dx}\right)^2}{1 + \left(\frac{d\xi}{dx}\right)^2} \tag{4.10}$$

Evaluating Equation 4.1 at $z = \xi(x)$ at point b, just below the fluid interface yields

$$p_b + \rho g \xi(x) - \mu_0 \int_0^{H_b(x)} M(H)dH = constant \tag{4.11}$$

Substituting the results of Equations 4.10 and 4.4 into Equation 4.2 yields the force balance at the fluid interface,

$$p_b - p_a + \frac{1}{2}\mu_0 \frac{\left(M_z(x) - M_x(x)\frac{d\xi}{dx}\right)^2}{1 + \left(\frac{d\xi}{dx}\right)^2} + \frac{\sigma \frac{d^2\xi}{dx^2}}{\left(1 + \left(\frac{d\xi}{dx}\right)^2\right)^{\frac{3}{2}}} = 0 \tag{4.12}$$

Note that the pressure just above the interface is atmospheric, $p_a = p_0$, whereas the pressure just below the interface is a function of x, $p_b = p_b(x)$. Eliminating p_b from Equations 4.11 and 4.12 leads to the governing equation for the meniscus shape,

$$p_0 - \frac{1}{2}\mu_0 \frac{\left(M_z(x) - M_x(x)\frac{d\xi}{dx}\right)^2}{1 + \left(\frac{d\xi}{dx}\right)^2} - \frac{\sigma \frac{d^2\xi}{dx^2}}{\left(1 + \left(\frac{d\xi}{dx}\right)^2\right)^{\frac{3}{2}}} + \rho g \xi\,(x) - \mu_0 \int_0^{H_b(x)} M(H)dH = constant \tag{4.13}$$

We can evaluate the constant by taking the limit of Equation 4.11 as $x \to \infty$. At that limit the interface is flat so that $\xi(x) = 0$, $\frac{d\xi}{dx} = 0$ and the constant has the value,

$$constant = p_0 - \frac{1}{2}\mu_0 M_z^2(x \to \infty) - \mu_0 \int_0^{H_b(x \to \infty)} MdH \tag{4.14}$$

Substitution of the constant in Equation 4.14 into Equation 4.13 yields the governing equation for the meniscus shape,

$$\rho g\xi\left(x\right)+\tfrac{1}{2}\mu_0\left(M_z^2(x\to\infty)-\frac{\left(M_z(x)-M_x(x)\frac{d\xi}{dx}\right)^2}{1+\left(\frac{d\xi}{dx}\right)^2}\right)-\frac{\sigma\frac{d^2\xi}{dx^2}}{\left(1+\left(\frac{d\xi}{dx}\right)^2\right)^{\frac{3}{2}}}+\mu_0\int_{H_b(x)}^{H_b(x\to\infty)}MdH=0 \tag{4.15}$$

It is convenient to introduce the dimensional capillary length a and the following non-dimensional variables

$$a=\sqrt{\frac{2\sigma}{\rho g}},\ \ \tilde{\xi}=\frac{\xi}{a},\ \ \tilde{x}=\frac{x}{a},\ \ \tilde{z}=\frac{z}{a},\ \ N=\frac{1}{2}\mu_0\frac{M_s^2a}{\sigma},\ \ \tilde{M}_z=\frac{M_z}{M_s},\ \ \tilde{M}_x=\frac{M_x}{M_s} \tag{4.16}$$

so that Equation 4.15 in non-dimensional form is

$$2\tilde{\xi}(\tilde{x})+N\left[\tilde{M}_z^2(\tilde{x}\to\infty)-\frac{\left(\tilde{M}_z(\tilde{x})-\tilde{M}_x(\tilde{x})\frac{d\tilde{\xi}}{d\tilde{x}}\right)^2}{1+\left(\frac{d\tilde{\xi}}{d\tilde{x}}\right)^2}+\int_{\tilde{H}_b(\tilde{x})}^{\tilde{H}_b(\tilde{x}\to\infty)}\tilde{M}d\tilde{H}\right]-\frac{\frac{d^2\tilde{\xi}}{d\tilde{x}^2}}{\left(1+\left(\frac{d\tilde{\xi}}{d\tilde{x}}\right)^2\right)^{\frac{3}{2}}}=0 \tag{4.17}$$

Representative parameters for Ferrotec MSG W11 (a water-based ferrofluid) are $\mu_0M_s=153.9$ G, $\rho=1200\ \frac{kg}{m^3}$, $\sigma=0.0384\ \frac{N}{m}$ so that $a=2.55$ mm and $N=6.4$, while for an oil-based ferrofluid like Ferrotec EFH1, $\mu_0M_s=421.2$ G, $\rho=1221\ \frac{kg}{m^3}$, $\sigma=0.0235\ \frac{N}{m}$ yielding $a=1.98$ mm and $N=59.5$ (see Tables 2.2 and 2.3).

When there are no magnetic forces so that $N=0$, Equation 4.17 becomes,

$$2\tilde{\xi}(\tilde{x})-\frac{\frac{d^2\tilde{\xi}}{d\tilde{x}^2}}{\left(1+\left(\frac{d\tilde{\xi}}{d\tilde{x}}\right)^2\right)^{\frac{3}{2}}}=0 \tag{4.18}$$

which has been solved by Landau and Lifschitz [23] and used in Chapter 3. Let

$$u=\frac{1}{\sqrt{1+\left(\frac{d\tilde{\xi}}{d\tilde{x}}\right)^2}} \tag{4.19}$$

so that Equation 4.18 can be written as

$$\frac{du}{d\tilde{\xi}}=-2\tilde{\xi} \tag{4.20}$$

This integrates to

$$u = -\tilde{\xi}^2 + 1 \tag{4.21}$$

where the integration constant was determined to be unity by evaluating Equations 4.19 and 4.21 at $\tilde{x} \to \infty$ where $\tilde{\xi} = 0$ and $\frac{d\tilde{\xi}}{d\tilde{x}} = 0$.

Then using Equation 4.19 with Equation 4.21 gives the differential equation

$$\frac{d\tilde{\xi}}{d\tilde{x}} = -\frac{\tilde{\xi}\sqrt{2-\tilde{\xi}^2}}{1-\tilde{\xi}^2} \tag{4.22}$$

with solution in implicit form

$$\tilde{x} = -\frac{1}{\sqrt{2}}\cosh^{-1}\frac{\sqrt{2}}{\tilde{\xi}} + \sqrt{2-\tilde{\xi}^2} + \frac{1}{\sqrt{2}}\cosh^{-1}\frac{\sqrt{2}}{\tilde{h}} - \sqrt{2-\tilde{h}^2} \tag{4.23}$$

where we use the boundary condition that

$$\tilde{\xi}\left(\tilde{x}=0\right) = \tilde{h} \tag{4.24}$$

with $\tilde{h}$ the non-dimensional fluid height at the $\tilde{x} = 0$ wall.

Usually, $\tilde{h}$ is not known, but rather the contact angle θ_0 is known at $\tilde{x} = 0$, so that

$$\left(\frac{d\tilde{\xi}}{d\tilde{x}}\right)_{\tilde{x}=0} = -\cot\theta_0 \tag{4.25}$$

Using Equations 4.19, 4.24, and 4.25 in Equation 4.21 gives

$$\tilde{h} = \sqrt{1-\sin\theta_0} \tag{4.26}$$

Note that mathematically there are four possible roots $\tilde{h} = \pm - \sqrt{1 \pm \sin\theta_0}$. However, only the smallest positive root is physical since it guarantees that $\tilde{\xi}(x) \geq 0$, and $\frac{d\tilde{\xi}}{d\tilde{x}} \leq 0$.

With an applied magnetic field, the parameters $\tilde{M}_z$ and $\tilde{M}_x$ in Equation 4.17 are non-zero functions of x, and a valid solution is not possible without exact knowledge of the fields just below the surface of the ferrofluid. We present in the following

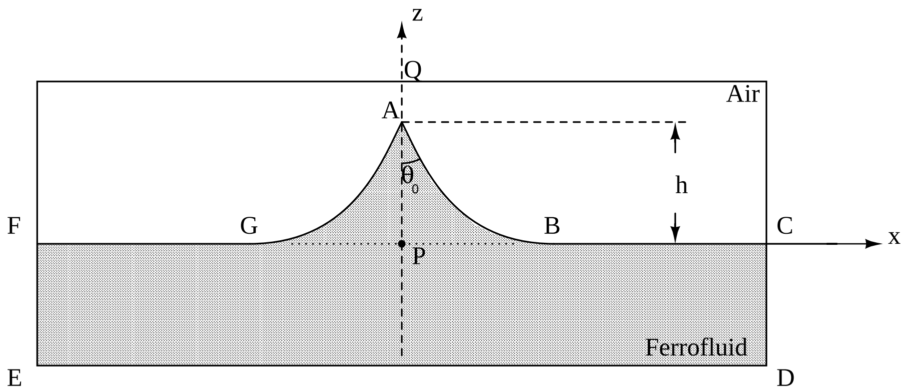

Figure 4-2: Schematic profile of ferrofluid meniscus formed on both sides of a vertical glass plate partially immersed in the middle of a large vessel of ferrofluid. The meniscus has a height h at the contact wall and a contact angle θ_0.

sections an approximate energy analysis that does not require exact knowledge of the magnetic fields.

4.2 The energy methodology

The total energy stored in the ferrofluid meniscus depends strongly on the height and shape of the meniscus. The implicit expression derived by Landau and Lifschitz (See Eq. 4.23 above) describes the exact shape of the meniscus in the absence of applied magnetic field but is not easy to manipulate mathematically; for the purposes of this energy analysis we re-examine the expression for the shape of the meniscus with no applied magnetic field given in Eq. 4.18 in two simple limits. First we present Rosensweig's linear meniscus shape approximate analysis in Sec. 4.3 [42]. Rosensweig simply replaces the meniscus curve with a straight line at the slope set by the contact angle of the fluid. Then in Sec. 4.4 we extend Rosensweig's energy minimization analysis to an exponential meniscus shape which approximates the actual shape of the meniscus in the limit when $\left|\frac{d\xi}{dx}\right| << 1$.

4.3 Linear meniscus profile

The approximate analysis assuming a linear meniscus profile correctly captures all the trends that we observed experimentally and provides physical insight into the surface effects of magnetic fields on ferrofluids. Fig. 4-3 shows the idealized shape of the ferrofluid in the container. The meniscus formed on both sides of the immersed slide is represented by a triangular zone (we choose to neglect the thickness of the slide). The total energy E per unit distance into the page is given by the expression,

$$E = E_S + E_W + E_G + E_M \tag{4.27}$$

where the total energy is given as the respective sum of surface, wall, gravitational and magnetic energies. The system achieves equilibrium when the condition,

$$\frac{\partial E}{\partial h} = 0 \tag{4.28}$$

is satisfied.

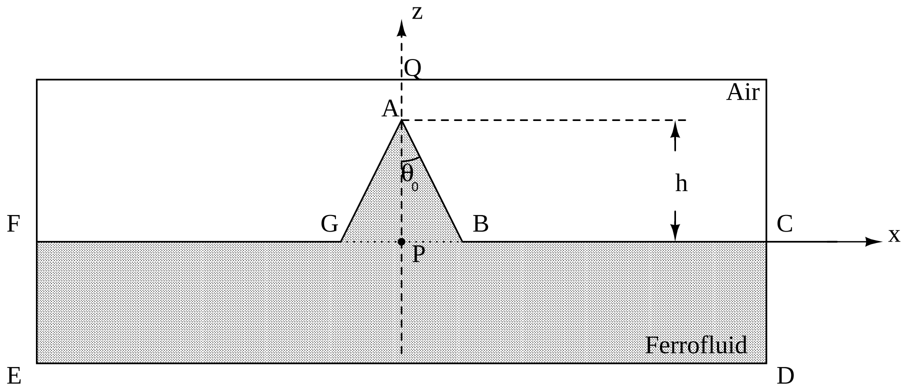

Figure 4-3: Idealized triangular model of ferrofluid meniscus. Straight lines starting from a height h and slanted at the contact angle θ_0 represent the meniscus formed around an immersed vertical glass plate.

In order to proceed with finding the equilibrium value of h, we must examine each of the different ferrofluid energies in turn.

4.3.1 Free surface energy, E_S

Interfacial surface tension σ represents the free energy stored per unit area of fluid surface. We will consider only the region $x > 0$ since by symmetry the total energy in the system would be simply double the value we obtain. Summing the surface free energy per unit depth over surfaces AG and AB as well as the horizontal surfaces FG and BC yields,

$$E_s = \sigma \left(\frac{h}{\cos \theta_0} - h \tan \theta_0 + \overline{PC} \right) \tag{4.29}$$

and

$$dE_s = \sigma \frac{1 - \sin \theta_0}{\cos \theta_0} dh \tag{4.30}$$

where $\overline{PC}$ is the distance between points P and C.

4.3.2 Wall interfacial energy, E_W

The wall interfacial energy E_W per unit depth into the page is given by the sum of the products of the areas covered by the ferrofluid/wall and the wall/gas interfaces with their respective interfacial free energies σ_{LS} and σ_{SG},

$$E_W = h\sigma_{LS} + (\overline{PQ} - h)\sigma_{SG}. \tag{4.31}$$

where $\overline{PQ}$ is the distance between points P and Q. This relationship can be simplified by using the Young-Dupre equation for vertical force balance equilibrium at the meniscus contact line, $\sigma_{LS} - \sigma_{SG} + \sigma \cos \theta_0 = 0$, yielding,

$$E_W = -h\sigma \cos \theta_0 + \overline{PQ}\sigma_{SG} \tag{4.32}$$

which in turn gives the differential form,

$$dE_W = -\sigma \cos \theta_0 dh \tag{4.33}$$

4.3.3 Gravitational energy, E_G

In order to compute the differential increase in gravitational energy due to an increment in meniscus height, we assume that the bulk volume of the ferrofluid greatly exceeds the volume of meniscus. Under this assumption, the level of the distant free surface of the ferrofluid remains constant as the meniscus rises or falls. The conservation of mass is taken into account and shown to have a negligible effect in Appendix A.

Integrating the gravitational potential over the meniscus region on one side of the glass plate yields the expression,

$$E_G = \frac{1}{6}\rho g h^3 \tan\theta_0 \tag{4.34}$$

and consequently the differential form,

$$dE_G = \frac{1}{2}\rho g h^2 \tan\theta_0 dh \tag{4.35}$$

Note that Eq. 4.34 can be interpreted as the gravitational potential energy of an object with mass per unit length equal to the total mass per unit length of ferrofluid in the meniscus region ($\frac{1}{2}h^2 \tan\theta_0\ \rho$) located at the center of mass of the triangle at height $h/3$.

4.3.4 Magnetic field energy, E_M

Unlike the expressions in previous sections, which were derived for the various types of energy stored in the meniscus, the magnetic energy E_M depends on field orientation and needs separate consideration of demagnetizing coefficients for horizontal and vertical magnetic fields. For magnetic fluid modeled by a constant magnetic susceptibility, $\chi = M/H$, the magnetic energy is given by Paris and Hurd's [30] familiar expression for linear magnetic materials,

$$E_M = -\frac{\mu_0}{2}\int \mathbf{M}\cdot\mathbf{H}_0 dV \tag{4.36}$$

where **M** is the actual magnetization vector inside the ferrofluid and $\mathbf{H}_0$ is the uniform applied magnetic field in the absence of magnetic material. Rosensweig [40] provides a more complete derivation of this result for linear magnetic materials than the discussion found in Paris and Hurd.

Even though the magnetization vector, **M** , generally varies spatially, we assume that it is spatially uniform throughout the meniscus region ABG and the bulk fluid FCDE. In this analysis, the magnetization **M** is collinear with the magnetic field intensity, **H**, inside each region of the ferrofluid. The relationship between the magnitudes of the magnetization inside the fluid M, the internal magnetic field intensity H and the externally applied field H_0 is approximately given in terms of a demagnetization coefficient D so that,

$$H = H_0 - DM \tag{4.37}$$

For linear materials $M = \chi H$, which when substituted into Eq. 4.37 leads to the expression,

$$M = \frac{\chi H_0}{1 + \chi D} \tag{4.38}$$

Further substitution of this expression for the magnetization M into the integral expression given by Eq. 4.36 yields,

$$E_M = -\frac{\mu_0}{2}\int_{V_M} \frac{\chi H_0^2}{1 + \chi D_M} dV_M - \frac{\mu_0}{2}\int_{V_B} \frac{\chi H_0^2}{1 + \chi D_B} dV_B \tag{4.39}$$

where the magnetic energy is written in terms of demagnetizing coefficients D_M and D_B for the meniscus and bulk ferrofluid regions respectively. Note that we shall prove later in this section that the demagnetizing coefficients are functions of θ_0 only and have no dependence on h.

The integration over the meniscus volume V_M and the bulk fluid volume V_B is very simply performed because M is considered constant in both regions by assumption.

$$E_M = -\frac{\mu_0}{4}\frac{\chi {H_0}^2}{1 + \chi D_M} hw - \frac{\mu_0}{2}\frac{\chi H_0^2}{1 + \chi D_B} V_B \tag{4.40}$$

where $w = h \tan \theta_0$. The corresponding incremental form is given by the expression,

$$dE_M = -\frac{\mu_0}{4} \frac{\chi {H_0}^2}{1 + \chi D_M} d(hw) - \frac{\mu_0}{2} \frac{\chi H_0^2}{1 + \chi D_B} dV_B \tag{4.41}$$

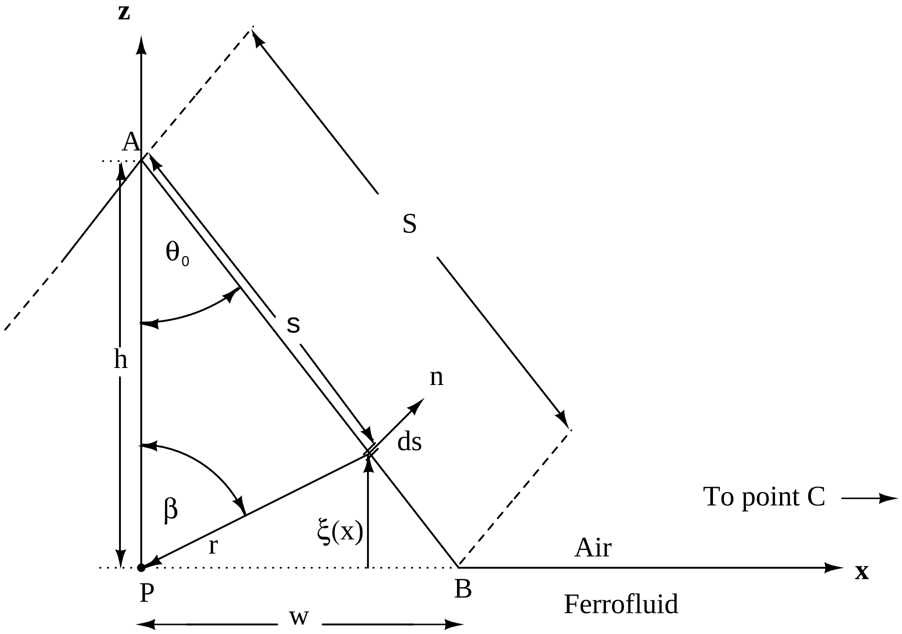

Figure 4-4: Expanded view of the meniscus region of the simple linear shape approximation of ferrofluid meniscus of Fig. 4-3. To derive the demagnetization factor the magnetic field is computed at the point P at the origin.

For conservation of mass to hold in an incompressible fluid requires the following relationship between dV_B and $d(hw)$,

$$d\left(\frac{1}{2}hw\right) + dV_B = 0 \tag{4.42}$$

with $w = h \tan \theta_0$, and

$$d(hw) = 2h \tan \theta_0 dh \tag{4.43}$$

Substitution of the geometric constraints of Eqs. 4.42 and 4.43 into Eq. 4.41 leads to,

$$dE_M = \frac{\mu_0}{2} \chi H_0^2 \frac{(D_B - D_M)}{(1 + \chi D_M)(1 + \chi D_B)} h \tan \theta_0 dh \tag{4.44}$$

Note that the expression for dE_M holds for both horizontal and vertical magnetic fields when expressed in the general terms of D_M and D_B. The demagnetization coefficients for the case of horizontal applied magnetic field, D_{MH} and D_{BH}, and the equivalent expressions for the case of vertical applied magnetic fields, D_{MV} and D_{BV}, are derived in the following sub-sections.

Horizontal field

Fig. 4-4 shows the idealized triangular shape of the meniscus formed on both sides of a thin glass plate partially immersed in a large ferrofluid vessel. We neglect the thickness of the thin glass plate in order to compute the demagnetization inside the fluid in response to a horizontal applied magnetic field. The demagnetization will be computed at a representative point P at the base of the triangle shown in Fig. 4-3.

The horizontal applied magnetic field results in a pole density on a free surface of the meniscus that is given by,

$$\sigma_M = \mu_0 \mathbf{M} \cdot \mathbf{n} = \pm \mu_0 M \cos\theta_0 \tag{4.45}$$

where $\mathbf{M}$ is the magnetization in the ferrofluid, and $\mathbf{n}$ is the unit out-going normal to the surface given by the expression,

$$\mathbf{n} = \pm\cos\theta_0 \mathbf{i}_x + \sin\theta_0 \mathbf{i}_z \tag{4.46}$$

Note that for positive H_x in Fig. 4-3 the positive pole density and the x-component of the normal vector correspond to surface AB whereas the negative pole density and the x-component of the normal vector correspond to surface AG.

The magnetization is horizontal at point P because vertical components of the demagnetization fields cancel by symmetry. The magnitude of demagnetization field due to the line source of width ds on surface AC, considered infinite in the y direction, is given by,

$$dH_r = \frac{\sigma_M ds}{2\mu_0 \pi r} = \frac{M\cos\theta_0 ds}{2\pi r} \tag{4.47}$$

where r is the distance from the line pole source to the point P and dH_r is collinear with r. The component of dH_r along the horizontal, *i.e.*, the x-direction, is given by $-\sin\beta dH_r$. An equal contribution is made by the corresponding negative line of poles situated on surface AG. Thus, the total contribution dH_x is given by,

$$dH_x = -2\sin\beta dH_r = -\frac{M\cos\theta_0\sin\beta}{\pi r}ds \tag{4.48}$$

so that the expression for the total demagnetization field at point P is,

$$H_x = -\frac{M}{\pi}\int_0^S \frac{\sin\beta\cos\theta_0}{r}ds \tag{4.49}$$

Furthermore, from the law of sines applied to the triangle in Fig. 4-4 we have that,

$$\frac{\sin\beta}{s} = \frac{\sin\theta_0}{r} \tag{4.50}$$

and from the law of cosines,

$$r^2 = s^2 + h^2 - 2sh\cos\theta_0 \tag{4.51}$$

Using the relations in Eqs. 4.50 and 4.51 we can rewrite Eq. 4.49 as,

$$H_x = -D_{MH}(\theta_0)M \tag{4.52}$$

where D_{MH}, the demagnetization coefficient, can be expressed as follows,

$$D_{MH}(\theta_0) = \frac{\sin 2\theta_0}{2\pi}\int_0^1 \frac{\varsigma d\varsigma}{\varsigma^2 + (1-2\varsigma)\cos^2\theta_0} \tag{4.53}$$

where $\varsigma = \frac{s}{S}$. Note that D_{MH} is independent of h and only a function of θ_0. The integral expression for D_{MH} has the following closed form solution,

$$D_{MH}(\theta_0) = \frac{\sin(2\theta_0)}{2\pi}\left[\frac{\pi}{2}\cot(\theta_0) + \ln(\tan\theta_0)\right] \tag{4.54}$$

By superposition, the net magnetic field at any wall point is given by,

$$H = H_0 - D_{MH}(\theta_0)M \tag{4.55}$$

A plot of $D_{MH}(\theta_0)$ is shown in the left inset in Fig. 4-5 where it can be seen that $D_{MH}(\pi/2) = 0$ and $D_{MH}(0) = \frac{1}{2}$. The demagnetizing coefficient in the bulk of the ferrofluid is zero,

$$D_{BH} = 0, \tag{4.56}$$

for the case of a horizontal applied magnetic field because segments EF and CD are assumed to be small compared to the horizontal dimension of the system and very distant from point P (see Fig. 4-3).

Vertical field

The vertical applied magnetic field results in a pole density on a free surface of the meniscus that is given by,

$$\sigma_M = \mu_0 \mathbf{M} \cdot \mathbf{n} = \mu_0 M \sin\theta_0 \tag{4.57}$$

where $\mathbf{M}$ is the actual magnetization and $\mathbf{n}$ is the unit normal to the surface given in Eq. 4.46. The magnetization is vertical at point P because horizontal components of the demagnetization fields cancel.

The magnitude of demagnetization field due to the line source of width ds on surface AC, considered infinite in the y direction, is given by,

$$dH_r = \frac{\sigma_M ds}{2\mu_0 \pi r} = \frac{M \sin\theta_0 ds}{2\pi r} \tag{4.58}$$

where r is the perpendicular distance from the line pole source to the point P and dH_r is collinear with r. The component of dH_r along the vertical, *i.e.*, the z-direction, is given by $-\cos\beta dH_r$. An equal contribution is made by the corresponding negative line of poles situation on surface AB. Thus, the total contribution dH_z at point P is given by

$$dH_z = -2dH_r \cos\beta = -M \sin\theta_0 \cos\beta \frac{ds}{\pi r} \tag{4.59}$$

From the geometry of the meniscus we can write,

$$\cos\beta = \frac{h^2 + r^2 - s^2}{2hr} \tag{4.60}$$

and

$$r^2 = h^2 + s^2 - 2hs\cos\theta_0 \tag{4.61}$$

Substitution of Eqs. 4.60 and 4.61 into Eq. 4.59 leads to,

$$dH_z = \frac{M \sin\theta_0 (h - s\cos\theta_0)}{\pi(h^2 + s^2 - 2hs\cos\theta_0)} \tag{4.62}$$

Defining $\varsigma = s/S$ the integral for H_z can be written as,

$$H_z = -\frac{M \sin 2\theta_0}{2\pi} \int_0^1 \frac{1-\varsigma}{\varsigma^2 + (1-2\varsigma)\cos^2\theta_0} \tag{4.63}$$

which is independent of h. The value of H_z obtained from integrating Eq. 4.63 accounts for the poles on the surface of the meniscus region. This field contribution must be augmented by poles of opposite sign on the bottom of the ferrofluid container (*i.e.*, on line segment ED shown in Fig. 4-3). These poles give a contribution of $-\frac{M}{2}$. Because $D_{MV} = -H_z/M$, the demagnetization coefficient can be expressed as,

$$D_{MV}(\theta_0) = \frac{\sin 2\theta_0}{2\pi} \left[\ln(\cot\theta_0) + \frac{\pi}{2}\tan\theta_0 \right] \tag{4.64}$$

Note that D_{MV} is independent of h and only a function of θ_0.

A plot of $D_{MV}(\theta_0)$ is presented on the right inset Fig. 4-5 where it can be seen that $D_{MV}(\pi/2) = 1$. A well-known result of elementary electromagnetics is that the demagnetization coefficients on orthogonal axes must sum to unity. This can be confirmed from adding Eqs. 4.64 and 4.54, or verified graphically from the insets in Fig. 4-5. The demagnetization coefficient in the bulk of the ferrofluid for the case of a vertical applied magnetic field is unity [50]:

$$D_{BV} = 1 \tag{4.65}$$

4.3.5 Governing equation for meniscus height

Substituting the expressions for dE_S, dE_W, dE_G, and dE_M into the differential form of Eq. 4.27, applying the minimization condition of Eq. 4.28, and putting the equation into dimensionless form yields the following quadratic equation for relative meniscus height $\frac{h}{a}$ where a is the capillary length,

$$\left(\frac{h}{a}\right)^2 + P(\chi, \theta_0) N_B \frac{h}{a} - (1 - \sin\theta_0) = 0 \tag{4.66}$$

where,

$$P(\chi, \theta_0) = \frac{\chi\left[D_M(\theta_0) - D_B\right]}{\left[1 + \chi D_M(\theta_0)\right]\left[1 + \chi D_B\right]}, \tag{4.67}$$

and N_B is the magnetic Bond number given by the expression,

$$N_B = \frac{\mu_0 H_0^2 a}{2\sigma}. \tag{4.68}$$

The roots of Eq. 4.66 are given by the expression,

$$\frac{h}{a} = -P(\chi, \theta_0)\frac{N_B}{2} + \sqrt{\left[P(\chi, \theta_0)\frac{N_B}{2}\right]^2 + (1 - \sin\theta_0)} \tag{4.69}$$

Meniscus height in unmagnetized fluid

In the absence of an applied magnetic field (*i.e.*, $N_B = 0$) Eq. 4.69 reduces to the simple expression,

$$\frac{h}{a} = \sqrt{1 - \sin\theta_0} \tag{4.70}$$

This result is identical to the prediction of the more rigorous Landau and Lifschitz expression for the height of the meniscus with no applied magnetic field given in Eq.

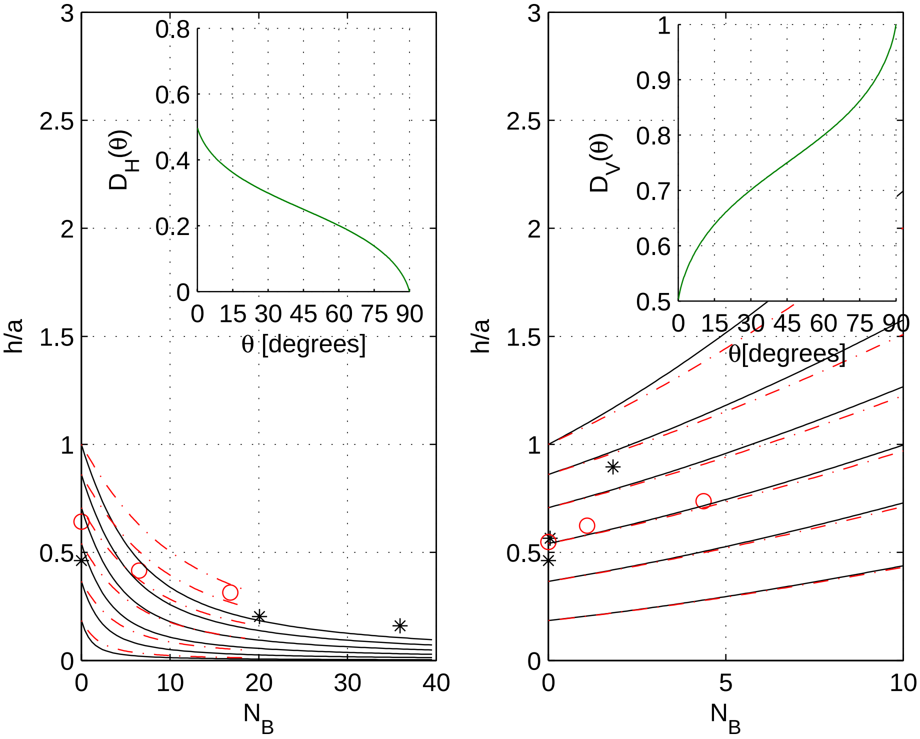

Figure 4-5: Meniscus height predictions of triangular shape model for horizontal applied field (left) and vertical applied field (right) with corresponding meniscus demagnetization coefficients (insets). Circles denote measure meniscus heights for water-based MSG W11 ferrofluid, dashed lines denote theory. Asterisks denote measured meniscus heights for oil-based EFH1 ferrofluid, solid lines denote theory. Values of $\theta_0 = 0, 15, 30, 45, 60, 75$ degrees correspond to curves in order from top to bottom.

4.26.

Meniscus height in horizontal applied magnetic field

We substitute into Eq. 4.67 the demagnetizing coefficients for a horizontal applied magnetic field given by the expressions in Eqs. 4.54 and 4.56,

$$P(\chi,\theta_0) = \frac{\chi D_{MH}(\theta_0)}{[1+\chi D_{MH}(\theta_0)]} \tag{4.71}$$

This substitution leads to the following expression for meniscus height,

$$\tfrac{h}{a} = -\tfrac{\chi D_{MH}(\theta_0)}{[1+\chi D_{MH}(\theta_0)]}\tfrac{N_B}{2} + \sqrt{\left[\tfrac{\chi D_{MH}(\theta_0)}{[1+\chi D_{MH}(\theta_0)]}\tfrac{N_B}{2}\right]^2 + (1-\sin\theta_0)} \tag{4.72}$$

A graph of $\frac{h}{a}$ vs. N_B with contact angle θ_0 as parameter, shown in Fig. 4-5, demonstrates that a horizontal applied magnetic field reduces the height of the meniscus at the wall, a trend which agrees with the observed experimental results of Chapter 3.

Meniscus height in vertical applied magnetic field

We substitute into Eq. 4.67 the demagnetizing coefficients for a vertical applied magnetic field expressed in Eqs. 4.64 and 4.65,

$$P(\chi,\theta_0) = \frac{\chi\left[D_{MV}(\theta_0)-1\right]}{(1+\chi)\left[1+\chi D_{MV}(\theta_0)\right]} \tag{4.73}$$

This substitution leads to the following expression for meniscus height,

$$\frac{h}{a} = -\frac{\chi\left[D_{MV}(\theta_0)-1\right]}{(1+\chi)\left[1+\chi D_{MV}(\theta_0)\right]}\frac{N_B}{2} + \sqrt{\left[\frac{\chi\left[D_{MV}(\theta_0)-1\right]}{(1+\chi)\left[1+\chi D_{MV}(\theta_0)\right]}\frac{N_B}{2}\right]^2 + (1-\sin\theta_0)} \tag{4.74}$$

A graph of $\frac{h}{a}$ vs. N_B with contact angle θ_0 as parameter is shown in Fig. 4-5. It can be seen that a vertical magnetic field increases the height of the meniscus at the wall. This trend is in agreement with experiments.

4.4 Exponential meniscus profile

In the limit where $\left|\frac{d\xi}{dx}\right| << 1$, the expression for the shape of the ferrofluid meniscus with no magnetic field given in Eq. 4.18 reduces to the following second order linear differential equation in dimensional form,

$$2\frac{\xi}{a} - a\frac{d^2\xi}{dx^2} = 0 \tag{4.75}$$

The profile of the meniscus $\xi(x)$ is then given by the solution,

$$\xi(x) = he^{-\sqrt{2}x/a} = he^{-\frac{x}{h}\cot\theta_0}; \quad x > 0 \tag{4.76}$$

which satisfies the boundary conditions,

$$\begin{aligned}
\xi(x = 0) &= h && (4.77)\\
\frac{d\xi}{dx}(x = 0) &= -\cot\theta_0 && (4.78)\\
\xi(x \longrightarrow \infty) &= 0 && (4.79)\\
\frac{d\xi}{dx}(x \longrightarrow \infty) &= 0 && (4.80)
\end{aligned}$$

where h is the height of the ferrofluid at the contact wall interface relative to the height of the ferrofluid in the bulk of the ferrofluid far away from the meniscus. Fig. 4-6 demonstrates how the simple linear profile first suggested by Rosensweig compares with the exponential profile and the analytical expression for the shape of the meniscus given by Eq. 4.23 for a contact angle of $\theta_0 = \frac{\pi}{4}$. The figure shows considerable agreement between the approximate exponential solution and the exact meniscus profile even though $\left|\frac{d\xi}{dx}(x = 0)\right| = 1$. The exponential approximation holds very well for $\frac{\pi}{2} > \theta_0 > \frac{\pi}{4}$. The meniscus geometry under an applied magnetic field is idealized as the decaying exponential profile depicted in Fig. 4-7, with the notion that the exponential profile approximates the actual surface profile.

As was done for the linear meniscus profile analysis in Section 4.3, the total energy E per unit depth of the system is the sum, on a per unit depth basis, of the free surface

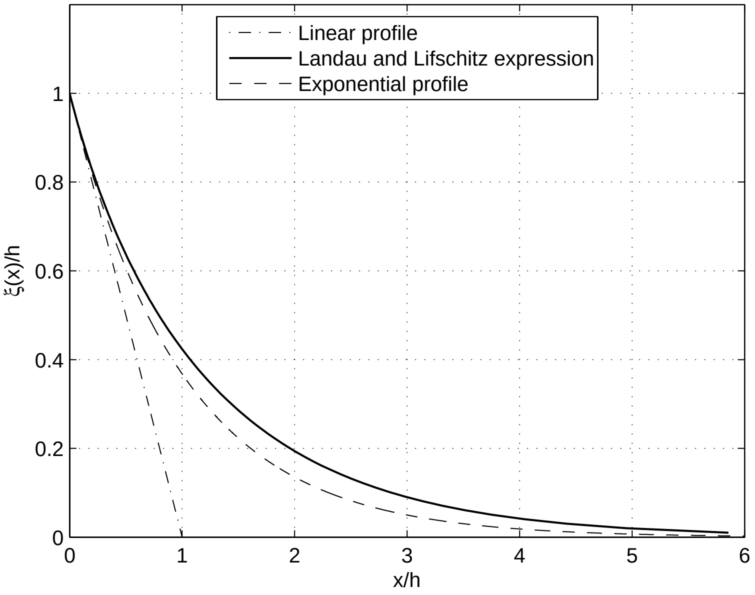

Figure 4-6: Comparison of different meniscus profile approximations with the Landau and Lifschitz expression with $\theta_0 = \frac{\pi}{4}$ and $h = 1$. The exponential profile (dash-dotted curve) better approximates the actual profile (solid curve) than the linear profile (dashed curve).

energy E_S, wall interfacial energy E_W, gravitational energy E_G, and magnetic energy E_M, now performed for an exponential meniscus profile.

$$E = E_S + E_W + E_G + E_M \tag{4.81}$$

The equilibrium state of the system corresponds to the condition

$$\frac{dE}{dh} = 0 \tag{4.82}$$

It will be found that the meniscus height is thereby determined explicitly.

To proceed, each of the terms on the right side of Eq. 4.81 is formulated in turn in the following sections.

4.4.1 Free surface energy, E_S

Interfacial tension σ is equivalent to free energy per unit area. Thus, per unit depth into the page of Fig. 4-7 the sum of surface energy over the meniscus surface can be written as,

$$E_s = \int_{x=0}^{\infty} \sigma ds \tag{4.83}$$

where ds, the incremental length of curve on the meniscus profile, can be expressed in terms of dx and $d\xi$ by the Pythagorean theorem,

$$ds = \sqrt{dx^2 + d\xi^2} = \sqrt{1 + \cot^2\theta_0 e^{-2\frac{x}{h}\cot\theta_0}}dx \tag{4.84}$$

Note that in the limit as $x \longrightarrow \infty$ the increment ds becomes equal to dx in the flat region of the meniscus. Consequently, the integral in Eq. 4.83 does not converge to a finite value. Since, however, we are mainly interested in the change in surface energy as a function of meniscus height we set the surface energy of a completely flat fluid surface as our zero energy reference. This leads to the integral expression,

$$E_S = \int_{x=0}^{\infty} \sigma \left(\sqrt{1 + \cot^2\theta_0 e^{-2\frac{x}{h}\cot\theta_0}} - 1\right) dx \tag{4.85}$$

which clearly converges to a finite value.

In order to evaluate E_s, we make the change of variable $u = \frac{x}{h}$ so that,

$$E_S = \sigma h \int_{u=0}^{\infty} \left(\sqrt{1 + \cot^2\theta_0 e^{-2u\cot\theta_0}} - 1\right) du \tag{4.86}$$

It is interesting to note from Eq. 4.86 that E_S scales linearly with h. Consequently $\frac{dE_s}{dh}$ depends only on θ_0 and can be written as,

$$dE_S = \sigma f(\theta_0) dh \tag{4.87}$$

where the function, $f(\theta_0)$, is given by,

$$\begin{aligned} f(\theta_0) &= \int_{u=0}^{\infty} \left(\sqrt{1+\cot^2\theta_0 e^{-2u\cot\theta_0}} - 1 \right) du \\ &= \tan\theta_0 \left[\csc\theta_0 - \left(1 + \ln\frac{1+\csc\theta_0}{2} \right) \right] \end{aligned} \tag{4.88}$$

4.4.2 Wall interfacial energy, E_W

This term accounts for the energetics associated with the wetting contact of the fluid with the wall.

$$E_W = \sigma_{LS} h + \sigma_{SG}(\overline{PQ} - h) \tag{4.89}$$

σ_{LS} is the liquid/solid interfacial energy per unit area and σ_{SG} the solid/gas interfacial energy. Because $\overline{PQ}$ is constant, the differential of E_W is found as

$$dE_W = (\sigma_{LS} - \sigma_{SG})dh \tag{4.90}$$

This relationship may be simplified using the Young-Dupre equation giving the condition for equilibrium of a liquid/solid/gas contact line.

$$\sigma_{LS} - \sigma_{SG} + \sigma\cos\theta_0 = 0 \tag{4.91}$$

Combining Eqs. 4.90 and 4.91 yields the desired expression for the differential dE_W,

$$dE_W = -\sigma\cos\theta_0 dh \tag{4.92}$$

4.4.3 Gravitational energy, E_G

The gravitational energy in the meniscus can be found by performing the following integral,

$$E_G = \int_{x=0}^{\infty} \int_{\xi=0}^{he^{-\frac{x}{h}\cot\theta_0}} \rho g \xi d\xi dx = \frac{1}{4} h^3 \rho g \tan\theta_0 \tag{4.93}$$

where the level surface of the fluid is considered the reference for zero energy. This expression neglects the lowering of the level surface of the fluid as the meniscus rises, a reasonable assumption if the volume of fluid in the meniscus region is much less than the total volume of fluid. The gravitational energy differential is given by,

$$dE_G = \frac{3}{4} h^2 \rho g \tan\theta_0 dh \tag{4.94}$$

4.4.4 Magnetic energy, E_M

The expression for E_M in Eq. 4.39 can be written in terms of demagnetizing factors as,

$$E_M = -\frac{\mu_0}{2} \chi H_0^2 \left(\frac{V_M}{1 + \chi D_M} + \frac{V_B}{1 + \chi D_B} \right) \tag{4.95}$$

From conservation of mass of the ferrofluid, considered as incompressible, it follows that,

$$dV_M + dV_B = 0 \tag{4.96}$$

An additional relationship for dV_M is obtained from integrating the area of the meniscus. Thus,

$$\begin{aligned} V_M &= \int_0^\infty \xi(x) dx = h^2 \tan\theta_0 && (4.97) \\ dV_M &= 2h \tan\theta_0 dh && (4.98) \end{aligned}$$

Finally, differentiating Eq. 4.95 and using Eqs. 4.96 and 4.98 to eliminate dV_B yields an expression for dE_M in the form

$$dE_M = -\mu_0 \chi H_0^2 \frac{\chi \left[D_B - D_M \right]}{\left[1 + \chi D_M \right] \left[1 + \chi D_B \right]} h \tan\theta_0 dh \tag{4.99}$$

Note that this expression for dE_M holds for both horizontal and vertical applied magnetic fields. The demagnetizing coefficients D_M and D_B for the case of horizontal applied magnetic field are derived in Sec. 4.4.4, while the equivalent expressions for the case of vertical applied magnetic field are derived in Sec. 4.4.4. The sections compute the demagnetizing coefficients for an idealized meniscus surface shape with a decaying exponential profile, as illustrated in Fig. 4-7. Demagnetization will be computed ignoring wall thickness. Thus the cross-section geometry of the fluid is a cusp with a fine tip. The coefficient pertains to fluid located at the origin (*i.e.*, at point P in the figure).

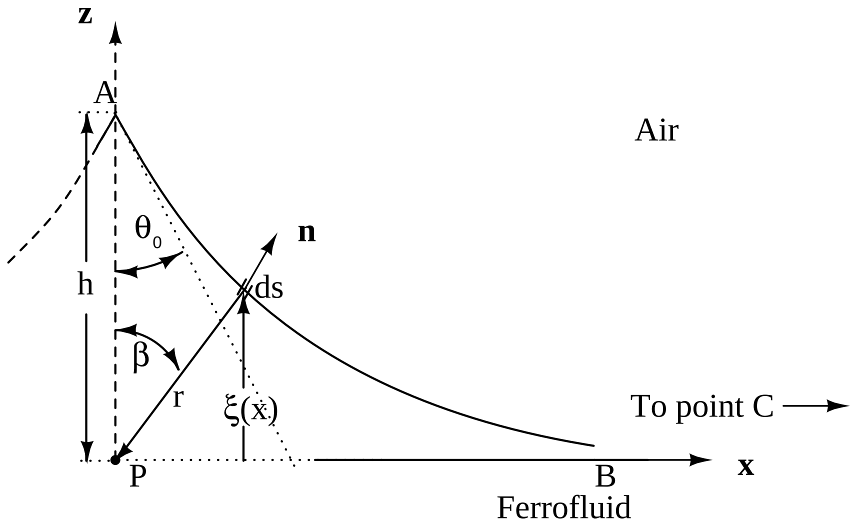

Figure 4-7: Idealized approximate exponential shape of the meniscus for demagnetization factor derivation. The magnetic field is computed at the point P at the origin.

Horizontal applied field

If we assume that the shape of the meniscus is described by the expression in Eq. 4.76 then we can proceed to calculate the demagnetizing coefficient in the meniscus region by following a procedure similar to that outlined in Sec. 4.3.4 for a linear approximate meniscus shape. The horizontal applied magnetic field results in a pole density on a free surface of the meniscus that is given by,

$$\sigma_M = \mu_0 \mathbf{M} \cdot \mathbf{n} = \frac{\mu_0 M \cot\theta_0 e^{-\frac{x}{h}\cot\theta_0}}{\sqrt{1 + \cot^2\theta_0 e^{-2\frac{x}{h}\cot\theta_0}}}, \tag{4.100}$$

where $\mathbf{M}$ is the actual magnetization (to be determined), and $\mathbf{n}$ is the unit normal to the surface given by the expression,

$$\mathbf{n} = \frac{\mathbf{i}_z - \frac{d\xi}{dx}\mathbf{i}_x}{\sqrt{1 + \left(\frac{d\xi}{dx}\right)^2}} \tag{4.101}$$

The magnetization is evaluated at point P and is purely horizontal because vertical components of the demagnetization fields cancel due to the symmetrical meniscus shape around the immersed glass plate.

The magnitude of demagnetization field in Fig. 4-7 due to the line source of width ds and magnetic surface charge density σ_M on surface ABC, considered infinite in the y direction, is given by,

$$dH_r = \frac{\sigma_M ds}{2\mu_0 \pi r} = \frac{M \cot\theta_0 e^{-\frac{x}{h}\cot\theta_0}}{2\pi\sqrt{x^2 + h^2 e^{-2\frac{x}{h}\cot\theta_0}}}dx, \tag{4.102}$$

where r is the distance from the line pole source to the point P. The component of dH_r along the horizontal, *i.e.*, the x-direction, is given by $-\sin\beta dH_r$. An equal contribution is made by the corresponding positive line of poles situated on surface AGF in Fig. 4-2. Thus, the total demagnetization contribution dH_x is given by

$$dH_x = -2\sin\beta dH_r. \tag{4.103}$$

Hence, from the geometry of the meniscus we can write,

$$dH_x = \frac{-2x}{\sqrt{x^2 + h^2 e^{-2\frac{x}{h}\cot\theta_0}}}dH_r = \frac{-M\cot\theta_0 x e^{-\frac{x}{h}\cot\theta_0}}{\pi\left(x^2 + h^2 e^{-2\frac{x}{h}\cot\theta_0}\right)}dx \tag{4.104}$$

Since $D_{MH} = \frac{-H_x}{M}$, the demagnetization coefficient can be expressed as,

$$D_{MH} = \frac{\cot\theta_0}{\pi}\int_{x=0}^{\infty} \frac{x e^{-\frac{x}{h}\cot\theta_0}}{x^2 + h^2 e^{-2\frac{x}{h}\cot\theta_0}}dx \tag{4.105}$$

To demonstrate that D_{MH} is independent of h and only a function of θ_0 we make

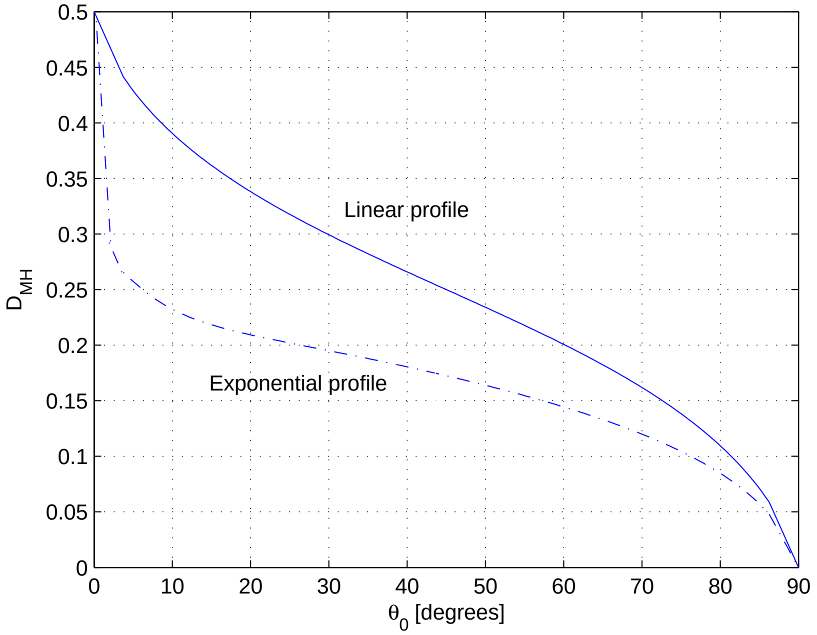

Figure 4-8: The demagnetizing factor of the meniscus as a function of θ_0 in the case of horizontal applied magnetic fields. The solid curve shows the result for a linear profile and the dashed curve for exponential profile.

the change of variables $u = \frac{x}{h}$ so that,

$$D_{MH} = \frac{\cot\theta_0}{\pi} \int_{u=0}^{\infty} \frac{ue^{-u\cot\theta_0}}{u^2 + e^{-2u\cot\theta_0}} du \tag{4.106}$$

Here it can be seen that D_{MH} depends only on the contact angle θ_0, and is independent of h. By superposition, the net magnetic field at any wall point is given by

$$\mathbf{H} = \mathbf{H}_0 - D_{MH}(\theta_0)\mathbf{M} \tag{4.107}$$

A plot of $D_{MH}(\theta_0)$ is presented in Fig. 4-8 where it can be seen that $D_{MH}(\pi/2) = 0$ and $D_{MH}(0) = \frac{1}{2}$. The demagnetizing coefficient in the bulk of the ferrofluid is zero for the case of a horizontal applied magnetic field, $D_{BH} = 0$, because segments EF and CD are assumed to be small compared to the horizontal dimension of the system and very distant from point P (see Fig. 4-2).

Vertical applied field

The vertical applied magnetic field results in a pole density on a free surface of the meniscus that is given by,

$$\sigma_M = \mu_0 \mathbf{M} \cdot \mathbf{n} = \frac{\mu_0 M}{\sqrt{1 + \cot^2 \theta_0 e^{-2\frac{x}{h}\cot\theta_0}}}, \tag{4.108}$$

where $\mathbf{M}$ is the actual magnetization and $\mathbf{n}$ is the unit normal to the surface. The magnetization is vertical at point P as horizontal components of the demagnetization fields cancel.

The magnitude of demagnetization field due to the line source of width ds on surface AC, considered infinite in the y direction, is given by,

$$dH_r = \frac{\sigma_M ds}{2\pi\mu_0 r} = \frac{M}{2\pi\sqrt{x^2 + h^2 e^{-2\frac{x}{h}\cot\theta_0}}} dx, \tag{4.109}$$

where r is the perpendicular distance from the line pole source to the point P. The component of dH_r along the vertical, *i.e.*, the z-direction, is given by $-\cos\beta dH_r$. An equal contribution is made by the corresponding negative line of poles situation on surface AGF. Thus, the total contribution dH_z is given by

$$dH_z = -2\cos\beta dH_r. \tag{4.110}$$

Hence from the geometry of the meniscus we can write,

$$dH_z = \frac{-2he^{-\frac{x}{h}\cot\theta_0}}{\sqrt{x^2 + h^2 e^{-2\frac{x}{h}\cot\theta_0}}} dH_r = \frac{-Mhe^{-\frac{x}{h}\cot\theta_0}}{\pi\left(x^2 + h^2 e^{-2\frac{x}{h}\cot\theta_0}\right)} dx \tag{4.111}$$

The value of H_z obtained from integrating Eq. 4.111 accounts for the poles on the surface of the meniscus region. This must be augmented by poles of opposite sign on the bottom of the ferrofluid container (*i.e.*, on line segment ED shown in Fig. 4-2). These poles give a contribution of $-\frac{M}{2}$. Since $D_{MV} = -H_z/M$, the demagnetization coefficient can be expressed as,

$$D_{MV} = \frac{1}{\pi}\int_{x=0}^{\infty} \frac{he^{-\frac{x}{h}\cot\theta_0}}{x^2 + h^2 e^{-2\frac{x}{h}\cot\theta_0}} dx + \frac{1}{2} \tag{4.112}$$

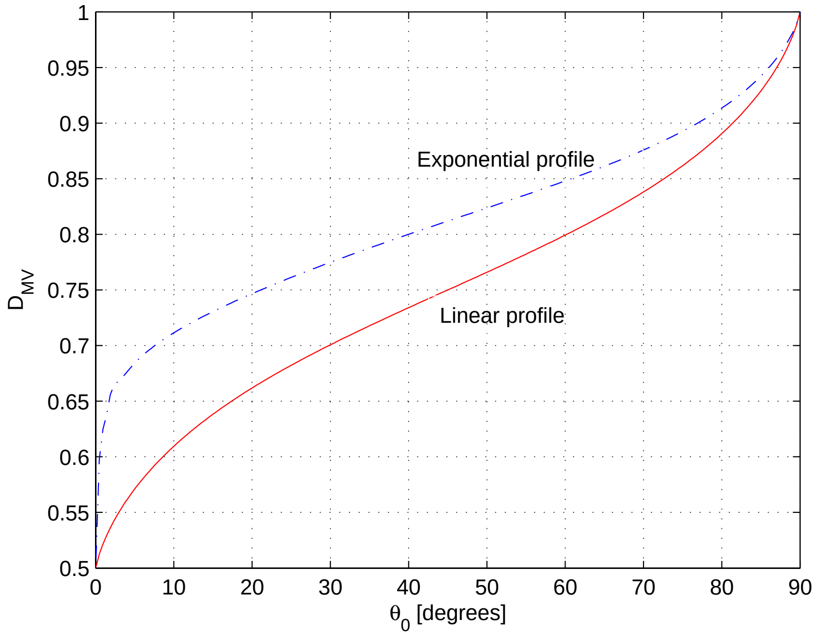

Figure 4-9: The demagnetizing factor in the meniscus as a function of θ_0 in the case of vertical applied magnetic fields. Linear profile (solid curve), exponential profile (dashed curve).

To demonstrate that D_{MH} is independent of h and only a function of θ_0 we make the change of variables $u = \frac{x}{h}$ so that,

$$D_{MV} = \frac{1}{\pi}\int_{u=0}^{\infty} \frac{e^{-u\cot\theta_0}}{u^2 + e^{-2u\cot\theta_0}} du + \frac{1}{2} \tag{4.113}$$

Here it can be seen that D_{MV} depends only on the contact angle θ_0, and is independent of h. By superposition, the net magnetic field at any wall point is given by

$$\mathbf{H} = \mathbf{H}_0 - D_{MV}(\theta_0)\mathbf{M} \tag{4.114}$$

A plot of $D_{MV}(\theta_0)$ is presented in Fig. 4-9 where it can be seen that $D_{MV}(\pi/2) = 1$ as expected. A well known result of elementary electromagnetics is that the demagnetization coefficients on orthogonal axes must sum to unity [29]. This can be confirmed from adding Eqs. 4.113 and 4.106

$$D_{MH}(\theta_0) + D_{MV}(\theta_0) = 1 \tag{4.115}$$

or verified graphically in Figs. 4-8 and 4-9. The demagnetization coefficient in the bulk of the ferrofluid for the case of a vertical applied magnetic field is unity, $D_{BV} = 1$.

4.4.5 Governing equation for meniscus height

Substituting the expressions for dE_S, dE_W, dE_G, and dE_M into the differential of dE of Eq. 4.81, applying the minimization condition of Eq. 4.82, and putting the equation into dimensionless form yields the following quadratic equation for relative meniscus height $\frac{h}{a}$ where a is the capillary length.

$$\left(\frac{h}{a}\right)^2 + \frac{4}{3}P(\chi, \theta_0)N_B\frac{h}{a} - \frac{2[\cos\theta_0 - f(\theta_0)]}{3\tan\theta_0} = 0 \tag{4.116}$$

where $f(\theta)$ is given in Eq. 4.88,

$$P(\chi, \theta_0) = \frac{\chi\left[D_M(\theta_0) - D_B\right]}{\left[1 + \chi D_M(\theta_0)\right]\left[1 + \chi D_B\right]}, \tag{4.117}$$

and N_B is the magnetic Bond number given by the expression,

$$N_B = \frac{\mu_0 H_0^2 a}{2\sigma}. \tag{4.118}$$

The roots of Eq. 4.116 are given by the expression,

$$\frac{h}{a} = -\frac{2}{3}P(\chi, \theta_0)N_B + \sqrt{\left[\frac{2}{3}P(\chi, \theta_0)N_B\right]^2 + \frac{2[\cos\theta_0 - f(\theta_0)]}{3\tan\theta_0}} \tag{4.119}$$

Meniscus height in the unmagnetized fluid

Taking Eq. 4.119 with $N_B = 0$, the height of the meniscus at the wall is given by,

$$\frac{h}{a} = \sqrt{\frac{2[\cos\theta_0 - f(\theta_0)]}{3\tan\theta_0}} \tag{4.120}$$

A graph of $\frac{h}{a}$ with $N_B = 0$ as a function of contact angle θ_0 is shown in Fig. 4-10. The figure compares the predictions of the exponential model against the Landau and Lifschitz result given by Eq. 4.26. The expression in Eq. 4.120 goes to infinity at $\theta_0 = 0$, but closely matches the Landau and Lifschitz expression for larger angles. For $\theta_0 = 40°$ the error between the result for the exponential approximation and the exact result is less than 10 %. The results of the linear approximate meniscus profile identically match the Landau and Lifschitz expression.

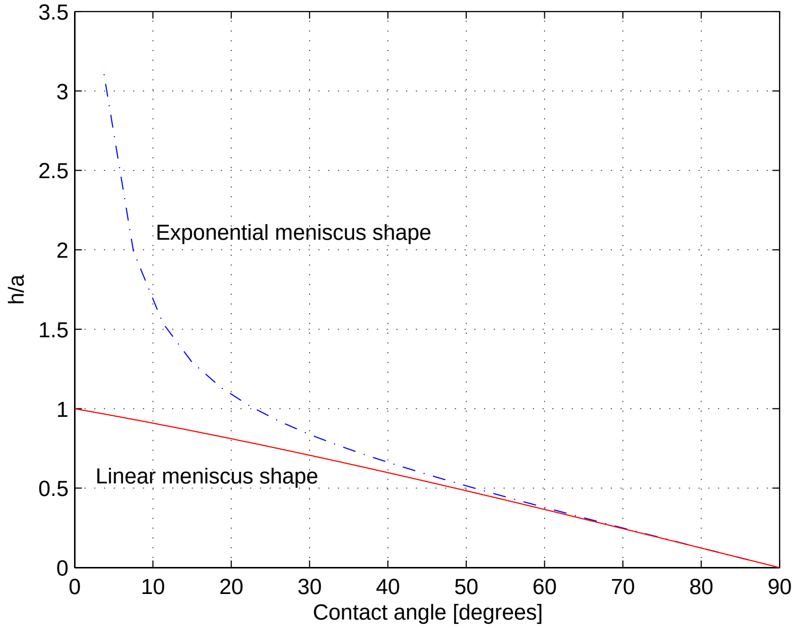

Figure 4-10: The meniscus height at the contact wall, h, as a function of contact angle θ_0 for zero applied magnetic field. Landau and Lifschitz result of Eq. 4.23 (solid curve) which matches the results for a linear meniscus shape, and the results for the exponential approximation give by Eq. 4.120 (dashed curve).

Meniscus height in horizontal applied magnetic field

We substitute into Eq. 4.117 the demagnetizing coefficients for a horizontal applied magnetic field derived in Sec. 4.4.4,

$$P(\chi, \theta_0) = \frac{\chi D_{MH}(\theta_0)}{[1 + \chi D_{MH}(\theta_0)]} \tag{4.121}$$

This leads to the following expression for meniscus height,

$$\frac{h}{a} = -\frac{2\chi D_{MH}(\theta_0)}{3[1+\chi D_{MH}(\theta_0)]} N_B + \sqrt{\left[\frac{2\chi D_{MH}(\theta_0)}{3[1+\chi D_{MH}(\theta_0)]} N_B\right]^2 + \frac{2[\cos\theta_0 - f(\theta_0)]}{3\tan\theta_0}} \tag{4.122}$$

A graph of $\frac{h}{a}$ vs. N_B with contact angle θ_0 as parameter as shown in Fig. 4-11 shows that a horizontal magnetic field reduces the height of the meniscus at the wall as observed in the experimental results presented in Chapter 3.

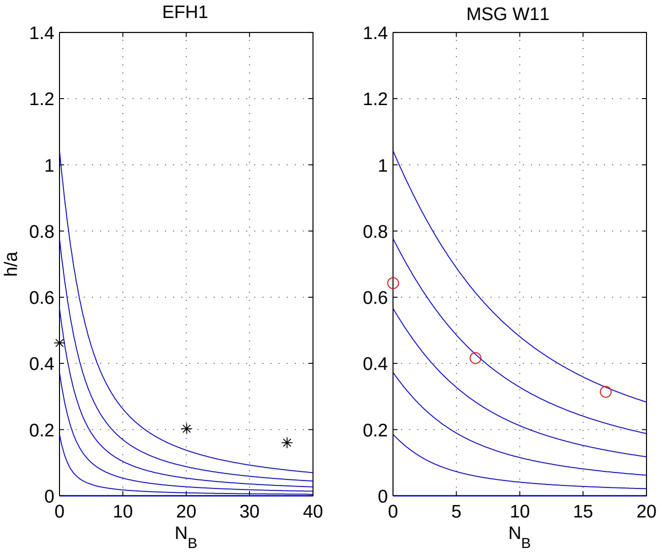

Figure 4-11: The meniscus height at the contact wall, h, as a function of applied horizontal magnetic field for different values of contact angles θ_0 for oil-based EFH1 (left panel) and water-based MSG W11 (right panel) ferrofluid. Shown curves correspond to values of $\theta_0 = 0, 15, 30, 45, 60, 75$ degrees from top curve downward. Applied horizontal magnetic field decreases the height of the meniscus in directional agreement with experimental results presented in Chapter 3.

Meniscus height in vertical applied magnetic field

We substitute into Eq. 4.117 the demagnetizing coefficients for a vertical applied magnetic field derived in Sec. 4.4.4,

$$P(\chi, \theta_0) = \frac{\chi\left[D_{MV}(\theta_0) - 1\right]}{(1+\chi)\left[1 + \chi D_{MV}(\theta_0)\right]} \tag{4.123}$$

This leads to the following expression for meniscus height,

$$\frac{h}{a} = -\frac{2\chi[D_{MV}(\theta_0)-1]N_B}{3(1+\chi)[1+\chi D_{MV}(\theta_0)]} + \sqrt{\left[\frac{2\chi[D_{MV}(\theta_0)-1]N_B}{3(1+\chi)[1+\chi D_{MV}(\theta_0)]}\right]^2 + \frac{2[\cos\theta_0 - f(\theta_0)]}{3\tan\theta_0}} \tag{4.124}$$

A graph of $\frac{h}{a}$ vs. N_B for various values of contact angle θ_0 as in Fig. 4-12 shows that the vertical magnetic field reduces the height of the meniscus at the wall. This trend agrees with the results of experiments in Chapter 3.

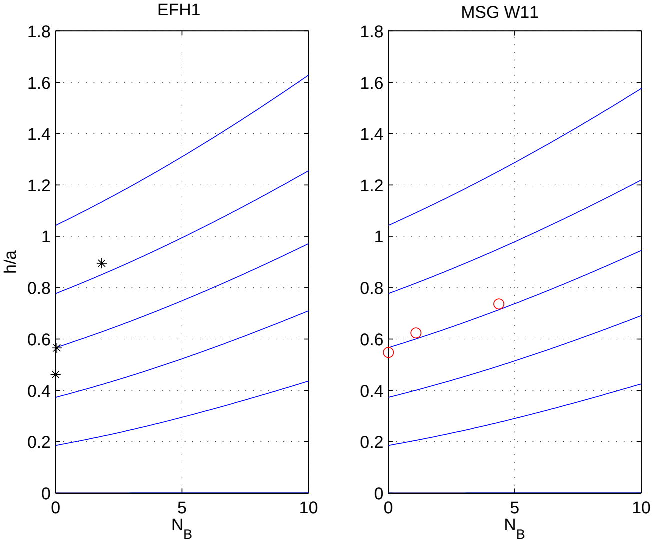

Figure 4-12: The meniscus height at the contact wall, h, as a function of applied vertical magnetic field for different values of contact angles θ_0. The height of the meniscus increases with applied vertical magnetic field in directional agreement with experimental results. The shown curves correspond to values of $\theta_0 = 0, 15, 30, 45, 60, 75$ degrees from top curve downward.

4.5 Discussion and future work

A possible direction for further theoretical analysis of the meniscus combines the interfacial force balance with an extended Bernoulli's equation, including magnetic effects [40], to write a governing equation for the shape of the ferrofluid meniscus. This effort would require a self-consistent solution of the ferrohydrodynamic Bernoulli's equation and the fringing field effects at the ferrofluid/air interface due to the curvature of the ferrofluid meniscus. An iterative Femlab finite element simulation can be used that first calculates the non-uniform magnetic fields due an assumed meniscus shape, then uses the calculated magnetic fields to solve the Ferrohydrodynamic Bernoulli's equation for a new estimate of the equilibrium shape of the meniscus. The new shape of the meniscus can be used subsequently to solve for the non-uniform magnetic fields until the results of the iteration converge.

Chapter 5

Steady, laminar and transition regime solutions to surface-driven-fluid flow in a fixed cylindrical container

5.1 Introduction

A model for the spin-up flow of magnetic fluid in a uniform magnetic field considers the interfacial deformation of a free ferrofluid surface in contact with the vessel and the resulting magnetic surface shear stress as the driving forces of the flow in the fluid. The surface-driven flow is believed to be two-dimensional axisymmetric and more intense than that produced by the spin diffusion model. However, to date the flow profile resulting from the surface-driven model remains undetermined. This chapter presents some closed form solutions to the driven-cylindrical-cavity fluid flow problem in the steady low Reynolds number limit as preliminary steps to an analytical description of the flow profile in the ferrofluid spin-up problem.

In Section 5.2 we consider the flow profile in a fixed cylinder with a rotating top face. The velocity profile at the surface of the fluid increases linearly with radial position in order to maintain no-slip with the rotating disk. The results of this analysis are verified with computational fluid dynamics simulations using the Femlab software package and shown to agree qualitatively with preliminary experiments performed by Rosensweig.

In Section 5.3 we investigate a cylinder driven by a constant azimuthal shear stress, $T_{\phi z} = T_0 \mathbf{i}_\phi$, on a thin annulus of thickness δ at the outside wall on the top face of the cylinder, including the limiting case where δ equals the entire cylinder radius R. We use the resulting flow profile to model the surface-driven flow in the magnetic fluid spin-up problem, with $\delta << R$ to represent the meniscus region near the cylinder wall and with T_0 to represent the magnetic shear stress on the ferrofluid meniscus.

Section 5.4 reexamines the surface-driven cylindrical cavity in the high Reynolds number limit where the assumption of negligible inertial effects breaks down. We develop Femlab finite element models to solve the full Navier-Stokes equations for velocity-driven and for surface-shear-stress-driven flows. The results of the finite element numerical simulations help define the regime where the low Reynolds number analytical solutions hold. We conclude from the numerical investigations that the analytical solutions developed for $R_E << 1$ remain accurate for the low Reynolds $R_E \approx 1$.

5.2 Low Reynolds number velocity-driven flow

Fig. 5-1 illustrates the geometry under consideration in this section: a cylindrical container of radius R and height L with a fixed lateral wall and bottom face. The top face, however, rotates around the axis of the cylinder at a constant angular velocity Ω. An incompressible viscous fluid of density ρ and viscosity η fills the cylinder so that the rotation of the top-face causes the fluid in contact with it to circulate about the z-axis in order to satisfy the no-slip condition. The analysis developed in this chapter assumes that fluid flow in the cylinder has reached the steady state and that the Reynolds number is much less than unity ($R_E = \frac{\rho \Omega R^2}{\eta} << 1$), so that inertial effects are by assumption negligible when compared to viscous forces.

The governing set of equations in this problem with no magnetic body forces are the Navier-Stokes and conservation of mass equations. The vector Navier-Stokes equation is given by,

$$\rho\left(\frac{\partial \mathbf{v}}{\partial t}+(\mathbf{v}\cdot\nabla)\mathbf{v}\right)=-\nabla p'+\eta\nabla^2\mathbf{v} \tag{5.1}$$

where $\mathbf{v}$ is the velocity of the fluid, ρ is the fluid density, and η is the fluid viscosity. Note that the definition of the effective pressure $p' = p + \rho g z$, where $g = 9.8\ \frac{m}{s^2}$ is the acceleration due to gravity, eliminates the need for an explicit treatment of gravitational effects.

The conservation of mass equation for an incompressible fluid is given by,

$$\nabla\cdot\mathbf{v}=0 \tag{5.2}$$

We can rewrite these governing equations in dimensionless form by defining the non-dimensional variables, $\tilde{\mathbf{v}} = \frac{\mathbf{v}}{R\Omega}$, $\tilde{p} = \frac{p'}{\Omega\eta}$, $\tilde{t} = \Omega t$, and $(\tilde{r},\ \tilde{z}) = (\frac{r}{R}, \frac{z}{R})$, where the characteristic length of the system is taken to be the radius of the cylinder R,

$$R_E\left(\frac{\partial \tilde{\mathbf{v}}}{\partial \tilde{t}}+(\tilde{\mathbf{v}}\cdot\tilde{\nabla})\tilde{\mathbf{v}}\right)=-\tilde{\nabla}\tilde{p}+\tilde{\nabla}^2\tilde{v} \tag{5.3}$$

In this analysis we are interested in the behavior of the fluid in the steady, laminar limit; consequently $\frac{\partial \mathbf{v}}{\partial t} \longrightarrow 0$ in the steady state and the Reynolds number is much less than unity $R_E << 1$. Under these assumptions viscous forces dominate the flow allowing us to neglect the inertial terms on the left hand side of Eqs. 5.1 and 5.3, and write the following simplified expression,

$$0=-\nabla p'+\eta\nabla^2\mathbf{v} \tag{5.4}$$

Further simplifications follow from the axisymmetry of the problem under consideration about the z-axis, so that $\frac{\partial}{\partial\phi} = 0$, and therefore $\mathbf{v}$ can be at most a function of

r and z only. For the purposes of this analysis we assume a flow of the form $v_\phi(r,z)$, and that the magnitudes of the $v_r(r,z)$ and $v_z(r,z)$ components of the flow are negligible when $R_E << 1$. Note that our assumed flow already satisfies the conservation of mass condition of Eq. 5.2. The azimuthal component of the Navier-Stokes equation for our assumed flow is then given by,

$$\frac{\partial}{\partial r}\left(\frac{1}{r}\frac{\partial}{\partial r}\left[rv_\phi\right]\right)+\frac{\partial^2 v_\phi}{\partial z^2}=0 \tag{5.5}$$

whereas the radial and axial components of the Navier-Stokes equation with $R_E << 1$ are,

$$\frac{\partial p'}{\partial r}\approx -R_E\frac{v_\phi^2}{r}\approx 0,\quad \frac{\partial p'}{\partial z}\approx 0 \tag{5.6}$$

Note that the magnitude of $R_E\frac{v_\phi^2}{r}$ is the first order estimate of the error in the simplified solution presented in this section. The solution to these equations must satisfy all of the following boundary conditions:

$$v_\phi(r,z)=\begin{cases} 0 & ;\, r=R;\ z=0 \\ \Omega r & ;\, z=L \\ \text{finite} & ;\, r=0 \end{cases} \tag{5.7}$$

The no-slip condition forces the fluid to be at rest at the stationary side wall ($r=R$) and bottom face ($z=0$) of the cylinder, whereas at the top face of the cylinder ($z=L$) the no-slip condition constrains the fluid to a velocity linear with radial position r. The symmetry about the z-axis dictates that the ϕ-directed velocity must vanish at $r=0$.

The form of the general solution to Eq. 5.5 can be found by using the method of separation of variables. If we assume that the solution has the form of a product of a function of r and a function of z, *i.e.*, $v_\phi(r,z)=f(r)g(z)$, then Eq. 5.5 can be written as,

$$\frac{1}{f(r)}\frac{\partial}{\partial r}\left(\frac{1}{r}\frac{\partial}{\partial r}\left[rf(r)\right]\right)+\frac{1}{g(z)}\frac{\partial^2 g(z)}{\partial z^2}=0 \tag{5.8}$$

Note that the left hand side of the equation is the sum of a term that is only a

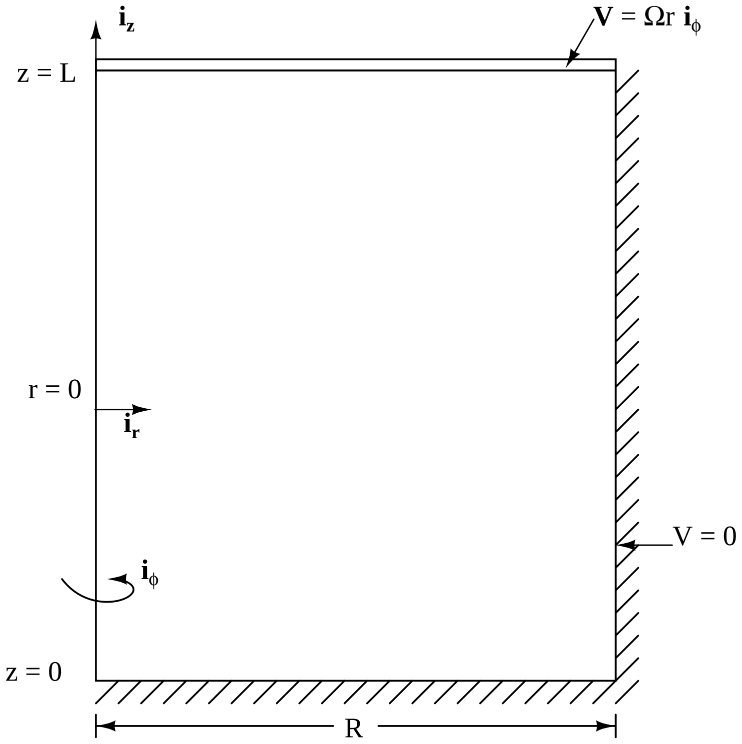

Figure 5-1: Illustration of the rotating top boundary value problem. The bottom face at $z = 0$ and $r = R$ side of the cylinder are fixed. The top-face, however, rotates at angular velocity Ω. At the boundaries the no-slip condition requires that the fluid must flow at the same velocity as the walls it contacts.

function of z and a term that is only a function of r. We can separate Eq. 5.8 into two separate second-order-ordinary differential equations,

$$\frac{1}{f(r)}\frac{d}{dr}\left(\frac{1}{r}\frac{d}{dr}\left[rf(r)\right]\right) = k^2 \tag{5.9}$$

and,

$$\frac{1}{g(z)}\frac{d^2g(z)}{dz^2} = -k^2 \tag{5.10}$$

where k^2 is the separation constant.

Eq 5.9 can be rewritten in the form of a first order modified Bessel differential equation:

$$r^2\frac{d^2f(r)}{dr^2} + r\frac{df(r)}{dr} - (k^2r^2+1)f(r) = 0 \tag{5.11}$$

with solution given by,

$$f(r) = AI_1(kr) + BK_1(kr) + Cr + \frac{D}{r} \tag{5.12}$$

where A, B, C, and D are arbitrary constants, and $I_1(kr)$ and $K_1(kr)$ are first order modified Bessel functions of the first and second kinds respectively. Note that the zero separation variable terms in the solution are given by Cr and $\frac{D}{r}$.

Similarly, Eq. 5.10 can be written as a linear constant coefficient first order differential equation,

$$\frac{d^2g(z)}{dz^2} = -k^2 g(z) \tag{5.13}$$

which has solutions given by,

$$g(z) = E\sin(kz) + F\cos(kz) + Gz + H \tag{5.14}$$

where E, F, G, and H are arbitrary constants.

The product of the expressions in Eqs. 5.12 and 5.14 yields the general form of the solution to Eq. 5.5 in terms of arbitrary constants,

$$\begin{aligned} v_\phi(r,z) &= [AI_1(kr) + BK_1(kr)]\sin(kz) + [CI_1(kr) + DK_1(kr)]\cos(kz) \\ &\quad + Erz + \frac{Fz}{r} + Gr + \frac{H}{r} + K \end{aligned} \tag{5.15}$$

This expression includes all of the zero and non-zero separation constant solutions, where k and the coefficients A through K are to be determined by the boundary conditions. We need not retain most of the terms in the general solution in Eq. 5.15. First the constants B, D, F, and H are set to zero because the first order modified Bessel function of the second kind K_1, $\frac{z}{r}$ and $\frac{1}{r}$ are infinite at $r = 0$, and therefore cannot be physical solutions. The constants K, G, C and D are set to zero to guarantee that the no-slip condition holds at $z = 0$. This leaves the expression,

$$v_\phi(r,z) = AI_1(kr)\sin(kz) + Erz \tag{5.16}$$

We now need to find the constants A and E that match the remaining boundary conditions at $r = R$ and at $z = L$.

To satisfy the no-slip condition at $z = L$ we must have that,

$$k = \frac{n\pi}{L} \tag{5.17}$$

and that

$$E = \frac{\Omega}{L} \tag{5.18}$$

Substitution of Equations 5.17 and 5.18 into Eq. 5.16 leads to,

$$v_\phi(r, z) = -AI_1(\frac{n\pi}{L}r)\sin(\frac{n\pi}{L}z) + \frac{\Omega}{L}rz \tag{5.19}$$

Note that evaluation of Eq. 5.19 at $z = L$ gives the expected linear velocity profile directly proportional to radius r at that boundary.

Finally we must determine a value A that satisfies the no-slip condition at r = R. Inspection of Eq. 5.19 at $r = R$ reveals that only a superposition of all the solutions in Eq. 5.19 can satisfy the constraint,

$$v_\phi(r = R, z = 0) = -\sum_{n=1}^{\infty} A_n I_1(\frac{n\pi}{L}R)\sin(\frac{n\pi}{L}z) + \frac{\Omega}{L}Rz \tag{5.20}$$

Hence to satisfy Eq. 5.20 we must find the Fourier series amplitudes A_n. The following Equation must be solved to compute the terms of the series A_n,

$$\sum_{n=1}^{\infty} A_n I_1(\frac{n\pi}{L}R)\sin(\frac{n\pi}{L}z) = \frac{\Omega}{L}Rz \tag{5.21}$$

In order to solve for A_n we multiply both sides of Eq. 5.21 by $\sin(\frac{m\pi}{L}z)$, then integrate both sides with respect to z from $z = 0$ to $z = L$,

$$\int_0^L \sum_{n=1}^{\infty} A_n I_1(\frac{n\pi}{L}R)\sin(\frac{n\pi}{L}z)\sin(\frac{m\pi}{L}z)dz = \int_0^L \frac{\Omega}{L}Rz\sin(\frac{m\pi}{L}z)dz \tag{5.22}$$

We utilize the orthogonality of sine functions and the integral identity,

$$\int u\sin(u)du = -u\cos(u) + \sin(u) \tag{5.23}$$

to evaluate the integrals on the left-hand and right-hand side of Eq. 5.22. The result is,

$$\frac{1}{2}LA_mI_1(\frac{m\pi R}{L}) = (-1)^{m+1}\frac{LR\Omega}{m\pi} \tag{5.24}$$

for $(m = 1, 2, 3, ...)$. Consequently the Fourier series coefficients are given by the expression,

$$A_m = \frac{-2\cos(m\pi)R\Omega}{m\pi I_1(\frac{m\pi R}{L})} \tag{5.25}$$

for $(m = 1, 2, 3...)$. The solution that satisfies all of the boundary conditions is therefore given by the expression,

$$v_\phi(r,z) = \frac{\Omega}{L}rz + \sum_{m=1}^{\infty}\frac{2\cos(m\pi)R\Omega}{m\pi I_1(\frac{m\pi R}{L})}I_1(\frac{m\pi}{L}r)\sin(\frac{m\pi}{L}z) \tag{5.26}$$

Fig. 5-2 shows the functional dependence of $v_\phi(r,z)$ plotting 1000 Fourier series terms in Eq. 5.26. The finite element program Femlab was also used to verify these plots for low Reynolds numbers; the numerical results (dashed curves) agree so well with the theoretical analysis (solid curves) that the slight deviations are generally indiscernible. Slight deviations can be seen for the $\frac{z}{L} = 1$ curve near $r/R = 1$. These are due to numerical errors and can be reduced by refining the finite element mesh.

5.3 Low Reynolds number surface-stress-driven flow

The geometry illustrated in Fig. 5-3 is very similar to the geometry investigated in Section 5.2. The flow in the cylinder is, however, now driven by an azimuthal shear stress of magnitude T_0 on a strip of width δ along the circumference of the top face (see Fig. 5-4). This model attempts to calculate a magnetic-field-induced shear stress on a thin ferrofluid meniscus region at $z = L$. Rosensweig *et al.* give the free surface stress acting on a circular meniscus of elevation h as $2\zeta\omega\sin\beta$ and the

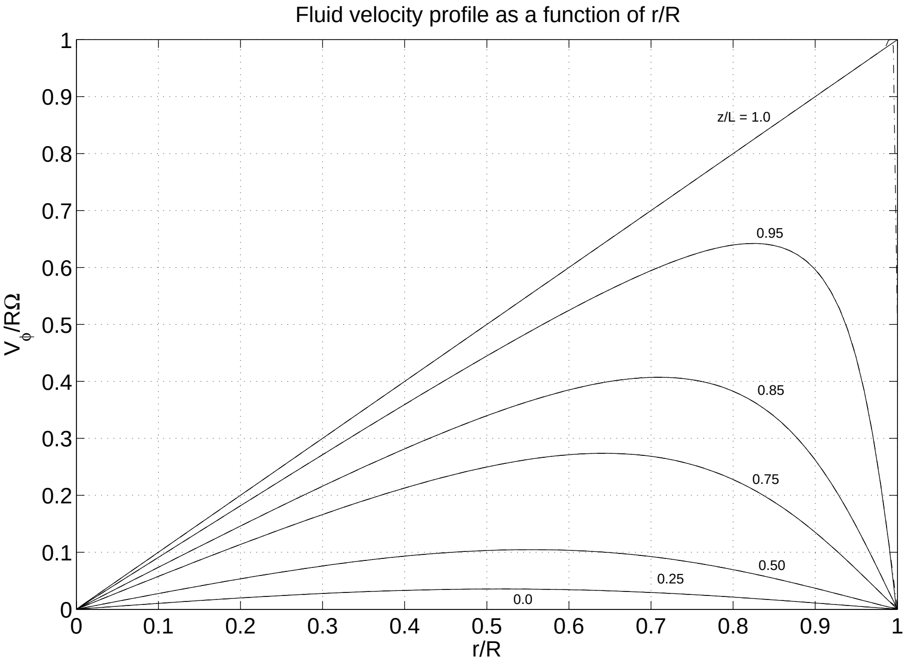

Figure 5-2: The dimensionless velocity $\frac{v_\phi}{R\Omega}$ as a function of $\frac{r}{R}$ for different values of $\frac{z}{L}$. Results shown are for a cylinder where $R = L$. Analytical expression of Eq. 5.26 summed up to 1000 Fourier series terms and plotted as solid lines. Femlab numerical solutions are plotted as dashed curves but are so accurate that they completely overlap the analytical curves.

associated surface couple as $4\pi R^2 \zeta \omega h$ [39]. These expressions when combined with the investigations in Chapters 3 and 4 allow the estimation of the surface shear stress magnitude T_0.

The governing equations in this case are still given by Eqs. 5.5 and 5.6. The boundary conditions for this set of differential equations, however, are now given by,

$$v_\phi(r,z) = \begin{cases} 0 & ;\, r = R;\, z = 0 \\ \text{finite} & ;\, r = 0 \end{cases} \tag{5.27}$$

$$T_{\phi z}(r,z) = \begin{cases} T_0 & ;\, R-\delta < r < R,\, z = L \\ 0 & ;\, 0 < r < R-\delta,\, z = L \end{cases} \tag{5.28}$$

Note that in terms of the parameters defined in the statement of the shear-driven problem the key non-dimensional parameter is $R_E = \frac{\rho R^2 T_0}{\eta^2}$. We assume that $R_E << 1$ in the following solution.

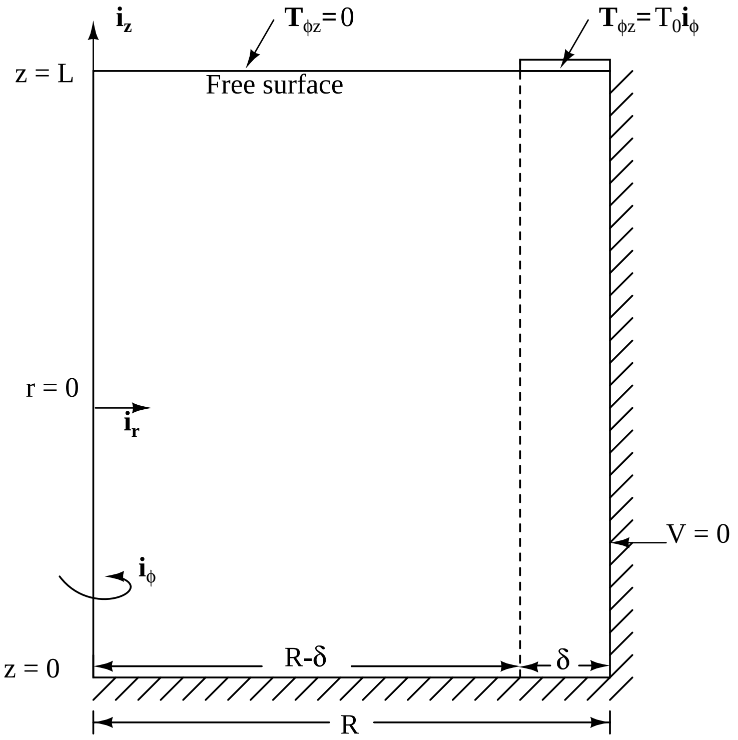

Figure 5-3: Illustration of the shear-stress driven boundary value problem. The bottom face at $z = 0$ and $r = R$ side of the cylinder are fixed. The top-face is stressed by an azimuthal shear stress $T_{\phi z} = T_0$ over an annular region of width δ. The rest of the top surface is free from shear stress (*i.e.*, $T_{\phi z} = 0$ for $0 < r < R - \delta$).

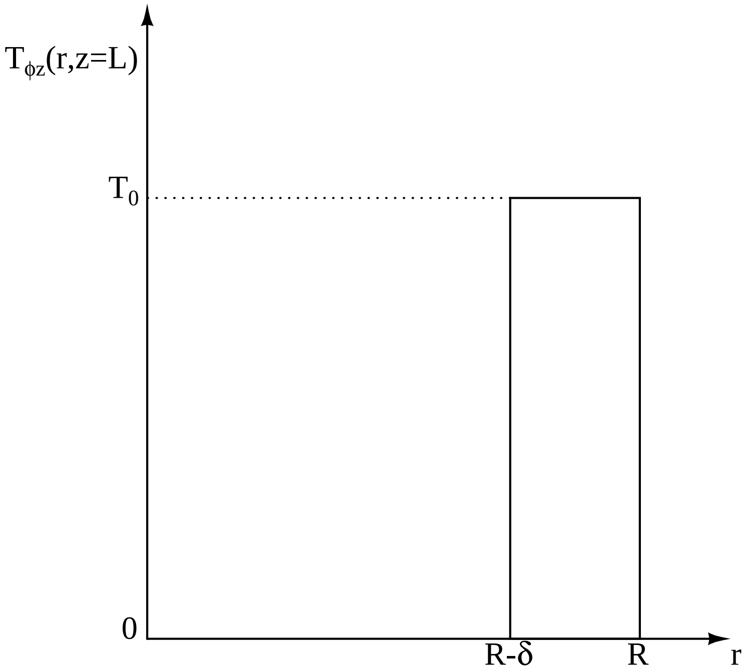

Figure 5-4: The shear stress at the top face of the cylinder $T_{\phi z}(r, z = L)$

If we assume the same general solution given by Eq. 5.15 and proceed to enforce the boundary conditions at $r = 0$ and $z = 0$ in the same manner demonstrated in that section we find that the solution requires imaginary k. We choose a solution of the form,

$$v_\phi(r, z) = AJ_1(\beta r)\sinh(\beta z) \tag{5.29}$$

where $k = j\beta$. We shall demonstrate that Eq. 5.29 satisfies all the boundary conditions given in Eq. 5.28.

The boundary condition $v_\phi(r = R, z) = 0$ requires that,

$$J_1(\beta R) = 0 \longrightarrow \beta = \frac{\alpha_n}{R} \tag{5.30}$$

where α_n is the n^{th} zero of the first order Bessel function of the first kind J_1.

All that remains is to determine the arbitrary constants A_n for each mode of Eq. 5.30 that satisfy the boundary condition on the stress at $z = L$. An infinite Bessel-Fourier series for the velocity is required to satisfy the boundary condition of Eq. 5.28,

$$v_\phi(r, z) = \sum_{n=1}^{\infty} A_n J_1(\frac{\alpha_n r}{R})\sinh(\frac{\alpha_n z}{R}) \tag{5.31}$$

Consequently, the stress distribution is given by the series,

$$T_{\phi z}(r, z = L) = \eta\frac{\partial v_\phi}{\partial z}|_{z=L} = \sum_{n=1}^{\infty} \eta\frac{\alpha_n}{R} A_n J_1(\frac{\alpha_n r}{R})\cosh(\frac{\alpha_n L}{R}) \tag{5.32}$$

which must match the boundary condition given by Eq. 5.28 and shown in Fig. 5-4.

We can use the orthogonality of Bessel functions of the first kind to solve for the series coefficients,

$$\eta\int_{r=0}^{R}\sum_{n=1}^{\infty}\tfrac{\alpha_n}{R}A_n J_1\left(\tfrac{\alpha_n r}{R}\right)J_1\left(\tfrac{\alpha_m r}{R}\right)\cosh(\tfrac{\alpha_n L}{R})r dr = \int_{r=0}^{R}T_{\phi z}(r, z = L)J_1\left(\tfrac{\alpha_m r}{R}\right)r dr \tag{5.33}$$

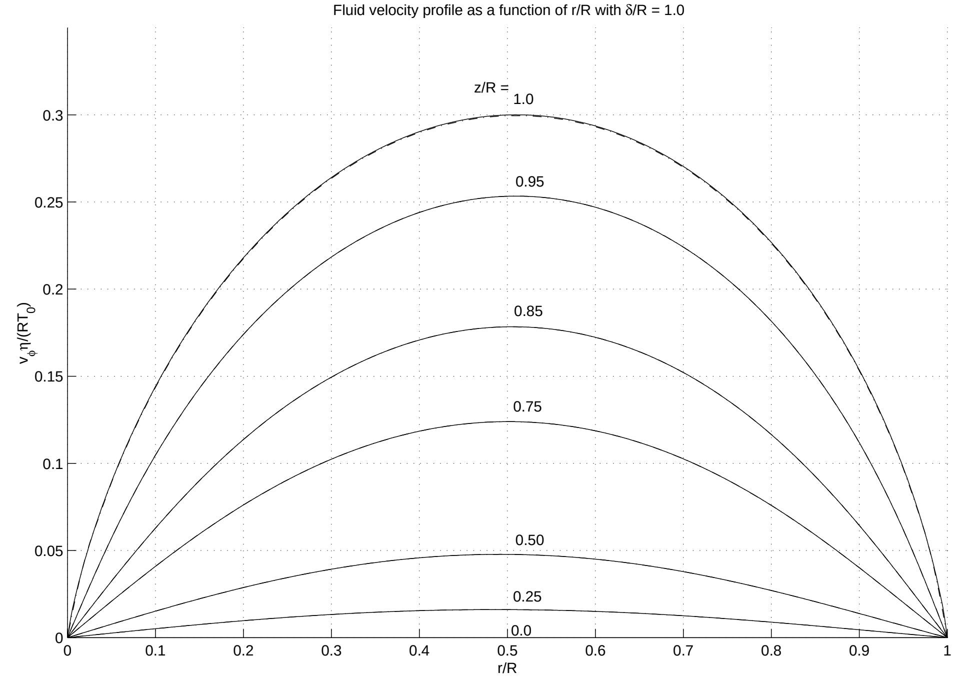

Figure 5-5: The dimensionless velocity $\frac{\eta v_\phi}{RT_0}$ as a function of $\frac{r}{R}$ for different values of $\frac{z}{L}$ for the low Reynolds number flow illustrated in Fig. 5-3. The non-dimensional width of the strip $\frac{\delta}{R}$ is 1.0. The plot shown is for a cylinder with $R = L$. The solid curves show the results of the analytical expression in Eq. 5.31 where the summation is performed up to 200 terms. Numerical results given by the dashed curves are so accurate that they completely overlap the analytical solutions.

which reduces to,

$$\frac{\eta}{R}\alpha_m A_m \cosh\left(\frac{\alpha_m L}{R}\right)\int_{r=0}^{R} J_1^2(\frac{\alpha_m r}{R}) r dr = \int_{r=R-\delta}^{R} T_0 J_1\left(\frac{\alpha_m r}{R}\right) r dr \tag{5.34}$$

where we have used the integral identities,

$$\int_{r=0}^{R} r J_\nu\left(\frac{\alpha_n r}{R}\right) J_\nu\left(\frac{\alpha_m r}{R}\right) dr = \begin{cases} 0 & ;\text{ if } m \neq n \\ \frac{R^2}{2}(J_{\nu+1}(\alpha_m))^2 & ;\text{ if } m = n \end{cases} \tag{5.35}$$

where α_m is the m^{th} zero of the ν^{th} order Bessel function of the first kind (in our problem $\nu = 1$). Finally, application of the following integral relationship on Eq.

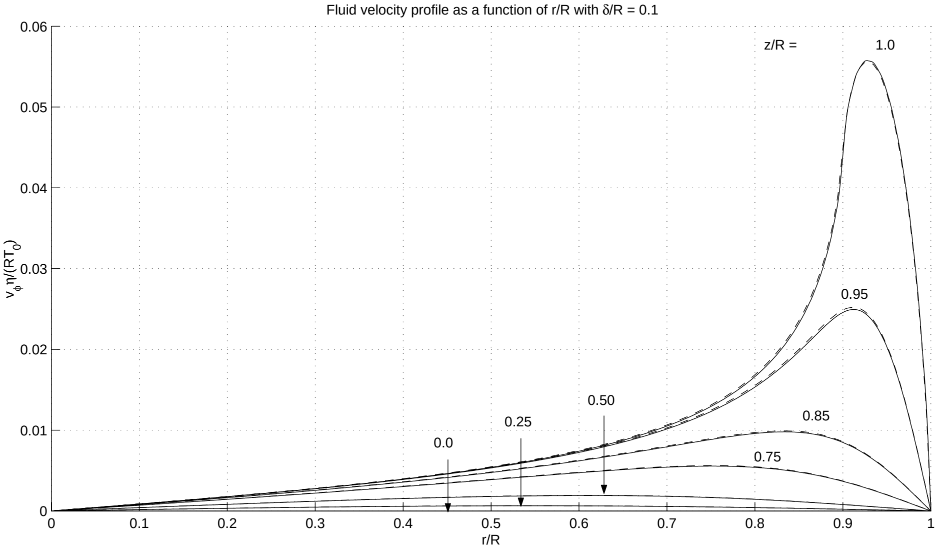

Figure 5-6: The dimensionless velocity $\frac{\eta v_\phi}{RT_0}$ as a function of $\frac{r}{R}$ for different values of $\frac{z}{L}$. The non-dimensional width of the strip $\frac{\delta}{R}$ is 0.1. The plot shown is for a cylinder with $R = L$. The solid curves are plots of the analytical expression in Eq. 5.31 with A_n given by Eq. 5.37 where the summation is performed up to 200 terms. Numerical results given by the dashed lines agree very well with the analytical curves.

5.34,

$$\int_{w=0}^{a} wJ_1(w)dw = \frac{a\pi}{2}\left(J_1(a)H_0(a) - J_0(a)H_1(a)\right) \tag{5.36}$$

where w is a dummy variable of integration, and H_0 and H_1 are Struve functions of zeroth and first order respectively, leads to the series coefficients given by,

$$A_m = \frac{\pi RT_0\left\{J_2(\alpha_m)H_1(\alpha_m) + b\left[J_0(b\alpha_m)H_1(b\alpha_m) - J_1(b\alpha_m)H_0(b\alpha_m)\right]\right\}}{\eta\alpha_m^2\cosh\left(\frac{\alpha_m L}{R}\right)J_2^2(\alpha_m)} \tag{5.37}$$

where $b = 1 - \frac{\delta}{R}$. These coefficients can be substituted into Eq. 5.31 to produce the velocity profiles for $\frac{\delta}{R}$ = 1.0, 0.1, and 0.05 as illustrated in Figs. 5-5, 5-6 and 5-7 respectively.

The finite element program Femlab was also used to verify these plots; the numerical results (dashed curves) agree with the theoretical analysis (solid curves). The small disagreement between the finite element analysis and the analytical expression is an artifact due to the mesh size. These errors are hard to discern and can be further

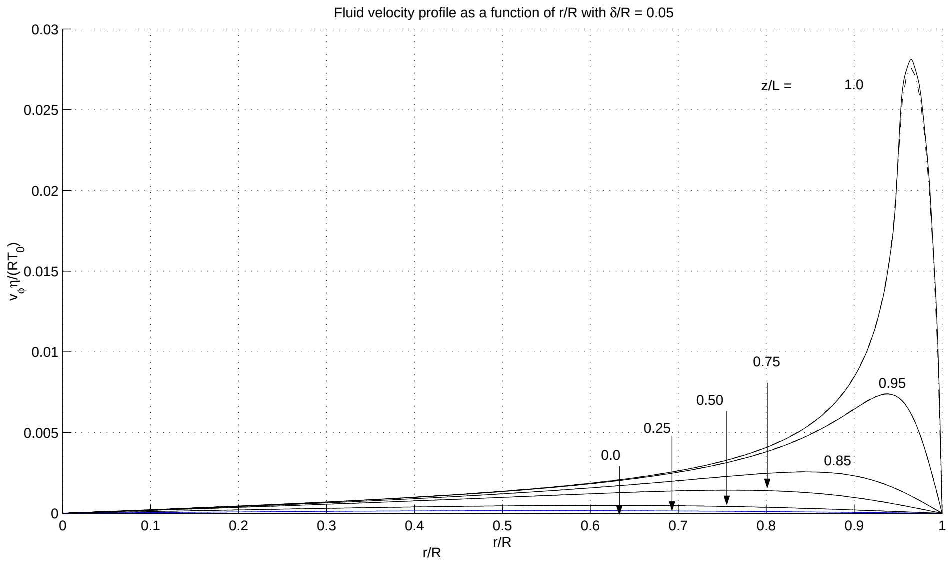

Figure 5-7: The dimensionless velocity $\frac{\eta v_\phi}{RT_0}$ as a function of $\frac{r}{R}$ for different values of $\frac{z}{L}$. The non-dimensional width of the strip $\frac{\delta}{R}$ is 0.05. The plot shown is for a cylinder with $R = L$. The solid curves are plots of the analytical expression in Eq. 5.31 with A_n given by Eq. 5.37 where the summation is performed up to 200 terms. Numerical results given by the dashed curves agree very well with analytical results.

arbitrarily reduced by refining the mesh elements. The effort would require only the allocation of more memory and computational resources to the Femlab finite element solver software.

Figs.5-5 to 5-7 illustrate that even though surface shear stress drives strong flows on the surface experiencing the shear stress, the flow decays quickly in z and r as you move away from the surface. Faster decay rates result for thinner strips of applied surface shear stress: examination of the figures shows that the ratio of the maximum fluid velocity at $\frac{z}{L} = 0.95$ to the maximum velocity at $\frac{z}{L} = 1.0$ is 0.83 for $\frac{\delta}{R} = 1.0$, 0.45 for $\frac{\delta}{R} = 0.1$ and 0.27 for $\frac{\delta}{R} = 0.05$. Fig. 5-8 shows how the velocity at the top surface of the cylinder decreases as the width of the surface shear stress strip decreases.

5.4 High Reynolds number flows

Unlike the analysis in sections 5.2 and 5.3, which hold for very low Reynolds number, the analysis in this section does not neglect the inertial terms in Eq. 5.1. The

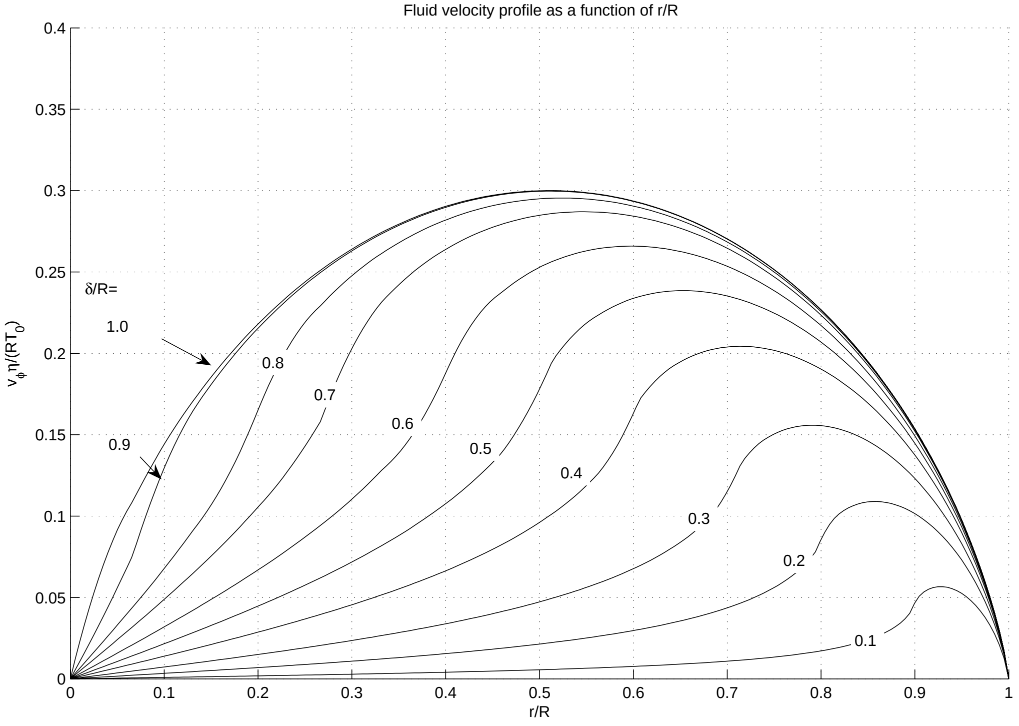

Figure 5-8: Numerical solutions of the dimensionless low Reynolds number azimuthal velocity $\frac{\eta v_\phi}{RT_0}$ as a function of $\frac{r}{R}$ at the top surface of the cylinder $(z/L = 1)$ in Fig. 5-3 for $L = R$ for different values of the relative width of the shear stress strip $\frac{\delta}{R}$.

assumption that the r and z components of the velocity profiles are negligible is not true for higher values of the Reynolds number. In general, the fluid velocity profile $\mathbf{v}$ can have radial, azimuthal, and axial components v_r, v_ϕ, and v_z respectively. The numerical study of the resulting three-dimensional recirculating flow sheds light on the conditions under which the assumptions and solutions of sections 5.2 and 5.3 hold.

The governing equations for the high Reynolds number flows are given by the full Navier Stokes equation,

$$\rho\left(\frac{\partial \mathbf{v}}{\partial t} + (\mathbf{v}\cdot\nabla)\mathbf{v}\right) = -\nabla p' + \eta\nabla^2\mathbf{v} \tag{5.38}$$

and the conservation of mass equation for an incompressible fluid,

$$\nabla \cdot \mathbf{v} = 0 \tag{5.39}$$

The high Reynolds number problem has four dependent variables: three velocity components and pressure. The investigation of the solutions to Eqs. 5.38 and 5.39 requires the use of finite element analysis method, in contrast to the simpler low Reynolds number solutions previously studied.

Cylindrical symmetry dictates that the dependent variables are functions of r and z only. Consequently, we need consider only the problem in a plane of constant ϕ, which greatly simplifies our analysis. In a plane of constant ϕ for $0 < r < R$ and $0 < z < L$, Eq. 5.38 in cylindrical coordinates for $v_r(r,z)$, $v_\phi(r,z)$, $v_z(r,z)$ and $p(r,z)$ reduces to,

$$\begin{align}
\rho\left(v_r\frac{\partial v_r}{\partial r} + v_z\frac{\partial v_r}{\partial z} - \frac{v_\phi^2}{r}\right) &= -\frac{\partial p'}{\partial r} + \eta\left[\frac{\partial}{\partial r}\left(\frac{1}{r}\frac{\partial}{\partial r}(r v_r)\right) + \frac{\partial^2 v_r}{\partial z^2}\right] \tag{5.40}\\
\rho\left(v_r\frac{\partial v_\phi}{\partial r} + v_z\frac{\partial v_\phi}{\partial z} + \frac{v_r v_\phi}{r}\right) &= \eta\left[\frac{\partial}{\partial r}\left(\frac{1}{r}\frac{\partial}{\partial r}(r v_\phi)\right) + \frac{\partial^2 v_\phi}{\partial z^2}\right] \tag{5.41}\\
\rho\left(v_r\frac{\partial v_z}{\partial r} + v_z\frac{\partial v_z}{\partial z}\right) &= -\frac{\partial p'}{\partial z} + \eta\left[\frac{1}{r}\frac{\partial}{\partial r}\left(r\frac{\partial}{\partial r}(v_z)\right) + \frac{\partial^2 v_z}{\partial z^2}\right] \tag{5.42}\\
& \tag{5.43}
\end{align}$$

and Eq. 5.39 reduces to,

$$\nabla \cdot \mathbf{v} = \frac{v_r}{r} + \frac{\partial v_r}{\partial r} + \frac{\partial v_z}{\partial z} = 0 \tag{5.44}$$

We studied this set of non-linear coupled differential equations using the Femlab finite element analysis package. Section 5.4.1 presents the results where the velocity flow profile in the cylindrical cavity is driven by a rotating top cover as shown in Fig. 5-1. Section 5.4.2 presents the flow profiles driven by a shear stress on a top surface strip of the fluid as shown in Fig. 5-3.

5.4.1 Velocity driven flows

The boundary conditions at the side walls and the bottom face of the cylinder in this case are that all three components of the velocity have to vanish by the no slip condition.

$$v_\phi(r,z) = \begin{cases} 0 & ;\, r = R;\, r = 0;\, z = 0 \\ \Omega r & ;\, z = L \end{cases} \tag{5.45}$$

$$v_r = 0 \quad ;\, r = R;\, r = 0;\, z = L;\, z = 0 \tag{5.46}$$

$$v_z = 0 \quad ;\, r = R;\, z = L;\, z = 0 \tag{5.47}$$

On the top face of the cylinder the r and z components of velocity must be zero while the ϕ component must be linearly proportional to the radius r. Furthermore, axial symmetry requires that the r and ϕ components of the velocity go to zero on the axis of the cylinder (*i.e.*, at $r = 0$). By symmetry only the z component of the velocity can have a non-zero value at $r = 0$.

Fig. 5-9 compares photographs of streamlines taken by Rosensweig to our numerical results. The solution for the velocity-driven flow equations interests us only as a means of verifying the correct implementation of the numerical model for the surface-stress-driven problem presented in Sec. 5.4.2. Specifically we verified that the numerical solution for vanishingly small Reynolds numbers R_E reproduced exactly the flow profiles illustrated in Fig. 5-2.

5.4.2 Surface-stress-driven flows

The no-slip condition requires that the three components of the velocity vanish at the side wall and bottom face of the cylindrical container.

$$v_\phi(r,z) = 0 \quad ;\, r = R;\, r = 0;\, z = 0 \tag{5.48}$$

$$v_r(r,z) = 0 \quad ;\, r = R;\, r = 0;\, z = 0 \tag{5.49}$$

$$v_z(r,z) = 0 \quad ;\, r = R;\, z = L;\, z = 0 \tag{5.50}$$

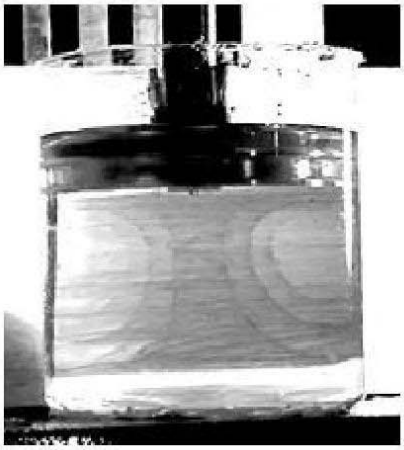

Photo 02038 -Gray

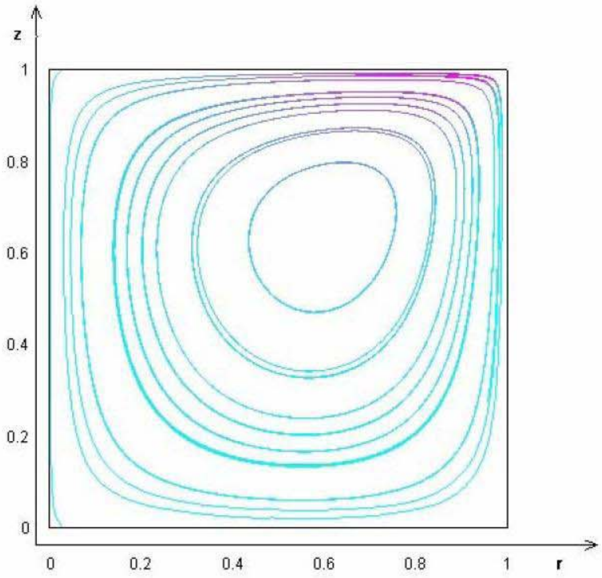

Figure 5-9: Comparison of experimental stream lines in Glycerin with food coloring dye photographed by R. Rosensweig with numerical simulation results for velocity driven flows. Top disk rotates at 2 rps corresponding to $R_E \approx 1$

Note that the radial velocity is not constrained at the top free surface of the cylinder at $z = L$. However, the z component of the velocity at the top surface has to be zero. Furthermore, axial symmetry requires that the r and ϕ components of the velocity go to zero on the axis of the cylinder (*i.e.*, at $r = 0$). By symmetry only the z component of the velocity can have a non-zero value at $r = 0$.

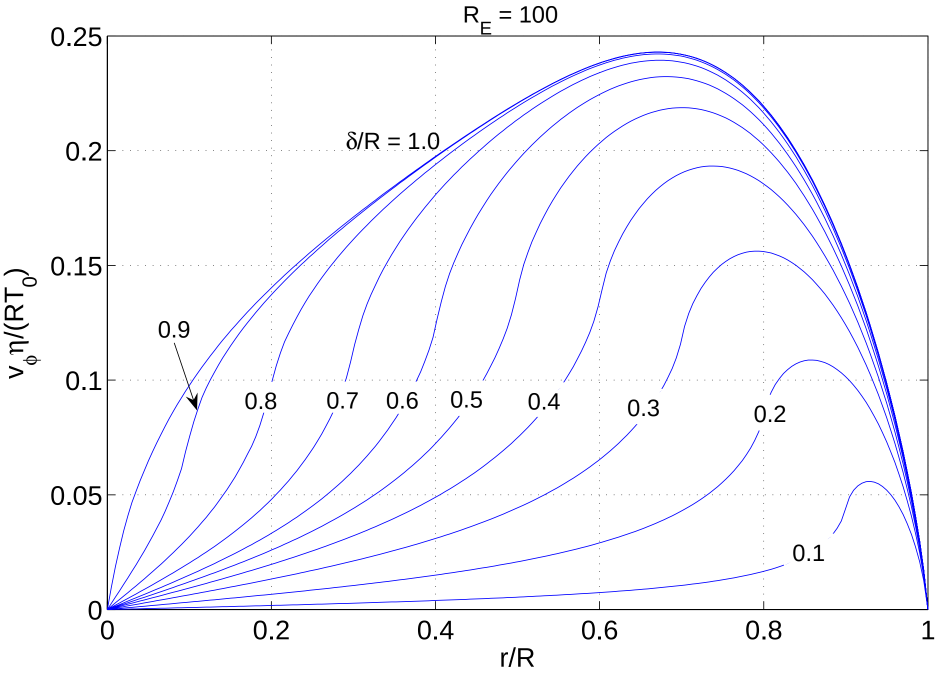

Figure 5-10: Reynolds number $R_E = 100$ numerical solutions of the dimensionless azimuthal velocity $\frac{\eta v_\phi}{RT_0}$ as a function of $\frac{r}{R}$ at the top surface of the cylinder in Fig. 5-3 for different values of the width of the shear stress strip $\frac{\delta}{R}$.

The stress on the top surface is given by,

$$T_{\phi z}(r,z) = \begin{cases} T_0 & ;\ R-\delta < r < R,\ z = L \\ 0 & ;\ 0 < r < R-\delta,\ z = L \end{cases} \tag{5.51}$$

where $0 < \delta < R$ is the width of the strip of fluid surface along which the shear stress is applied.

Figs. 5-10 and 5-11 show how the velocity at the top surface of the cylinder decreases as the width of the surface shear stress strip decreases for Reynolds numbers $R_E = 100$ and 500 respectively. It is instructive to compare the flow profiles in both

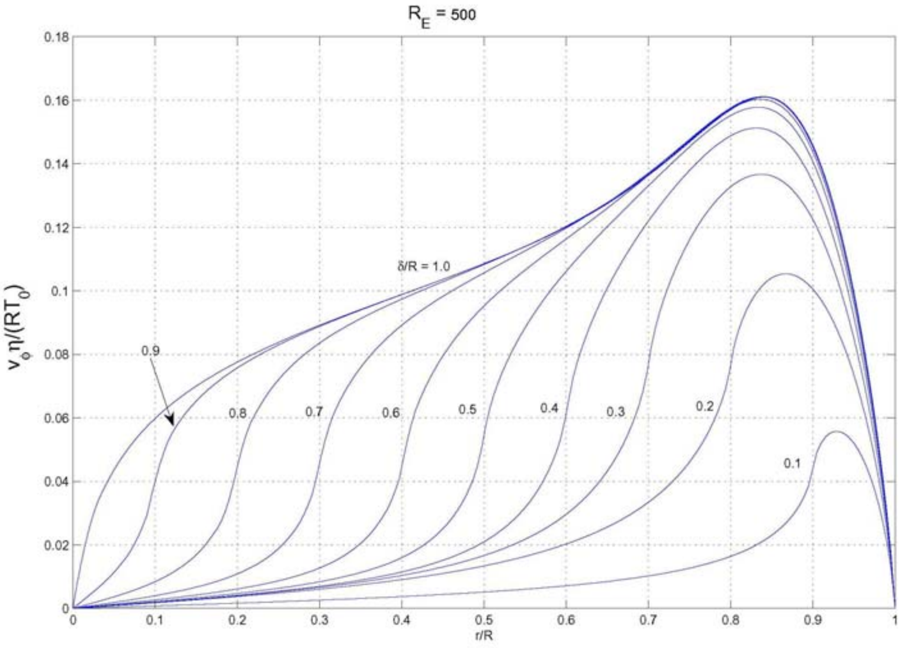

Figure 5-11: Reynolds number $R_E = 500$ numerical solutions of the dimensionless azimuthal velocity $\frac{\eta v_\phi}{RT_0}$ as a function of $\frac{r}{R}$ at the top surface of the cylinder in Fig. 5-3 for different values of the width of the shear stress strip $\frac{\delta}{R}$.

of these figures with the low Reynolds number limit shown in Fig. 5-8. Regimes with very high Reynolds numbers lead to significant departures from the simple analytical solution presented in Sec. 5.3.

Figs. 5-12 to 5-14 show the recirculation cells that develop in the r-z plane for the surface shear-stress-driven cylinder with $\delta/R = 0.05$, 0.1 and 1.0 respectively. Only the stream lines for Reynolds number $R_E = 500$ are shown because we found that the shape of the stream lines does not depend strongly on the value of the Reynolds number. The magnitude of the maximum velocity on the r-z stream lines scales approximately linearly with Reynolds R_E with proportionality factors of 8.6×10^{-8} and 1.35×10^{-6} for $\frac{\delta}{R} = 0.05$ and 0.1 respectively. Figs. 5-15 and 5-16 show the z-directed flow along the axis of the cylinder ($r = 0$) for $\delta/R = 0.05$ and 0.1 respectively. Flow along the axis of the cylinder constitutes a reliable measure of the strength of recirculating flows, which we see are insignificant compared to the azimuthal component of the velocity, v_ϕ, even at a Reynolds numbers $R_E = 10$.

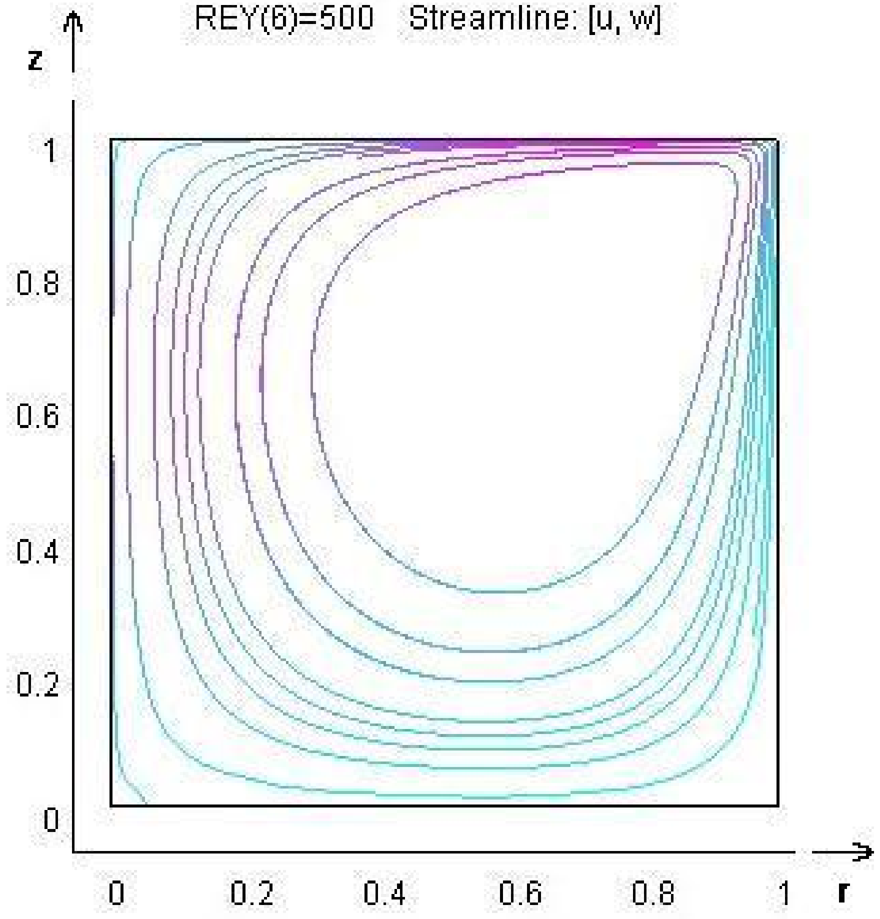

Figure 5-12: Numerical solution for the r-z plane stream lines for the surface shear stress-driven problem illustrated in Fig. 5-3. The recirculation cells shown are for a Reynolds number value of 500, and shear stress strip width of $\delta/R = 0.05$.

In conclusion, the numerical investigation of high Reynolds number flows presented in this section leads us to conclude that the assumptions underlying the simple analytical solution presented in Sec. 5.3 break down for regimes with Reynolds numbers $R_E \gg 10$. The analytical solution is valid for Reynolds numbers with order of magnitude $R_E \ll 10$ and holds to within engineering approximations even for Reynolds numbers on the order of magnitude of 10.

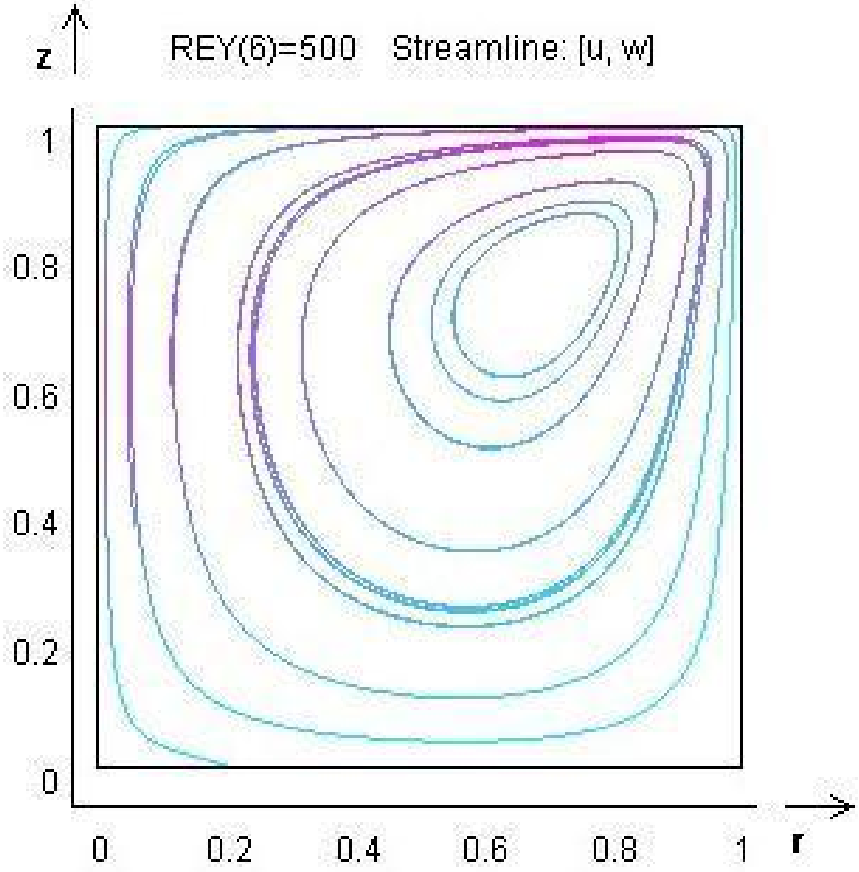

Figure 5-13: Numerical solution for the r-z plane stream lines for the surface shear stress-driven problem illustrated in Fig. 5-3. The recirculation cells shown are for a Reynolds number value of 500, and shear stress strip width of $\delta/R = 0.1$.

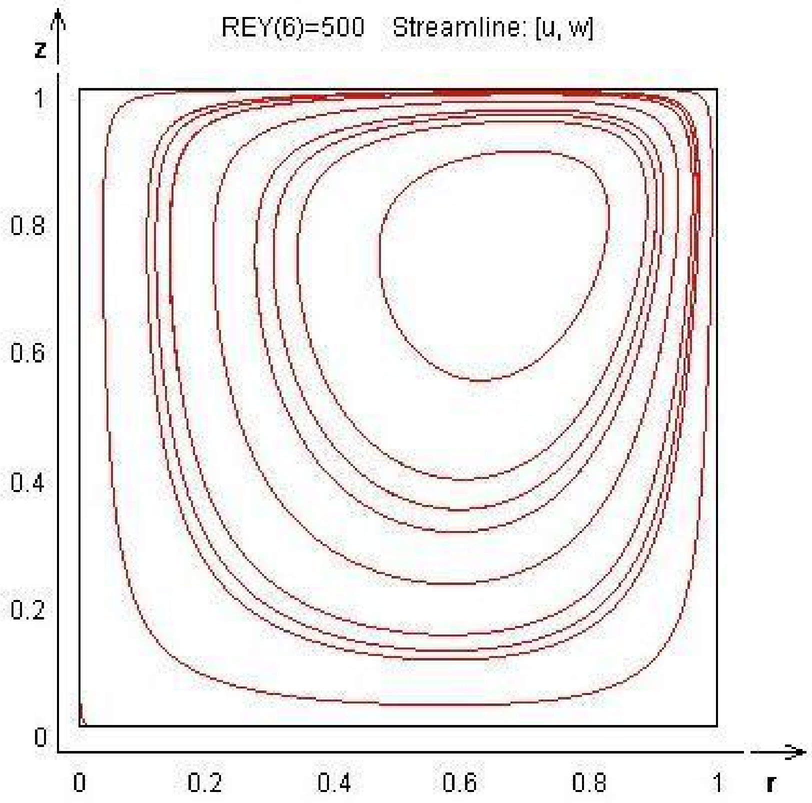

Figure 5-14: Numerical solution for the r-z plane stream lines for the surface shear stress-driven problem illustrated in Fig. 5-3. The recirculation cells shown are for a Reynolds number value of 500, and shear stress strip width of $\delta/R = 1.0$.

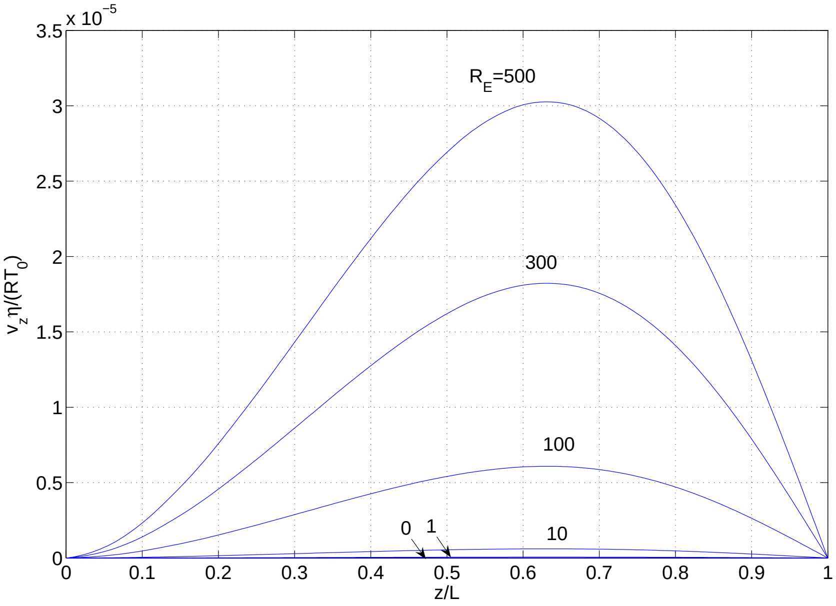

Figure 5-15: Femlab numerical solutions for the dimensionless z-directed velocity $\frac{\eta v_z}{RT_0}$ as a function of $\frac{z}{L}$ on the axis of the cylinder in Fig. 5-3 ($\frac{r}{R} = 0$) for different Reynolds number values with $R = L$. The width of the stress strip $\frac{\delta}{R} = 0.05$.

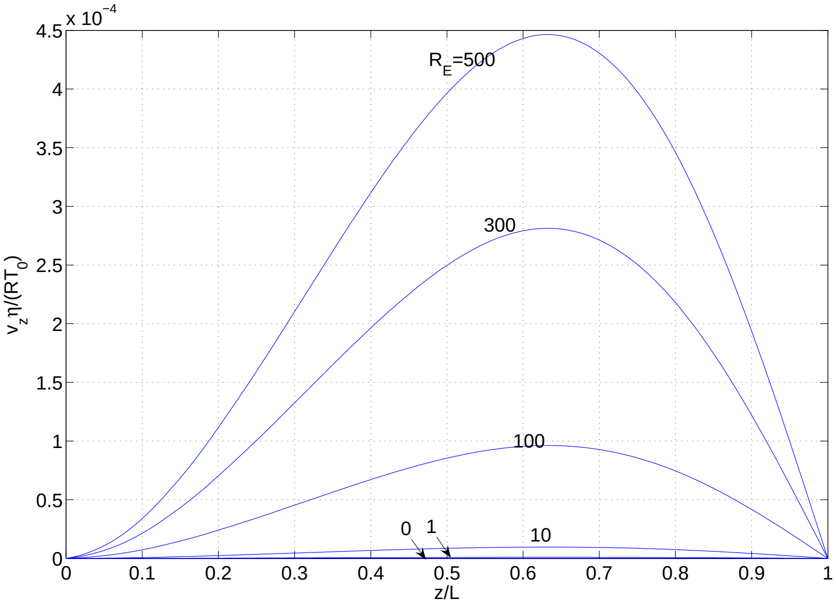

Figure 5-16: Femlab numerical solutions for the dimensionless z-directed velocity $\frac{\eta v_z}{RT_0}$ as a function of $\frac{z}{L}$ on the axis of the cylinder in Fig. 5-3 ($\frac{r}{R} = 0$) for different Reynolds number values with $R = L$. The width of the stress strip $\frac{\delta}{R} = 0.1$.

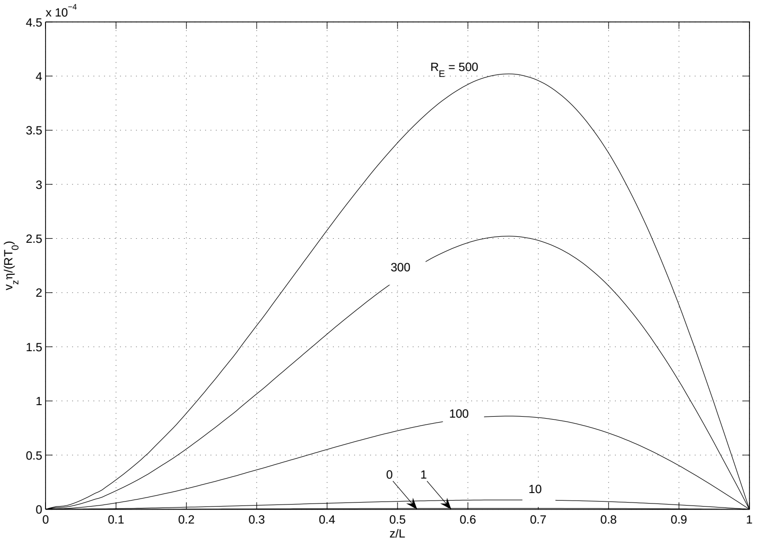

Figure 5-17: Femlab numerical solutions for the dimensionless z-directed velocity $\frac{\eta v_z}{RT_0}$ as a function of $\frac{z}{L}$ at $\frac{r}{R} = 0.25$ for different Reynolds number values with $R = L$. The width of the stress strip $\frac{\delta}{R} = 0.1$.

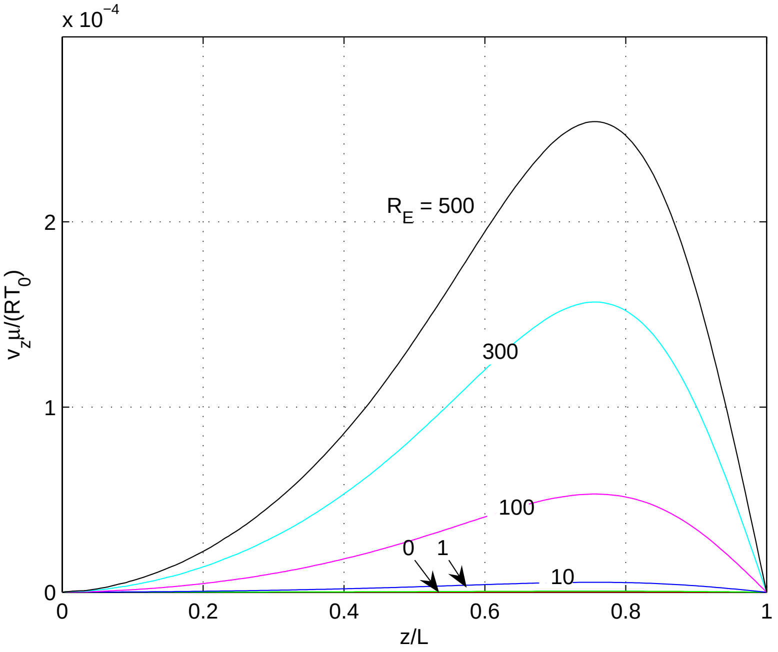

Figure 5-18: Femlab numerical solutions for the dimensionless z-directed velocity $\frac{\eta v_z}{RT_0}$ as a function of $\frac{z}{L}$ at $\frac{r}{R} = 0.5$ for different Reynolds number values with $R = L$. The width of the stress strip $\frac{\delta}{R} = 0.1$.

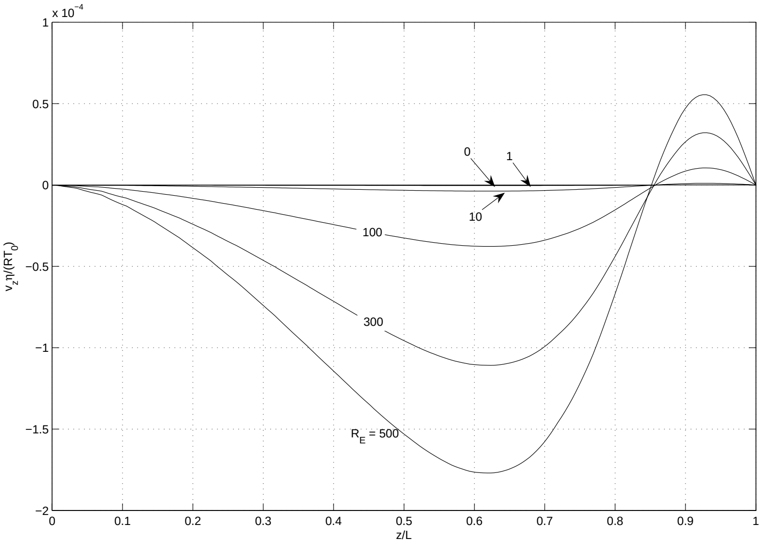

Figure 5-19: Femlab numerical solutions for the dimensionless z-directed velocity $\frac{\eta v_z}{RT_0}$ as a function of $\frac{z}{L}$ at $\frac{r}{R} = 0.75$ for different Reynolds number values with $R = L$. The width of the stress strip $\frac{\delta}{R} = 0.1$.

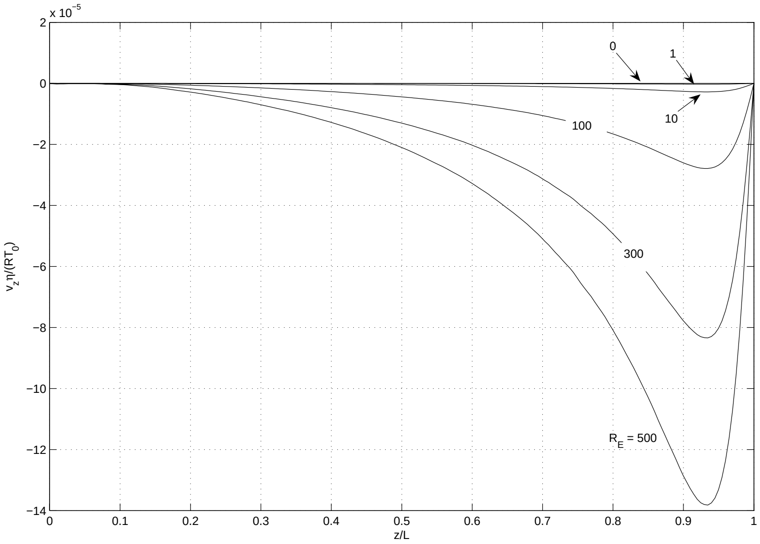

Figure 5-20: Femlab numerical solutions for the dimensionless z-directed velocity $\frac{\eta v_z}{RT_0}$ as a function of $\frac{z}{L}$ at $\frac{r}{R} = 0.99$ for different Reynolds number values with $R = L$. The width of the stress strip $\frac{\delta}{R} = 0.1$.

Chapter 6

Quasi-two-dimensional ferrofluid pattern formation in Hele-Shaw cells

6.1 Introduction

Thin layers of ferrofluid confined with an immiscible non-magnetic fluid between two glass plates in a Hele-Shaw cell configuration and stressed by a dc magnetic field normal to the layers form intricate labyrinth patterns [44]. This chapter documents the characterization of a new class of ferrofluid instabilities that arise for thin layers of ferrofluid confined in glass Hele-Shaw cells with simultaneously applied, in-plane-rotating and dc-axial magnetic fields. The spectacular two-dimensional equilibrium patterns associated with these instabilities exhibit combinations of smooth spirals, circular drops and small droplets of opaque ferrofluid arranged on a clear immiscible non-magnetic fluid background [34, 12, 33]. Interestingly, Bacri *et al.* observed similar patterns but on a microscopic scale ($\sim 50\mu$ma) by examining phase separations and failures of colloidal stability in ferrofluids in rotating applied magnetic [4].

6.2 Experimental investigation of Hele-Shaw cells in rotating magnetic fields

We used the experimental apparatus shown in Fig. 6-1 to investigate the instabilities due to simultaneous in-plane-rotating and dc-axial uniform-magnetic fields using a fluorocarbon-based ferrofluid drop constrained to the two-dimensional geometry of a Hele-Shaw cell. The stator winding of a three-phase, two-pole motor excites a uniform clockwise-rotating magnetic field in the plane of the Hele-Shaw cell for our measurements. An electromagnet surrounding the stator winding produces a uniform-dc magnetic field normal to the plane of the cell. A non-magnetic stand supports the Hele-Shaw cell in the central region of the apparatus where the magnetic fields are highly uniform. The non-uniformities due to end effects, non-ideal winding and slot harmonics are insignificant in the central region of the stator. We investigated rotating field strengths up to $\sim$100 gauss rms at rotational frequencies between 20 and 40 Hz. The dc-axial field strengths investigated went up to $\sim$250 gauss. Note that the thin disk of ferrofluid distorts the uniform in-plane magnetic field.

The Hele-Shaw cells used in this investigation consist of two glass plates separated by a small gap filled with fluorocarbon-based ferrofluid and a 50/50 mixture of isopropyl alcohol and de-ionized water known as propanol. We found that this mixture prevents the ferrofluid from wetting the glass plates and therefore allows us easily to observe the behavior of the ferrofluid drop. A video camera placed directly above the experimental setup was used to monitor and record the effects of various combinations of applied magnetic fields on the ferrofluid drop. The experimental results presented in this paper are for three Hele-Shaw cells with gap thicknesses $\sim$0.9, 1.1, and 1.4 mm. The experiments were performed for each of the three cell gap thicknesses filled by $\sim$200μl of Ferrotec Corporation's NBF-1677 fluorocarbon-based ferrofluid having $\sim$10 nm diameter magnetite particles, a low-field-magnetic susceptibility $\sim$3 and saturation magnetization $\sim$400 gauss.

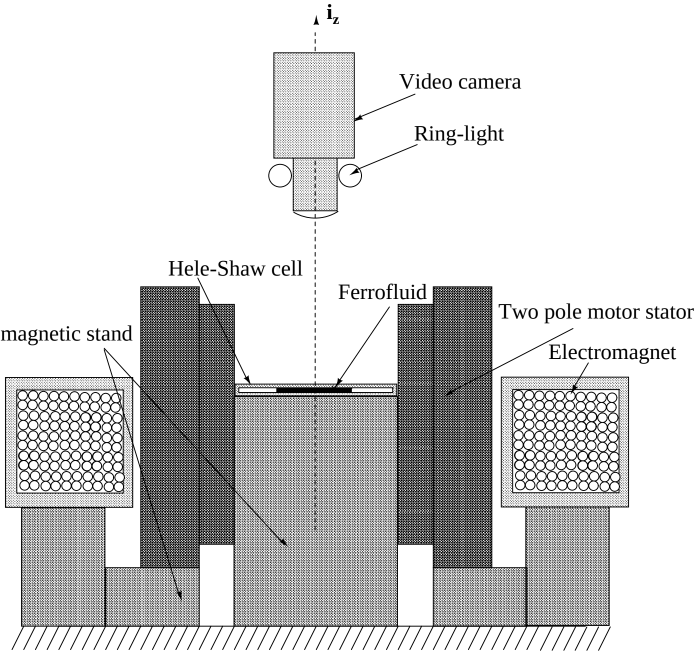

Figure 6-1: The experimental setup for investigating the behavior of a thin-layer of ferrofluid in a Hele-Shaw cell with a three-phase, two-pole stator winding to excite the uniform rotating magnetic field and an electromagnet to produce the uniform dc-axial field.

6.3 Experimental results

With no applied magnetic field, the ferrofluid coalesces into a single large circular drop held together by surface tension. In a uniform dc-axial magnetic field of strength up to ∼250 gauss, a ferrofluid drop in a Hele-Shaw cell readily forms the familiar labyrinth pattern. With subsequent application of an in-plane 20-40 Hz rotating magnetic field of strength up to ∼100 gauss rms, smooth spirals form that bend in the same direction as the applied in-plane magnetic field rotation. Weak applied rotating magnetic fields fail to bend the initial labyrinth pattern into spirals while excessively strong fields tear the spirals into many separate small spiral and circular structures. The example sequences shown in Fig. 6-2 demonstrate how labyrinth instabilities transform into multi-leaf-clover-shaped clusters of smooth spirals under the influence of a 25 Hz, ∼40 gauss rms applied in-plane clockwise rotating magnetic field with a 150-155 gauss uniform dc magnetic field [24].

If, alternatively, the rotating magnetic field is applied before the dc-axial magnetic

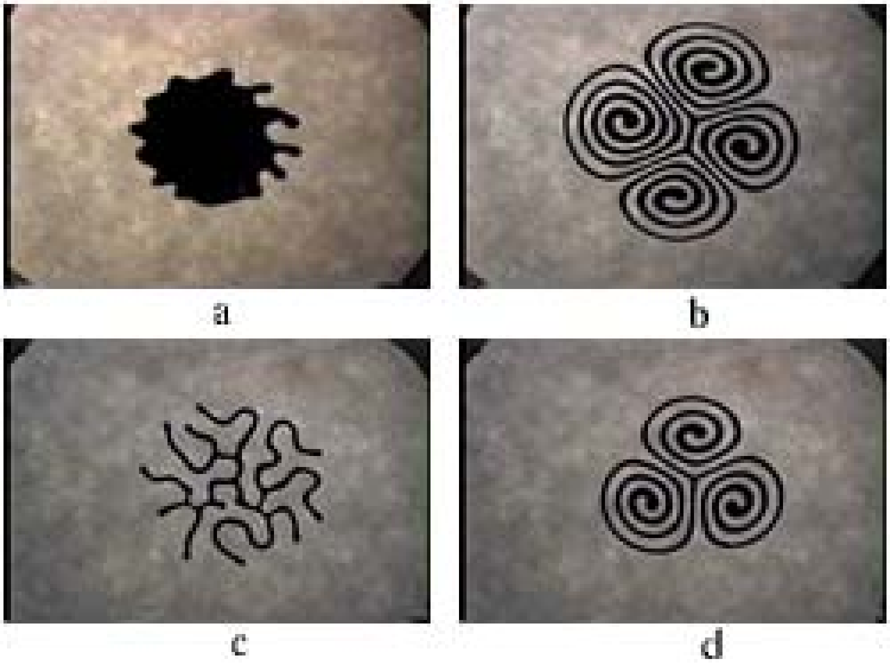

Figure 6-2: A 1.1 mm gap Hele-Shaw cell with 200μl of ferrofluid starts to form a labyrinth pattern when stressed by a $\sim$150 gauss uniform dc axial magnetic field (a). Spirals develop with the subsequent application of a 25 Hz, $\sim$40 gauss rms uniform in-plane clockwise-rotating magnetic field (b). A more elaborate labyrinth pattern develops for a 1.1 mm Hele-Shaw cell with $\sim$100μl of ferrofluid stressed by a 155 gauss dc axial magnetic field (c). Subsequent application of a 25 Hz, $\sim$40 gauss rms uniform in-plane clockwise-rotating magnetic field leads to a clover shaped cluster of smooth spirals (d).

field, the ferrofluid drop co-rotates with the applied magnetic field and holds together as a single circular drop for low values of applied dc-axial magnetic field and no labyrinth pattern forms. Gradual increase of the applied dc-axial magnetic field causes the apparent area of the ferrofluid drop to expand until the applied dc-axial magnetic field exceeds a threshold value and an abrupt phase-transition occurs. A thin ferrofluid layer is observed to suddenly peel off the top glass surface of the Hele-Shaw cell revealing many ferrofluid droplets arranged in a regular pattern inside a thick ring of ferrofluid. The steady state patterns form beneath a thin film of ferrofluid before their abrupt appearance. Fig. 6-3 illustrates the described progression with increasing applied dc-axial field strength for a 200μl drop of ferrofluid in a 1.1 mm gap Hele-Shaw cell initially stressed by a 25 Hz, $\sim$40 gauss rms rotating magnetic field.

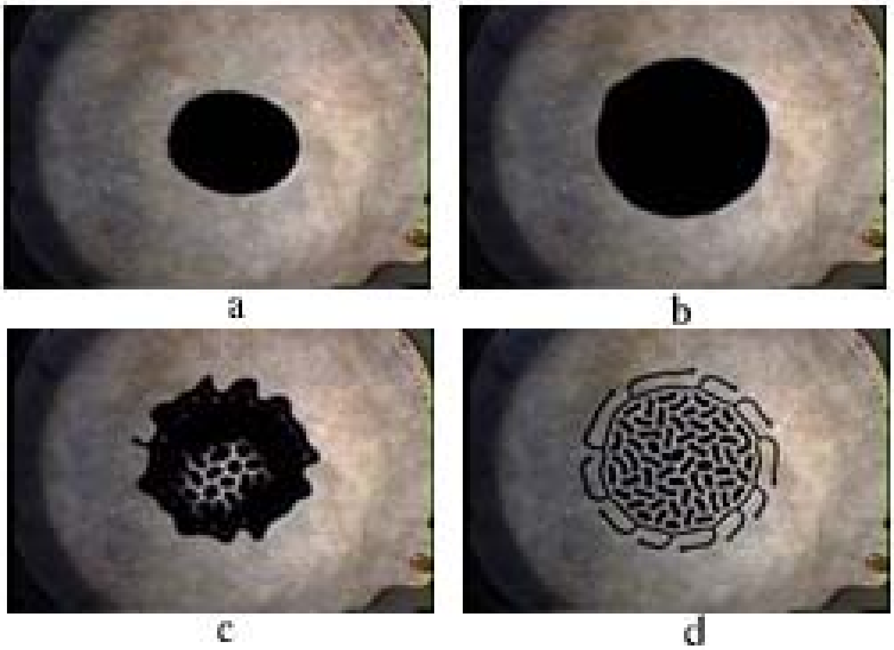

Figure 6-3: Sequence showing the apparent increase in ferrofluid drop area prior to the phase-transition in a 1.1 mm gap Hele-Shaw cell. The ferrofluid drop co-rotates with the magnetic field but remains unchanged in size and shape with an applied 25 Hz, ∼40 gauss rms in-plane rotating magnetic field (a). With the subsequent application of ∼120 gauss dc-axial magnetic field no labyrinth pattern forms, but the apparent area of the ferrofluid drop increases to approximately twice the initial area (b). When the applied dc-axial field is gradually increased to ∼170 gauss the ferrofluid peels off the top glass surface of the Hele-Shaw cell revealing an already formed droplet pattern (c) which deforms as the dc axial field is further increased to ∼230 gauss (d).

The described phase-transition instability occurs only for a small range of rotating magnetic field strengths. When the rotating field strength is at the lower limit of this range, the drop fails to hold together against the dc-axial field and labyrinth "fingers" form readily. At the other extreme, a large dc-axial field tears the ferrofluid drop apart. For the conditions of the sequence shown in Fig. 6-3 the range of rotating field strengths was observed to extend from ∼30 to ∼55 gauss rms. Figs. 6-4 and 6-5 show sample steady state patterns for various rotating field strengths in this range.

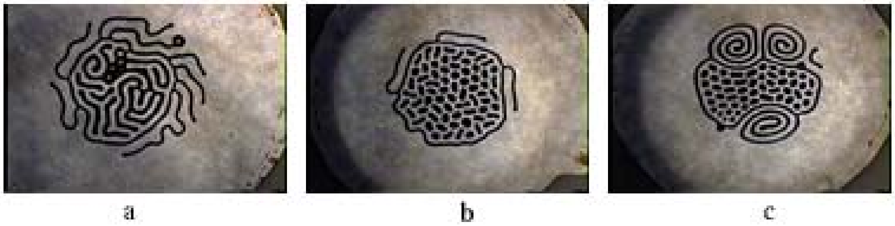

Figure 6-4: Pictures of the steady-state ferrofluid 1.1 mm gap Hele-Shaw cell pattern after the application of 25 Hz in-plane clockwise rotating magnetic fields of different magnitudes followed by a ∼230 gauss dc-axial field. The magnitude of the rotating field in (a) is ∼30 gauss rms, (b) ∼44 gauss rms, and (c) ∼50 gauss rms.

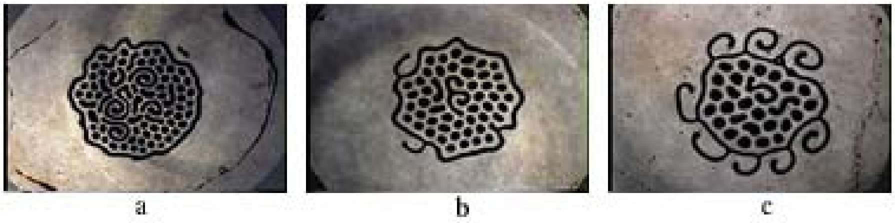

Figure 6-5: Pictures of the steady-state pattern for Hele-Shaw cells with 200μl of ferrofluid each stressed by a 30 Hz in-plane clockwise rotating magnetic field showing a reduction in the number of smaller droplets in cells with bigger cell gap thicknesses. The most droplets (∼105) were observed with the 0.9 mm gap cell with an applied in-plane clockwise rotating magnetic field strength of ∼80 gauss rms and dc-axial field strength 230 gauss (a), followed by approximately 55 droplets in the 1.1 mm gap cell with rotating magnetic field strength ∼30 gauss rms and dc-axial field strength 230 gauss (b), and finally the 1.4 mm gap cell with rotating magnetic field strength ∼30 gauss rms and dc-axial field strength of 140 gauss showed ∼30 droplets(c).

6.4 Linear model

For the purposes of this theoretical analysis the behavior of the ferrofluid in the Hele-Shaw cell is idealized as the formation of N smaller cylinders as illustrated in Fig. 6-6. Furthermore, we assume the ferrofluid cylinders are spaced far enough apart for them to be magnetically non-interacting. Letting U denote the total energy of a ferrofluid configuration, we have,

$$U = U_s + U_m \tag{6.1}$$

where U_s is the interfacial tension energy and U_m is the magnetostatic energy. The energy of the configuration will be formulated as the summation over N cylinders with identical interfacial and magnetostatic energies. In Section 6.4.1 we solve for the demagnetizing field inside a cylinder of ferrofluid. The results will subsequently be used in Section 6.4.2 to write a full expression for the energy U and perform a calculus of minimization to determine the equilibrium number of ferrofluid cylinders.

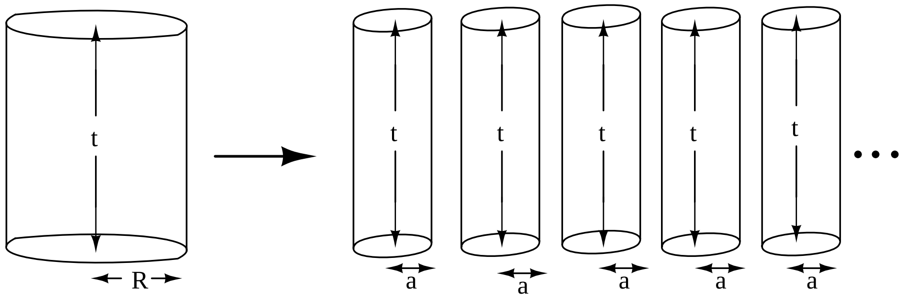

Figure 6-6: Idealized representation of the breakup of a ferrofluid Hele-Shaw-cell drop into a collection of identical smaller droplets.

6.4.1 Ferrofluid demagnetization coefficient

Figure 6-7 illustrates the geometry of a cylindrical ferrofluid droplet in a uniform-dc-vertical magnetic field. Before deriving an expression for the magnetostatic energy stored in a cylinder of ferrofluid we first must solve for the magnetic field inside the bulk of the cylinder. In the following analysis we assume uniform magnetization at all points within the ferrofluid. Such uniform magnetization in an external-uniform magnetic field would hold exactly for the case of spheroidal and ellipsoidal droplets, but holds only approximately for cylindrical droplets.

The magnetization is given by $\mathbf{M} = \chi\mathbf{H}$, where χ is the magnetic susceptibility of the ferrofluid. The field intensity, $\mathbf{H}$, within a cylinder of ferrofluid, is reduced from the applied field intensity $\mathbf{H_0}$ due to the demagnetization field $\mathbf{H_d}$ which results from magnetic surface charge on the top and bottom faces of a cylindrical droplet. We neglect the contributions of neighboring cylinders to the demagnetizing field within

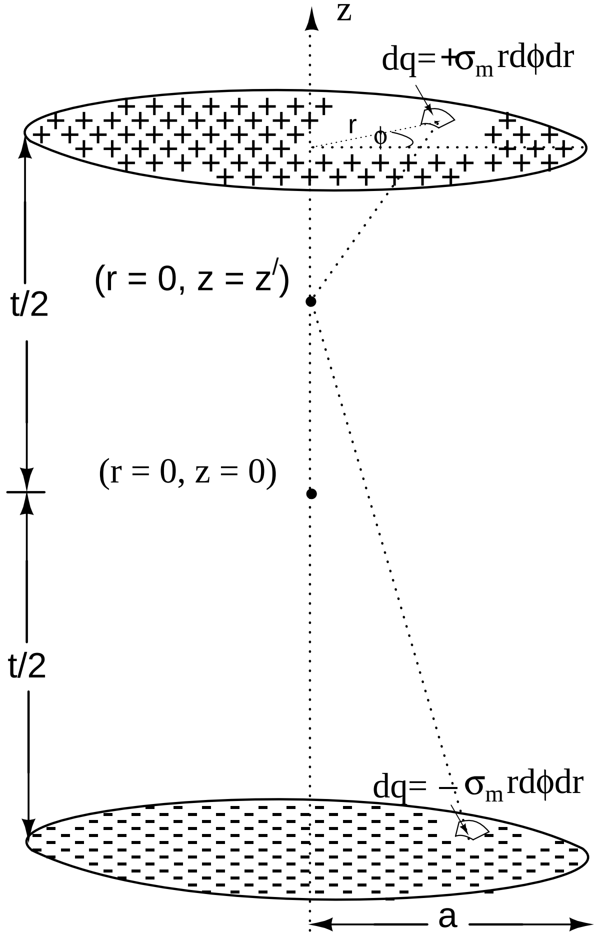

Figure 6-7: Schematic of magnetic field geometry under consideration for computation of the demagnetization field at the center of the cylinder $(r = 0, z = 0)$ from magnetic surface charge densities $\sigma_m = \pm\mu_0 M$ at the top and bottom faces of the cylindrical droplets.

a cylinder of ferrofluid. Thus,

$$\mathbf{H} = \frac{\mathbf{M}}{\chi} = \mathbf{H_0} + \mathbf{H_d} = \mathbf{H_0} - D\mathbf{M} \Longrightarrow \mathbf{M} = \frac{\chi H_0}{1 + \chi D} \tag{6.2}$$

where D is the demagnetization coefficient defined by the expression,

$$\mathbf{H_d} = -D\mathbf{M} \tag{6.3}$$

We can approximate D by solving for the demagnetizing field at the center, ($z = 0$, $r = 0$), of a uniformly magnetized cylinder of ferrofluid, $\mathbf{M} = M\mathbf{i_z}$, with radius a and height t as shown in Figure 6-7. The uniform $\mathbf{M}$ has no divergence within the bulk of the cylinder and hence no magnetic volume charge density ($i.e.$, $\rho_m = -\mu_0 \nabla \cdot \mathbf{M} = 0$). Therefore $\mathbf{H_d}$ results solely from the magnetic-surface-charge density σ_m present on the top and bottom faces of the cylinder containing non-zero $\mathbf{M}$. The magnetic surface charge densities are given by,

$$\sigma_m = \pm \mu_0 M \tag{6.4}$$

where the upper and lower faces of the cylinder carry positive and negative surface charge densities respectively. In the region of space under consideration for this field problem, there is no current density $\mathbf{J}$. Therefor, Ampere's law requires, that $\mathbf{H_d}$ be curl-free,

$$\nabla \times \mathbf{H_d} = \mathbf{J} = 0 \tag{6.5}$$

Moreover, since the divergence of $\mathbf{B}$ is zero and $\mathbf{B} = \mu_0(\mathbf{H} + \mathbf{M})$ we can write the expression,

$$\nabla \cdot \mathbf{H_d} = -\nabla \cdot \mathbf{M_d} = \frac{\rho_m}{\mu_0} \tag{6.6}$$

where ρ_m is the magnetization volume charge density and $\mu_0 = 4\pi \times 10^{-7}$ Hy/m is the magnetic permeability of free space. By analogy to electrostatics we introduce the scalar magnetic potential ψ so that $\mathbf{H_d} = -\nabla\psi$ which leads to the familiar Poisson's equation,

$$\nabla^2\psi = -\frac{\rho_m}{\mu_0} \tag{6.7}$$

which can be solved by performing the superposition integral on the surface charge densities on the top and bottom faces of the cylinder to find the magnetic field intensity along the $r = 0$ axis of the cylinder,

$$\psi = \frac{1}{4\pi\mu_0}\int_0^{2\pi}\int_0^a \left(\frac{1}{\sqrt{r'^2 + \left(z - \frac{t}{2}\right)^2}} - \frac{1}{\sqrt{r'^2 + \left(z + \frac{t}{2}\right)^2}}\right)\sigma_m r' dr' d\phi' \tag{6.8}$$

This integral evaluates to the expression,

$$\psi = \frac{\sigma_m t}{2\mu_0}\left(\sqrt{\left(\frac{a}{t}\right)^2 + \left(\frac{z}{t} - \frac{1}{2}\right)^2} - \sqrt{\left(\frac{a}{t}\right)^2 + \left(\frac{z}{t} + \frac{1}{2}\right)^2} + \left|\frac{z}{t} + \frac{1}{2}\right| - \left|\frac{z}{t} - \frac{1}{2}\right|\right) \tag{6.9}$$

which holds for any value of z on the $r = 0$ axis of the cylinder. Inside the cylinder, however, we have that $-\frac{1}{2} < \frac{z}{t} < \frac{1}{2}$, which in turn implies that in this region ψ is given by,

$$\psi = \frac{\sigma_m t}{2\mu_0}\left(\sqrt{\left(\frac{a}{t}\right)^2 + \left(\frac{z}{t} - \frac{1}{2}\right)^2} - \sqrt{\left(\frac{a}{t}\right)^2 + \left(\frac{z}{t} + \frac{1}{2}\right)^2} + \frac{2z}{t}\right) \tag{6.10}$$

By analogy to electrostatics, again, the field intensity follows as the negative gradient of ψ,

$$\mathbf{H_d} = -\frac{\partial\psi}{\partial z}\mathbf{i_z} = -\frac{\sigma_m}{2\mu_0}\left(\frac{\frac{z}{t} - \frac{1}{2}}{\sqrt{\left(\frac{a}{t}\right)^2 + \left(\frac{z}{t} - \frac{1}{2}\right)^2}} - \frac{\frac{z}{t} + \frac{1}{2}}{\sqrt{\left(\frac{a}{t}\right)^2 + \left(\frac{z}{t} + \frac{1}{2}\right)^2}} + 2\right)\mathbf{i_z} \tag{6.11}$$

Assuming that the aspect ratio $\frac{a}{t}$ is large we approximate the field intensity along the z-axis as uniform at the value it has at the midpoint $z = 0$,

$$\mathbf{H_d} \approx \mathbf{H_d}(z = 0) = \frac{\sigma_m}{\mu_0}\left(\frac{1}{\sqrt{\left(\frac{2a}{t}\right)^2 + 1}} - 1\right)\mathbf{i_z} \tag{6.12}$$

Substituting the expression for σ_m from Equation 6.4 leads to,

$$\mathbf{H_d} = \mathbf{M}\left(\frac{1}{\sqrt{\left(\frac{2a}{t}\right)^2+1}} - 1\right) \tag{6.13}$$

Consequently, the demagnetization coefficient D is given by,

$$D = 1 - \frac{1}{\sqrt{1+\left(\frac{2a}{t}\right)^2}} \tag{6.14}$$

6.4.2 Minimum-energy-ferrofluid pattern

If a ferrofluid cylinder with radius R and height t splits to form N smaller radius cylinders of radius a and height t, the conservation of ferrofluid volume requires that,

$$\pi R^2 t = N\pi a^2 t \tag{6.15}$$

which leads to the relationship,

$$a = \frac{R}{\sqrt{N}} \tag{6.16}$$

From Figure 6-7 the interfacial energy stored in N cylinders of radius a is given by,

$$U_s = 2N\pi a t\gamma \tag{6.17}$$

where γ denotes the interfacial surface tension. In addition, energy is stored in the magnetic field associated with this configuration. The magnetic energy stored in N ferrofluid cylinders can be written as,

$$U_m = -\frac{1}{2}\mu_0 \int \mathbf{M}\cdot\mathbf{H_0} dV = -\frac{\mu_0}{2}\frac{N\pi a^2 t\chi H_0^2}{1+\chi D} \tag{6.18}$$

where the magnetization is assumed to be approximately uniform in the ferrofluid. Substitution of Equation 6.16 into Equations 6.17 and 6.18 yields,

$$U_s \;=\; 2\pi R t\gamma\sqrt{N} \tag{6.19}$$

$$U_m \quad = \quad -\frac{\mu_0}{2}\frac{\pi R^2 t \chi H_0^2}{1+\chi D} \tag{6.20}$$

Note that from Equations 6.14 and 6.16, the demagnetization coefficient D in Equation 6.20 is now given by,

$$D = 1 - \frac{1}{\sqrt{1+\frac{1}{N}\left(\frac{2R}{t}\right)^2}} \tag{6.21}$$

The total energy U stored in the configuration is the sum of interfacial and magnetic energies,

$$U = U_s + U_m = 2\pi R t \gamma \sqrt{N} - \frac{\frac{\mu_0}{2}\pi R^2 t \chi H_0^2}{1+\chi\left(1-\frac{1}{\sqrt{1+\frac{1}{N}\left(\frac{2R}{t}\right)^2}}\right)} \tag{6.22}$$

This expression can be rewritten in non-dimensional terms as,

$$\tilde{U} = \sqrt{N} + \frac{\frac{1}{2}\tilde{R} N_B \chi}{1+\chi\left(1-\frac{1}{\sqrt{1+\frac{(2\tilde{R})^2}{N}}}\right)} \tag{6.23}$$

where we define the non-dimensional energy $\tilde{U}$, the magnetic Bond number N_B, and a non-dimensional radius $\tilde{R}$ as,

$$\tilde{U} = \frac{U}{2\pi R t \gamma}, \quad N_B = \frac{\mu_0 H_0^2 t}{2\gamma}, \quad \tilde{R} = \frac{R}{t} \tag{6.24}$$

The minimization of the total energy given in Equation 6.23 yields,

$$\frac{\partial \tilde{U}}{\partial N} = \frac{1}{\sqrt{N}} - \frac{\frac{1}{4}\tilde{R}^3 N_B \chi^2}{N^2\left(\frac{1}{4}+\frac{\tilde{R}^2}{N}\right)^{\frac{3}{2}}\left(1+\chi\left(1-\frac{1}{\sqrt{1+\frac{1}{N}\left(\frac{2\tilde{R}}{t}\right)^2}}\right)\right)^2} = 0 \tag{6.25}$$

The magnetic Bond number, $N_B = N_{BO}$, at equilibrium is,

$$N_{BO} = 4\left(1+\frac{N}{(2\tilde{R})^2}\right)^{\frac{3}{2}}\left(\frac{1}{\chi}+\left(1-\frac{1}{\sqrt{1+\frac{1}{N}\left(\frac{2\tilde{R}}{t}\right)^2}}\right)\right)^2 \tag{6.26}$$

6.5 Linear model results

The general dependence of the magnetic Bond number on N and $\tilde{R}$ shown in Fig. 6-8 illustrates the existence of a minimum value of Bond number, N_{BO}, independent of $\tilde{R}$, beneath which no solution exists for any value of N. Furthermore, Figs. 6-8 and 6-9 shows that for values of N_B greater than the threshold value N_{BO}, N is double valued. A more exact analysis is needed to determine whether this curious feature is a mathematical artifact since the existence of more than one stable pattern under identical experimental conditions has not yet been observed.

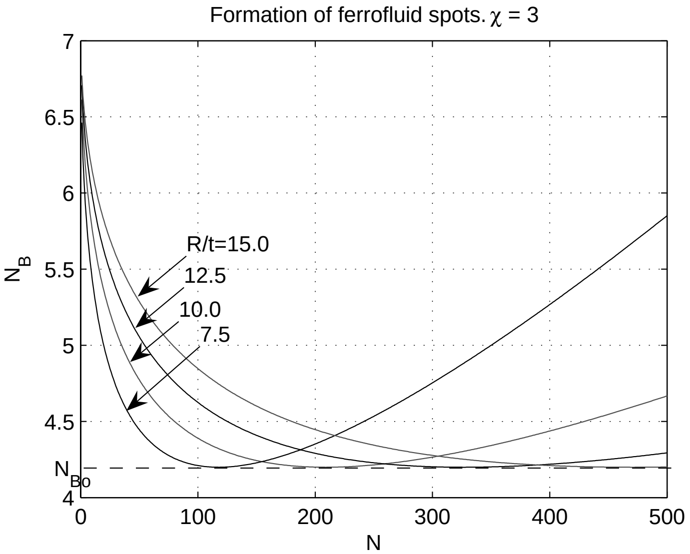

Figure 6-8: The Bond number, N_B, at equilibrium as a function of N for $\chi = 3$.

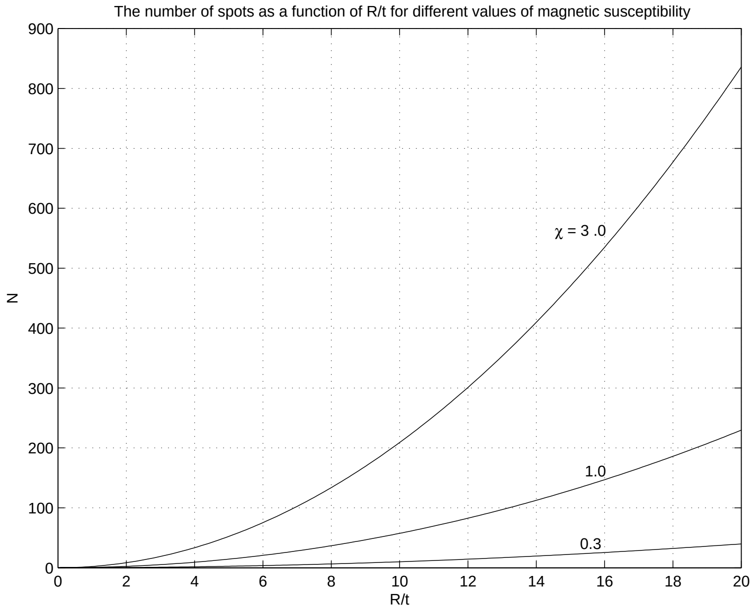

Figure 6-9: The number of cylinders, N, at the threshold Bond number N_{BO} as a function of $\tilde{R} = R/t$ and χ.

The expression for the threshold value is given by,

$$N_{BO} = \left(\frac{\chi^2+6\chi+3+(1+\chi)\sqrt{9+18\chi+\chi^2}}{6+12\chi}\right)^{\frac{3}{2}} \left(2+\frac{2}{\chi}-\frac{4\sqrt{2}}{\sqrt{5\chi^2+\frac{3\left(3+\sqrt{9+18\chi+\chi^2}\right)}{\chi^2}}}\right)^2 \tag{6.27}$$

which can be derived by setting $\frac{\partial N_B}{\partial N}$ and finding the local minimum of the expression given in Equation 6.26. The threshold for instability is then associated with an equilibrium number of cylinders N, given by the following expression,

$$N = \frac{2\tilde{R}^2}{3+6\chi}\left(\chi^2-6\chi-3+(1+\chi)\sqrt{9+18\chi+\chi^2}\right) \tag{6.28}$$

While the threshold-applied magnetic field for the phase-transition-like instability is independent of $\tilde{R}$, the number of small cylinders that appear after the instability occurs depends strongly on the value of $\tilde{R}$ as illustrated in Fig. 6-9. The results of our experimental investigation qualitatively agree with the predictions of this energy minimization analysis: Fig. 6-5 verifies the reduction in the number of ferrofluid

R [mm]	t [mm]	v_r [μl]	adjusted R/t
8.4	0.9	106	6.4
7.6	1.1	64.1	5.7
6.7	1.4	55.1	4.1

Table 6.1: The non-dimensional parameter R/t was adjusted to take into account the volume of ferrofluid in the ring and spirals surrounding the small droplets in the Hele-Shaw cell phase transformation. The volume of the ferrofluid in the surrounding strip, v_r, was subtracted from the initial ferrofluid volume of 200 μl. The difference in volume was used to compute a new effective value of R.

droplets with increasing gap thickness for the same initial drop volume.

Quantitatively, the number of ferrofluid droplets predicted by the minimum energy analysis generally agrees with experimentally observed values. To compare our approximate analysis with measurements we consider only the volume of the ferrofluid in the small droplets to compute the initial drop's aspect ratio (*i.e.*, we subtract the volume of the ferrofluid in the ring surrounding the droplets from the initial volume as documented in Table 6.1). For $t =\sim$ 0.9, 1.1 and 1.4 mm, the adjusted aspect ratios R/t of ~6.4, 5.7, and 4.1 lead to model predictions that ~100, 70, 30 droplets should form after the phase transition; experiments show that approximately 80, 60 and 30 droplets form respectively. The model-predicted threshold magnetic field strength values of ~90, 75 and 70 gauss for the respective aspect ratios R/t of ~6.4, 5.7, and 4.1, agree well with the observed experimental threshold values of ~99, 85, and 70 gauss. The threshold value was taken to be the value of the magnetic field that leads to an approximately 20% increase in apparent ferrofluid drop area from its initial value with no applied magnetic field. The magnetic field values at which the ferrofluid peels off the top glass surface and reveals the droplets are much higher than the incipience of the phase-like transition. The peel-off magnetic field values are ~210, 180, 120 gauss respectively.

6.6 Non-linear analysis

The magnetic field intensity inside the ferrofluid droplet, H_a, is related to applied magnetic field H_o by the expression,

$$H_a = H_o - DM_a(H_a) \tag{6.29}$$

where D is the demagnetization factor and M_a is the magnetization. The analysis in this section assumes that the demagnetization coefficient D inside the ferrofluid droplet is constant. The assumption of a linear magnetization relation however is relaxed and the magnetization characteristic M_a is assumed to follow the non-linear Langevin relation given by,

$$M_a(H_a) = M_s\left(\coth(\beta H_a) - \frac{1}{\beta H_a}\right) \tag{6.30}$$

where

$$\beta = \frac{3\chi}{M_s} \tag{6.31}$$

Substitution of Eq. 6.30 into Eq. 6.29 leads to the expression,

$$\beta(H_o - H_a) = \alpha_o - \alpha_a = 3\chi D M_s\left(\coth(\alpha_a) - \frac{1}{\alpha_a}\right) \tag{6.32}$$

where $\alpha = \beta H$ and appropriate subscripts denote the non-dimensional magnetic intensities inside (subscript a) and outside (subscript o) the ferrofluid droplet. Eq. 6.32 is a transcendental equation, having no closed-form analytical solution; fortunately the equation can be easily solved by numerical or graphical methods. Such a solution would completely determine the functions $\alpha_a(D, \alpha_o)$, and $M_a(D, \alpha_o)$ and their derivatives with respect to D and α_o.

The numerical computation of $\alpha_a(D, \alpha_o)$, and $M_a(D, \alpha_o)$ determines the magnetostatic energy stored in a ferrofluid droplet (See discussion in Appendix B). The total stored energy, U, in the ferrofluid Hele-Shaw cell system is then given by the expression,

$$U = 2\pi R t \gamma \sqrt{N} - \frac{\mu_0}{2}\pi R^2 t \left(D M_a^2 + \frac{M_s^2}{3\chi} \ln\left[\frac{\sinh \alpha_a}{\alpha_a}\right]\right) \tag{6.33}$$

Normalization of the total energy by the surface tension energy in the initial ferrofluid drop of radius R yields

$$\tilde{U} = \frac{U}{2\pi R t \gamma} = \sqrt{N} - \frac{1}{2}\frac{\mu_0 M_s^2 t}{2\gamma}\frac{R}{t}\left(D\tilde{M}_a^2 + \frac{1}{3\chi}\ln\left[\frac{\sinh \alpha_a}{\alpha_a}\right]\right) \tag{6.34}$$

This expression of the total non-dimensional energy in the Hele-Shaw cell ferrofluid system can be minimized with respect to the demagnetization factor D

$$\frac{\partial \tilde{U}}{\partial D} = \frac{1}{2\sqrt{N}}\frac{\partial N}{\partial D} - \frac{1}{2}\frac{\mu_0 M_s^2 t}{2\gamma}\frac{R}{t}\left[\tilde{M}_a^2 + \tilde{M}_a\left(2D\left[1 - \coth^2\alpha_a + \frac{1}{\alpha_a^2}\right] + \frac{1}{3\chi}\right)\frac{\partial \alpha_a}{\partial D}\right] = 0 \tag{6.35}$$

where we have used the following relation derived from using the chain rule on Eq. 6.32,

$$\frac{\partial \tilde{M}_a}{\partial D} = \left(1 - \coth^2\alpha_a + \frac{1}{\alpha_a^2}\right)\frac{\partial \alpha_a}{\partial D} \tag{6.36}$$

The minimum value of D as a function of α_o is therefore given by,

$$\frac{2}{(1-(1-D)^2)^{\frac{3}{2}}} + \frac{1}{2}\frac{\mu_0 M_s^2 t}{2\gamma}\left[\tilde{M}_a^2 + \tilde{M}_a\left(2D + \frac{1}{3\chi}\right)\frac{\partial \alpha_a}{\partial D}\right] = 0 \tag{6.37}$$

The one-to-one correspondence between the number of droplets N and D leads to the number of drops that minimizes the total energy stored in a Hele-Shaw cell ferrofluid system. Fig. 6-10 shows the minimum energy curves for the linear and non-linear magnetization analyses for $R/t = 4.1$, 5.7, and 6.4.

6.7 Discussion and future work

The non-linear analysis predicts that 88, 70, and 37 small droplets form for ratios $\frac{R}{t} = 6.4$, 5.7 and 4.1, slightly lower than the number of droplets predicted by the linear magnetization model. The predicted number of droplets for both models are in better agreement for lower values of initial aspect ratio R/t (See Fig. 6-11). Furthermore, the non-linear model predicts the occurrence of the phase-like transition from one drop to many smaller droplets at critical value of Bond number $N_{BO} \approx 3.0$. The value of the critical Bond number predicted by the linear model is higher at approximately 4.2.

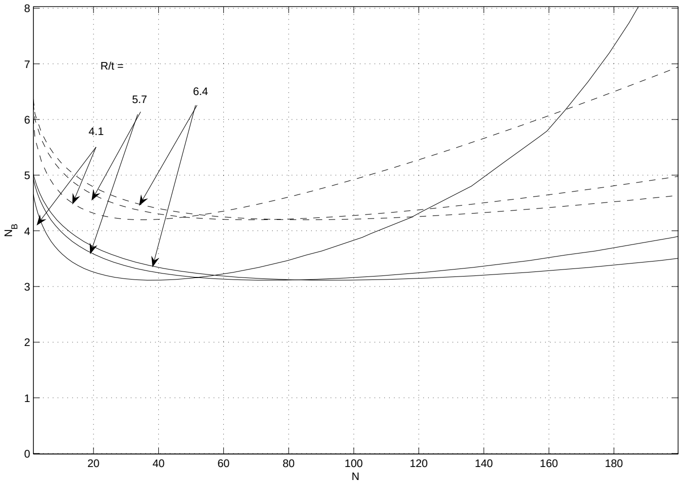

Figure 6-10: Plots of minimum energy curves for linear (dashed line) and non-linear (solid line) magnetization analysis for $\chi = 3$ corresponding to $NBF-1677$ fluorocarbon based ferrofluid. Curves shown correspond to experiments with initial ferrofluid drop to Hele-Shaw cell gap thickness ratio R/t = 4.1, 5.7, and 6.4. The non-linear model predicts a phase-like transition from one drop to many smaller droplets at Bond number $N_{BO} \approx 3.0$ while the linear model predicts a higher Bond number of approximately 4.2.

Comparison of the linear and non-linear models clearly indicates that non-linear magnetization lowers the predicted value of the threshold magnetic Bond number. Moreover, the non-linear correction brings the predicted number of droplets to closer agreement with experimental results. Lastly, the intractability of the non-linear model requires the use of numerical methods to compute the energy minimization criteria for the ferrofluid Hele-Shaw cell system. The linear analysis, however, results in analytical expressions that are easier to study.

The main source of discrepancy between experimental and theoretical results is due to the gross simplification of modeling the phase-like transition in the Hele-Shaw cell system as the transition from one large drop of ferrofluid into many smaller droplets of ferrofluids. This over-simplification ignores significant features of the two-dimensional ferrofluid pattern that forms inside the Hele-Shaw cell after the occurrence of the phase-like transition. These features include the surrounding circular strip of ferrofluid that encloses the ferrofluid droplets and the spirals projecting out of the surrounding strip of ferrofluid. Removing such assumptions as (i) uniform magnetic field inside the ferrofluid droplet, (ii) non-interaction between ferrofluid droplets and (iii) neglecting the rotating magnetic field in the energy analysis, might improve the predictions of the model at the cost of increased model complexity.

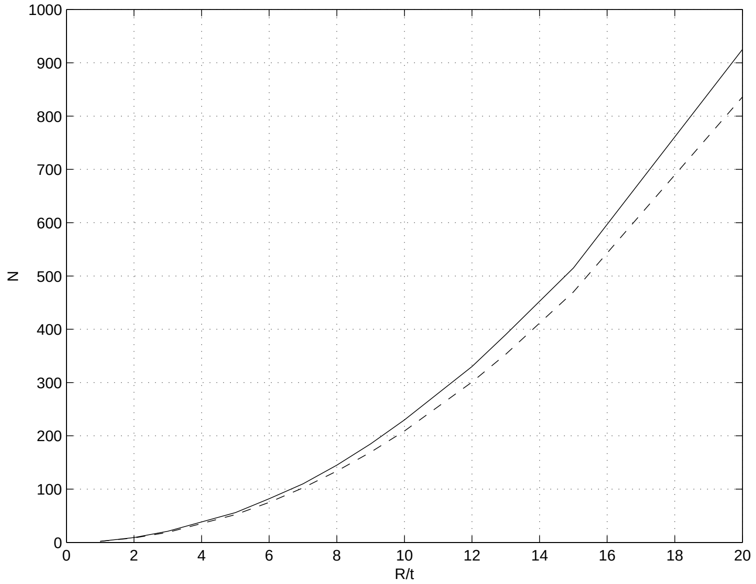

Figure 6-11: Equilibrium number of droplets N as a function of R/t for $\chi = 3$. The shown values minimize the total energy in the ferrofluid Hele-Shaw system according to the linear (dashed line) and non-linear (solid line) magnetization analysis.

Chapter 7

Experimental investigation of Ferrofluid spin-up phenomena

The velocity distribution in the bulk of a ferrofluid cannot be measured by laser Doppler or streak path techniques due to the opacity of ferrofluids. Pulsed ultrasound velocimetry allows, however, for the real-time measurement of velocity profiles in opaque fluids [6, 7, 17, 46]. Experimental measurements of the velocity field in the bulk of the ferrofluid provides the information required to answer many of the questions that arise from reviewing the ferrofluid spin-up literature. Investigations of ferrofluid spin-up in the literature do not report the flow field inside the bulk of the ferrofluid, being limited to studying only the flow profile on the free-surface of the opaque ferrofluid by recording the motion of various kinds of floating tracer beads and particles.

The pulsed ultrasound technique uses reflections off of small tracer particles or air bubbles suspended in the fluid flow. The technique then uses the time of flight of the reflected ultrasound beams to estimate the velocity of the tracer particles. Each ultrasound probe measures the component of the velocity along the emitted beam at every point along the beam. By definition the velocity is measure positive if the flow is away from the probe and negative if the flow is towards the ultrasound probe. Combining the readings of multiple probes at various positions and angles allows the measurement of the velocity at many points in the flow field. In ferrofluid applications, tracer particles of sizes around 50-200 microns must be added to the fluid. The 5-15 nm ferrofluid particles are too small to scatter the ultrasound effectively. Commonly used particles include plastic polyethylene spheres, corn pollen, and hollow spheres of SiO_2. In our experiments we found it necessary to add GrilTex-P1 latex particles, produced by EMS chemie, Switzerland, to the ferrofluid to improve the quality of the reflected ultrasound signal. These copolyamide spherical particles with an average diameter of 50 μm have a density of 1.1 g/cc and are practically neutrally buoyant in water-based ferrofluid. During the course of the experiments, we would, however, stir the ferrofluid vigorously by hand once every day to prevent the particles from settling, thus maintaining the dispersion of tracer particles necessary for a high level of ultrasonic echoes.

The pulsed ultrasound technique has the advantage of non-disruptive measurement of the flow profile; the ultrasound probes can be placed in the outside walls of the ferrofluid container without contacting the ferrofluid. However, this increases ultrasound energy losses because the signal must couple from the probe to the container wall and from container wall into the fluid. Walls made out of materials that have an acoustic impedance similar to that of ferrofluids (like Plexiglas) can maximize transmissivity between the container wall and the ferrofluid.

This chapter presents the preliminary results of our investigation of ferrofluid spin-up flow phenomena in MSG W11 and EMG705 water based ferrofluids with the Signal Processing DOP2000 ultrasound velocimeter. Unlike previous reports in the literature which are restricted to optical observations at the top ferrofluid/air interface, the ultrasound technique overcomes the difficulty that the ferrofluid opacity poses, enabling us to measure the velocity profiles in the bulk of the ferrofluid

7.1 Experimental setup

Figs. 7-1 to 7-3 show the experimental apparatus we used to investigate the flow in the bulk of a cylindrical container of water-based ferrofluid with a free top surface undergoing spin-up flow driven by a uniform counter-clockwise rotating magnetic field.

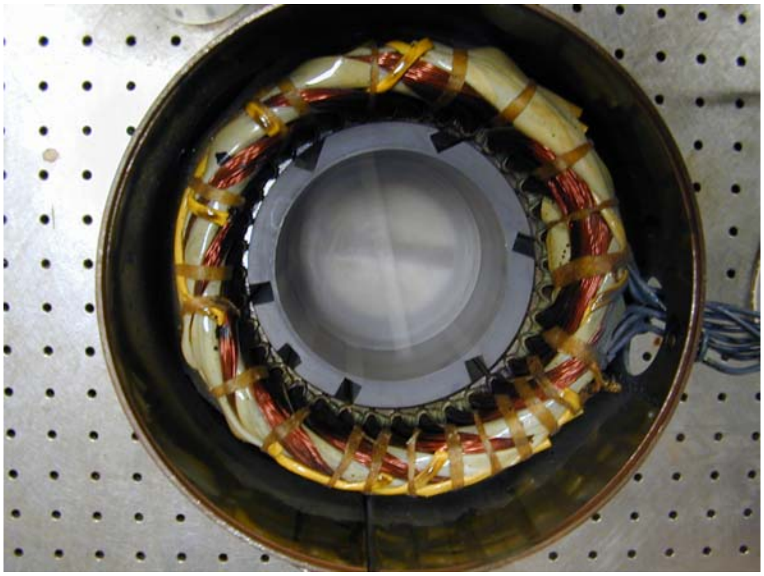

Figure 7-1: Photograph showing top view of an empty cylindrical experimental container inside the stator winding. Ultrasound probes were inserted into the grooves in the side wall to measure velocity profiles along different secants.

The uniform rotating magnetic field is produced by the stator winding of a two-pole three-phase motor. The motor's rotor was removed and replaced by a polycarbonate cylindrical vessel filled to a height of 50 mm with water-based ferrofluid. A video camera placed directly above the experiment was used to monitor the behavior of the top ferrofluid/air interface. Channels grooved at different angles from the radial normal to the cylinder's lateral side housed the ultrasound velocimeter probe (See Fig. 7-1). The depth of grooved channels was specified to leave a thin thickness of wall intact (< 5 mm) so that the ultrasound probe does not directly contact the ferrofluid. Ultrasound gel was used at the interface of the probe and the vessel wall to couple the ultrasound signal through the vessel wall to the bulk of the ferrofluid more effectively. Table 7.2 shows the values of geometric parameters for the spin-up experimental apparatus.

The cylindrical polycarbonate container used in these experiments was designed to fit snugly into the 78 mm diameter bore of a three phase, 2-pole motor stator winding in order to guarantee that the ferrofluid is radially centered along the axis of the stator winding where the applied magnetic field is most uniform. To maintain high magnetic field uniformity, the container was also centered vertically within the

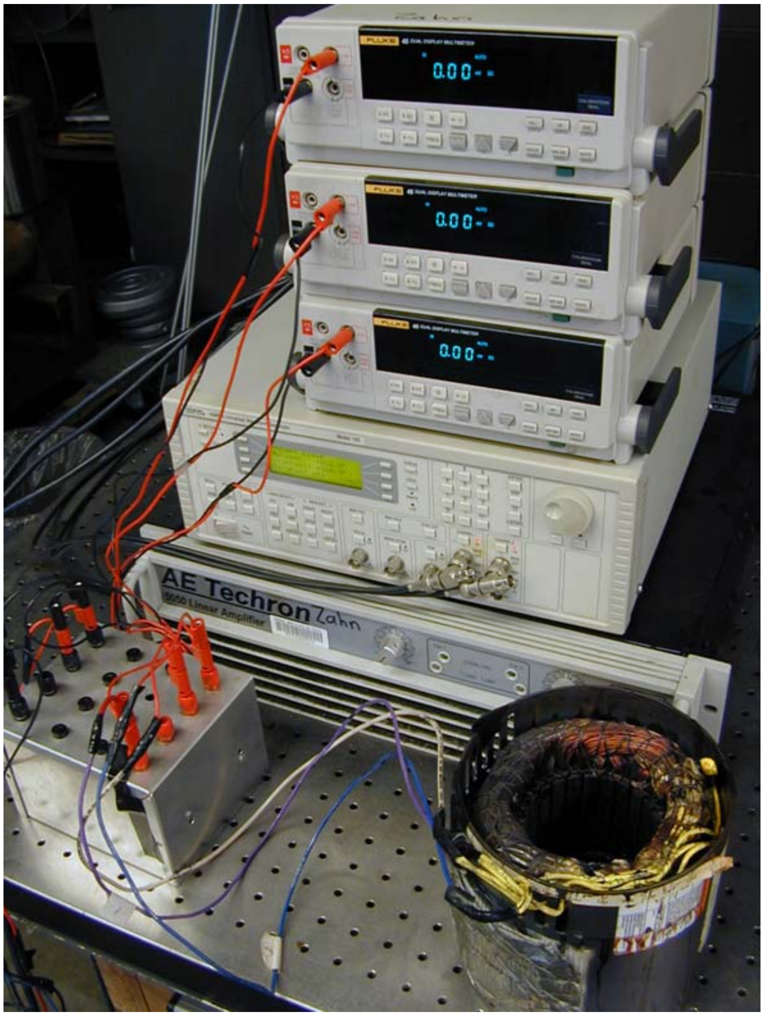

Figure 7-2: Photograph of the spin-up experimental apparatus showing the three-phase, two-pole stator winding driven by the AE Techron 5050 linear amplifier and the Wavetek Datron 40 MS/s universal waveform generator. The three Fluke multimeters are connected in ac-current mode to monitor and set the currents in each phase to have the same magnitude.

stack of the stator's iron core. The uniform magnetic fields inside the stator winding were generated with balanced-three-phase-sinusoidal currents to create clockwise or counter-clockwise rotating uniform magnetic fields. We grounded one of the phases of the stator winding and excited the remaining two phases at 0° and $\pm 60^\circ$ to generate clockwise or counter-clockwise rotating uniform magnetic fields. Fig. 7-2 shows the experimental setup used to generate the waveforms we input to the stator winding. Measurements were taken at frequencies from 10 to 1000 Hz with input currents of up to 4 Amps rms. The currents at higher frequencies were limited to lower values of amperes to avoid overheating and damage to the stator winding. In the stator winding used for these experiments each 1 Amp rms generates a uniform magnetic field of 38 gauss rms in the absence of ferrofluid. The 10 mm non-magnetic wall thickness of polycarbonate cylindrical container which separates the ferrofluid from the stator iron leads to small demagnetization effects outside the test vessel. The field values reported in this chapter correspond, however, to the external applied magnetic field strength and do not account for the demagnetizing effect of the ferrofluid. For a long cylinder of ferrofluid with magnetic susceptibility χ the internal magnetic field H_i is given in terms of the external magnetic field H_0 by the expression $H_i = H_0 - MD$ so that $H_i = \frac{H_0}{1+\chi/2}$. With no ferrofluid the magnetic field was measured to be highly uniform over the experimental volume inside the stator winding. The in-plane field at mid-height was found to vary by less than 2% over the radial dimension, by less than 18% along the z-axis at $r = 0$ from the center of the iron core to the top and bottom edges, and had negligible azimuthal variation throughout the volume.

We added 1 gram of Latex tracer particles to every 0.1 liters of water-based ferrofluid or equivalently less than 1% by weight. This amount of tracer particle produced much higher reflected echo signals than obtained by introducing air bubbles, significantly improving the quality and repeatability of our measurements without perceptibly changing the velocity flow profiles in our experiments. The tracer-particle/ferrofluid suspension requires more than 24 hours to precipitate enough Latex tracer particles to the bottom of the cylindrical container to cause significant degradation of the reflected ultrasound signals. Our experience shows, however, that the

Ultrasound probe	
Frequency	4 [MHz]
Diameter	8.0 [mm]
Length	10.0 [mm]
Case material	Epoxy
Output wire	Radial
Other spec.	Non-magnetic
Device settings	
PRF	$\sim$ 1–10 [kHz]
Emitting frequency	4.0 [MHz]
Emitting power	Low–Medium
Burst length	8 cycles
Number of gates	$\sim$ 200

Table 7.1: Ultrasound probe specifications and typical settings of DOP2000 ultrasound velocimeter.

signal quality can be maintained at its initial quality by simply vigorously stirring the suspension by hand at the start of every day of measurements after the experimental sample has been left unstirred overnight. Further stirring during the day was not necessary.

Also, we have found it important to prevent the ferrofluid from heating up during the tests to avoid temperature-gradient-driven, thermal-convection bulk flows in the fluid. The currents flowing in the stator winding's coils heat up the whole stator due to ohmic losses in the copper winding. Special care was taken after each set of tests to turn off the currents and allow enough time for the motor stator to cool down to room temperature; an electric fan helped accelerate the tedious cooling process. The polycarbonate material of the cylindrical ferrofluid container also acted as a heat insulator. These combined measures assured that the ferrofluid remained at a practically uniform and constant temperature throughout an experimental test set.

To gain confidence in the measurements reported in this chapter we performed a series of preliminary experiments. For example, we regularly confirmed the direction of rotation of the applied uniform rotating magnetic field at low frequencies ($\sim$ 10 Hz) with a small compass. Another regular check that we performed was to stir

Apparatus Geometry		
R	Inner cylinder radius	28.7 [mm]
R_m	Stator iron radius	39.0 [mm]
α	Probe angle	15° [ ]
z_f	Height of ferrofluid	50.0 [mm]
z_p	Probe position	25.0 [mm]
d_w	Cylinder wall thickness	10.0 [mm]

Table 7.2: Summary of dimensions of spin-up flow experiment.

the fluid slowly by hand, both clockwise and counterclockwise, while observing the polarity of the velocimeter's measured velocity profiles. Finally, to verify the magnitude of the velocities reported by the ultrasound velocimeter the theoretically known velocity profiles were measured for water and oil in a concentric cylinder Couette geometry. Appendix C demonstrates that the profiles reported by the velocimeter are in satisfactory agreement with known classical theoretical expressions for non-magnetic fluids.

7.2 Measurement of the spin-up flow velocity profile

The velocimeter measures only the component of the velocity parallel to the axis of the probe. The device records the parallel component of the velocity as a function of time at every point along the path of the ultrasound beam. Table 7.1 documents the configuration of the DOP2000 velocimeter and lists typical device settings. Due to the finite width of the ultrasound beam, the velocity recorded at every point is the spatial average of the velocity over a small volume. The geometry necessary to interpret the ultrasound velocimeter data can be derived from Fig. 7-4 which shows a top-view of the ferrofluid vessel in the spin-up experiment.

The ultrasound probe was inserted into the outer cylinder wall at an angle $\alpha = 10°$ from the radial direction $\mathbf{i}_r$ at a height $z = 25$ mm from the bottom of the ferrofluid

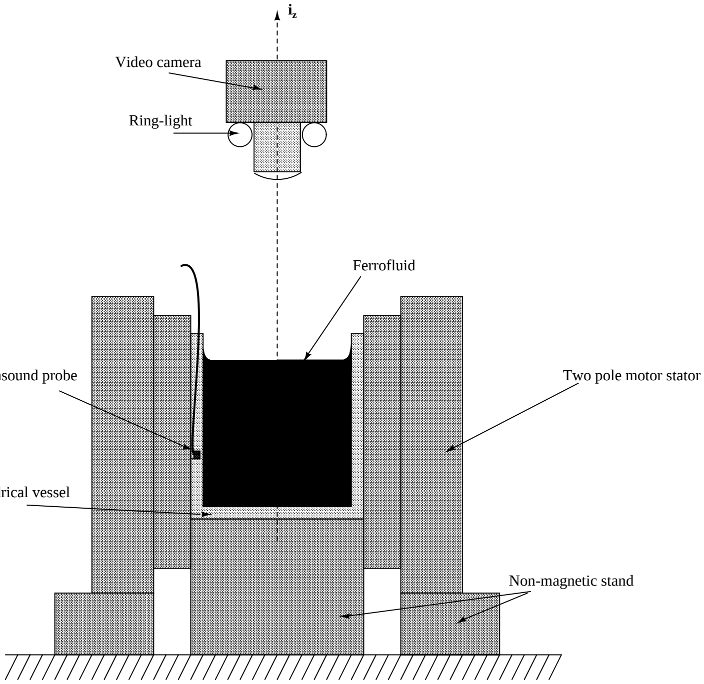

Figure 7-3: Configuration of motor stator winding and cylindrical vessel for the ultrasound spin-up flow profile measurement experiment. A three-phase, two-pole motor stator winding was used to excite a counter-clockwise rotating uniform magnetic field.

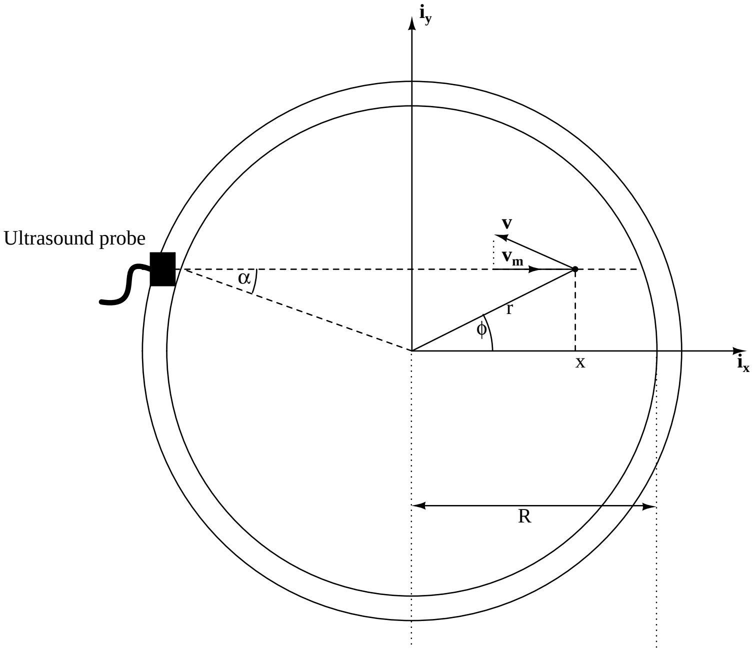

Figure 7-4: Geometry for spin-up flow profile measurement experiment. The ultrasound probe measures the component of the fluid velocity parallel to the probe's axis.

(*i.e.*, approximately in the middle of the 50 mm height of ferrofluid in the vessel). The probe emits a horizontal ultrasonic beam and measures the component of fluid velocity parallel to the direction of the beam at every point along the beam. Thus, the z- and r-components of the fluid velocity can be measured directly by ultrasound beams pointing in the vertical and radial directions respectively. Measurement of the ϕ-component of the velocity requires processing of the velocity measured on the ultrasound beam path shown in Fig. 7-4. From the figure we see that the radius r at a point on the ultrasound beam path is given by,

$$r = \sqrt{\left(x^2 + (R\sin\alpha)^2\right)} \tag{7.1}$$

The velocity of the fluid at any point in the fluid is most generally given by,

$$\mathbf{v}(r,z) = v_r(r,z)\mathbf{i}_r + v_\phi(r,z)\mathbf{i}_\phi + v_z(r,z)\mathbf{i}_z \tag{7.2}$$

On the ultrasound beam path this general expression can be rewritten as,

$$\mathbf{v}(r,z) = v_r(r,z)\left(\frac{x}{r}\mathbf{i}_x + \frac{R\sin\alpha}{r}\mathbf{i}_y\right) + v_\phi(r,z)\left(\frac{-R\sin\alpha}{r}\mathbf{i}_x + \frac{x}{r}\mathbf{i}_y\right) + v_z(r,z)\mathbf{i}_z \tag{7.3}$$

However, the velocity measured by the velocimeter at a point on the ultrasound beam path has at most only r- and ϕ-components, because the z-component of the velocity is perpendicular to the r-ϕ plane. The ultrasound probe shown in Fig. 7-4 measures only the x-component of the fluid velocity at every point along the beam path. Therefore the velocity profile measured by the velocimeter, v_m, is given by,

$$v_m(x) = -v_\phi(r)\frac{R\sin\alpha}{\sqrt{x^2 + (R\sin\alpha)^2}} + v_r(r)\frac{x}{\sqrt{x^2 + (R\sin\alpha)^2}} \tag{7.4}$$

This means that to deduce the velocity profile $v_\phi(r,z)$ from the ultrasound velocimeter profile we must first directly measure the radial component of the velocity $v_r(r,z)$ and then use the expression,

$$v_\phi(r) = -v_m(x)\frac{\sqrt{x^2 + (R\sin\alpha)^2}}{R\sin\alpha} + v_r(r)\frac{x}{R\sin\alpha} \tag{7.5}$$

The radial component of the velocity can be measured directly by aligning the ultrasound beam with the diameter of the vessel (*i.e.*, the probe angle $\alpha = 0$).

7.3 Results for MSG W11 water-based ferrofluid

Experiments were conducted on MSG W11 water-based ferrofluid in a container with and without a top cover as illustrated in Fig. 7-5. The figure also illustrates how velocity profiles were recorded at different heights z in each of the two sets of measurements presented in this section. The results for the covered container presented in Sec. 7.3.1 show only the effects of bulk momentum coupling of the rotating magnetic field. The results in Sec 7.3.2 are for a container of ferrofluid without a top cover and show the effects of both spin diffusion and surface-shear-stress-driven flows.

These experiments were conducted with the ferrofluid container axially and radially centered within the stator iron stack so that the ferrofluid container lies in a region with a highly uniform applied magnetic field. The non-uniformity of the magnetic field at the top and bottom ends of the stator iron stack has a very strong effect on the direction and speed of rotation measured at the surface of the ferrofluid [39]. On the other hand, the bulk of the ferrofluid was consistently observed to co-rotate with the applied magnetic field in all of our experiments.

7.3.1 MSG W11 water-based ferrofluid with top cover

The spin-up velocity profiles measured in the bulk of MSG W11 water-based ferrofluid are shown in Figs. 7-6 to 7-8. The figures show that when subject to a counter-clockwise rotating magnetic field the bulk ferrofluid in the cylindrical vessel undergoes rigid-body-like counter-clockwise rotation at a constant angular velocity. Only near the walls of the cylinder does the no-slip condition force the fluid flow to

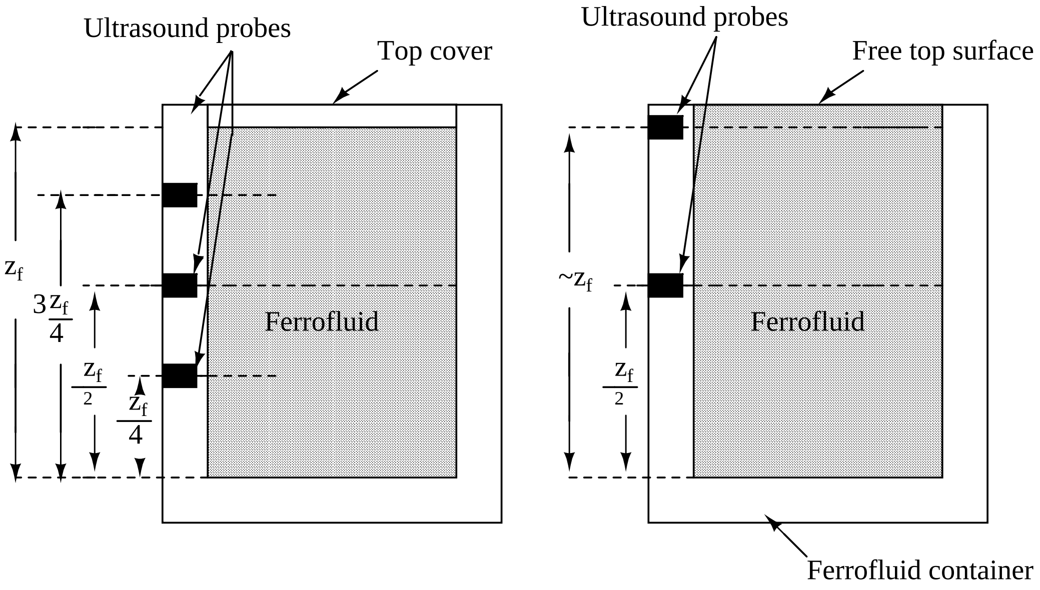

Figure 7-5: The placement of the ultrasound probes at different values of z in containers of ferrofluid with and without a top cover. The top cover of the left cylindrical container forces zero flow at $z = z_f$ and reduces surface shear stress effects, whereas in the right container the absence of the top cover allows the free top surface to develop surface-shear-stress-driven flows. The ultrasound probe needs to be entirely submerged beneath the top surface for accurate velocity measurements.

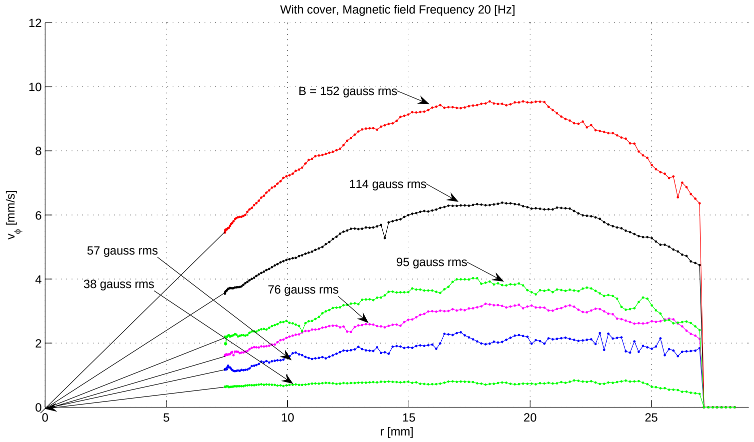

Figure 7-6: The azimuthal component of spin-up flow profiles at $z = \frac{z_f}{2}$ for MSG W11 water-based ferrofluid excited by a magnetic field rotating counter-clockwise at 20 Hz. In the central region ($r < 15$ mm) the flow profiles resemble the linear profile of a fluid in rigid body co-rotation with the applied magnetic field. The velocity must be zero at the $r = R$ stationary wall. The cylindrical container was covered so that there were no free ferrofluid surfaces.

differ significantly from rigid-body rotation. At any given frequency, higher values of the applied magnetic field strength lead to higher rotational velocities.

Figs. 7-9 and 7-10 show the effects of applied magnetic field strength and rotation frequency on the observed bulk rotational speed of the ferrofluid Ω. We used the slopes of the linear region of the measured velocity profiles as an estimate for the bulk ferrofluid rotational speed. For low frequencies of applied rotating magnetic field the bulk rotational speed of the ferrofluid increases with the applied rotating magnetic field frequency. We measured a maximum in ferrofluid bulk rotation at each value of applied rotating magnetic field strength. Fig. 7-9 shows that at higher frequencies the rigid-body rotation of the ferrofluid saturates or begins to decrease slowly with applied frequency for any given rotating magnetic field strength. On the other hand, the bulk rotational speed of the ferrofluid Ω was observed to increase monotonically with applied rotating magnetic field strength (See Fig. 7-10).

The no-slip condition applies at the top and bottom stationary surfaces of the covered cylindrical container. We measured the velocity profiles at $z = \frac{z_f}{4}$ and $z = \frac{3z_f}{4}$ and at the center, $z = \frac{z_f}{2}$, of the cylindrical container. This investigation of the

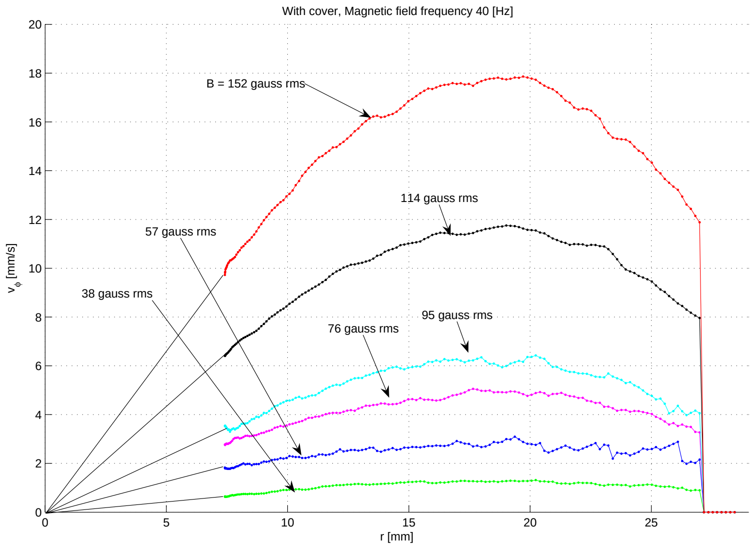

Figure 7-7: Azimuthal flow profiles at $z = \frac{z_f}{2}$ for MSG W11 water-based ferrofluid excited by a magnetic field rotating counter-clockwise at 40 Hz. A flat top cover on the filled ferrofluid container eliminates the free surface and prevent the formation of a meniscus.

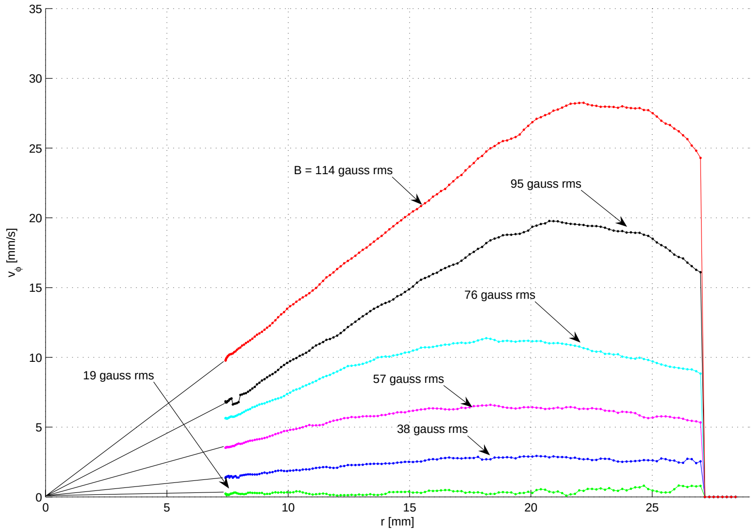

Figure 7-8: Azimuthal flow profiles at $z = \frac{z_f}{2}$ for MSG W11 water-based ferrofluid excited by a magnetic field rotating counter-clockwise at 200 Hz. This flow profile results when water-based ferrofluid in a container without a free surface was placed in a uniform rotating applied magnetic field.

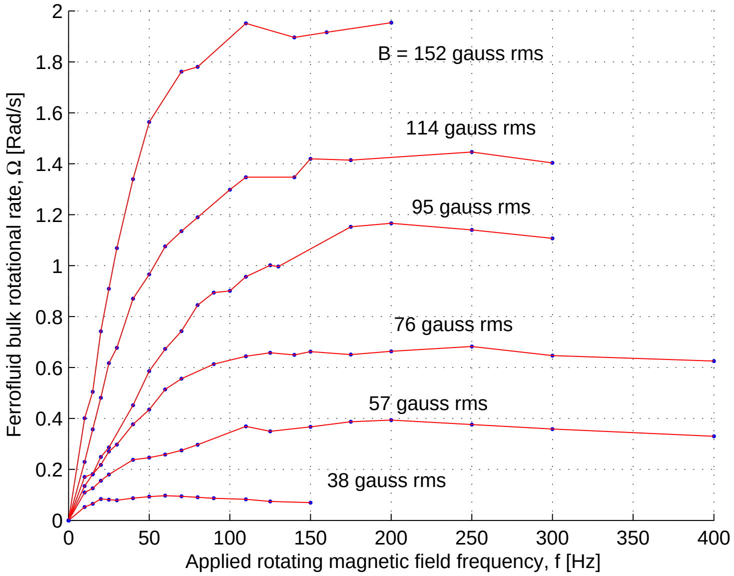

Figure 7-9: Relation between the bulk rotational rate in the central region of the MSG W11 ferrofluid, $\Omega = \frac{v_\phi}{r}$, and the frequency of the applied rotating magnetic field for various magnetic field strengths. The ultrasound probe was placed at height $z = \frac{z_f}{2}$ in the outside wall of a cylindrical container with a top cover.

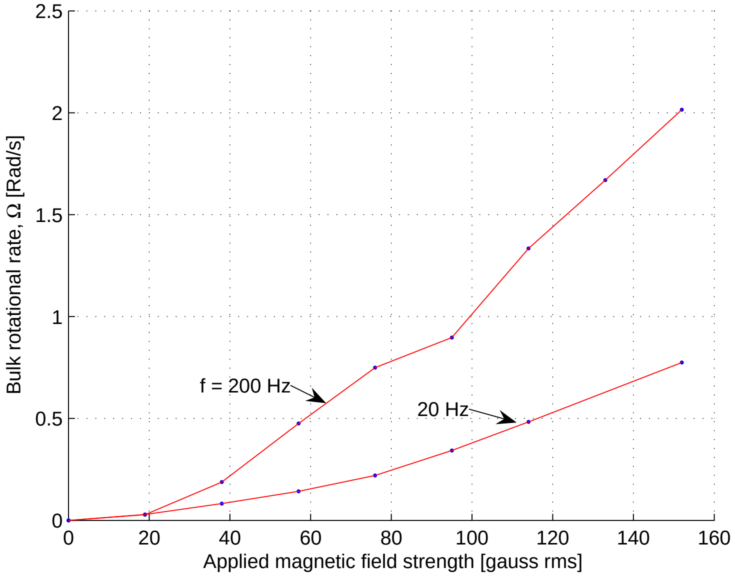

Figure 7-10: Relation between the bulk rotational rate in the central region of the ferrofluid $\Omega = \frac{v_\phi}{r}$ at $z = z_f/2$ and the applied magnetic field strength for various frequencies in a covered container of MSG W11 water-based ferrofluid. The rate of rotation increases monotonically with applied field strength for the investigated range of magnetic field strengths.

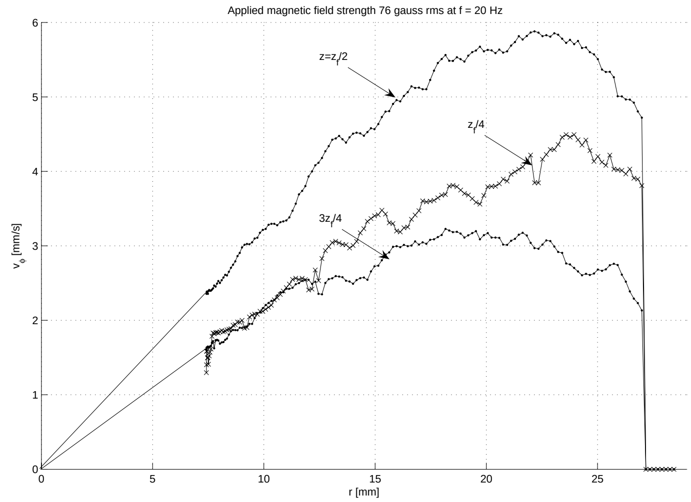

Figure 7-11: Azimuthal flow profiles at $z = \frac{z_f}{2}$, $z = \frac{z_f}{4}$ and $\frac{3z_f}{4}$ excited by a 76 gauss rms magnetic field rotating counter-clockwise at 200 Hz in a covered container of MSG W11 water-based ferrofluid.

dependence of the azimuthal velocity profile on z shows the symmetry of the covered spin-up flow. As expected, the experimental data in Fig. 7-11 and Fig. 7-12 demonstrate that there are higher flow rates at the vertical center of the cylindrical container than near the top and bottom faces of the cylindrical container. Ideally, the curves for $z = \frac{z_f}{4}$ and $\frac{3z_f}{4}$ should completely overlap in both figures. Experimental results show some discrepancy especially in Fig. 7-11. The ferrofluid in the container is, however, observed to consistently co-rotate with the applied-uniform-rotating-magnetic field. Most significantly, these experiments demonstrate that there is significant rotational flow in the bulk of the ferrofluid in the absence of any free surfaces.

7.3.2 MSG W11 water-based ferrofluid without top cover

The ferrofluid/air interface at the top surface of the ferrofluid is observed by eye to rotate in the clockwise direction for a counter-clockwise-rotating applied magnetic field; reversal of the applied magnetic field's rotation results in the reversal of the ferrofluid flow near the surface and in the volume. In the experiments presented in this section the ferrofluid container was centered axially and radially in the stator iron stack so that the ferrofluid container was in a region of highly uniform magnetic

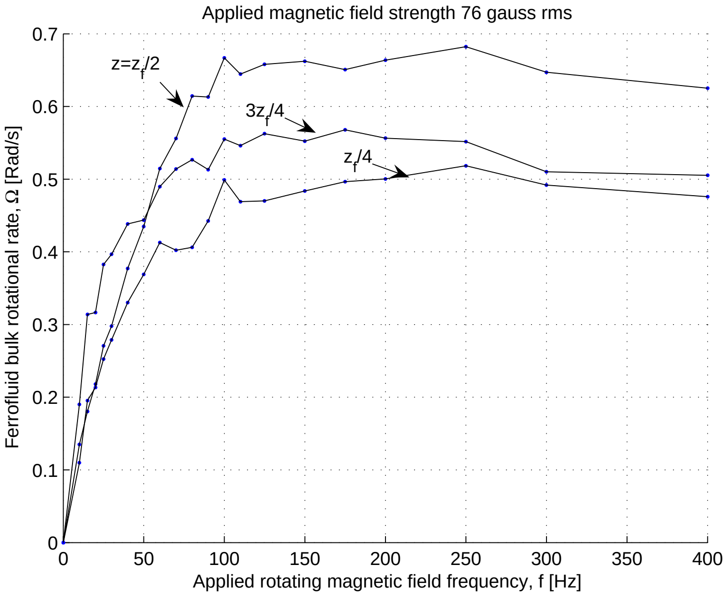

Figure 7-12: Relation between the rotational rate in the bulk of the MSG W11 water-based ferrofluid and the frequency of the applied rotating magnetic field at 76 gauss rms at $z = \frac{z_f}{2}$, $\frac{z_f}{4}$ and $\frac{3z_f}{4}$ in a covered container of water-based ferrofluid.

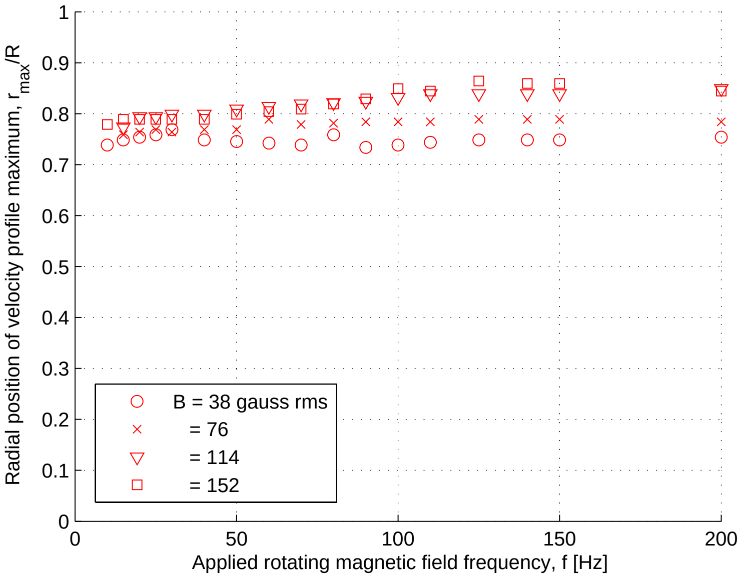

Figure 7-13: The radial position, r_{max}/R, of the measured velocity profile's maximum value for MSG W11 water-based ferrofluid.

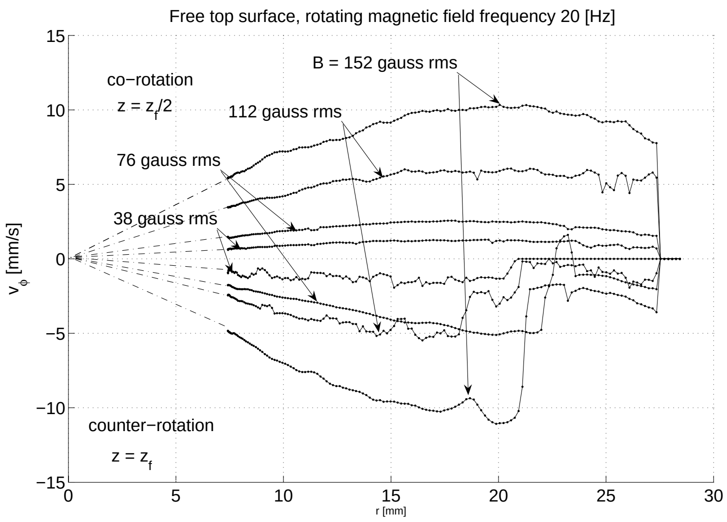

Figure 7-14: The azimuthal component of spin-up flow profiles at $z = \frac{z_f}{2}$ and near the top free surface excited by a magnetic field rotating counter-clockwise at 20 Hz. The positive curves correspond to co-rotating ferrofluid bulk flow profiles measured at $z = \frac{z_f}{2}$, while the negative curves correspond to the counter-rotating flows near the top free surface of the MSG W11 water-based ferrofluid.

field. The approximate rate of rotation at the surface was also estimated by observing the trajectories of surface bubbles and small particles.

The spin-up velocity profiles measured in the bulk of the water-based ferrofluid and near the top free surface of the ferrofluid rotate in opposite directions as demonstrated by the sample flow profiles shown in Figs. 7-14 to 7-16 for applied rotating magnetic field frequencies of 20, 40, and 200 Hz. The flow in the bulk of the ferrofluid was measured with the ultrasound probes and found to co-rotate with the applied rotating magnetic field. Indeed, the flow at the vertical center of the ferrofluid container $z = \frac{z_f}{2}$ exhibited trends and behavior very similar to the case of the covered container presented in the previous section. Interestingly, our observations conclusively demonstrate that the bulk and top free surface of the ferrofluid rotate in opposite directions. Note that the abrupt changes in velocity shown in the surface flow profiles in Figs. 7-14 to 7-16 are spurious artifacts due to measurement difficulties with ultrasound reflections from the fluid/gas interface. The abrupt changes in velocity do not appear in the bulk measurements because the ultrasound beam is far from the ferrofluid/air interface. In summary, our experiments confirm that while the

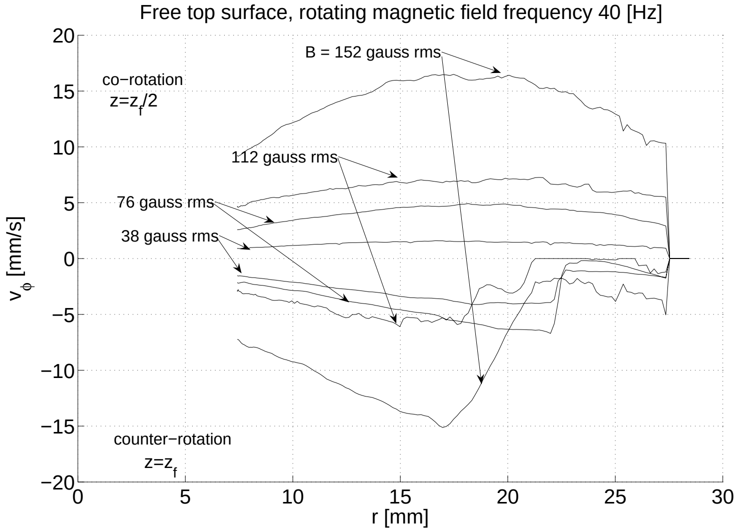

Figure 7-15: Azimuthal flow profiles at $z = \frac{z_f}{2}$ and near the top free surface of the MSG W11 water-based ferrofluid excited by a magnetic field rotating counter-clockwise at 40 Hz. The ferrofluid flow co-rotates with the applied magnetic field at $z = \frac{z_f}{2}$ (positive curves) and counter-rotates near the free surface (negative curves).

ferrofluid bulk co-rotates with the applied magnetic field, the ferrofluid free surface counter-rotates against the rotating applied magnetic field. The rate of bulk rotation is observed to be lower for the container without a top cover, than for a corresponding case with a covered container with no surface flow.

Figs. 7-17 and 7-18 show the effect of applied magnetic field strength and rotational frequency on the observed bulk and surface rotational speeds of the ferrofluid measured at $z = \frac{z_f}{2}$ and near $z = z_f$. Negative values of rotational speed signify that the fluid counter-rotates with reference to the applied magnetic field. For low frequencies of applied rotating magnetic field the bulk rotational speed of the ferrofluid scales in proportion to the applied rotating magnetic field frequency. The trend in the bulk rotational speed saturates at higher values of applied magnetic field frequency. The bulk rotational speed of the ferrofluid increases monotonically with applied magnetic field strength in all the tests performed in this experimental investigation. Fig. 7-19 shows the optically observed rotational speeds on the free surface of the ferrofluid. Note that the highest reported velocities occur on the surface of the ferrofluid.

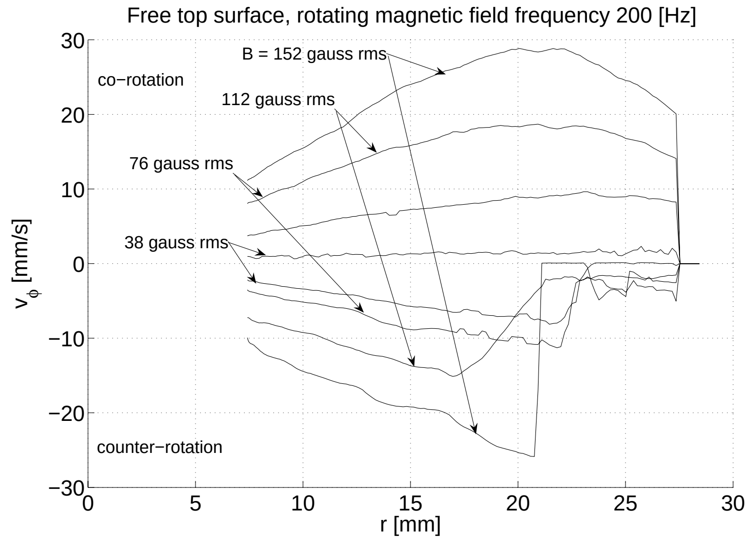

Figure 7-16: MSG W11 water-based ferrofluid azimuthal flow profiles at $z = \frac{z_f}{2}$ and near the top free surface excited by a magnetic field rotating counter-clockwise at 200 Hz. This flow near the free top surface (negative curves) rotates opposite the flow in the bulk of the ferrofluid (positive curves) measured at $z = \frac{z_f}{2}$ and opposite the applied rotating magnetic field.

7.3.3 Ferrofluid flow reversal

Further investigation of the change in the spin-up velocity profile between the surface and bulk of the ferrofluid was required in order to verify the measured flow reversal between the top free surface and bulk of the ferrofluid reported in Sec. 7.3.2. Fig. 7-20 illustrates the two experimental configurations used to investigate the flow of the ferrofluid near the ferrofluid/air interface. In configuration A the surface of the ferrofluid is initially aligned with the bottom rim of the iron stack of the stator winding. In configuration B the surface of the ferrofluid is initially aligned with the top rim of the iron stack of the stator winding. The steady state velocity profiles were measured as the amount of ferrofluid in the container was increased incrementally by injecting 2.5 ml of ferrofluid with a syringe. Each injected increment of ferrofluid increased the height of the ferrofluid in the contained by 1 mm. The velocity profiles were measured for applied 10 and 50 Hz rotating uniform magnetic fields of 76 gauss rms.

A plausible explanation for the flow reversal phenomena builds on Rosensweig's

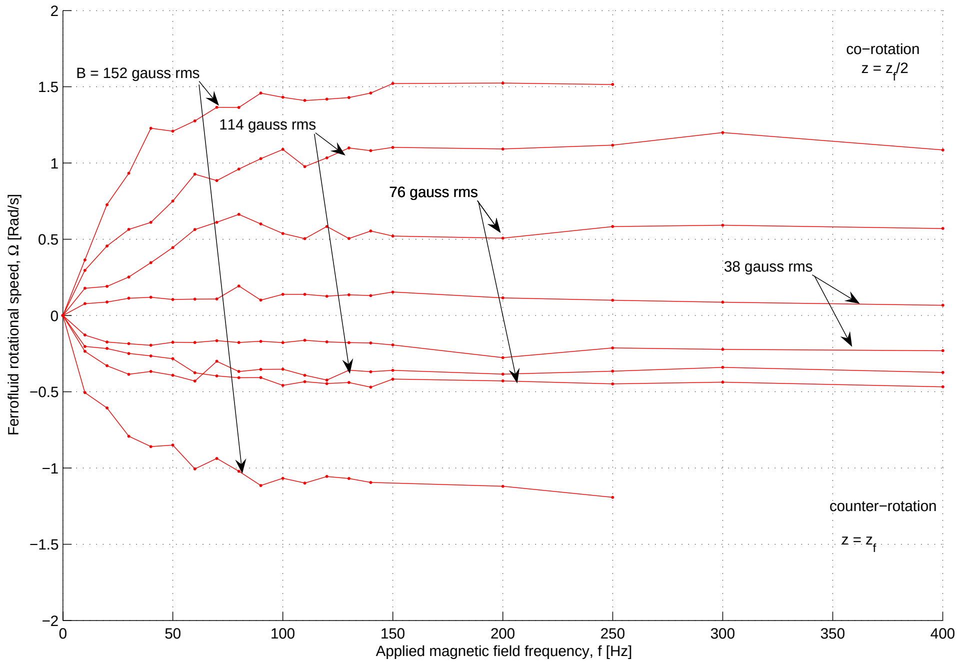

Figure 7-17: The rotational rates, $\Omega = \frac{v_\phi}{r}$, in the central bulk region, $z = \frac{z_f}{2}$ with $\Omega > 0$, and near the free top surface of MSG W11 water-based ferrofluid with $\Omega < 0$, for various magnetic field amplitudes as a function of the frequency of the applied rotating magnetic field.

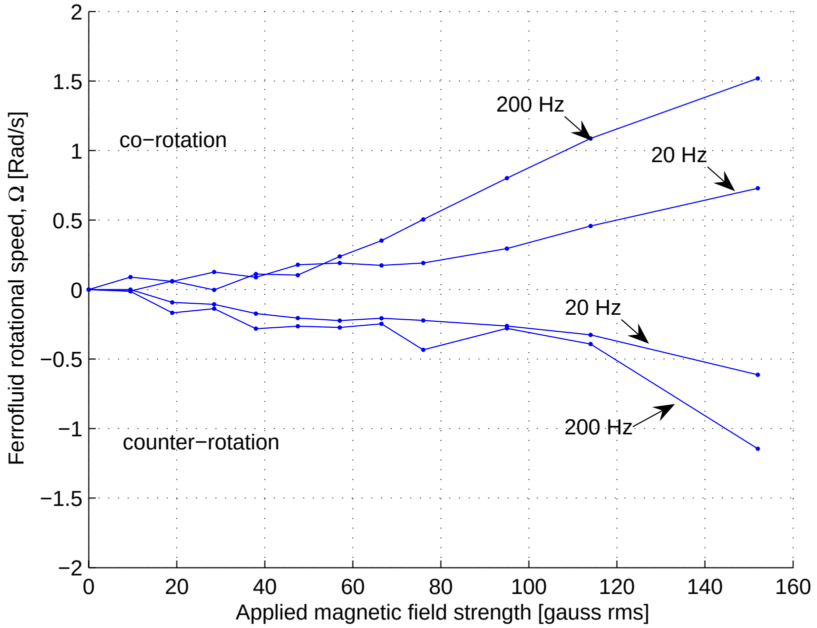

Figure 7-18: Central region bulk ($\Omega > 0$) and near free top surface rotational rates ($\Omega < 0$), $\Omega = \frac{v_\phi}{r}$, of the ferrofluid dependence on the applied magnetic field strength for various frequencies in a container of MSG W11 water-based ferrofluid without a top cover. The negative curves correspond to the counter-rotating flow near the free top surface of the water-based ferrofluid.

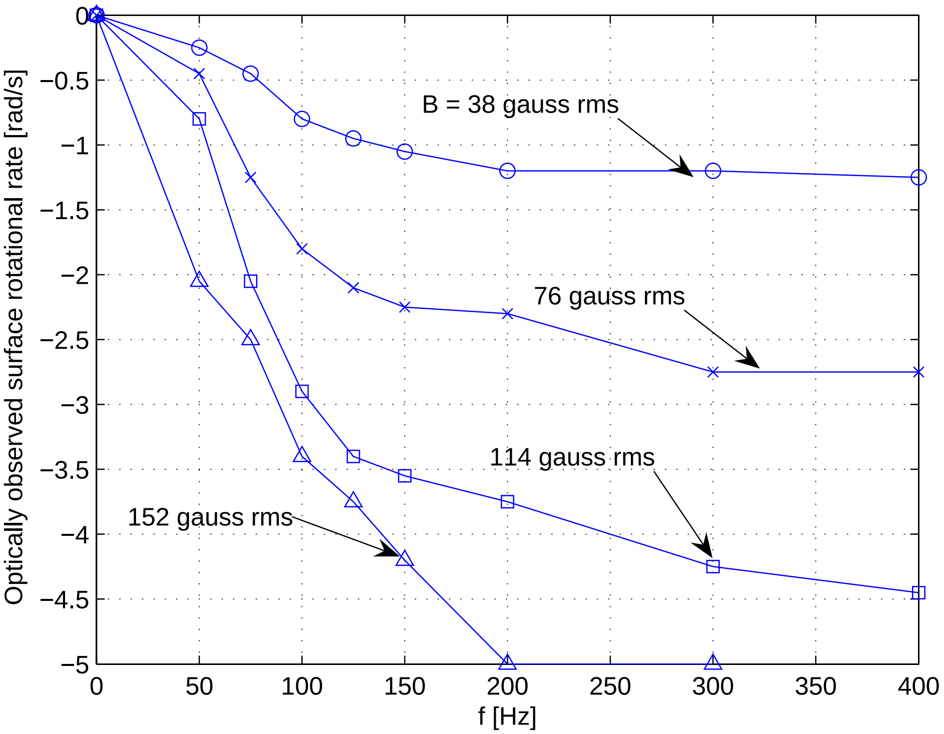

Figure 7-19: The rotational rates, $\Omega = \frac{v_\phi}{r}$, observed optically on the free top surface of MSG W11 water-based ferrofluid with $\Omega < 0$ (counter-rotation) as a function of the frequency of the applied rotating magnetic field for various magnetic field amplitudes.

observation of the dependence of direction of ferrofluid surface flow on the curvature of the meniscus [39]. In configuration A the ferrofluid interface is drawn upwards towards the region with higher magnetic field strengths which might cause the meniscus to have convex shape. Conversely in configuration B the strong field region is below the interface and the shape of the meniscus is concave. A measurement of surface shape to determine the effects of fringe fields on the curvature of the meniscus would verify this hypothesis. Preliminary laser measurements have shown that the curvature of the ferrofluid/air interface changes from concave to convex at the bottom of an energized stator as hypothesized. Unfortunately, the laser reflection technique from Chapter 3 cannot be used to measure the exact shape of the ferrofluid air interface with this experimental configuration because the stator winding occludes the ferrofluid container.

Fig. 7-21 plots the change of rotational rate, $\Omega = \frac{v_\phi}{r}$, of the ferrofluid as the height of the ferrofluid is increased in increments of 1 mm. The figure shows a flow reversal in configuration B. Initially, when the ultrasound probe is close to the surface of the ferrofluid we measure a counter-rotating flow. When more ferrofluid was added, the probe is no longer near the surface and the measured flow co-rotates with applied magnetic field. In configuration A, however, the fluid is measured to always co-rotate with the applied magnetic field. We also observed by eye that the surface of the ferrofluid co-rotated with the applied magnetic field in this configuration.

7.4 Results for EMG705 water-based ferrofluid

This section presents experimental results for EMG705 water-based ferrofluid. EMG705 is significantly higher in quality and price than MSG W11. We have only performed a subset of the measurements that we presented for MSG W11 in Sec. 7.3.

7.4.1 EMG705 water-based ferrofluid with top cover

Figs. 7-22 to 7-24 show velocity profiles for frequencies of 20, 40 and 200 Hz. The thick curves in the figures are actual experimental data points reported by the velocimeter

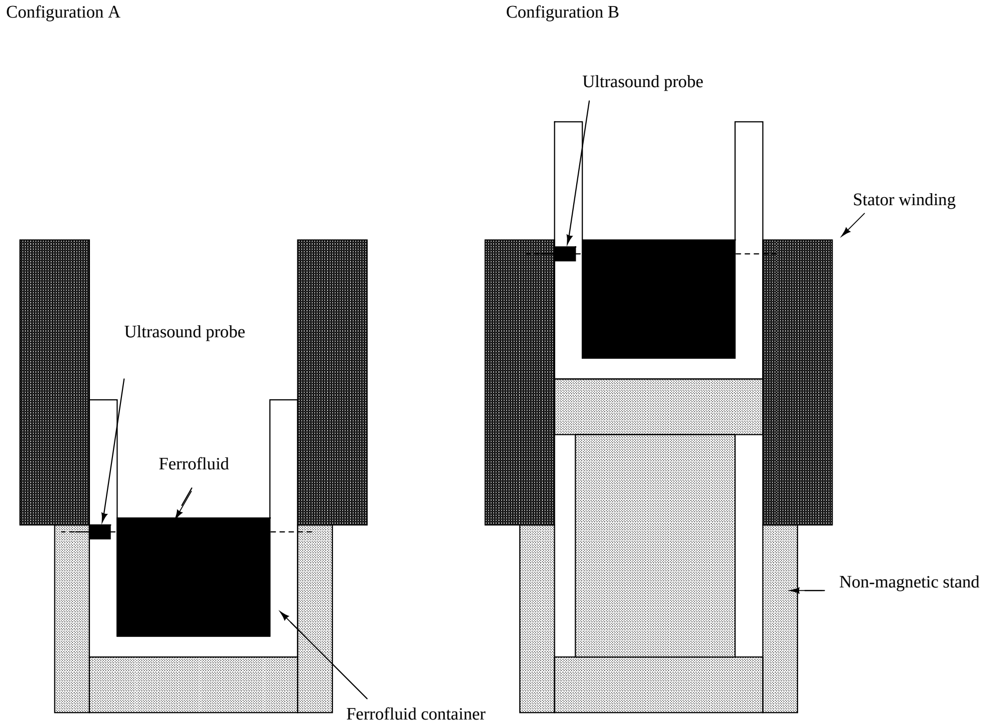

Figure 7-20: Experimental configurations A and B to investigate the z-dependence of the velocity profiles near the ferrofluid/air interface.

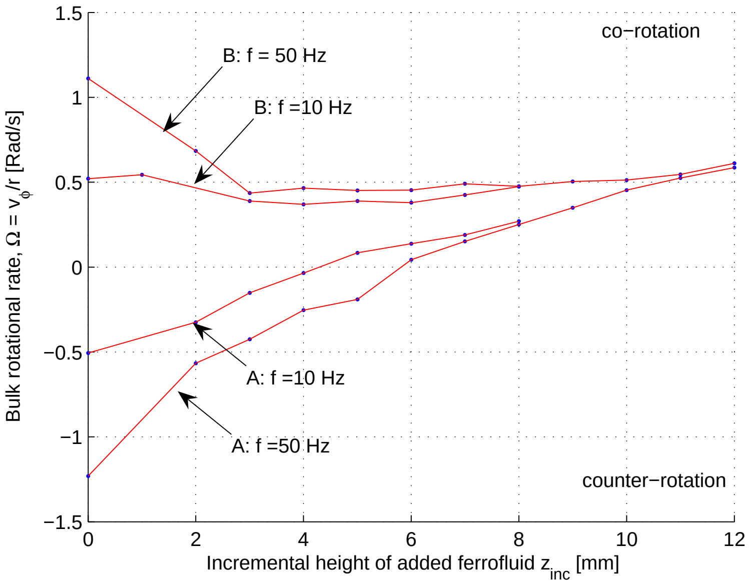

Figure 7-21: Measured change of rotational rate, $\Omega = \frac{v_\phi}{r}$, of MSG W11 ferrofluid as the height of the ferrofluid is increased in increments of 1 mm. The experiments were conducted with 10 and 50 Hz rotating uniform magnetic fields of 76 gauss rms. Configuration A measures the change in velocity near an interface located in the bottom fringing fields of the motor stator winding and configuration B measures near an interface located at the top fringing fields of the motor stator winding.

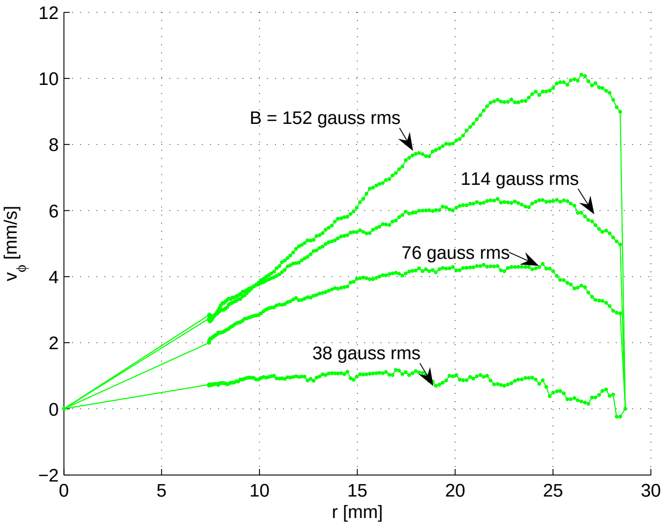

Figure 7-22: Co-rotating azimuthal flow profiles at $z = \frac{z_f}{2}$ for EMG705 water-based ferrofluid excited by a magnetic field rotating counter-clockwise at 20 Hz. This co-rotating flow profile results when a water-based ferrofluid in a container without a free surface is placed in a uniform rotating applied magnetic field.

over the measured range of radial positions. We used thin lines in each case to extrapolate the data for radial positions where measurements are unavailable.

Fig. 7-25 summarizes the bulk rotation rate of the ferrofluid in our experimental results for all the frequencies and magnitudes of applied uniform magnetic fields, demonstrating that EMG705 exhibits the same spin-up flow trends observed for MSG W11. The bulk rates of flow for EMG705 are, however, slightly lower than the flow rates in MSG W11 water-based ferrofluid. Fig. 7-27 shows the radial position of the maximum velocity for different frequencies and currents.

Fig. 7-26 shows velocity profiles measured at three different heights: $z = \frac{z_f}{4}$, $z = \frac{3z_f}{4}$ and $z = \frac{z_f}{2}$, as illustrated in the covered cylindrical configuration in Fig. 7-5. In the covered configuration, the no-slip condition applies at the top and bottom stationary surfaces of the container. The data shows the even symmetry of the covered spin-up flow across the plane $z = \frac{z_f}{2}$. As expected, the experimental data shows that there are higher flow rates in the center of the cylindrical container than near the top and bottom faces of the cylindrical container. Note that in theory, the velocity profiles measured at $z = \frac{z_f}{4}$, $z = \frac{3z_f}{4}$ should be identical; the measured curves agree

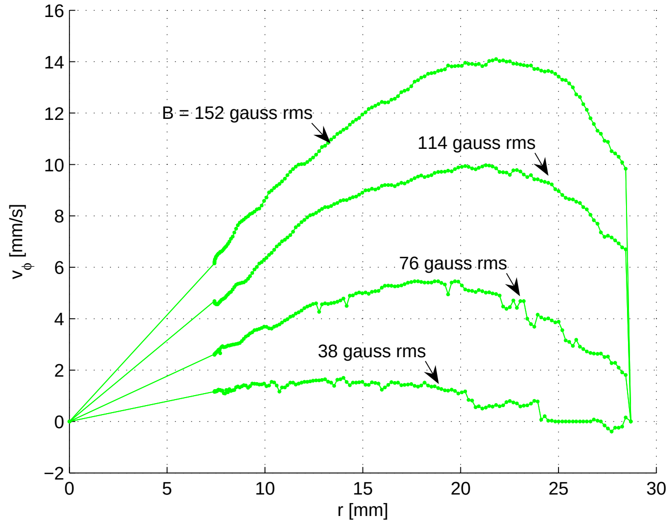

Figure 7-23: Co-rotating azimuthal flow profiles at $z = \frac{z_f}{2}$ for EMG705 water-based ferrofluid excited by a magnetic field rotating counter-clockwise at 40 Hz. The ferrofluid container was covered by a flat cover to eliminate the free surface and prevent the formation of a meniscus.

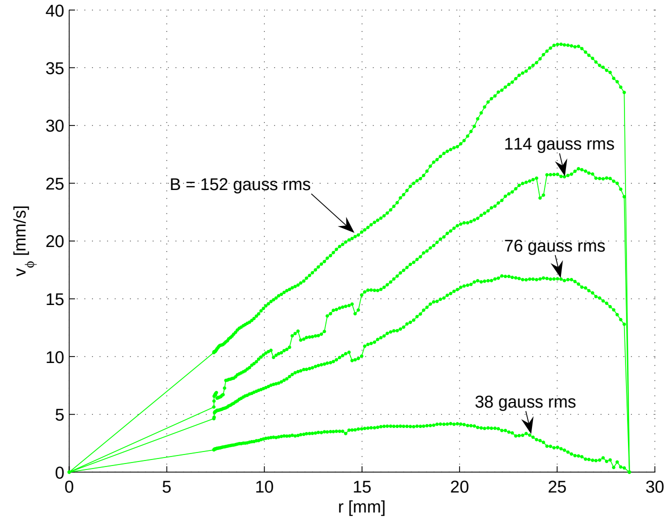

Figure 7-24: Co-rotating azimuthal flow profiles in a container without a free surface at $z = \frac{z_f}{2}$ for EMG705 water-based ferrofluid excited by a magnetic field rotating counter-clockwise at 200 Hz.

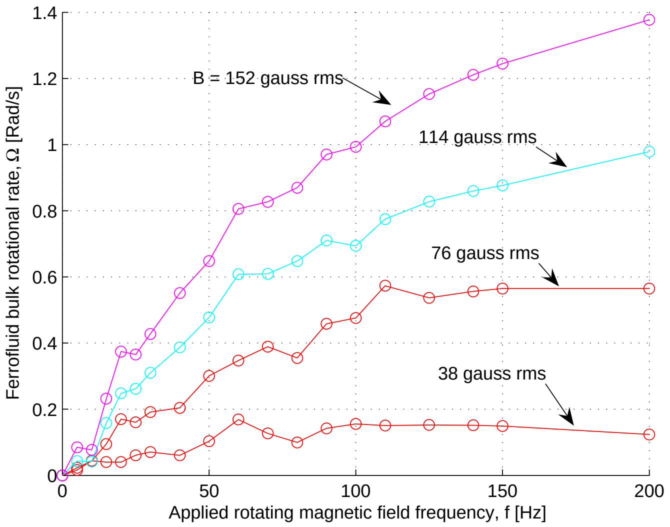

Figure 7-25: Relation between the co-rotating bulk rotational rate in the central region of the EMG705 water-based ferrofluid, $\Omega = \frac{v_\phi}{r}$, and the frequency of the applied rotating magnetic field for various magnetic field strengths. The ultrasound probe was placed at height $z = \frac{z_f}{2}$ on the outside of a cylindrical container with a top cover.

very well within experimental error.

7.4.2 EMG705 water-based ferrofluid without top cover

The spin-up velocity profiles measured in the bulk of the EMG705 water-based ferrofluid and near the top free surface of the ferrofluid rotate in opposite directions as demonstrated by the sample flow profiles shown in Fig. 7-28 for applied rotating magnetic field frequency of 80 Hz.

7.4.3 Transient velocity profiles

In contrast to the previous sections in this chapter, which focused on measurements of steady state velocity profiles, this section summarizes the results of a brief preliminary investigation of turn-on and turn-off transients. Ultrasound velocimetry was used to record the velocity profile at the central region, $z = z_f/2$, of a covered cylindrical container of EMG705 ferrofluid. Figs. 7-29 to 7-34 show the bulk rotational rate of the ferrofluid as a function of time for 38, 76, 114 gauss rms.

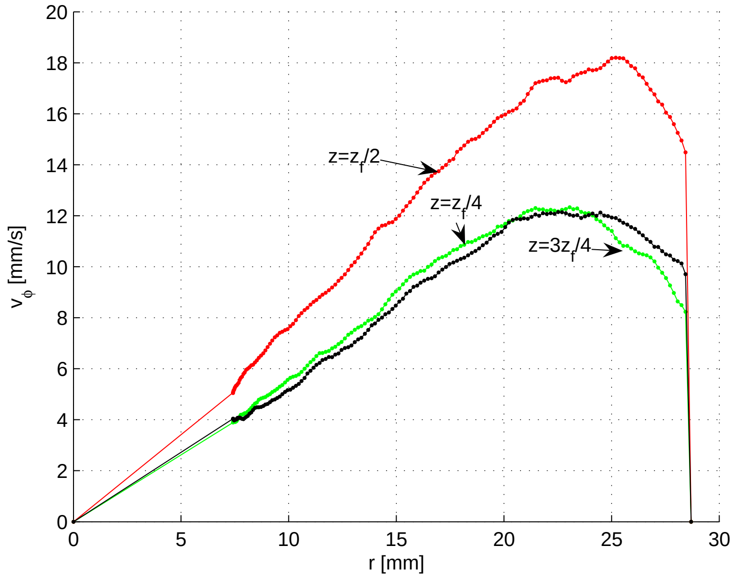

Figure 7-26: Co-rotating azimuthal flow profiles at $z = \frac{z_f}{2}$, $z = \frac{z_f}{4}$ and $\frac{3z_f}{4}$ excited by a 76 gauss rms magnetic field rotating counter-clockwise at 200 Hz in a covered container of EMG705 water-based ferrofluid.

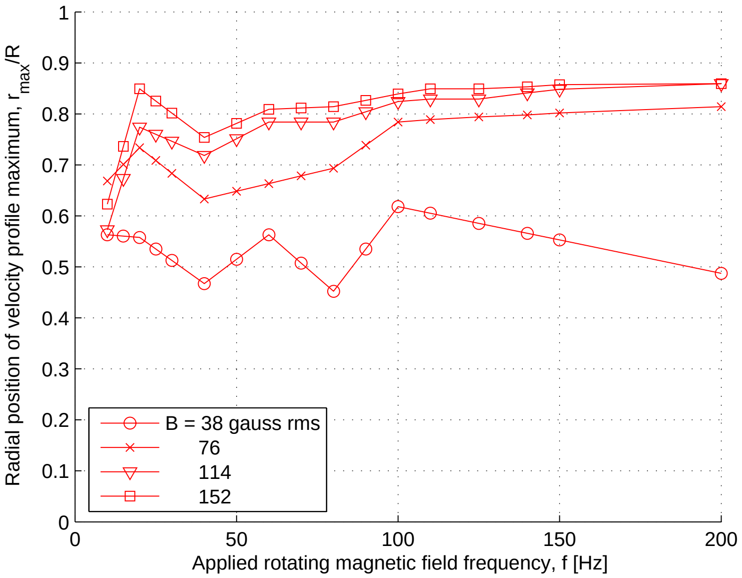

Figure 7-27: The radial position, r_{max}/R, of the measured velocity profile's maximum value for EMG705 water-based ferrofluid.

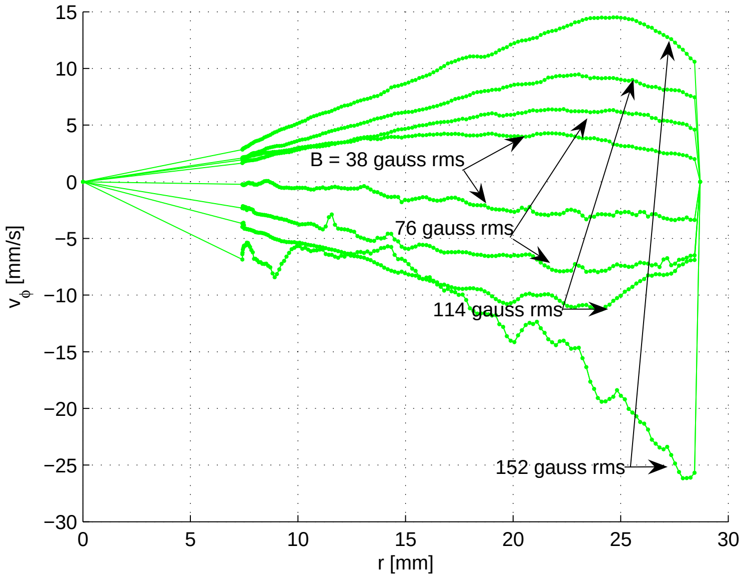

Figure 7-28: The azimuthal component of spin-up flow profiles at $z = \frac{z_f}{2}$ and near the top free surface excited by a magnetic field rotating counter-clockwise at 80 Hz. The positive curves correspond to co-rotating ferrofluid bulk flow profiles measured at $z = \frac{z_f}{2}$, while the negative curves correspond to the counter-rotating flows near the top free surface of the EMG705 water-based ferrofluid.

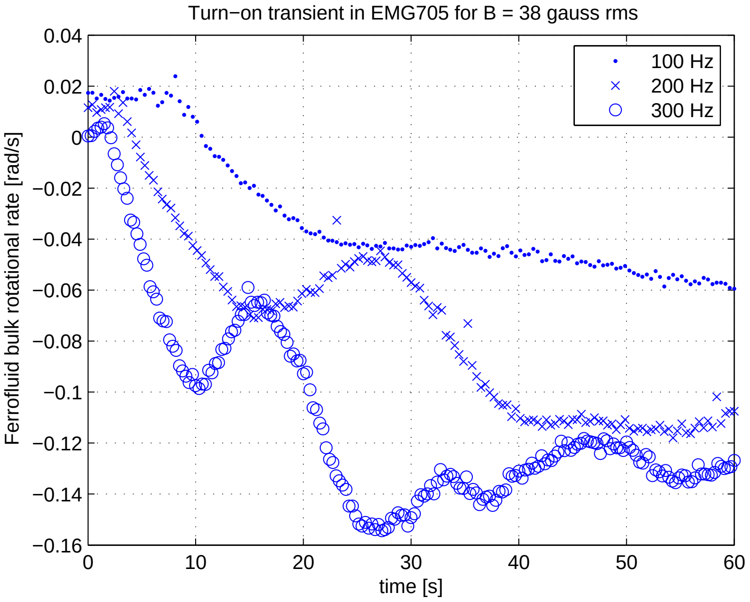

Figure 7-29: The turn-on transient in EMG705 water based ferrofluid in a 38 gauss rms rotating uniform magnetic field for various rotating field frequency. A steady state rotational rate develops in the bulk of the ferrofluid initially at rest.

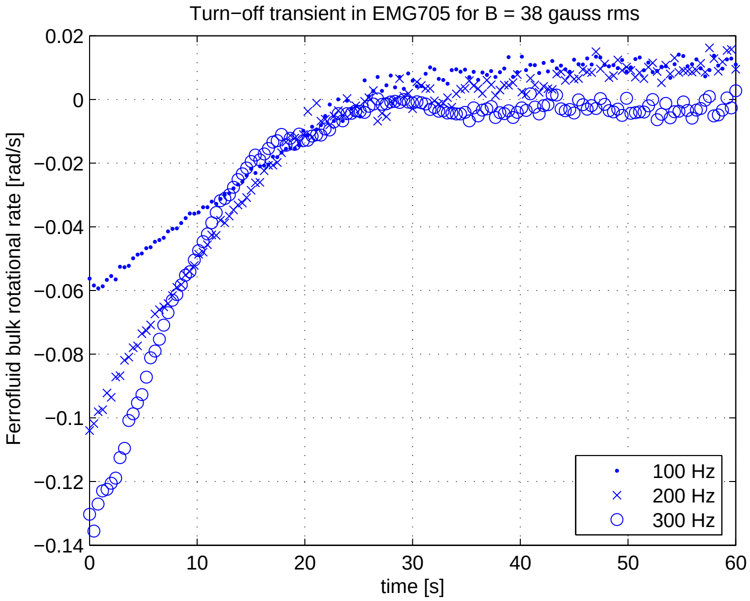

Figure 7-30: The turn-off transient in EMG705 water based ferrofluid initially driven by a 38 gauss rms rotating uniform magnetic field for various rotating field frequency. The steady state rotational rate steadily decreases untill the bulk of the ferrofluid is at rest.

The turn-on transients in Figs. 7-29, 7-31 and 7-33 have characteristic times that decrease for higher rotating magnetic field strengths and frequencies. On the other hand, the turn-off transients in Figs. 7-30, 7-32 and 7-34 have characteristic times on the order of ~ 20 s independent of rotating magnetic field strength and frequency. The turn-off transients are viscous dominated and are larger than the turn-on transient characteristic times.

7.5 Discussion and future work

This section presents a brief overview and summary of some of the most salient results for this chapter's spin-up experiments with MSG W11 and EMG705 water based ferrofluids in containers with and without a top cover. We conclude with recommendations for further contributions and investigations that would build on our results.

Firstly, while the central region of the ferrofluid developed linear rigid body motion

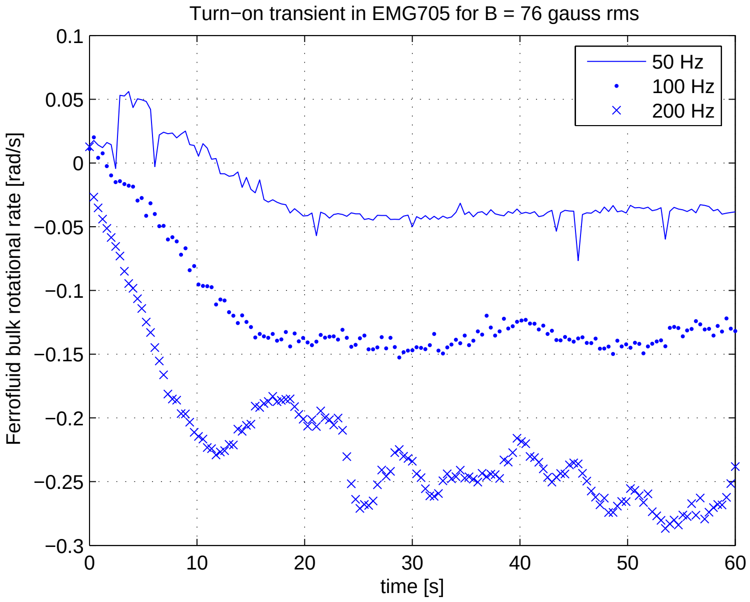

Figure 7-31: The turn-on transient in EMG705 water based ferrofluid in a 76 gauss rms rotating uniform magnetic field for various rotating field frequency. A steady state rotational rate develops in the bulk of the ferrofluid initially at rest.

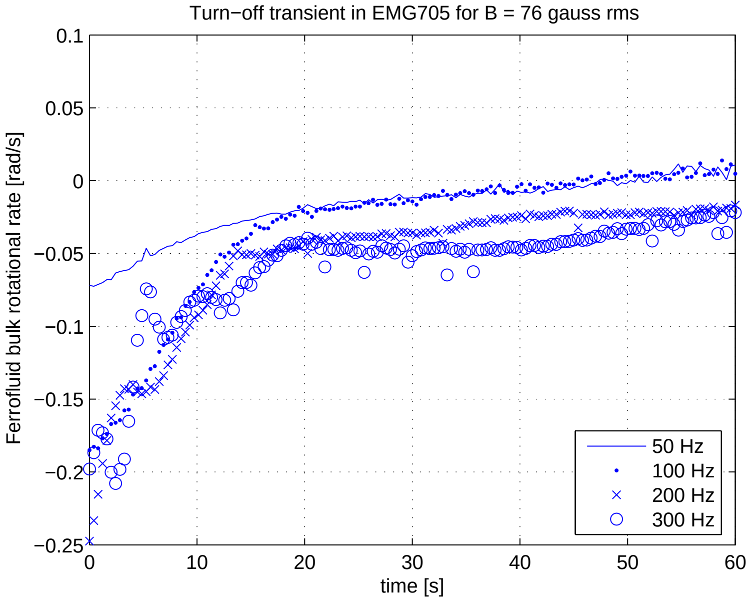

Figure 7-32: The turn-off transient in EMG705 water based ferrofluid in a 76 gauss rms rotating uniform magnetic field for various rotating field frequency. The steady state rotational rate steadily decreases untill the bulk of the ferrofluid is at rest.

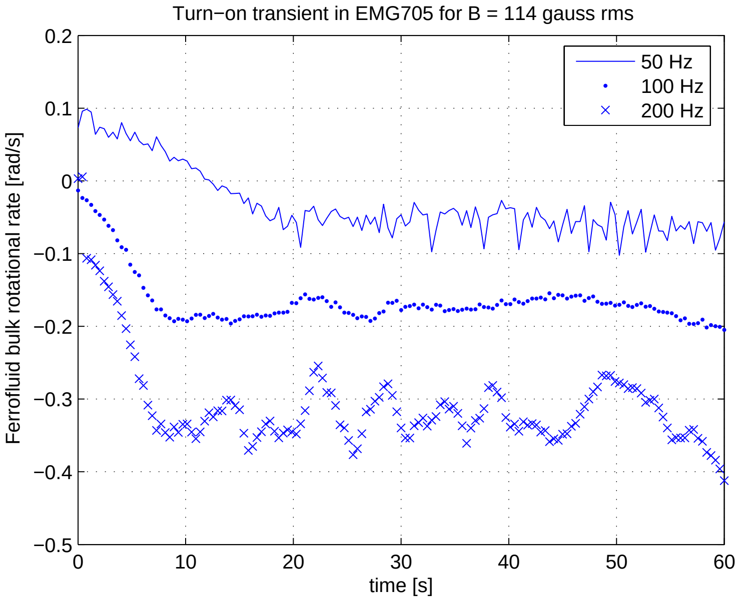

Figure 7-33: The turn-on transient in EMG705 water based ferrofluid in a 114 gauss rms rotating uniform magnetic field for various rotating field frequency. A steady state rotational rate develops in the bulk of the ferrofluid initially at rest.

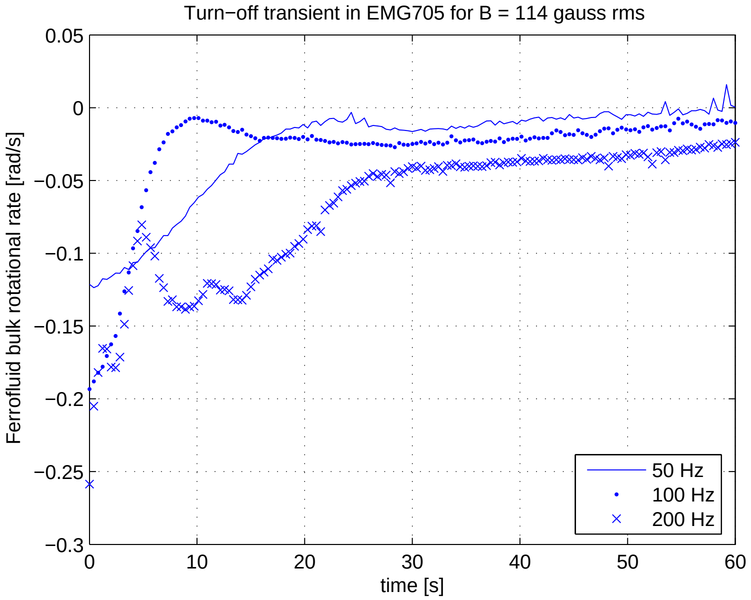

Figure 7-34: The turn-off transient in EMG705 water based ferrofluid in a 114 gauss rms rotating uniform magnetic field for various rotating field frequency. The steady state rotational rate steadily decreases untill the bulk of the ferrofluid is at rest.

velocity profiles, the velocity profiles reached a maximum value and dropped to zero near the stationary outer wall of the cylinder. This occurs not in a thin boundary layer but over a significant region near the wall. The maximum velocities measured for EMG705 were consistently lower than those measured for MSG W11 under the same experimental conditions.

Secondly, in all of the experimental cases presented in this chapter the ferrofluid in the bulk region rotated consistently in the same direction as the applied uniform rotating magnetic field. This observation holds for MSG W11 and EMG705 even in experiments where the cylindrical container was not covered, and the free surface clearly rotated opposite to the magnetic field.

Moreover, we measured significant volume flows even in the case of a covered container with no free surfaces. The flows scaled with applied rotating magnetic field frequency and current, and were demonstrated to be symmetric about the plane $z = z_f/2$ for a covered container.

Finally, both optical observation at the surface of the ferrofluid and ultrasound measurement just beneath the surface reveal that the fluid counter-rotates with respect to the applied rotating magnetic field on the top surface of the ferrofluid. Measurements show that the largest magnitude of the flow velocity occurs right at the surface layer of the uncovered ferrofluid cylindrical container.

It is easy to claim that fringing field non-uniformities arise when we introduce the ferrofluid into the bore of the stator winding despite the great care we took to generate uniform magnetic fields in our experiments and perhaps even to attribute our results to field gradient effects. In addition, two-pole stator windings have slots, teeth, end effects, winding factors *etc.* that introduce non-uniformities and higher order harmonics. We believe that fields inside the ferrofluid cylinder are adequately uniform: the ferrofluid cylinder approximates a spherical vessel since its dimensions are such that the diameter is approximately equal to its height. Spherical vessels are more difficult to handle and are not as readily available as cylindrical ones. Future work should investigate flow profiles in spherical vessels of ferrofluid to dispel any lingering doubts or misgivings about the results we presented in this chapter. Instead of using a commercial two pole machine stator a long, thin, non-magnetic, smooth, hollow cylinder could be wound with at least two sinusoidal winding distributions specifically for this experiment. Alternatively, multiple phases of spherical coils, based on the so-called “fluxballs” of Appendix B, could be wound around spherical container of ferrofluid to produce highly uniform rotating magnetic fields.

Chapter 8

Numerical simulation of ferrofluid spin-up

8.1 Ferrofluid spin-up governing equations

This chapter uses fluid dynamical equations of motion modified to account for internal nanoparticle rotation to describe the behavior of non-conducting magnetic fluids in uniform rotating magnetic fields. The expressions for the conservation of linear and angular momentum for incompressible fluid describe how the fluid velocity $\mathbf{v}$ and spin velocity $\boldsymbol{\omega}$ arise from applied magnetic body torques and forces. In conjunction with these fluid mechanical equations, Maxwell's equations and the constitutive relation for a ferrofluid–as given by the magnetization relaxation equation–are essential for a complete hydrodynamic description of ferrofluid spin-up. It is essential that we self-consistently account for coupling between mechanical flows and magnetic fields to describe correctly the experimentally measured rotation velocity of ferrofluids in rotating magnetic fields. Just as the magnetic body force and torque densities drive the flow and spin velocities of the ferrofluid, fluid motion and spin also affect the magnetic field and consequently the magnetic force and torque densities.

The solutions presented in this chapter satisfy the full coupled set of fluid dynamical and magnetic equations without making the simplifying assumptions in the magnetization relaxation relation–made in Shliomis' analysis–that decouple mechanical and magnetic variables. We make the assumption that the fluid flow velocity, spin velocity, torque and force densities are only functions of radial position r. This ignores possible variations along the axial direction z from boundary conditions on the top cover and bottom surface of the cylindrical container. This assumption holds in the middle region of the ferrofluid container in the limit when the top and bottom faces of the cylinders are infinitely far away. Addressing flows that are a function of two or even three dimensions is a relatively straightforward–albeit algebraically more involved and numerically more intensive–extension of our analysis.

8.1.1 Fluid mechanics governing equations

The equations governing the ferrohydrodynamic torque-driven spin-up flow for an incompressible ferrofluid (*i.e.*, $\nabla \cdot \mathbf{v} = 0$) are given by the expressions for the conservation of linear momentum,

$$\rho \frac{D\mathbf{v}}{Dt} = -\nabla p + 2\zeta \nabla \times \boldsymbol{\omega} + (\zeta + \eta) \nabla^2 \mathbf{v} + \mathbf{F} \tag{8.1}$$

and the conservation of angular momentum,

$$J \frac{D\boldsymbol{\omega}}{Dt} = 2\zeta (\nabla \times \mathbf{v} - 2\boldsymbol{\omega}) + \eta' \nabla^2 \boldsymbol{\omega} + (\lambda' + \eta') \nabla(\nabla \cdot \boldsymbol{\omega}) + \mathbf{T} \tag{8.2}$$

where $\mathbf{v}$ is the velocity, $\boldsymbol{\omega}$ is the spin velocity, p is the pressure, ρ is the density, J is the local moment of inertia per unit volume, η is the dynamic viscosity, η' is the shear coefficient of the spin viscosity, λ' is the bulk coefficient of spin viscosity, ζ is the vortex viscosity, the time-average magnetic body force density is given by $\mathbf{F} =< \mu_0 \mathbf{M} \cdot \nabla \mathbf{H} >$, and the time-average magnetic body torque density in the ferrofluid is $\mathbf{T} =< \mu_0 \mathbf{M} \times \mathbf{H} >$. Note that the delimiters $<>$ signify the computation of the time-average torque and force densities that lead to steady velocity and spin-velocity profiles.

We non-dimensionalize Eqs. 8.1 and 8.2 with respect to reference parameters such as the frequency of the applied rotating magnetic field Ω_e, the radius of the vessel R, and a reference magnetic field intensity H_0,

$$R_E \frac{D\tilde{\mathbf{v}}}{D\tilde{t}} = -\tilde{\nabla}\tilde{p} + 2\frac{\zeta}{\eta}\tilde{\nabla} \times \tilde{\boldsymbol{\omega}} + \left(1 + \frac{\zeta}{\eta}\right)\tilde{\nabla}^2\tilde{\mathbf{v}} + \tilde{\mathbf{F}} \tag{8.3}$$

$$R_E \left(\frac{J}{\rho R^2}\right)\frac{D\tilde{\boldsymbol{\omega}}}{D\tilde{t}} = 2\frac{\zeta}{\eta}\left(\tilde{\nabla} \times \tilde{\mathbf{v}} - 2\tilde{\boldsymbol{\omega}}\right) + \frac{\eta'}{R^2\eta}\tilde{\nabla}^2\tilde{\boldsymbol{\omega}} + \frac{\lambda' + \eta'}{R^2\eta}\tilde{\nabla}(\tilde{\nabla} \cdot \tilde{\boldsymbol{\omega}}) + \tilde{\mathbf{T}} \tag{8.4}$$

where $R_E = \frac{\rho\Omega_e R^2}{\eta}$,$\tilde{\mathbf{v}} = \frac{\mathbf{v}}{\Omega_e R}$, $\tilde{\boldsymbol{\omega}} = \frac{\boldsymbol{\omega}}{\Omega_e}$, $\tilde{r} = \frac{r}{R}$, $\tilde{t} = \Omega_e t$, $\tilde{p} = \frac{p}{\mu_0 H_0^2}$, $\tilde{\mathbf{F}} = \frac{R\mathbf{F}}{\mu_0 H_0^2}$, and $\tilde{\mathbf{T}} = \frac{\mathbf{T}}{\mu_0 H^2}$.

In the steady state, time derivatives vanish $\frac{\partial}{\partial t} \to 0$. For an axisymmetric cylinder of infinite height in the z direction we neglect variations in z and ϕ (*i.e.*, $\frac{\partial}{\partial z}$, and $\frac{\partial}{\partial \phi} \to 0$) and only investigate solutions with the form $\tilde{\mathbf{v}} = \tilde{v}_\phi(\tilde{r})\mathbf{i}_\phi$, $\tilde{\boldsymbol{\omega}} = \tilde{\omega}_z(\tilde{r})\mathbf{i}_z$, $\tilde{\mathbf{T}} = \tilde{T}_z(\tilde{r})\mathbf{i}_z$, $\tilde{\mathbf{F}} = \tilde{F}_\phi(\tilde{r})\mathbf{i}_\phi$ which simplify the expressions in Eqs. 8.3 and 8.4 to,

$$\tilde{T}_z(\tilde{r}) + 2\frac{\zeta}{\eta}\left(\frac{\partial \tilde{v}_\phi}{\partial \tilde{r}} + \frac{\tilde{v}_\phi}{\tilde{r}} - 2\tilde{\omega}_z\right) + \frac{\eta'}{R^2\eta}\left(\frac{\partial^2 \tilde{\omega}_z}{\partial \tilde{r}^2} + \frac{1}{\tilde{r}}\frac{\partial \tilde{\omega}_z}{\partial \tilde{r}}\right) = 0 \tag{8.5}$$

$$\tilde{F}_\phi(\tilde{r}) - 2\frac{\zeta}{\eta}\frac{\partial \tilde{\omega}_z}{\partial \tilde{r}} + \left(1 + \frac{\zeta}{\eta}\right)\left(\frac{\partial^2 \tilde{v}_\phi}{\partial \tilde{r}^2} + \frac{1}{\tilde{r}}\frac{\partial \tilde{v}_\phi}{\partial \tilde{r}} - \frac{\tilde{v}_\phi}{\tilde{r}^2}\right) = 0 \tag{8.6}$$

Equations 8.5 and 8.6 determine the ferrofluid mechanical variables $\tilde{v}_\phi$ and $\tilde{\omega}_z$ for a given body torque density $\tilde{T}_z$ and body force density $\tilde{F}_\phi$ as a function of radius $\tilde{r}$. The body torque and force densities result from an applied rotating magnetic field and in turn depend on the mechanical variables $\tilde{v}_\phi$ and $\tilde{\omega}_z$. Note that the $\tilde{\nabla} \cdot \tilde{\boldsymbol{\omega}}$ term in Eq. 8.4 vanishes in Eq. 8.5 for $\tilde{\boldsymbol{\omega}} = \tilde{\omega}_z(\tilde{r})\mathbf{i}_z$. Unlike the divergence of the velocity $\nabla \cdot \mathbf{v}$ which must alway be zero for an incompressible fluid, the divergence of the spin velocity $\nabla \cdot \boldsymbol{\omega}$ generally can be non-zero.

The no-slip boundary condition on the velocity requires that the velocity goes to zero at the stationary wall of the container as given by the expression,

$$\tilde{v}_\phi(\tilde{r} = 1) = 0 \tag{8.7}$$

The boundary condition on the spin velocity, however, is not as straightforward. We chose to investigate a boundary condition of the form,

$$\tilde{\omega}_z(\tilde{r}=1) = \frac{1}{2}\gamma\left(\frac{\partial \tilde{v}_\phi}{\partial \tilde{r}}|_{\tilde{r}=1} + \frac{\tilde{v}_\phi(\tilde{r})}{\tilde{r}}|_{\tilde{r}=1}\right) = \frac{1}{2}\gamma\frac{\partial \tilde{v}_\phi}{\partial \tilde{r}}|_{\tilde{r}=1} \tag{8.8}$$

where γ is a parameter that is either 0 or 1. If $\gamma = 0$ then the spin velocity $\tilde{\boldsymbol{\omega}}$ satisfies a no-slip condition at the stationary boundaries (*i.e.,* $\tilde{\boldsymbol{\omega}} = 0$ at the wall). On the other hand, $\gamma = 1$ implies that the spin velocity balances half the vorticity at a stationary boundary, $\tilde{\boldsymbol{\omega}} = \frac{1}{2}\nabla \times \tilde{\mathbf{v}}$ (*i.e.,* the magnetic nanoparticles roll freely on the lateral cylinder wall).

8.1.2 Magnetic governing equations

This analysis in this section starts from Maxwell's Equations in the magneto quasistatic limit with the magnetization relaxation constitutive relation and develops a set of governing equations describing the magnetic field dynamics in the ferrofluid. Ferrofluids do not conduct significant currents, therefore the current density $\mathbf{J}$ is set to zero in Ampère's law:

$$\nabla \times \mathbf{H} = 0 \rightarrow \mathbf{H} = -\nabla\psi \tag{8.9}$$

where we have exploited the mathematical result that any irrotational field can be written as the gradient of a scalar potential function ψ.

Gauss' law states that the magnetic flux density $\mathbf{B}$ is always solenoidal. Substituting the constitutive relation $\mathbf{B} = \mu_0(\mathbf{H}+\mathbf{M})$, we can rewrite Gauss' law in the form,

$$\nabla \cdot \mathbf{B} = \nabla \cdot \mu_0(\mathbf{H}+\mathbf{M}) = 0 \rightarrow \nabla \cdot \mathbf{H} = -\nabla \cdot \mathbf{M} \tag{8.10}$$

Further substitution of the relationship in Eq. 8.9 into Eq. 8.10 leads to the expression,

$$\nabla^2\psi = \nabla \cdot \mathbf{M} \tag{8.11}$$

Note that the expression in Eq. 8.11 takes the form of Poisson's equation, where $-\mu_0\nabla \cdot \mathbf{M}$ acts like an effective magnetic charge density.

The rotating uniform magnetic field in our spin-up experiment is generated by the stator-winding of a two-pole motor. A standard idealized model of a 2-pole stator replaces the current in the slots of the stator with a traveling sinusoidal surface current density $K_z = \Re\left\{\hat{K}_z e^{j(\Omega_e t - \phi)}\right\}$. Since the surface current density exciting the fields rotates at a frequency Ω_e, the magnetic variables $\mathbf{H}$, ψ, and $\mathbf{M}$ for the uniform magnetic field spin-up problem can be written in complex phasor notation as follows

$$\begin{aligned}
\mathbf{H}(r,\phi,t) &= \Re\left\{\hat{\mathbf{H}}(r)e^{j(\Omega_e t-\phi)}\right\} = \Re\left\{H_0\hat{\tilde{\mathbf{H}}}(\tilde{r})e^{j(\tilde{t}-\phi)}\right\} \\
\psi(r,\phi,t) &= \Re\left\{\hat{\psi}(r)e^{j(\Omega_e t-\phi)}\right\} = \Re\left\{H_0R\hat{\tilde{\psi}}\,(\tilde{r})e^{j(\tilde{t}-\phi)}\right\} \\
\mathbf{M}(r,\phi,t) &= \Re\left\{\hat{\mathbf{M}}(r)e^{j(\Omega_e t-\phi)}\right\} = \Re\left\{H_0\hat{\tilde{\mathbf{M}}}(\tilde{r})e^{j(\tilde{t}-\phi)}\right\}
\end{aligned} \tag{8.12}$$

where we use a small hat symbol above the variables to stress the distinction between the mechanical variables $\mathbf{v}$ and $\boldsymbol{\omega}$, which are not time harmonic, and time harmonic variables with complex amplitudes $\hat{\mathbf{M}}$, $\hat{\mathbf{H}}$, $\hat{\psi}$. Non-dimensional magnetic quantities are normalized to a reference magnetic field strength H_0 as $\tilde{\mathbf{H}} = \frac{\mathbf{H}}{H_0}$, $\tilde{\mathbf{M}} = \frac{\mathbf{M}}{H_0}$, and $\tilde{\psi} = \frac{\psi}{H_0 R}$. Note that the angle ϕ in radians is already dimensionless.

Using the complex exponential forms from Eq. 8.12 in Eq. 8.11 leads to,

$$\frac{\partial^2\hat{\tilde{\psi}}}{\partial\tilde{r}^2} + \frac{1}{\tilde{r}}\frac{\partial\hat{\tilde{\psi}}}{\partial\tilde{r}} - \frac{\hat{\tilde{\psi}}}{\tilde{r}^2} = \frac{\partial\hat{\tilde{M}}_r}{\partial\tilde{r}} + \frac{\hat{\tilde{M}}_r}{\tilde{r}} - j\frac{\hat{\tilde{M}}_\phi}{\tilde{r}} \tag{8.13}$$

To relate the magnetization vector $\mathbf{M}$ to the magnetic field intensity $\mathbf{H}$ we use the constitutive relation given by the ferrofluid relaxation equation,

$$\frac{\partial\mathbf{M}}{\partial t} + (\mathbf{v}\cdot\nabla)\mathbf{M} + \mathbf{M}(\nabla\cdot\mathbf{v}) = \boldsymbol{\omega}\times\mathbf{M} + \frac{1}{\tau}(\chi\mathbf{H} - \mathbf{M}) \tag{8.14}$$

where the $\nabla\cdot\mathbf{v}$ term vanishes for an incompressible fluid and the relaxation time constant $\tau = \left(\frac{1}{\tau_N} + \frac{1}{\tau_B}\right)^{-1}$ results from a parallel combination of a Néel relaxation process with time constant τ_N and a Brownian process with time constant τ_B. Substitution of the complex exponential form from Eq. 8.12 into Eq. 8.14 leads to the expression,

$$j\hat{\tilde{\mathbf{M}}} + (\tilde{\mathbf{v}}\cdot\tilde{\nabla})\hat{\tilde{\mathbf{M}}} = \tilde{\boldsymbol{\omega}}\times\hat{\tilde{\mathbf{M}}} + \frac{1}{\Omega_e\tau}(\chi\hat{\tilde{\mathbf{H}}} - \hat{\tilde{\mathbf{M}}}) \tag{8.15}$$

This equation can be further simplified by considering ferrofluid flows with $\tilde{\boldsymbol{\omega}} = \tilde{\omega}_z(\tilde{r})\mathbf{i}_z$, and $\tilde{\mathbf{v}} = \tilde{v}_\phi(\tilde{r})\mathbf{i}_\phi$,

$$\left(j\left[1-\frac{\tilde{v}_\phi(r)}{\tilde{r}}\right]+\frac{1}{\Omega_e\tau}\right)\hat{\tilde{M}}_r+\left(\tilde{\omega}_z-\frac{\tilde{v}_\phi(\tilde{r})}{\tilde{r}}\right)\hat{\tilde{M}}_\phi=\frac{\chi}{\Omega_e\tau}\hat{\tilde{H}}_r \tag{8.16}$$

$$\left(j\left[1-\frac{\tilde{v}_\phi(r)}{\tilde{r}}\right]+\frac{1}{\Omega_e\tau}\right)\hat{\tilde{M}}_\phi-\left(\tilde{\omega}_z-\frac{\tilde{v}_\phi(\tilde{r})}{\tilde{r}}\right)\hat{\tilde{M}}_r=\frac{\chi}{\Omega_e\tau}\hat{\tilde{H}}_\phi \tag{8.17}$$

With some algebraic manipulation of Eqs. 8.16 and 8.17 we can now express the magnetization vector as a function of magnetic field intensity and the mechanical state of the ferrofluid as given by the matrix expression,

$$\begin{bmatrix}\hat{\tilde{M}}_r\\ \hat{\tilde{M}}_\phi\end{bmatrix}=\frac{\chi\begin{bmatrix}1+j\Omega_e\tau\left(1-\tilde{\Omega}_m(\tilde{r})\right) & -\Omega_e\tau\left(\tilde{\omega}_z(\tilde{r})-\tilde{\Omega}_m(\tilde{r})\right)\\ \Omega_e\tau\left(\tilde{\omega}_z(\tilde{r})-\tilde{\Omega}_m(\tilde{r})\right) & 1+j\Omega_e\tau\left(1-\tilde{\Omega}_m(\tilde{r})\right)\end{bmatrix}\begin{bmatrix}\hat{\tilde{H}}_r\\ \hat{\tilde{H}}_\phi\end{bmatrix}}{1+\left(\Omega_e\tau\right)^2\left(1-\tilde{\omega}_z(\tilde{r})\right)\left(1+\tilde{\omega}_z(\tilde{r})-2\tilde{\Omega}_m(\tilde{r})\right)+2j\Omega_e\tau\left(1-\tilde{\Omega}_m(\tilde{r})\right)} \tag{8.18}$$

where we have identified $\tilde{\Omega}_m(\tilde{r}) = \frac{\tilde{v}_\phi(\tilde{r})}{\tilde{r}}$ from Eqs. 8.16 and 8.17 as the non-dimensional mechanical rotation rate of the ferrofluid as a function of radius. We can use Eq. 8.9 to relate $\hat{\tilde{\mathbf{H}}}$ to $\hat{\tilde{\psi}}$

$$\begin{bmatrix}\hat{\tilde{H}}_r\\ \hat{\tilde{H}}_\phi\end{bmatrix}=-\begin{bmatrix}\frac{\partial\hat{\tilde{\psi}}}{\partial\tilde{r}}\\ -j\frac{\hat{\tilde{\psi}}}{\tilde{r}}\end{bmatrix} \tag{8.19}$$

Substitution of Eq. 8.19 into Eq. 8.18 leads to the expression,

$$\begin{bmatrix}\hat{\tilde{M}}_r\\ \hat{\tilde{M}}_\phi\end{bmatrix}=\frac{-\chi\begin{bmatrix}1+j\Omega_e\tau\left(1-\tilde{\Omega}_m(\tilde{r})\right) & -\Omega_e\tau\left(\tilde{\omega}_z(\tilde{r})-\tilde{\Omega}_m(\tilde{r})\right)\\ \Omega_e\tau\left(\tilde{\omega}_z(\tilde{r})-\tilde{\Omega}_m(\tilde{r})\right) & 1+j\Omega_e\tau\left(1-\tilde{\Omega}_m(\tilde{r})\right)\end{bmatrix}\begin{bmatrix}\frac{\partial\hat{\tilde{\psi}}}{\partial\tilde{r}}\\ -j\frac{\hat{\tilde{\psi}}}{\tilde{r}}\end{bmatrix}}{1+\left(\Omega_e\tau\right)^2\left(1-\tilde{\omega}_z(\tilde{r})\right)\left(1+\tilde{\omega}_z(\tilde{r})-2\tilde{\Omega}_m(\tilde{r})\right)+2j\Omega_e\tau\left(1-\tilde{\Omega}_m(\tilde{r})\right)} \tag{8.20}$$

Eqs. 8.13 and 8.20 describe the magnetic state of a ferrofluid undergoing spin-up in terms of the mechanical variables. These two equations can be solved for $\hat{\tilde{\psi}}$ and consequently for $\hat{\tilde{\mathbf{H}}}$ and $\hat{\tilde{\mathbf{M}}}$ if $\tilde{v}_\phi$ and $\tilde{\omega}_z$ are known functions of radius. The boundary condition on the magnetic potential, $\tilde{\psi}$, is given by the expression,

$$\tilde{H}_\phi(\tilde{r}=1) = -\frac{1}{\tilde{r}}\frac{\partial\tilde{\psi}}{\partial\phi}|_{\tilde{r}=1} = -\tilde{K}_z \rightarrow \hat{\tilde{\psi}}\,(\tilde{r}=1) = j\hat{\tilde{K}}_z \tag{8.21}$$

which follows from the boundary condition on the discontinuity of the tangential component of the magnetic field at an interface carrying a surface current density.

The time-average magnetic body torque density and the magnetic body force density can be directly computed from known **H** and **M** fields,

$$\tilde{\mathbf{T}} = \frac{1}{2}\Re\{\hat{\tilde{\mathbf{M}}} \times \hat{\tilde{\mathbf{H}}}^*\} = \frac{1}{2}\Re\{\hat{\tilde{M}}_r\hat{\tilde{H}}_\phi^* - \hat{\tilde{M}}_\phi\hat{\tilde{H}}_r^*\}\mathbf{i}_z \tag{8.22}$$

$$\tilde{\mathbf{F}} = \frac{1}{2}\Re\left\{\hat{\tilde{\mathbf{M}}}\cdot\tilde{\nabla}\hat{\tilde{\mathbf{H}}}^*\right\} = \frac{1}{2}\Re\left\{\left(\hat{\tilde{M}}_r\frac{\partial}{\partial\tilde{r}} - \frac{j}{\tilde{r}}\hat{\tilde{M}}_\phi\right)\begin{bmatrix}\hat{\tilde{H}}_r^*\,\mathbf{i}_r\\ \hat{\tilde{H}}_\phi^*\,\mathbf{i}_\phi\end{bmatrix} + \begin{bmatrix}\frac{\hat{\tilde{M}}_\phi\hat{\tilde{H}}_\phi^*}{\tilde{r}}\mathbf{i}_r\\ \frac{\hat{\tilde{M}}_\phi\hat{\tilde{H}}_r^*}{\tilde{r}}\mathbf{i}_\phi\end{bmatrix}\right\} \tag{8.23}$$

Substitution of the appropriate relations from Eq. 8.18 into Eq. 8.22 leads to the following expression for the torque density,

$$\tilde{T}_z = \frac{\chi}{2}\Re\left\{\frac{\left[1+j\Omega_e\tau\left(1-\tilde{\Omega}_m(\tilde{r})\right)\right]\left[\hat{\tilde{H}}_r\hat{\tilde{H}}_\phi^* - \hat{\tilde{H}}_\phi\hat{\tilde{H}}_r^*\right] + \Omega_e\tau\left[\tilde{\Omega}_m(\tilde{r}) - \tilde{\omega}_z(\tilde{r})\right]\left[|\hat{\tilde{H}}_r|^2 + |\hat{\tilde{H}}_\phi|^2\right]}{1+\Omega_e^2\tau^2(1-\tilde{\omega}_z(\tilde{r}))\left[1+\tilde{\omega}_z(\tilde{r})-2\tilde{\Omega}_m(\tilde{r})\right] + 2j\Omega_e\tau\left[1-\tilde{\Omega}_m(\tilde{r})\right]}\right\} \tag{8.24}$$

Similarly the force density can be computed using the relations in Eq. 8.23 resulting in the following expression:

$$\begin{aligned}\tilde{F}_r &= \frac{\chi}{2}\Re\left\{\frac{\hat{\tilde{H}}_r\left(\left[1+j\Omega_e\tau\left(1-\tilde{\Omega}_m(\tilde{r})\right)\right]\frac{\partial\hat{\tilde{H}}_r^*}{\partial\tilde{r}} - \frac{j}{\tilde{r}}\Omega_e\tau\left(\tilde{\omega}_z(\tilde{r})-\tilde{\Omega}_m(\tilde{r})\right)\hat{\tilde{H}}_r^*\right)}{1+\Omega_e^2\tau^2(1-\tilde{\omega}_z(\tilde{r}))\left[1+\tilde{\omega}_z(\tilde{r})-2\tilde{\Omega}_m(\tilde{r})\right]+2j\Omega_e\tau\left[1-\tilde{\Omega}_m(\tilde{r})\right]}\right\} \\ &\quad -\frac{\chi}{2}\Re\left\{\frac{\hat{\tilde{H}}_\phi\left(\left[1+j\Omega_e\tau\left(1-\tilde{\Omega}_m(\tilde{r})\right)\right]\frac{j}{\tilde{r}}\hat{\tilde{H}}_r^* + \Omega_e\tau\left(\tilde{\omega}_z(\tilde{r})-\tilde{\Omega}_m(\tilde{r})\right)\frac{\partial\hat{\tilde{H}}_r^*}{\partial\tilde{r}}\right)}{1+\Omega_e^2\tau^2(1-\tilde{\omega}_z(\tilde{r}))\left[1+\tilde{\omega}_z(\tilde{r})-2\tilde{\Omega}_m(\tilde{r})\right]+2j\Omega_e\tau\left[1-\tilde{\Omega}_m(\tilde{r})\right]}\right\} \\ &\quad +\frac{\chi}{2}\Re\left\{\frac{\Omega_e\tau(\tilde{\omega}_z-\widetilde{\Omega_m})\frac{\hat{\tilde{H}}_r\hat{\tilde{H}}_\phi^*}{\tilde{r}} + (1+j\Omega_e\tau(1-\tilde{\Omega}_m))\hat{\tilde{H}}_\phi\hat{\tilde{H}}_\phi^*}{1+\Omega_e^2\tau^2(1-\tilde{\omega}_z(\tilde{r}))\left[1+\tilde{\omega}_z(\tilde{r})-2\tilde{\Omega}_m(\tilde{r})\right]+2j\Omega_e\tau\left[1-\tilde{\Omega}_m(\tilde{r})\right]}\right\}\end{aligned} \tag{8.25}$$

for the r-component of the force density and,

$$\begin{aligned}
\tilde{F}_\phi \quad = \quad & \frac{\chi}{2}\Re\left\{\frac{\hat{\tilde{H}}_r\left(\left[1+j\Omega_e\tau\left(1-\tilde{\Omega}_m(\tilde{r})\right)\right]\frac{\partial \hat{\tilde{H}}_\phi^{\,*}}{\partial \tilde{r}}-\frac{j}{\tilde{r}}\Omega_e\tau\left(\tilde{\omega}_z(\tilde{r})-\tilde{\Omega}_m(\tilde{r})\right)\hat{\tilde{H}}_\phi^{\,*}\right)}{1+\Omega_e^2\tau^2(1-\tilde{\omega}_z(\tilde{r}))\left[1+\tilde{\omega}_z(\tilde{r})-2\tilde{\Omega}_m(\tilde{r})\right]+2j\Omega_e\tau\left[1-\tilde{\Omega}_m(\tilde{r})\right]}\right\} \\
& -\frac{\chi}{2}\Re\left\{\frac{\hat{\tilde{H}}_\phi\left(\left[1+j\Omega_e\tau\left(1-\tilde{\Omega}_m(\tilde{r})\right)\right]\frac{j}{\tilde{r}}\hat{\tilde{H}}_\phi^{\,*}+\Omega_e\tau\left(\tilde{\omega}_z(\tilde{r})-\tilde{\Omega}_m(\tilde{r})\right)\frac{\partial \hat{\tilde{H}}_\phi^{\,*}}{\partial \tilde{r}}\right)}{1+\Omega_e^2\tau^2(1-\tilde{\omega}_z(\tilde{r}))\left[1+\tilde{\omega}_z(\tilde{r})-2\tilde{\Omega}_m(\tilde{r})\right]+2j\Omega_e\tau\left[1-\tilde{\Omega}_m(\tilde{r})\right]}\right\} \\
& +\frac{\chi}{2}\Re\left\{\frac{\Omega_e\tau(\tilde{\omega}_z-\tilde{\Omega_m})\frac{\hat{\tilde{H}}_r\hat{\tilde{H}}_r^{\,*}}{\tilde{r}}+(1+j\Omega_e\tau(1-\tilde{\Omega}_m))\hat{\tilde{H}}_\phi\hat{\tilde{H}}_r^{\,*}}{1+\Omega_e^2\tau^2(1-\tilde{\omega}_z(\tilde{r}))\left[1+\tilde{\omega}_z(\tilde{r})-2\tilde{\Omega}_m(\tilde{r})\right]+2j\Omega_e\tau\left[1-\tilde{\Omega}_m(\tilde{r})\right]}\right\} \qquad (8.26)
\end{aligned}$$

for the ϕ-component.

8.2 Flows with negligible spin diffusion coefficients ($\eta' = 0, \lambda' = 0$)

Before proceeding to solve Eqs. 8.3 and 8.4 numerically, it is perhaps instructive to consider first the limit where spin diffusion effects are negligible. Most researchers in the field use this approach to conclude that there can be no ferrofluid spin-up flow in uniform magnetic fields [40]. We will show that careful examination of the underlying assumption reveals that this accepted wisdom in the ferrofluid literature is misleading since it holds under a very limited set of simplifying assumptions.

If η' is zero then we can simplify Eq. 8.2 in the viscous dominated limit to the expression,

$$\mathbf{T} + 2\zeta(\nabla \times \mathbf{v} - 2\boldsymbol{\omega}) = 0 \qquad (8.27)$$

Taking the curl of both sides of Eq. 8.27

$$\nabla \times \boldsymbol{\omega} = \frac{\mu_0}{4\zeta}\nabla \times (\mathbf{M} \times \mathbf{H}) + \frac{1}{2}\nabla \times (\nabla \times \mathbf{v}) \qquad (8.28)$$

Substitution of the expression from Eq. 8.28 into Eq. 8.1 in the viscous dominated limit leads to,

$$-\nabla p + \zeta\nabla \times (\nabla \times \mathbf{v}) + (\zeta + \eta)\nabla^2\mathbf{v} + \frac{\mu_0}{2}\nabla \times (\mathbf{M} \times \mathbf{H}) + \mu_0(\mathbf{M} \cdot \nabla)\mathbf{H} = 0 \quad (8.29)$$

This can be rewritten by using the known vector identity, $\nabla\times(\nabla\times\mathbf{v}) = \nabla(\nabla\cdot\mathbf{v}) - \nabla^2\mathbf{v}$, resulting in the following expression,

$$-\nabla p + \eta\nabla^2\mathbf{v} + \frac{\mu_0}{2}\nabla \times (\mathbf{M} \times \mathbf{H}) + \mu_0(\mathbf{M} \cdot \nabla)\mathbf{H} = 0 \quad (8.30)$$

Another known vector identity, $\nabla \times (\mathbf{M} \times \mathbf{H}) = \mathbf{M}(\nabla \cdot \mathbf{H}) - \mathbf{H}(\nabla \cdot \mathbf{M}) + (\mathbf{H} \cdot \nabla)\mathbf{M} - (\mathbf{M}\cdot\nabla)\mathbf{H}$, can be used to simplify the torque term in Eq. 8.30 if we note that

$$\nabla \cdot \mathbf{H} = -\nabla \cdot \mathbf{M} \quad (8.31)$$

since $\mathbf{B} = \mu_0(\mathbf{H} + \mathbf{M})$ and $\nabla \cdot \mathbf{B} = 0$. This leads to the torque term given by the expression,

$$\nabla \times (\mathbf{M} \times \mathbf{H}) = (\mathbf{H} + \mathbf{M})(\nabla \cdot \mathbf{H}) + (\mathbf{H} \cdot \nabla)\mathbf{M} - (\mathbf{M} \cdot \nabla)\mathbf{H} \quad (8.32)$$

The governing ferrohydrodynamic equation is then given by,

$$-\nabla p + \eta\nabla^2\mathbf{v} + \frac{\mu_0}{2}(\mathbf{M} \cdot \nabla\mathbf{H}) + \frac{1}{2}\mathbf{B}(\nabla \cdot \mathbf{H}) + \frac{\mu_0}{2}\mathbf{H} \cdot \nabla\mathbf{M} = 0 \quad (8.33)$$

Two of the driving terms in Eq. 8.33 can be combined together with the aid of the known vector identity,

$$(\mathbf{H} \cdot \nabla)\mathbf{M} + (\mathbf{M} \cdot \nabla)\mathbf{H} = \nabla(\mathbf{H} \cdot \mathbf{M}) - \mathbf{H} \times (\nabla \times \mathbf{M}) - \mathbf{M} \times (\nabla \times \mathbf{H}) \quad (8.34)$$

resulting in the expression,

$$-\nabla p + \eta\nabla^2\mathbf{v} + \frac{1}{2}\mathbf{B}(\nabla \cdot \mathbf{H}) + \frac{\mu_0}{2}[\nabla(\mathbf{H} \cdot \mathbf{M}) - \mathbf{H} \times (\nabla \times \mathbf{M})] = 0 \quad (8.35)$$

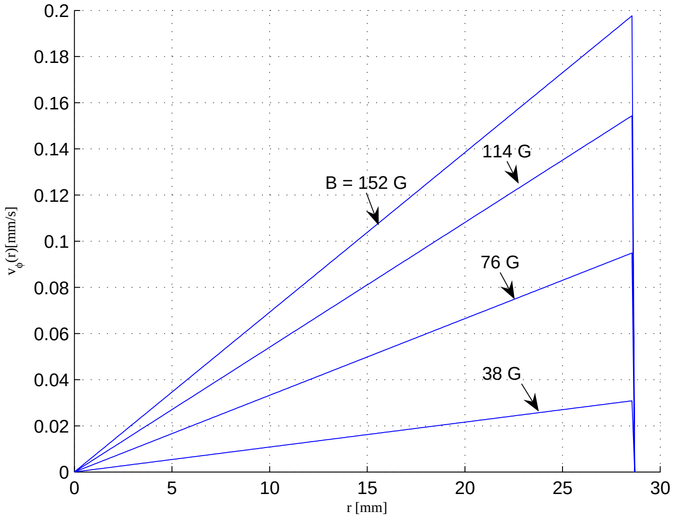

Figure 8-1: Velocity flow profiles obtained by numerically solving the spin-up model without a spin diffusion term (*i.e.*, with spin viscosity $\eta' = 0$). The simulation was run for the parameters of MSG W11 listed in Table 8.1 with $\tau = 1 \times 10^{-5}$ s and $f = 200$ Hz. Note that $\Omega_e = 2\pi f$.

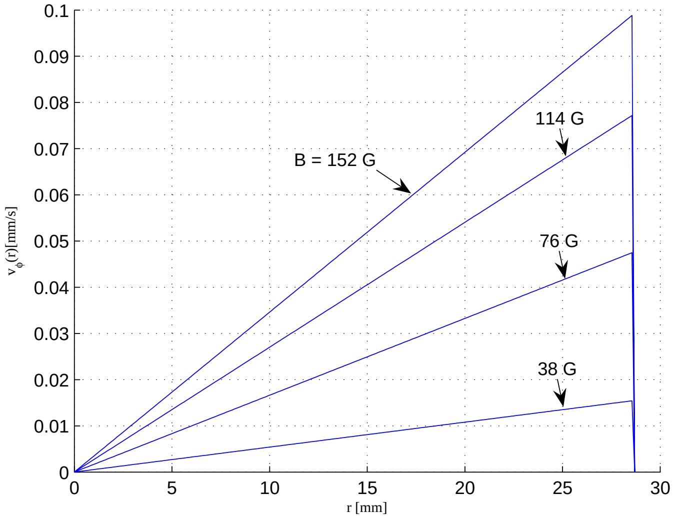

Figure 8-2: Velocity flow profiles obtained by numerically solving the spin-up model without a spin diffusion term (*i.e.*, with spin viscosity $\eta' = 0$). The simulation was run for the parameters of MSG W11 listed in Table 8.1 with $\tau = 1 \times 10^{-5}$ s and $f = 100$ Hz.

where we have used the fact that $\nabla \times \mathbf{H} = 0$ in a non-conducting medium. Finally we can lump the $\nabla(\frac{\mu_0 \mathbf{H}\cdot\mathbf{M}}{2})$ term into the pressure and write,

$$-\nabla \left\{ p + \frac{\mu_0 \mathbf{H} \cdot \mathbf{M}}{2} \right\} + \eta \nabla^2 \mathbf{v} + \frac{1}{2}\mathbf{B}(\nabla \cdot \mathbf{H}) - \frac{1}{2}\mu_0 \mathbf{H} \times (\nabla \times \mathbf{M}) = 0 \tag{8.36}$$

Although Pshenichnikov and Lebedev derive the driving terms in Eq. 8.36 [31], they choose to neglect them. An applied uniform rotating magnetic field in the ferrofluid means that $\nabla \cdot \mathbf{H} = 0$. The gradient of a potential such as $\nabla \left\{ p + \mu_0 \frac{\mathbf{H}\cdot\mathbf{M}}{2} \right\}$ cannot induce a rotational effect. The only remaining term is $-\frac{1}{2}\mu_0 \mathbf{H} \times (\nabla \times \mathbf{M})$. This term is non-zero unless $\nabla \times \mathbf{M} = 0$. Does a spatially uniform $\mathbf{H}$ necessarily imply that $\mathbf{M}$ must also be uniform? From Eq. 8.31 we can write Poisson's equation for the magnetic potential,

$$\nabla^2 \psi = \nabla \cdot \mathbf{M} \tag{8.37}$$

Examination of the constitutive relation between $\mathbf{M}$ and $\mathbf{H}$ given by the magnetization relaxation equation,

$$\frac{\partial \mathbf{M}}{\partial t} + (\mathbf{v} \cdot \nabla)\mathbf{M} = \boldsymbol{\omega} \times \mathbf{M} + \frac{1}{\tau}(\chi \mathbf{H} - \mathbf{M}) \tag{8.38}$$

is necessary to solve for the fields $\mathbf{M}$ and $\mathbf{H}$.

From Eq. 8.27 we have the following expression,

$$\boldsymbol{\omega} = \frac{1}{4\zeta}\mathbf{M} \times \mathbf{H} + \frac{1}{2}\nabla \times \mathbf{v} \tag{8.39}$$

which when substituted into Eq. 8.38 yields,

$$\frac{\partial \mathbf{M}}{\partial t} + (\mathbf{v} \cdot \nabla)\mathbf{M} + \frac{1}{4\zeta}\left[\mathbf{M}(\mathbf{M} \cdot \mathbf{H}) - \mathbf{H}|\mathbf{M}|^2\right] + \frac{1}{2}\mathbf{M} \times \nabla \mathbf{v} - \frac{1}{\tau}(\chi \mathbf{H} - \mathbf{M}) = 0 \tag{8.40}$$

If we neglect the velocity of the ferrofluid, $\mathbf{v} \approx 0$, then Eq. 8.40 can be rewritten as,

$$\frac{\partial \mathbf{M}}{\partial t} + \frac{1}{4\zeta}\left[\mathbf{M}(\mathbf{M} \cdot \mathbf{H}) - \mathbf{H}|\mathbf{M}|^2\right] - \frac{1}{\tau}(\chi \mathbf{H} - \mathbf{M}) = 0 \tag{8.41}$$

In the phasor notation of 8.12 this expression leads to,

$$\hat{\mathbf{M}} = \frac{\chi + c_1(r)}{1 + c_2(r)\tau + j\Omega_e\tau}\hat{\mathbf{H}} \tag{8.42}$$

where the $c_1(r)$ and $c_2(r)$ are scalar functions of r equal to $\frac{\tau}{4\zeta}|\hat{\mathbf{M}}|^2$ and $\frac{\tau}{4\zeta}(\hat{\mathbf{M}} \cdot \hat{\mathbf{H}}^*)$ respectively. The governing equation for the magnetic field given by Eq. 8.37 reduces to,

$$\nabla^2\hat{\psi} = \nabla \cdot \frac{\chi + c_1(r)}{1 + c_2(r)\tau + j\Omega_e\tau}\hat{\mathbf{H}} \tag{8.43}$$

When both convective terms $\boldsymbol{\omega} \times \mathbf{M}$ and the $(\mathbf{v} \cdot \nabla)\mathbf{M}$ in Eq. 8.38 are neglected the magnetization relaxation equation becomes,

$$\frac{\partial \mathbf{M}}{\partial t} = \frac{1}{\tau}(\chi\mathbf{H} - \mathbf{M}) \tag{8.44}$$

which when written in terms of the sinusoidal steady state phasor notation of Eq. 8.12 becomes,

$$\hat{\mathbf{M}} = \frac{\chi}{1 + j\Omega_e\tau}\hat{\mathbf{H}} = (\chi' + j\chi'')\hat{\mathbf{H}} \tag{8.45}$$

Eq. 8.45 shows that a rotating magnetic field $\mathbf{H}$ drives a time-lagging rotating magnetization $\mathbf{M}$. Neglecting both the spin velocity and linear velocity terms in Eq. 8.38 reduces Eq. 8.37 to Laplace's equation,

$$\nabla^2\psi = 0 \tag{8.46}$$

which results in uniform $\mathbf{H}$ and $\mathbf{M}$ thus eliminating the $-\frac{1}{2}\mu_0\mathbf{H} \times (\nabla \times \mathbf{M})$ driving term in Eq. 8.36. The torque density is spatially uniform in this limit and is given by,

$$\mathbf{T} = \frac{1}{2}\mu_0\Re\{\hat{\mathbf{M}} \times \hat{\mathbf{H}}^*\} = \frac{\mu_0\chi H_0^2(\Omega_e\tau)}{1 + (\Omega_e\tau)^2} \tag{8.47}$$

If $\eta' = 0$ there can be no spin-up flow in uniform applied rotating magnetic fields only if the spin velocity and linear velocity terms in the magnetization relaxation equation are neglected.

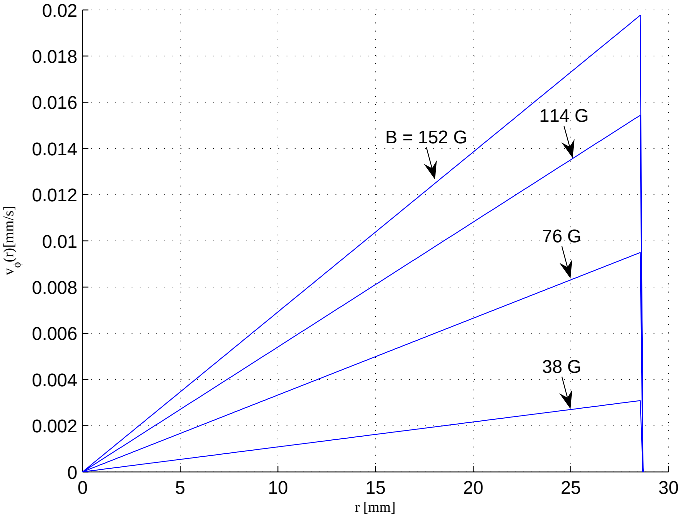

Figure 8-3: Velocity flow profiles obtained by numerically solving the spin-up model without a spin diffusion term (*i.e.*, with spin viscosity $\eta' = 0$). The simulation was run for parameters of with $\tau = 1 \times 10^{-5}$ s and $f = 20$ Hz.

Figs. 8-1 to 8-3 show that non-zero flow profiles exist in the ferrofluid when the spin viscosity η' is set to zero. The magnitude of the velocity for zero spin viscosity is very small, but increases rapidly for non-zero spin viscosities as demonstrated in Fig. 8-4.

8.3 Numerical algorithms

We approach the numerical solution for the full ferrofluid spin-up governing equations by decoupling the system non-linear differential equations into two linear subproblems that are easily solved by FEMLAB finite element models. The schematic diagram in Fig. 8-5 illustrates the iterative procedure used to solve numerically the full set of governing equations for ferrofluid spin-up. The algorithm starts with initial guesses for the body torque and force densities as functions of radius. The assumed forms for $\tilde{T}_z(\tilde{r})$, $\tilde{F}_\phi(\tilde{r})$ and $\tilde{F}_r(\tilde{r})$ are then used to solve numerically the fluid mechanical governing equations given by Eqs. 8.5 and 8.6 for $\tilde{v}_\phi(\tilde{r})$ and $\tilde{\omega}_z(\tilde{r})$. These results are subsequently input into the magnetization constitutive relation in Sec. 8.1.2. The electro-magnetic governing equations given by the expressions in Eqs. 8.13 and 8.20

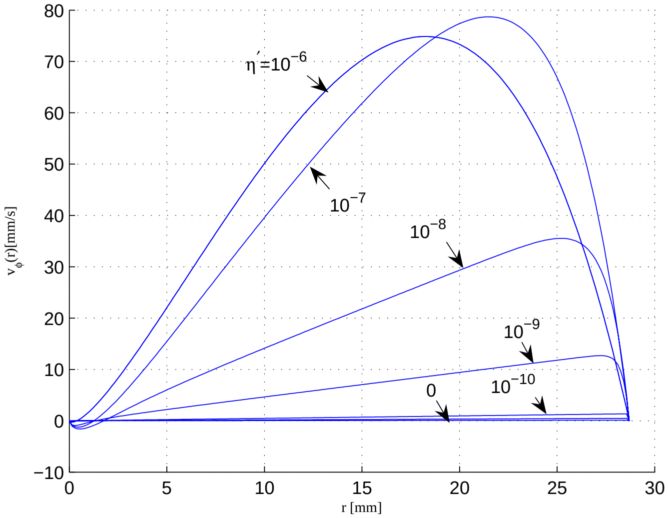

Figure 8-4: Velocity flow profiles obtained by numerically solving the spin-up model for zero and non-zero spin diffusion. The simulation was run for the parameters of MSG W11 listed in Table 8.1 with $\tau = 1 \times 10^{-5}$ s and $f = 20$ Hz.

are numerically solved for the magnetic potential $\tilde{\psi}(\tilde{r})$. Knowledge of $\tilde{\psi}(\tilde{r})$ determines the magnetic field intensity $\tilde{\mathbf{H}}$ and magnetization vector $\tilde{\mathbf{M}}$ and consequently a new estimate of the body torque and force densities.

The new estimate can be used as input to the fluid mechanics governing equations to produce new estimates for the velocity and spin velocity. The algorithm allows this iterative procedure to continue until the successive estimates converge on a final value and further iterations have negligible effect on the solution. Table 8.1 summarizes the parameters used for MSG W11 and EMG705 spin-up simulations.

FEMLAB, the numerical finite element multiphysics package from Comsol, was used to perform the spin-up simulations. This software package possesses three important features that enabled the solution of the spin-up problem outlined in the previous section. Firstly, FEMLAB enables us to define and solve general partial differential equations. Secondly, it handles complex numbers and variables in differential equations. Thirdly, problem definition in FEMLAB is not limited to a graphical user interface. A scripting language allows us to define FEMLAB models in terms of simple commands that can be incorporated into MATLAB scripts [54].

The algorithm outlined converges to a solution to the ferrofluid spin-up problem

Parameter	Value	Method
$\mu_0 H_0$	$38\sqrt{2} \times 10^{-4}$ tesla	Reference peak magnetic field
R	0.027 m	Caliper
MSG W11		
χ	0.65	VSM measurements
η	2.02 $\mathrm{mNs/m^2}$	Viscometry measurement
ϕ_m	2.75%	VSM measurements
ζ	0.83×10^{-4} $\mathrm{Ns/m^2}$	$\zeta = \frac{3}{2}\phi_m \eta$
EMG705		
χ	1.89	VSM measurements
η	2.48 $\mathrm{mNs/m^2}$	Viscometry measurement
ϕ_m	3.69%	VSM measurements
ζ	1.37×10^{-4} $\mathrm{Ns/m^2}$	$\zeta = \frac{3}{2}\phi_m \eta$

Table 8.1: Parameter values for Ferrotec's MSG W11 and EMG705 water-based ferrofluids. Estimates of τ and η' are obtained by fitting the simulations to the spin up experiments. The reference value of the magnetic field, $\mu_0 H_0$, corresponds to a current of 1 Amp in each of the three stator windings.

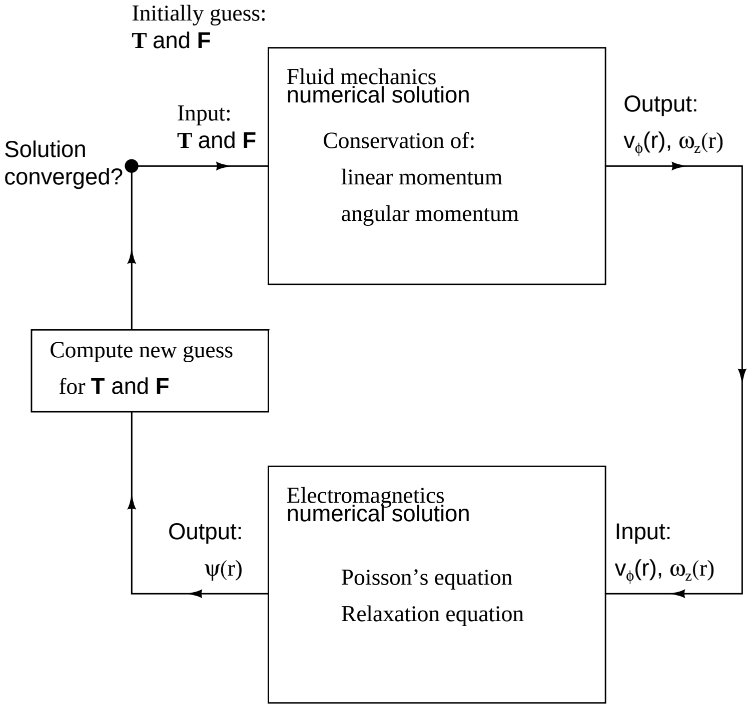

Figure 8-5: Schematic of algorithm to numerically solve the governing equations for ferrofluid spin up. By guessing an initial functional form for the torque and force densities we decouple the spin-up problem into two linear subproblems.

when all the mechanical and magnetic properties of the ferrofluid are known. Most of the required properties of ferrofluids, like the density, viscosity, low-field magnetic susceptibility and saturation magnetization, were measured directly through the independent experimental techniques described in Chapter 2. The magnetic relaxation time τ and the spin-viscosity η' are difficult to measure directly. Theoretical consideration for finding estimates of η' are based on dilute limit approximations and may not apply at the concentration levels used in the studies we present in this thesis.

Fig. 8-6, illustrates the method used to search for values of η' and τ that best match the results of the numerical simulation to ultrasound velocity measurements. The algorithm first fully maps out a region in τ-η' space for each value of experimentally applied magnetic field strength and frequency. The algorithm runs hundreds of numerical simulations and stores all the solution data for subsequent processing. The code usually ran over a few nights on a dedicated computer. Once the solution space is mapped, the algorithm could plot contours of constant peak profile velocity v_{max}

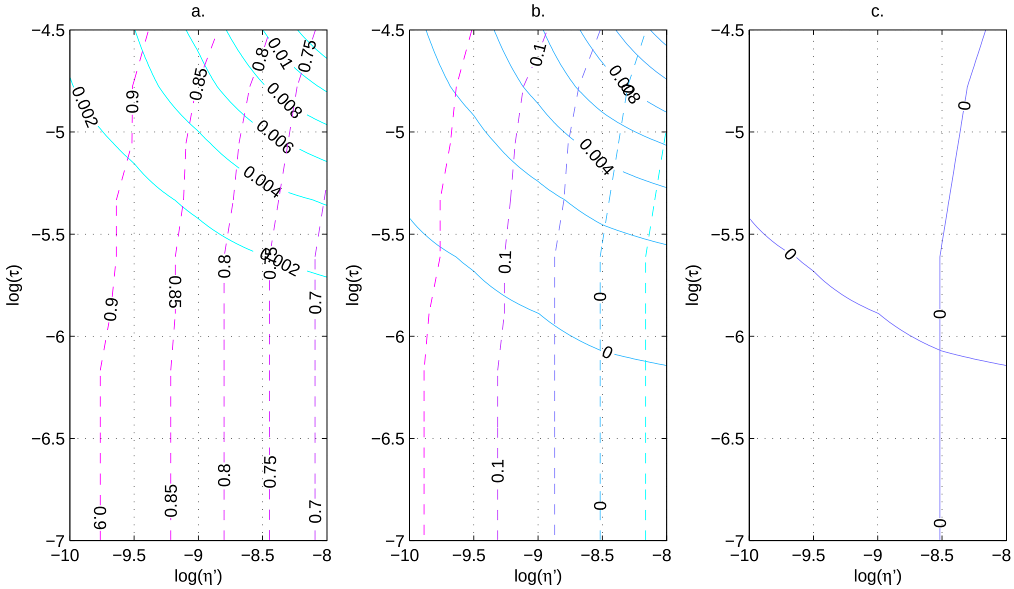

Figure 8-6: Sequence illustrating the method used to find the values of τ and η' in the 2d search space that best fit numerical simulation results to experimental data. Panel a: The algorithm first runs an extensive array of numerical simulations to fully map out contours of constant peak velocity magnitude v_{max}(solid contours), and peak velocity radial position (dashed contours) for any given applied magnetic field strength and frequency. Panel b: The experimentally measured values of peak velocity magnitude, and peak velocity radial position for the applied magnetic field strength and frequency are subtracted from the contours. Panel c: The intersection of the two contours labeled zero is the point in τ-η' space that best matches simulation to experiment.

and contours of constant peak velocity radial position r_{max}/R as illustrated in panel a of Fig. 8-6. Each experimental result for a given applied magnetic field strength and frequency corresponds to the intersection of a particular v_{max} contour and a r_{max}/R contour. This is seen more clearly in panel b of the figure, where the contours are offset by the experimentally measured values. The algorithm can easily compute the intersection of the contours labeled zero shown in panel c.

8.4 Results and discussion

The algorithms outlined in Sec. 8.3 were used to estimate fit values $\tau = 1.20 \times 10^{-5} \pm 1.18 \times 10^{-5}$ s and $\eta' = 3.15 \times 10^{-9} \pm 1.13 \times 10^{-9}$ kg-m/s for MSG W11 water-based ferrofluid. If we assume that Brownian processes dominate the relaxation time constant, $i.e., \tau = \tau_B = 3V\eta/kT$, these values result in average particle diameter of $\sim$ 21.0 nm, with a high value of 27.4 nm and a low value of 2.4 nm. The characteristic diffusion length defined by the approximate dilute-limit relationship, $\eta' \sim \eta l^2$, can be estimated to have a mean value of 1.2 mm, with a high value of 1.5 mm and a low value of 1.0 mm.

The estimates for EMG705 were $\tau = 1.37 \times 10^{-6} \pm 1.27 \times 10^{-6}$ s and $\eta' = 4.23 \times 10^{-9} \pm 2.62 \times 10^{-9}$. Based on the best fit relaxation time constant results. average particle diameter is 7.4 nm, with a high value of 10.0 nm and low value of 7.2 nm. Estimating the diffusion length from the dilute limit theory relation for η' results in an average value of 1.3 mm, with a high value estimate of 1.7 mm and a low value of 0.8 mm. Ideally only one pair of τ and η' fit parameters should fit all the flow profile data. Fig. 8-7 shows the scatter of η' and τ fit parameters for each experimental measurement of velocity profile for MSG W11 water-based ferrofluid, while Fig. 8-8 shows the scatter for EMG705 water-based ferrofluid.

The preceding calculation of ferrofluid physical parameters from flow data illustrates the sensitivity of key ferrofluid properties like the magnetization relaxation time τ and the spin viscosity η' to small variations in particle size and diffusion length respectively. Fig. 8-9 shows the sensitivity of the radial position of the peak velocity to η' and τ for a rotating magnetic field strength of 114 gauss rms and rotational frequency of 250 Hz. Fig. 8-10 shows the sensitivity of the value of the maximum velocity to η' and τ for a rotating magnetic field strength of 114 gauss rms and rotational frequency of 250 Hz.

Although ferrofluids are modeled as continua of mono-dispersed non-interacting nanoparticles, they are more accurately characterized by a distribution of particle sizes around an average value. Moreover, it has been suggested that the magnetic particles agglomerate to form long chains of particles due to interaction between the particles when magnetic fields are applied [28]. Other authors report microscopic failures of colloidal stability even in relatively weak magnetic fields, $\sim$ 10 gauss, resulting in the separation of ferrofluids into two liquids of different particle concentrations [4].

H_a [G rms]	τ [s]	η'[kg$\frac{m}{s}$]
MSG W11 (at 30 Hz) [Fig. 8-11]		
38	2.6×10^{-6}	3.1×10^{-9}
76	6.4×10^{-6}	2.1×10^{-9}
114	1.2×10^{-5}	1.0×10^{-8}
152	1.5×10^{-5}	2.1×10^{-8}
MSG W11 (at 50 Hz) [Fig. 8-12]		
38	1.2×10^{-6}	1.1×10^{-8}
76	2.5×10^{-6}	3.3×10^{-9}
114	2.1×10^{-5}	6.8×10^{-9}
152	2.9×10^{-5}	1.9×10^{-8}
MSG W11 (at 100 Hz) [Fig. 8-13]		
38	1.3×10^{-6}	2.5×10^{-10}
76	2.6×10^{-5}	2.2×10^{-9}
114	2.6×10^{-5}	2.2×10^{-9}
152	2.6×10^{-5}	1.3×10^{-8}

Table 8.2: Best fit values of τ and η' for different applied magnetic field strengths for MSG W11 water-based ferrofluid.

Tables 8.2 and 8.3 summarize the best fit values of η' and τ used in Figs. 8-11 to 8-16 that fit all experimental data points well. Figs. 8-11 to 8-13 compare measured velocity profiles and simulation results for MSG W11 water-based ferrofluid in applied magnetic field frequencies of 30, 50 and 100 Hz. Note that each figure uses a different value of η' and τ for the theoretical curves as documented in Table 8.2. Figs. 8-14 and 8-16 compare measured velocity profiles and simulation results for EMG705 water-based ferrofluid in applied magnetic field frequencies of 20, 40 and 200 Hz. Note again that each figure uses a different value of η' and τ for the theoretical curves (See Table 8.3).

The numerical results show a very small reversal of flow for low values of r that we have not observed experimentally. The small magnitudes predicted for reversed flows and their presence near $r = 0$ poses serious challenges for ultrasound velocimetry.

H_a [G rms]	τ [s]	$\eta'[\mathrm{kg}\frac{m}{s}]$
EMG705 (at 20 Hz) [Fig. 8-14]		
38	7.9×10^{-7}	3.5×10^{-9}
76	8.0×10^{-7}	3.1×10^{-9}
114	6.2×10^{-7}	3.4×10^{-9}
152	1.2×10^{-6}	3.0×10^{-9}
EMG705 (at 40 Hz) [Fig. 8-15]		
38	3.2×10^{-7}	1.6×10^{-8}
76	3.4×10^{-7}	1.8×10^{-8}
114	3.0×10^{-7}	8.1×10^{-9}
152	2.9×10^{-7}	7.9×10^{-9}
EMG705 (at 200 Hz) [Fig. 8-16]		
38	4.8×10^{-7}	1.5×10^{-9}
76	5.0×10^{-7}	1.1×10^{-9}
114	4.6×10^{-7}	5.0×10^{-10}
152	6.8×10^{-7}	5.1×10^{-10}

Table 8.3: Best fit values of τ and η' for different applied magnetic field strengths for EMG705 water-based ferrofluid.

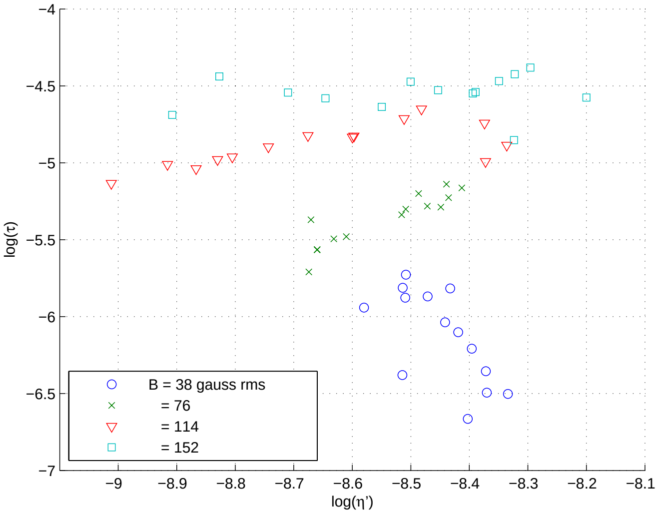

Figure 8-7: Scatter plot showing the different fit values of η' and τ for each MSG W11 water-based ferrofluid experimental magnetic field strength and frequency.

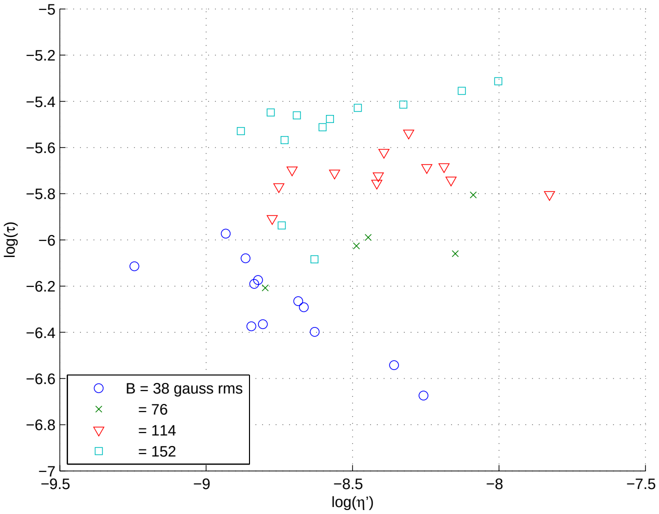

Figure 8-8: Scatter plot showing the different fit values of η' and τ for each MSG W11 water-based ferrofluid experimental magnetic field strength and frequency.

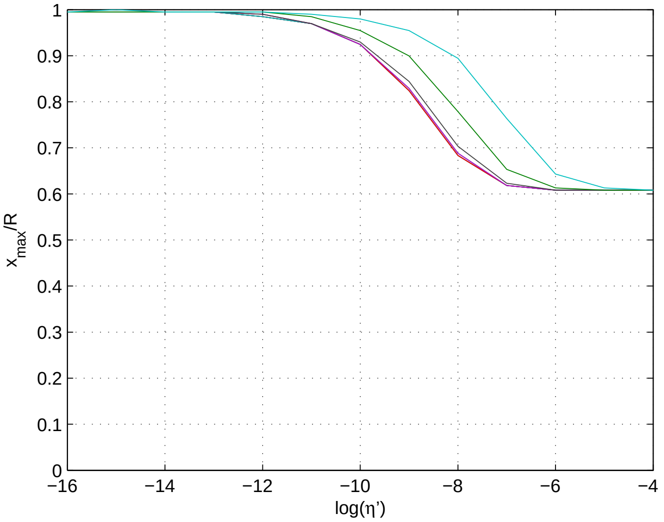

Figure 8-9: Sensitivity of the maximum velocity to the value of η' and τ for a magnetic field strength of 114 gauss rms and rotational frequency of 250 Hz. Curves shown for $\tau = 1 \times 10^{-7}$, 5×10^{-7}, 1×10^{-6}, 5×10^{-6}, and 1×10^{-5} s.

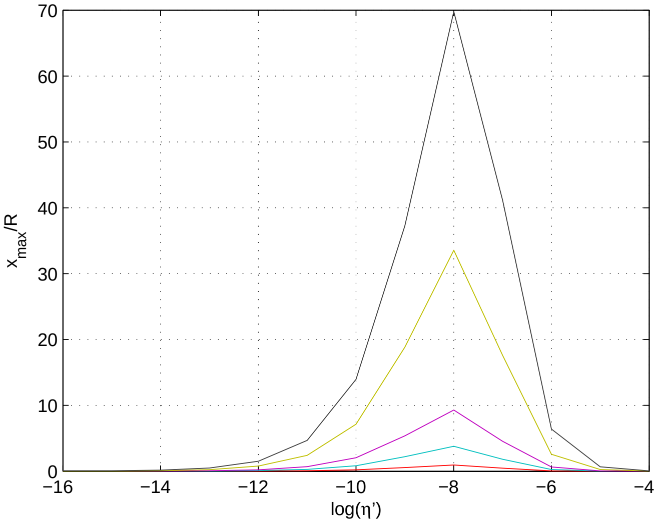

Figure 8-10: Sensitivity of the radial position of maximum velocity to the value of η' and τ for a magnetic field strength of 114 gauss rms and rotational frequency of 250 Hz. Curves shown for $\tau = 1 \times 10^{-7}$, 5×10^{-7}, 1×10^{-6}, 5×10^{-6}, and 1×10^{-5} s.

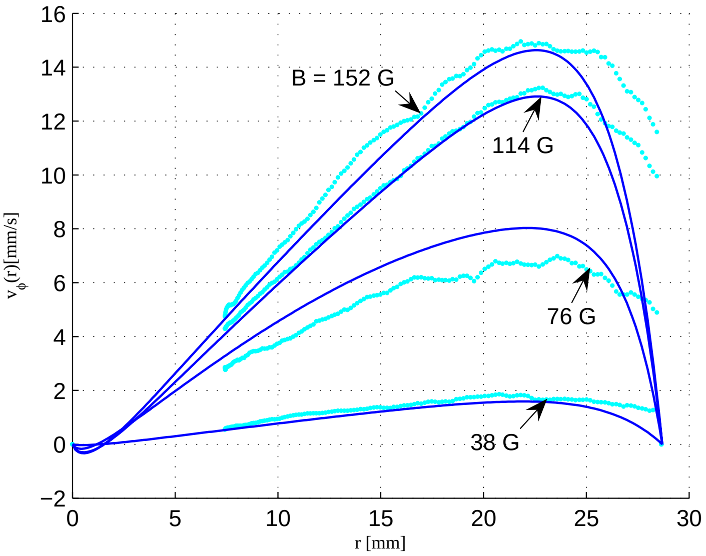

Figure 8-11: Comparison of experimentally measured (thick dotted curves) and numerically computed ferrofluid spin-up velocity profiles (thin solid curves) for a 30 Hz rotating magnetic field for MSG W11 water-based ferrofluid. The numerical plots were generated using the fit values listed in Table 8.2.

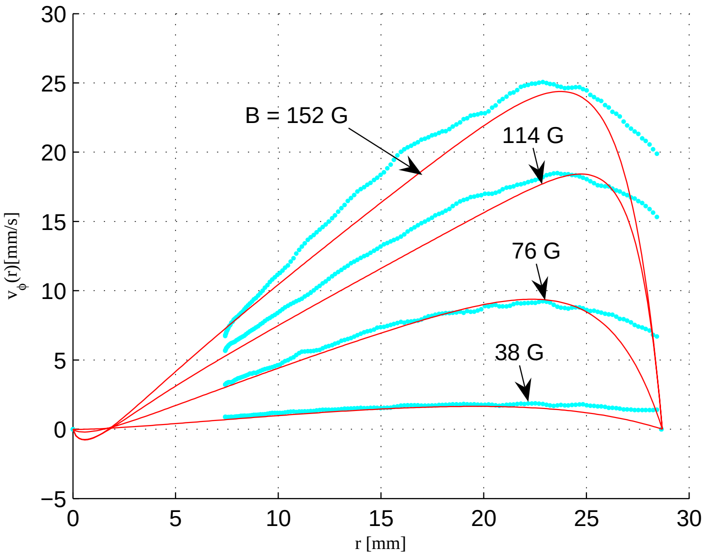

Figure 8-12: Comparison of experimentally measured (thick dotted curve) and numerically computed ferrofluid spin-up velocity profiles (thin solid curve) for a 50 Hz rotating magnetic field for MSG W11 water-based ferrofluid. Table 8.2 summarizes the fit parameters that were used to generate the numerical plots.

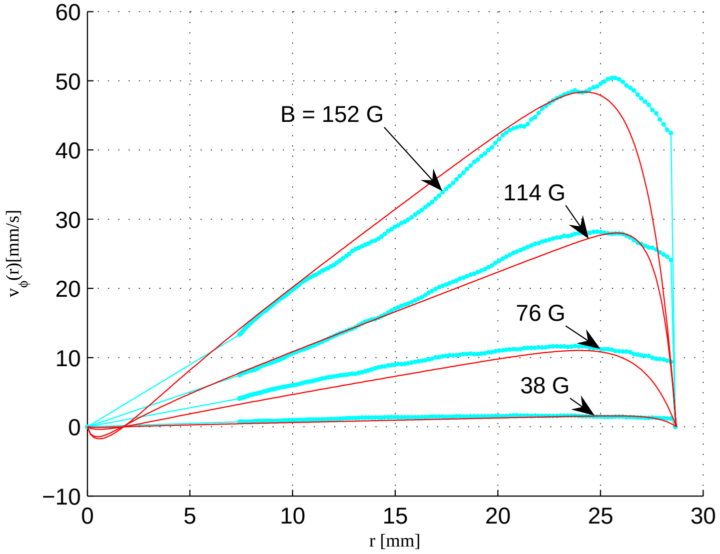

Figure 8-13: Comparison of experimentally measured (thick dotted curves) and numerically computed ferrofluid spin-up velocity profiles (thin solid curves) for a 100 Hz rotating magnetic field for MSG W11 water-based ferrofluid. The fit values listed in Table 8.2 were used to generate numerical results.

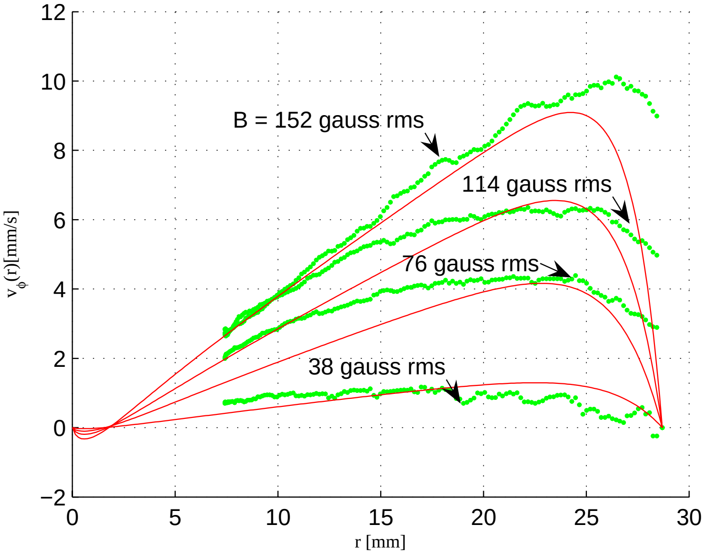

Figure 8-14: Comparison of experimentally measured (thick dotted curve) and numerically computed ferrofluid spin-up velocity profiles (thin solid curve) for a 20 Hz rotating magnetic field for EMG705 water-based ferrofluid (see Table 8.3 for fit values used to generate the numerical results in this figure).

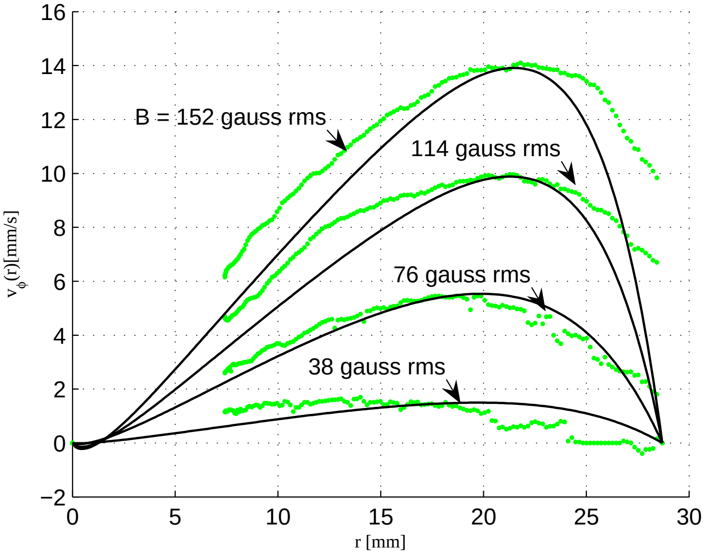

Figure 8-15: Comparison of experimentally measured (thick dotted curve) and numerically computed ferrofluid spin-up velocity profiles (thin solid curve) for a 40 Hz rotating magnetic field for EMG705 water-based ferrofluid (see Table 8.3 for fit values used to generate the numerical results in this figure).

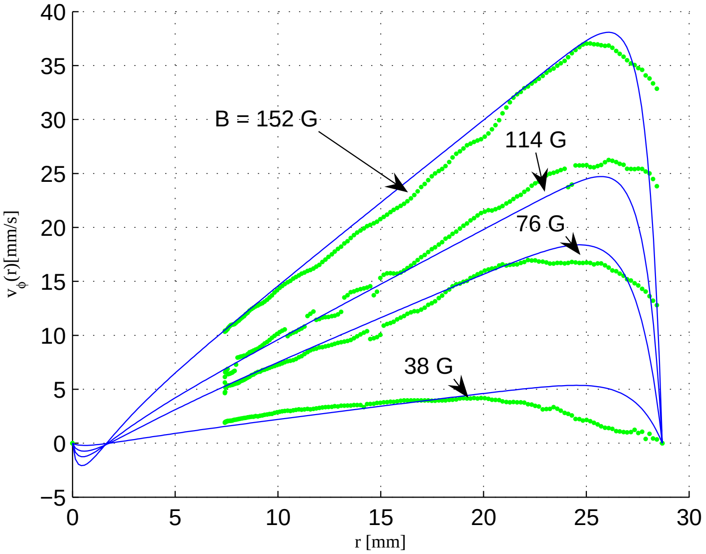

Figure 8-16: Comparison of experimentally measured (thick dotted curve) and numerically computed ferrofluid spin-up velocity profiles (thin solid curve) for a 200 Hz rotating magnetic field for EMG705 water-based ferrofluid (see Table 8.3 for fit values used to generate the numerical results in this figure).

Chapter 9

Concluding remarks

9.1 Key contributions

Ferrofluid surface and volume effects in uniform dc and rotating magnetic fields are studied in order to develop analytical and numerical first principle models. The following points summarize the key contributions to ferrofluid spin-up research made in this thesis:

- Volume flow in ferrofluid spin-up is experimentally found to be co-rotational with the magnetic field and opposite to the surface-meniscus coupled flow. Co-rotating volume flow occurs in ferrofluid containers with and without a free surface. These experimental investigations were independently repeated and verified by our collaborators in the Rinaldi research group. We were the first to observe and measure: (i) flow reversal between the co-rotating ferrofluid bulk and counter rotating free surface and (ii) flow profiles in a filled and sealed container of ferrofluid without a free surface.
- Numerical simulation of spin-up flow including contributions from the linear and spin velocity terms in the relaxation equation is carried out with relaxation time and effective spin viscosity determined from fits to the data. Theory and numerical analysis have shown that, with the inclusion of the linear and spin velocity terms in the magnetic relaxation equation, spin-up flow occurs in a

uniform magnetic field even if the the spin viscosity is zero, $\eta' = 0$. Neglecting the linear and spin velocity terms in the magnetic relaxation equation results in no spin-up flow in a uniform rotating magnetic field.

- The influence of magnetic field on meniscus height and shape is experimentally determined. A uniform horizontal applied magnetic field is observed to lower the height of the ferrofluid meniscus, while a vertical applied magnetic field is observed to increase the meniscus height. Experimental results are shown to agree with energy minimization analyses.
- Analytical-low-Reynolds-number limiting solutions are developed for a surface shear strip driven flow in a cylindrical cavity. The solutions are extended to high Reynolds number recirculation flows with numerical finite element methods.
- An expression is derived for the energy of a magnetized volume of non-linearly magnetizable material and the result used to determine the influence of rotating field on the morphology of drops of ferrofluid in a Hele-Shaw cell with comparisons made to experiments.
- Appendix C validates the ultrasonic probe technique using Taylor-Couette flow.

9.2 Critique of results

Ferrofluid spin-up dynamics remains a rich field for further study and there are many open questions. The following questions, raised but not fully resolved by our research efforts, offer potential areas for further research:

- Ideally, a single value of spin viscosity and magnetization relaxation time constant would fit all experimental values. In our experiments the best fit values of theory to experiment spread over a range from one to two orders of magnitude.
- The spin-up model does not predict the experimentally observed saturation of bulk rotation at such a low frequency as ~ 150 Hz. This is a major cause

of the scatter in fit values for the spin viscosity and the magnetization relaxation time. The discrepancy might indicate that microscopic structure of the ferrofluid might change under the applied magnetic fields.

- The average experimental fit for spin viscosity, η', exceeds the theoretical estimates by many orders of magnitude. Theoretical considerations for finding estimates of spin viscosity are (i) based on dilute limit approximations and (ii) less than rigorous adaptations of kinetic theory analyses for the viscosities of gases. Our values, however, are ~ 8 orders of magnitude off, which remains a cause for serious concern in the absence of a plausible explanation or hypothesis.

- Numerical simulations for bulk driven spin-up neglect recirculation, whereas experiments show some moderate recirculation flows. A full simulation of spin-up with both r and z dependence was considered but not implemented. Instead we focused on the more tractable problem of solving for the primary azimuthally directed flow.

9.3 Future work

In closing, we suggest the following natural directions for future work to extend and build upon the results presented in this thesis:

- Record start-up transient time sequence for ferrofluids in a covered container for various applied field strengths and rotating field frequencies with ultrasound velocimetry. This investigation could show (i) the development from initial rest of a steady state velocity profile and (ii) the dependence of the 90% rise time to the steady state value as a function of applied rotating field strength and frequency. The turn-off transient should be recorded in each experimental case as a reference. We presented some preliminary transient measurements in Section 7.4.3.

- Experimentally investigate radial and axial recirculation velocity profiles in EMG705 and MSG W11. Examine the effects of reversing the direction of rotation of the magnetic field on the direction symmetry and shape of recirculation flow.

- Extend the finite element analysis model to handle two dimensional axisymmetric solutions to investigate numerically the effects of recirculating flows in spin-up flow.

Appendix A

Conservation of mass correction to gravitational potential term in Chapter 4

This Appendix considers a conservation of mass correction to the incremental change in gravitational energy dE_G due to a change in meniscus height dh given by Eq. 4.35 in Sec. 4.3.3 for a linear meniscus profile. Conservation of mass for an incompressible fluid requires that the level of the ferrofluid in the bulk decrease if the meniscus rises as shown schematically in Fig. A-1.

Superposition gives the total gravitational potential energy of the initial state of the system in Fig. A-1 as the sum of the gravitational potentials of equivalent point masses, $\rho L_1 W$ and $\frac{1}{2}\rho h^2 \tan\theta$, at the center-of-mass heights $\frac{L_1}{2}$ and $L_1 + \frac{h_1}{3}$ respectively.

$$E_1 = \frac{1}{2}\rho g \left[W L_1^2 + h_1^2 \left(\frac{h_1}{3} + L_1 \right) \tan\theta_0 \right] \tag{A.1}$$

A similar argument, *mutatis mutandis*, for the final state gives,

$$E_2 = \frac{1}{2}\rho g \left[W L_2^2 + h_2^2 \left(\frac{h_2}{3} + L_2 \right) \tan\theta_0 \right] \tag{A.2}$$

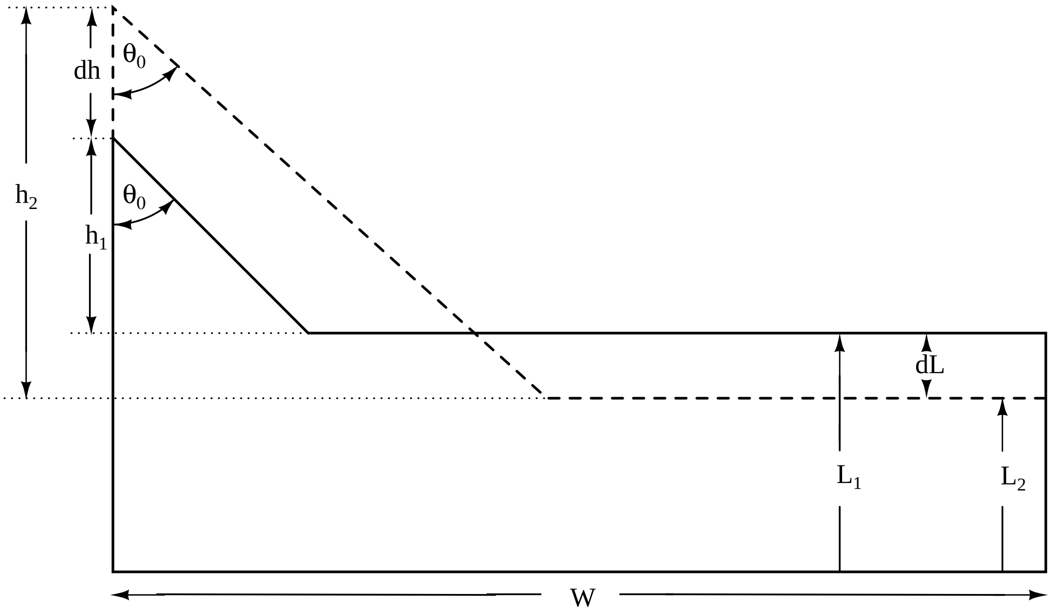

Figure A-1: Schematic of ferrofluid meniscus and bulk region showing the effects of taking mass conservation into account as the height of the meniscus increases.

The change in gravitational potential is then given by,

$$\Delta E_G = E_2 - E_1 = \frac{1}{2}\rho g \left[W\left(L_2^2 - L_1^2\right) + \left\{ h_2^2\left(\frac{h_2}{3} + L_2\right) - h_1^2\left(\frac{h_1^2}{3} + L_1\right)\right\}\tan\theta_0 \right] \tag{A.3}$$

We define the initial state as,

$$\begin{aligned} L_1 &= L \\ h_1 &= h \end{aligned} \tag{A.4}$$

and the final state as,

$$\begin{aligned} h_2 &= h + dh \\ L_2 &= L + dL \end{aligned} \tag{A.5}$$

where dh and dL are small increments. It can be easily shown from Eq. 4.42 that dL and dh are related by,

$$dL = -\frac{h}{W - h\tan\theta_0}\tan\theta_0 dh \tag{A.6}$$

Substitution of Eqs. A.4, A.5 and A.6 into Eq. A.3 leads to the expression,

$$\Delta E_G = \frac{1}{2}\rho g h^2 \tan\theta_0 \left(1 + \frac{2L}{W}\tan\theta_0\right) \tag{A.7}$$

where we have retained only terms that first order in dh. Note that this expression reduces to the result in Sec. 4.3.3 in the limit when $W \to \infty$. Although L can be large its value must remain finite if we are to have a meaningful gravitational potential reference point.

Appendix B

Non-linear energy considerations in ferrofluids: fluxball analysis

B.1 Introduction

The electrical energy is a useful thermodynamic function for computing forces of electrical origin and mechanical work in electromechanical systems. The energy function for continuum electromechanical systems can be computed simply by evaluating the integral expression

$$W = \int_V \int_0^B \mathbf{H} \cdot d\mathbf{B} dv \tag{B.1}$$

where the volume of integration V extends over all the space where magnetic fields excited by the system are present. For linear materials, $\mathbf{B} = \mu\mathbf{H}$, the integral relations reduce to a familiar result,

$$W = \int_V \frac{1}{2}\mathbf{H} \cdot \mathbf{B} dv = \int_V \frac{1}{2}\mu H^2 dv \tag{B.2}$$

The change in energy, ΔW, due to the introduction of a magnetic material with permeability μ_a and volume V_a into a region of free space that initially had a magnetic field intensity $\mathbf{H}_0$ and flux density, $\mathbf{B}_0 = \mu_0 \mathbf{H}_0$, is given by the expression,

$$\Delta W = \int_V \frac{1}{2} \left(\mathbf{H} \cdot \mathbf{B} - \mathbf{H}_0 \cdot \mathbf{B}_0 \right) dv \tag{B.3}$$

where $\mathbf{H}$ and $\mathbf{B}$ are the magnetic field intensity and flux density after the introduction of the magnetic material. The volume of integration V in Eq. B.3 extends over all space. Paris and Hurd [30], however, show that Eq. B.3 reduces to the following integral over the finite volume of the linear magnetic material V_a,

$$\Delta W = -\frac{1}{2} \int_{V_a} (\mu_a - \mu_0) \mathbf{H} \cdot \mathbf{H}_0 dv \tag{B.4}$$

The derivation of Eq. B.4 assumes no energy exchange through the electrical terminals of the system (*i.e.*, constant magnetic flux through source coils) and that the magnetic fields go to zero as $r \longrightarrow \infty$ at a rate of decay faster than $\frac{1}{r^{3/2}}$.

Paris and Hurd use Eq. B.4 in Example 6-2 of section 6.6 of their book to illustrate the computation of the energy of a sphere of radius a and permeability μ_a surrounded by free space in an infinite uniform magnetic field $\mathbf{H}_0 = H_0 \mathbf{i}_z$. The field solution to this classical problem is given by,

$$\mathbf{H}(r, \theta) = \begin{cases} H_0 \left(\frac{3\mu_0}{2\mu_0 + \mu_a} \right) \mathbf{i}_z & ; r < a \\ \\ H_0 \left[\cos\theta \left(1 + \frac{2a^3}{r^3} \frac{\mu_a - \mu_0}{2\mu_0 + \mu_a} \right) \mathbf{i}_r - \sin\theta \left(1 - \frac{a^3}{r^3} \frac{\mu_a - \mu_0}{2\mu_0 + \mu_a} \right) \mathbf{i}_\theta \right] & ; r > a \end{cases} \tag{B.5}$$

Using the field solution of Eq. B.5 in Eq. B.4 the change in magnetic energy is,

$$\Delta W = -\frac{1}{2} \left[(\mu_a - \mu_0) \left(H_0 \frac{3\mu_0}{2\mu_0 + \mu_a} \right) H_0 \right] \frac{4}{3} \pi a^3 = -2\pi a^3 \mu_0 H_0^2 \frac{\mu_a - \mu_0}{\mu_a + 2\mu_0} \tag{B.6}$$

However, the application of Eq. B.3 and brute force integration over all space of the field in Eq. B.5 yields,

$$\Delta W = \frac{2}{3} \pi a^3 \mu_0 H_0^2 \frac{\mu_a - \mu_0}{\mu_a + 2\mu_0} \tag{B.7}$$

This discrepancy in magnitude and sign seems paradoxical since Eq. B.4 was derived from Eq. B.3. In reality, the apparent discrepancy results from the violation of the assumption about the rate of decay of the magnetic fields at infinity being greater than $\frac{1}{r^{3/2}}$. Paris and Hurd's Example 6-2, page 287, poses a constant magnetic field at infinity which in turn means infinite potential at infinity. This contradicts the assumptions of the derivation of the formula for the change in magnetic energy on page 284. To resolve the paradox, this Chapter begins by investigating the limit of the field solution of a sphere of linear magnetic material in a finite-sized source of uniform magnetic field as the field source radius goes to infinity. Subsequently, Sec. B.3 extends the energy analysis to non-linear materials with any magnetization constitutive law but particularly examines solutions for materials with magnetization characteristics described by the Langevin equation. Computing the magnetic energy storage in many of the ferrofluid problems requires this extension of the energy formula to non-linear materials for large magnetic fields beyond the initial linear region. The results, however, are very general and hold for any system with non-linear magnetic materials.

B.2 Linear magnetic material

To find the initial magnetic fields before the introduction of the sphere of magnetic material we solve the two-region problem illustrated in Fig. B-1. The figure shows a surface current $\mathbf{K}_0 = \frac{Ni_0}{2b} \sin\theta \mathbf{i}_\phi$ on the surface of a sphere of radius r = b [14]. Such a current distribution results from tightly winding a current-carrying coil so that the N-turns are uniformly distributed in z. A spherical shell with such a current distribution is called a "flux ball" and is a convenient way of making a uniform magnetic field within a spherical coil (See video [27]). The regions inside and outside the flux ball in Fig. B-1 have the magnetic permeability of free space μ_0.

B.2.1 Magnetic field solution

We begin the solution of the outlined magnetic field problem by noting that the magnetic fields inside and outside the spherical coil are curl-free (*i.e.*, $\nabla \times \mathbf{H}_0 = 0$) because there are no volume current densities in either of the two regions. Consequently, we can define a magnetic scalar potential ψ such that,

$$\mathbf{H}_0 = -\nabla\psi_0 \tag{B.8}$$

and the magnetic potential ψ_0 satisfies Laplace's Equation.

$$\nabla^2\psi_0 = \frac{1}{r^2}\frac{\partial}{\partial r}r^2\frac{\partial\psi_0}{\partial r} + \frac{1}{r^2\sin\theta}\frac{\partial}{\partial\theta}\sin\theta\frac{\partial\psi_0}{\partial\theta} = 0 \tag{B.9}$$

where we assume axisymmetric fields, so that ψ_0 does not depend on the azimuthal angle ϕ.

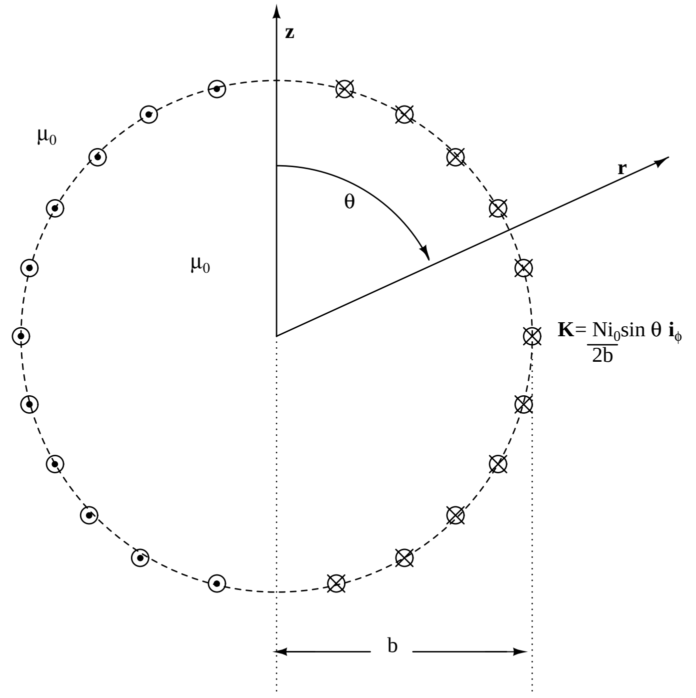

Figure B-1: Two-region geometry, before the introduction of a sphere of magnetic material, illustrating the surface current distribution at $r = b$.

Initially the magnetic fields must satisfy the boundary conditions at $r = b$,

$$\begin{aligned} \mathbf{i}_r &\times [\mathbf{H}_0(r=b_+) - \mathbf{H}_0(r=b_-)] = \tfrac{Ni_0}{2b}\sin\theta\mathbf{i}_\phi \\ \mathbf{i}_r &\cdot [\mathbf{B}_0(r=b_+) - \mathbf{B}_0(r=b_-)] = 0 \end{aligned} \tag{B.10}$$

where the tangential component, H_θ, of the magnetic field intensity at the $r = b$

boundary is discontinuous in the surface current and the normal component of the flux density, B_r, is continuous.

The field solution to this problem is given by,

$$\mathbf{H}_0(r,\theta) = \begin{cases} \frac{Ni_0}{3b}\mathbf{i}_z & ; r < b \\ \\ \frac{Ni_0 b^2}{6r^3}(2\cos\theta\mathbf{i}_r + \sin\theta\mathbf{i}_\theta) & ; r \geq b \end{cases} \tag{B.11}$$

The magnetic field inside the flux ball is uniform and z-directed. Outside the flux ball, the magnetic field intensity is inversely proportional to r^3 and has a dipole dependence with equivalent moment $\mathbf{m} = \frac{2}{3}Ni_0\pi b^2$. The magnetic field intensity far away from the flux ball drops to zero rapidly as $\frac{1}{r^3}$.

Fig. B-2 illustrates the flux ball after a sphere of magnetizable material with permeability μ_a and radius a, with $a < b$, is brought inside it. Initially, the sphere of magnetizable material was unmagnetized and far away from the flux ball (where $\mathbf{H} = 0$). To find the magnetic fields after the introduction of the sphere of magnetizable material, we must solve the three-region problem shown in Fig. B-2, where,

$$\mu(r) = \begin{cases} \mu_a & ; r < a \\ \\ \mu_0 & ; r > a \end{cases} \tag{B.12}$$

To use the energy method to compute the mechanical work necessary to introduce a sphere of magnetic material into the flux ball, we must require no additional energy flow through the electrical terminals (*i.e.*, we must consider an isolated system). This means that the net flux linked by the coils, λ, must remain constant as the magnetic sphere is brought inside the flux ball. Since by definition $\lambda = Li$, the current after the introduction of the magnetic material, i, must decrease from the initial current i_0 to account for the increase in flux ball winding inductance. The relationship between i and i_0 that maintains the flux linkage constant is derived in Sec. B.2.2.

The solution must satisfy Laplace's equation (Eq. B.9) in regions $r < a$, $a < r < b$

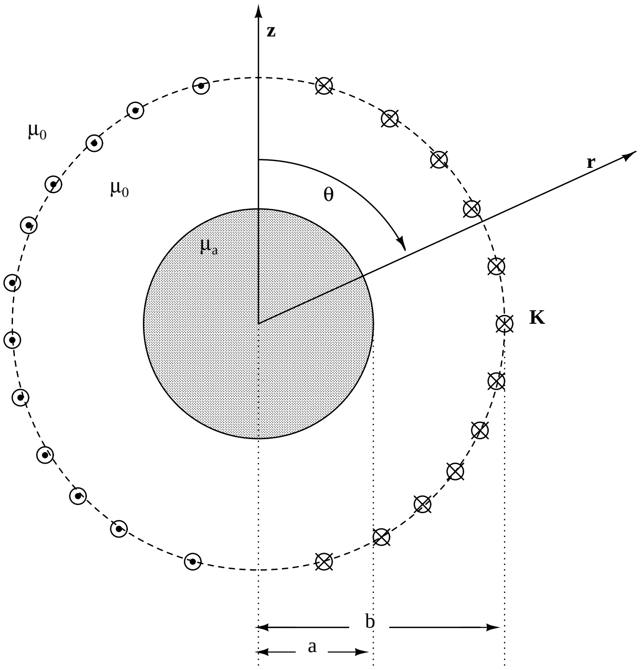

Figure B-2: Three-region geometry after the introduction of a sphere of magnetic permeability μ_a requiring satisfaction of boundary conditions at $r = a$ and $r = b$.

and $r > b$ with the following set of boundary conditions,

$$\begin{aligned}
\mathbf{i}_r &\times & [\mathbf{H}(r=b_+) - \mathbf{H}(r=b_-)] = \tfrac{Ni}{2b}\sin\theta\mathbf{i}_\phi \\
\mathbf{i}_r &\cdot & [\mathbf{B}(r=b_+) - \mathbf{B}(r=b_-)] = 0 \\
\mathbf{i}_r &\times & [\mathbf{H}(r=a_+) - \mathbf{H}(r=a_-)] = 0 \\
\mathbf{i}_r &\cdot & [\mathbf{B}(r=a_+) - \mathbf{B}(r=a_-)] = 0
\end{aligned} \tag{B.13}$$

The magnetic field is then given by,

$$\mathbf{H}(r,\theta) = \begin{cases} \frac{Ni}{3b}\left(\frac{3\mu_0}{2\mu_0+\mu_a}\right)\mathbf{i}_z & ;\, r < a \\ \frac{Ni}{3b}\left[\cos\theta\left(1 + \frac{2a^3}{r^3}\frac{\mu_a-\mu_0}{2\mu_0+\mu_a}\right)\mathbf{i}_r - \sin\theta\left(1 - \frac{a^3}{r^3}\frac{\mu_a-\mu_0}{2\mu_0+\mu_a}\right)\mathbf{i}_\theta\right] & ;\, a < r < b \\ \frac{Nib^2}{3r^3}\left[\frac{1}{2} + \frac{a^3}{b^3}\frac{\mu_a-\mu_0}{2\mu_0+\mu_a}\right](2\cos\theta\mathbf{i}_r + \sin\theta\mathbf{i}_\theta) & ;\, r > b \end{cases} \tag{B.14}$$

where again the solution in the innermost region is a uniform z-directed magnetic field and the outermost region has a dipole field decay with magnetic moment $\mathbf{m} = 4\pi\frac{Ni}{3}\left(\frac{1}{2} + \frac{a^3}{b^3}\frac{\mu_a-\mu_0}{2\mu_0+\mu_a}\right)\mathbf{i}_z$. The field in the region $a < r < b$ has both uniform and dipole magnetic field components.

B.2.2 Constant flux condition

Rather than hold the current i constant, to compute the change in energy the flux linkage λ must be held constant. This insures that the system under consideration is isolated so that no additional electrical energy goes through the terminals from a source when the magnetizable sphere is introduced.

$$\lambda_0 = \lambda \tag{B.15}$$

Initially, before the introduction of a sphere of magnetic material into the flux ball, the magnetic flux linked by a coil loop on the spherical shell located at an angle θ is simply given by the product of the uniform flux density inside the sphere ($r < b$) and the area of a circle with radius $b\sin\theta$,

$$\Phi_0(\theta) = \mu_0|\mathbf{H}_0(r<b,\theta)|^2\left[\pi(b\sin\theta)^2\right] = \mu_0\frac{Ni_0}{3b}\pi b^2\sin^2\theta \tag{B.16}$$

The total flux linkage is the integral of flux per coil multiplied by the coil density integrated over the whole shell, as given by the expression,

$$\lambda_0 = \int_0^\pi \Phi_0(\theta)\frac{N}{2}\sin\theta d\theta = \int_0^\pi \mu_0\frac{N^2}{6}i_0\pi b\sin^3 d\theta = \frac{2\pi b}{9}\mu_0 N^2 i_0 \tag{B.17}$$

Similarly, after the introduction of a sphere of magnetic material inside the flux ball we integrate the magnetic fields given by Eq. B.14 to find the flux linked by the flux ball winding,

$$\begin{aligned}\Phi(\theta) &= \int_{\phi=0}^{2\pi}\int_0^\theta \mu_0\{\mathbf{H}(r=b)\cdot\mathbf{i}_r\}b^2\sin\theta' d\theta' d\phi \\ &= \pi b\mu_0\frac{Ni}{3}\left(1+\frac{2a^3}{b^3}\frac{\mu_a-\mu_0}{2\mu_0+\mu_a}\right)\sin^2\theta \end{aligned}\tag{B.18}$$

The flux linkage is given by,

$$\lambda = \int_0^{\pi} \Phi(\theta)\frac{N}{2}\sin\theta d\theta = \frac{2\pi}{9}b\mu_0\left(1+\frac{2a^3}{b^3}\frac{\mu_a-\mu_0}{2\mu_0+\mu_a}\right)N^2 i \tag{B.19}$$

The constraint that $\lambda = \lambda_0$ relates the currents as,

$$i = \frac{1}{1+2\frac{a^3}{b^3}\frac{\mu_a-\mu_0}{2\mu_0+\mu_a}}i_0 \tag{B.20}$$

As a check, note that $\lambda = \lambda_0$ and $i = i_0$ when $\mu_a = \mu_0$.

B.2.3 Mechanical work

The difference in the total energy stored in this electrically isolated system equals the mechanical work required to move the magnetic material from the zero magnetic field region far away from the flux ball to the uniform magnetic field region inside the flux ball.

$$\Delta W = W - W_0 \tag{B.21}$$

where W corresponds to the energy stored in the magnetic field after the introduction of the magnetic material inside the flux ball. This field is described by the solution in Eq. B.14 which must be integrated over all space,

$$W = \tfrac{1}{2}\left(\mu_a|\mathbf{H}(r<a,\theta)|^2\right)\tfrac{4}{3}\pi a^3 + \pi\int_0^{\pi}\left[\int_a^b \mu_0|\mathbf{H}(r,\theta)|^2 r^2\sin\theta dr + \int_b^{\infty}\mu_0|\mathbf{H}(r,\theta)|^2 r^2\sin\theta dr\right]d\theta \tag{B.22}$$

The magnetic energy stored in the magnetic fields of Eq. B.11, where the magnetic material is far away from the magnetic field of the flux ball is given by,

$$W_0 = \frac{1}{2}\left[\left(\mu_0|\mathbf{H}_0(r,\theta)|^2\right)\frac{4}{3}\pi b^3 + 2\pi\int_{\theta=0}^{\pi}\int_{r=b}^{\infty}\mu_0|\mathbf{H_0}(r,\theta)|^2 r^2\sin\theta dr d\theta\right] \tag{B.23}$$

Integrating the expressions for W and W_0 and substituting into Eq. B.21 yields,

$$\Delta W = \frac{-2a^3b^3\mu_0\left(\mu_a-\mu_0\right)\pi}{2a^3(\mu_a-\mu_0)+b^3(2\mu_0+\mu_a)}\left(\frac{Ni_0}{3b}\right)^2 \tag{B.24}$$

where the relationship between i and i_0 given by Eq. B.20 was substituted into Eqs. B.22-B.24. Note that this result is identical to the answer given by applying the Paris and Hurd formula of Eq. B.4 to the flux ball problem using the field solutions in Eqs. B.14 and B.11,

$$\Delta W = -\frac{1}{2}\int_{V_a}(\mu_a - \mu_0)\mathbf{H}\cdot\mathbf{H}_0 dv = \frac{-2a^3 b^3 \mu_0\,(\mu_a - \mu_0)\,\pi}{2a^3(\mu_a - \mu_0) + b^3(2\mu_0 + \mu_a)}\left(\frac{Ni_0}{3b}\right)^2 \tag{B.25}$$

Furthermore, taking the limit of the result in Eq. B.24 as $b \longrightarrow \infty$, $\frac{Ni_0}{3b} \longrightarrow H_0$ leads to the expression,

$$\Delta W = -\frac{2\pi a^3 \mu_0(\mu_a - \mu_0)H_0^2}{(2\mu_0 + \mu_a)} \tag{B.26}$$

which agrees with the expression for the amount of work required to introduce a sphere of magnetizable material with permeability μ_a into a uniform magnetic field H_0 computed by Paris and Hurd using Eq. B.4.

B.3 Nonlinear magnetic material

In this section we follow the same procedure as outlined in Sec. B.2 to find the magnetic fields before and after the introduction of a sphere of non-linear magnetic material. We begin by solving the three-region problem illustrated in Fig. B-2 where the innermost sphere consists of a non-linear magnetic material with a magnetization curve that follows the Langevin relation (Eq. B.33). The flux density in this problem is given by,

$$\mathbf{B} = \begin{cases} \mu_0(\mathbf{M} + \mathbf{H}) & ; r < a \\ \\ \mu_0\mathbf{H} & ; r > a \end{cases} \tag{B.27}$$

We then use the field solution to compute the change in the energy of the flux ball system after the magnetic material is introduced inside the flux ball.

B.3.1 Magnetic field solution

In the absence of volume current flow ($\mathbf{J} = 0$), the magnetic field intensity remains curl-free. Therefore, a scalar potential ψ exists and can be defined similar to the linear case in Section B.2.1

$$\nabla \times \mathbf{H} = 0 \longrightarrow \mathbf{H} = -\nabla\psi \tag{B.28}$$

The magnetic flux density must always have zero divergence according to Gauss' law,

$$\nabla \cdot \mathbf{B}(H) = 0 \tag{B.29}$$

where, unlike the derivation in Sec. B.2.1, we no longer restrict the constitutive relationship between **B** and **H** to be linear,

$$\mathbf{B} = \mu_0(\mathbf{M}(H) + \mathbf{H}) \tag{B.30}$$

Substitution of the constitutive relationship (Eq. B.30) into Eq. B.29 yields,

$$(\nabla \cdot \mathbf{M}(H) + \nabla \cdot \mathbf{H}) = 0 \tag{B.31}$$

The divergence of $\mathbf{M}(H)$ in the first term in Eq. B.31 generally takes a nonzero value over a region of space unless the magnetic field intensity is uniform in that region. In the sphere of material inside the flux ball the magnetic field intensity has to be spatially uniform and z-directed by symmetry regardless of whether the sphere's magnetic material is linear or non-linear ($i.e.$, $\mathbf{H}(r < a, \theta) = H_a\mathbf{i}_z$). Consequently, the magnetization of the sphere is also uniform and z-directed $\mathbf{M} = M_a\mathbf{i}_z$. Thus, in the case of the flux ball problem, Laplace's equation applies in the sphere of non-linear magnetic material as well as in the free space regions,

$$\nabla \cdot \mathbf{M} = 0, \nabla \cdot \mathbf{H} = 0 \longrightarrow \nabla^2\psi = 0 \tag{B.32}$$

The non-linear magnetization characteristic $\mathbf{M}(H_a)$ of the sphere is modeled by the Langevin relation,

$$\mathbf{M}(H_a) = M_a(H_a)\mathbf{i}_z = M_s\left(\coth(\beta H_a) - \frac{1}{\beta H_a}\right)\mathbf{i}_z \tag{B.33}$$

where M_s is the saturation magnetization and $\beta = \frac{\mu_0 M_s}{nkT}$, with n equal to the number of magnetic dipoles per unit volume, k the Boltzmann constant, and T is the absolute temperature in Kelvin.

The solution to the field problem with non-linear material must satisfy the boundary conditions,

$$\begin{aligned}
\mathbf{i}_r &\times [\mathbf{H}(r=b_+) - \mathbf{H}(r=b_-)] = & \tfrac{Ni}{2b}\sin\theta\mathbf{i}_\phi \\
\mathbf{i}_r &\cdot [\mathbf{B}(r=b_+) - \mathbf{B}(r=b_-)] = & 0 \\
\mathbf{i}_r &\times [\mathbf{H}(r=a_+) - \mathbf{H}(r=a_-)] = & 0 \\
\mathbf{i}_r &\cdot (\mathbf{B}(r=a_+) - \mathbf{B}(r=a_-)) = & 0
\end{aligned} \tag{B.34}$$

The solution to Laplace's equation and to the boundary conditions in terms of the operating value of uniform magnetization of the inner sphere M_a is,

$$\mathbf{H}(r,\theta) = \begin{cases} \left(\frac{Ni}{3b} - \frac{M_a}{3}\right)\mathbf{i}_z & ; r < a \\ \cos\theta\left(\frac{Ni}{3b} + \frac{2a^3}{3r^3}M_a\right)\mathbf{i}_r - \sin\theta\left(\frac{Ni}{3b} - \frac{a^3}{3r^3}M_a\right)\mathbf{i}_\theta & ; a < r < b \\ \frac{b^3}{3r^3}\left(\frac{Ni}{2b} + \frac{a^3}{b^3}M_a\right)(2\cos\theta\mathbf{i}_r + \sin\theta\mathbf{i}_\theta) & ; r > b \end{cases} \tag{B.35}$$

Note that this solution is the superposition of the fields of the flux ball current winding and a uniformly z-directed magnetized sphere of radius a.

To find the operating value of the magnetization of the non-linear magnetic material M_a, we note that the magnetic field intensity inside the sphere of material is

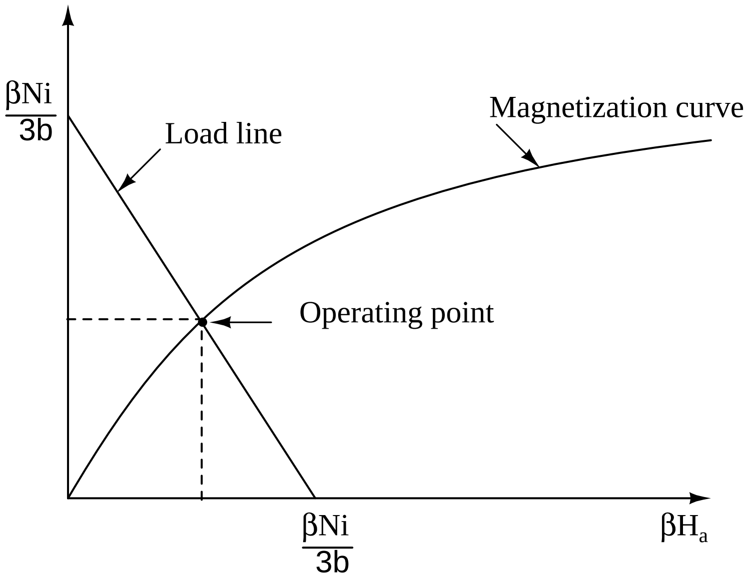

Figure B-3: Graphical solution to the transcendental relation in Eq. B.37. A non-linear magnetic material with a Langevin magnetization characteristic is introduced into the uniform field region inside a flux ball.

related to the externally applied magnetic field intensity $\frac{Ni}{3b}$ by the expression,

$$\mathbf{H}(r < a, \theta) = H_a \mathbf{i}_z = \left[\frac{Ni}{3b} - \frac{M_a(H_a)}{3} \right] \mathbf{i}_z \tag{B.36}$$

Substitution of the constitutive relation of Eq. B.33 in Eq. B.36 leads to the non-dimensional equation,

$$\beta \left(\frac{Ni}{3b} - H_a \right) = \chi_m \left(\coth \beta H_a - \frac{1}{\beta H_a} \right) \tag{B.37}$$

where the magnetic susceptibility $\chi_m = \frac{\beta M_s}{3}$ is the Langevin susceptibility at low magnetic fields. Eq. B.37 is transcendental and has no closed form solution. It can, however, be easily solved graphically or numerically for βH_a and the corresponding value of $M_a(\beta H_a)$. The left hand side of the equation is a linear function of βH_a and is called the load line, whereas the right hand side is a non-linear function of βH_a and is called the magnetization curve. Fig. B-3 illustrates a graphical solution method where the left-hand and right hand sides of Eq. B.37 are plotted separately as functions of βH_a. Eq. B.37 can also be solved numerically by iteration. Once the magnetization M_a inside the sphere of non-linear material is known, it can be substituted into Eq. B.35 to find the magnetic field everywhere in space. Fig. B-4 shows the plots of the magnetic field intensity inside the sphere of magnetic material as a function of externally applied magnetic field intensity for room temperature water-based, oil-based and fluorocarbon based ferrofluids. As expected, the predictions of the linear and non-linear magnetization models are near identical for low values of applied magnetic field and differ for higher applied field intensities as the Langevin curve approaches saturation.

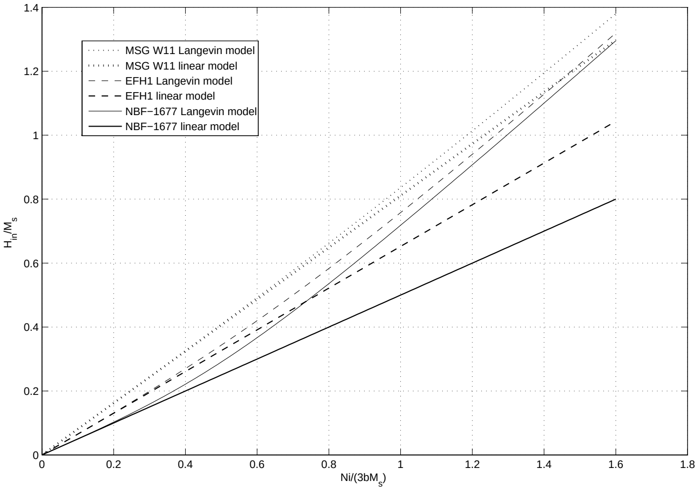

Figure B-4: The intensity of the uniform magnetic field inside the sphere of magnetic material in the flux ball system (these results are independent of the non-dimensional geometric parameter $\frac{a}{b}$) for linear (solid line) and non-linear (dashed line) Langevin magnetization models as a function of applied external magnetic field. The linear and non-linear model-predicted curves converge for low intensities of applied magnetic field and differ for higher applied magnetic field intensities as expected for room temperature MSG W11 water-based, EFH1 oil-based, and fluorocarbon-based ferrofluid.

B.3.2 Constant flux condition

To ensure that the system under consideration is isolated we have set the current before and after the introduction of the non-linear material so that the flux linked by the flux ball winding remains constant,

$$\lambda_0 = \lambda. \tag{B.38}$$

In Sec. B.2.2, Eq. B.17 we showed that before the introduction of a sphere of magnetic material into the flux ball, the flux linkage is given by the expression,

$$\lambda_0 = \int_0^\pi \Phi_0(\theta)\frac{N}{2}\sin\theta d\theta = \frac{2\pi b}{9}\mu_0 N^2 i_0 \tag{B.39}$$

Similarly, after the introduction of a sphere of non-linear magnetic material inside the flux ball we integrate the magnetic fields given by Eq. B.35 to find the flux linked by the flux ball winding,

$$\Phi(\theta) = \int_{\phi=0}^{2\pi}\int_0^\theta \mu_0 \mathbf{i}_r \cdot \mathbf{H}(r=b) b^2 \sin\theta' d\theta' d\phi = \pi b^2 \mu_0 \left(\frac{Ni}{3b} + \frac{2a^3}{3b^3}M_a\right)\sin^2\theta \tag{B.40}$$

The flux linkage is given by,

$$\lambda = \int_0^\pi \Phi(\theta)\frac{N}{2}\sin\theta d\theta = \frac{2}{3}\mu_0 N\pi b^2 \left(\frac{Ni}{3b} + \frac{2a^3}{3b^3}M_a\right) \tag{B.41}$$

The constraint that $\lambda = \lambda_0$ leads to,

$$i_0 = i + \frac{2a^3}{b^2 N}M_a \tag{B.42}$$

Note that this result reduces to Eq. B.20 in the linear limit where $M_a = \frac{3(\mu_a - \mu_0)}{2\mu_0 + \mu_a}\frac{Ni}{3b}$.

B.3.3 Mechanical work

The energy density w_a for a non-linear material with a Langevin magnetization characteristic is given by the expression,

$$\begin{aligned} w_a &= \int_0^B \mathbf{H}\cdot d\mathbf{B} = \mathbf{B}\cdot\mathbf{H} - \int_0^H \mathbf{B}\cdot d\mathbf{H} \\ &= B_a H_a - \mu_0 \int_0^{H_a}\left[H_a + M_s\left(\coth(\beta H_a) - \frac{1}{\beta H_a}\right)\right] dH_a \end{aligned} \tag{B.43}$$

Eq. B.43 integrates to the energy density inside the sphere of non-linear magnetic material. The energy density outside the sphere is the usual expression for free space, so that the energy density as a function of r is given by the expression,

$$w(r) = \begin{cases} \frac{\mu_0 H_a^2}{2} + \mu_0 H_a M_a - \frac{\mu_0 M_s}{\beta} \ln\left(\frac{\sinh \beta H_a}{\beta H_a}\right) & ; r < a \\ \\ \frac{1}{2}\mu_0 |\mathbf{H}(r > a, \theta)|^2 & ; r > a \end{cases} \tag{B.44}$$

Thus the value of βH_a found by solving Eq. B.37 also determines the energy density in the nonlinear material. Once the magnetic field is known for all r, the total energy can be computed by integrating the magnetic energy density over all space.

$$W = w_a\left(\tfrac{4}{3}\pi a^3\right) + 2\pi \int_0^\pi \tfrac{1}{2}\mu_0 \left[\int_a^b |\mathbf{H}(r > a, \theta)|^2 r^2 dr + \int_b^\infty |\mathbf{H}(r > b, \theta)|^2 r^2 dr\right] \sin\theta d\theta \tag{B.45}$$

The total energy after the introduction of the magnetic material is given by,

$$W = -\mu_0 \frac{\pi}{9}\left[2a^3 M_a (M_a - 2\frac{Ni}{b}) - b\,(Ni)^2 + 4a^3 \frac{M_s^2}{\chi_m} \ln\left(\frac{\sinh \beta H_a}{\beta H_a}\right)\right] \tag{B.46}$$

From Eq. B.23 the total energy before the introduction of the magnetic material is given by,

$$W_0 = \frac{1}{9}\mu_0 \pi b N^2 i_0^2 \tag{B.47}$$

The difference in energy yields the mechanical work necessary to introduce a ball of non-linear magnetic material into the uniform field region of a flux ball,

$$\Delta W = -\frac{2}{9}\pi a^3 \left[\mu_0 \left(1 + 2\frac{a^3}{b^3}\right) M_a^2 + \frac{2\mu_0 M_s^2}{\chi_m} \ln\left(\frac{\sinh \beta H}{\beta H}\right)\right] \tag{B.48}$$

Note that as expected this expression reduces to Eq. B.24 in the linear limit where $M_a = \frac{3(\mu_a - \mu_0)}{2\mu_0 + \mu_a}\frac{Ni}{3b}$. Fig. B-5 shows a comparison of the total energy stored in the flux ball system as a function of applied magnetic field intensity for non-linear and linear models of the three different types of ferrofluids we use in our experiments. Again, the predictions of the linear and non-linear models agree for low values of applied magnetic field intensity and differ for higher values of applied field.

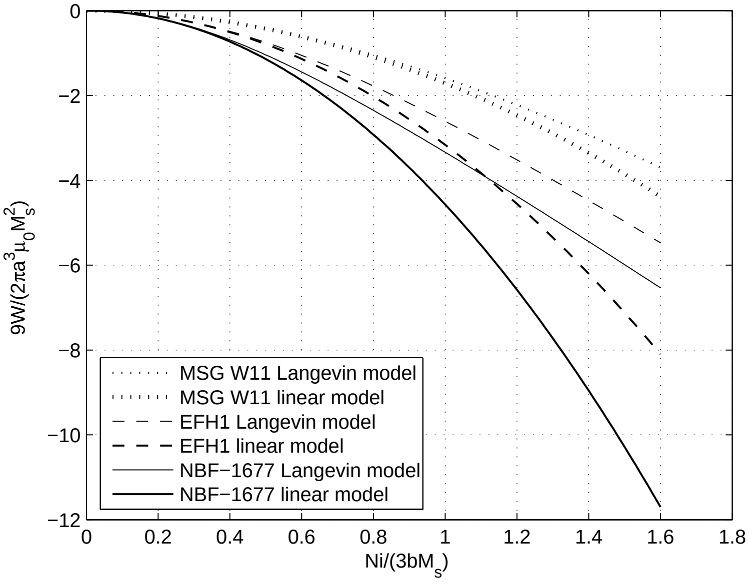

Figure B-5: The energy stored in the flux ball system (with $\frac{a}{b} = \frac{1}{4}$) for linear (solid line) and non-linear (dashed line) magnetization models. The top pair of curves corresponds to water-based ferrofluid, the middle pair to oil-based ferrofluid and the bottom pair to fluorocarbon based ferrofluid. As expected the non-linear model-predictions agree with the linear model predictions for low intensities of applied magnetic field.

The change in energy due the introduction of a non-linear magnetic material of volume V_a can also be computed by the following integral over the finite volume V_a,

$$\Delta W = -\frac{1}{2}\int_{V_a}\left(\mathbf{H}_0\cdot\mathbf{B} - \mathbf{H}\cdot\mathbf{B}_0 + \mathbf{H}\cdot\mathbf{B} - 2\int_0^B \mathbf{H}\cdot d\mathbf{B}\right)dv \tag{B.49}$$

The derivation of this result is included in Sec. B.4. For the flux ball problem the general expression of Eq. B.49 simplifies to,

$$\Delta W = -\frac{1}{2}\int_{V_a}\left(\mu_0(H_0 - H_a)M_a + 2\mu_0\int_0^{H_a} M_a dH_a\right)dv \tag{B.50}$$

Using the field solutions in Eq. B.35 and the condition set by Eq. B.42 the expression for energy difference ΔW evaluates to,

$$\Delta W = -\frac{1}{2}\left[\frac{1}{3}\mu_0 M_a^2\left(2\frac{a^3}{b^3}+1\right)+\frac{\mu_0 M_s^2}{3\chi_m}\ln\left(\frac{\sinh\beta H_a}{\beta H_a}\right)\right]\frac{4}{3}\pi a^3 \tag{B.51}$$

This result agrees with the result obtained by integrating the energy density over all space given by Eq. B.48. Furthermore, in the limit of $b \longrightarrow \infty$ and $\frac{Ni_0}{3b} \longrightarrow H_0$, the constant flux condition in Eq. B.42 becomes,

$$i = i_0 \tag{B.52}$$

Consequently, the transcendental relation in Eq. B.37 becomes,

$$\beta\left(H_0 - H_a\right) = \chi_m\left(\coth\beta H_a - \frac{1}{\beta H_a}\right) \tag{B.53}$$

The energy needed to introduce a sphere of non-linear Langevin magnetic material of radius a into an infinite z-directed uniform field H_0 is,

$$\Delta W = -\frac{1}{2}\left[\frac{1}{3}\mu_0 M_a^2+\frac{\mu_0 M_s^2}{3\chi_m}\ln\left(\frac{\sinh\beta H_a}{\beta H_a}\right)\right]\frac{4}{3}\pi a^3 \tag{B.54}$$

This expression also reduces to Eq. B.26 in the linear limit where $M_a = \frac{3(\mu_a-\mu_0)}{2\mu_0+\mu_a}\frac{Ni}{3b}$ and H_a is given by Eq. B.5 for $r < a$.

B.4 Energy considerations in non-linear magnetic media

In this section we consider the amount of work required to introduce a material with a non-linear magnetization characteristic into the field of a fixed distribution of short-circuited, current-carrying loops of perfectly conducting wires. Each perfectly conducting short-circuited loop links a constant magnetic flux regardless of the configuration of magnetic materials and other sources of magnetic field in the system. With constant flux the system remains thermodynamically isolated and no power flows through the electrical terminals when the configuration of the magnetic materials changes.

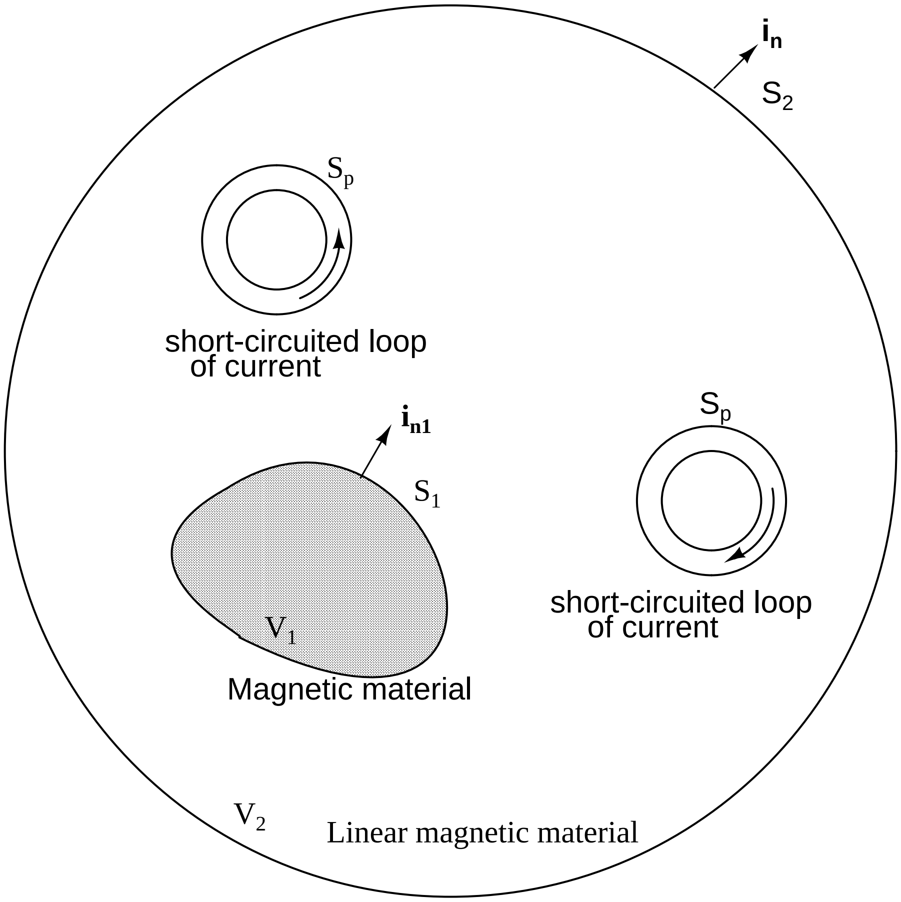

Figure B-6: Schematic for change in energy calculations when linear or non-linear magnetizable media with volume V_1 is introduced into a volume V_2 of linear media. In order to impose a constant flux constraint the sources of magnetic field are short-circuited current loops while the current density $\mathbf{J} = 0$ in the volume.

Fig. B-6 shows a volume V_1 of non-linear magnetic material that was introduced into a region of linear magnetic material V_2 with short-circuited current-carrying loops of perfectly conducting material. The flux linkages of such magnetic field sources are fixed. The energy before the introduction of the magnetic material is given by the integral expression,

$$W_1 = \frac{1}{2} \int_V \mathbf{H}_1 \cdot \mathbf{B}_1 dv \tag{B.55}$$

where $V = V_1 + V_2$; $\mathbf{H}_1 = -\nabla \psi_1$ and $\mathbf{B}_1 = \mu_0 \mathbf{H}_1$ represent the initial field variables.

After the introduction of the magnetic substance the energy is given by,

$$W_2 = \frac{1}{2}\int_{V_2} \mathbf{H}\cdot\mathbf{B}dv + \int_{V_1}\left\{\int_0^B \mathbf{H}\cdot d\mathbf{B}\right\}dv \tag{B.56}$$

where $\mathbf{H} = -\nabla\psi$ and $\mathbf{B}$ represent the new field variables. The energy change resulting from the introduction of the magnetic substance is,

$$\begin{aligned} \Delta W &= W_2 - W_1 \\ &= \frac{1}{2}\int_{V_2}(\mathbf{H}\cdot\mathbf{B} - \mathbf{H}_1\cdot\mathbf{B}_1)dv + \int_{V_1}\left\{\int_0^B \mathbf{H}\cdot d\mathbf{B} - \frac{1}{2}\mathbf{H}_1\cdot\mathbf{B}_1\right\}dv \end{aligned} \tag{B.57}$$

The first integral term in Eq. B.57 extending over volume V_2 can be rewritten as,

$$\begin{aligned} \frac{1}{2}\int_{V_2}(\mathbf{H}\cdot\mathbf{B} - \mathbf{H}_1\cdot\mathbf{B}_1)dv &= \frac{1}{2}\int_{V_2}(\mathbf{H}+\mathbf{H}_1)\cdot(\mathbf{B}-\mathbf{B}_1)dv \\ &= -\frac{1}{2}\int_{V_2}\nabla(\psi+\psi_1)\cdot(\mathbf{B}-\mathbf{B}_1)dv \end{aligned} \tag{B.58}$$

where we recognize that in the linear material in V_2, $\mathbf{H}_1\cdot\mathbf{B} = \mathbf{H}\cdot\mathbf{B}_1$. Using the vector identity,

$$\nabla\cdot f\mathbf{A} = \mathbf{A}\cdot\nabla f + f\nabla\cdot\mathbf{A} \tag{B.59}$$

the last integral term in Eq. B.58 can be further simplified,

$$\begin{aligned} -\tfrac{1}{2}\textstyle\int_{V_2} & \nabla(\psi+\psi_1)\cdot(\mathbf{B}-\mathbf{B}_1)dv \\ = \quad & \frac{1}{2}\int_{V_2}\left\{(\psi+\psi_1)\nabla\cdot(\mathbf{B}-\mathbf{B}_1) - \nabla\cdot[(\psi+\psi_1)(\mathbf{B}-\mathbf{B}_1)]\right\}dv \\ = \quad & -\frac{1}{2}\int_{V_2}\nabla\cdot[(\psi+\psi_1)(\mathbf{B}-\mathbf{B}_1)]dv \end{aligned} \tag{B.60}$$

where we have used the fact that $\nabla\cdot\mathbf{B} = 0$ and $\nabla\cdot\mathbf{B}_1 = 0$ to eliminate the $\nabla\cdot(\mathbf{B}-\mathbf{B}_1)$ term. Using the divergence theorem on the result of Eq. B.60 leads to the integral,

$$-\frac{1}{2}\int_{V_2}\nabla\cdot[(\psi+\psi_1)(\mathbf{B}-\mathbf{B}_1)]dv = -\frac{1}{2}\oint_{\Sigma}(\psi+\psi_1)(\mathbf{B}-\mathbf{B}_1)\cdot\mathbf{i}_n dS \tag{B.61}$$

where the integrand $(\psi+\psi_1)(\mathbf{B}-\mathbf{B}_1)\cdot\mathbf{i}_n$ is evaluated over the closed surface Σ which forms the boundary of volume V_2, including the surface S_1 which bounds the volume V_1, the surfaces S_p, bounding the current source coils, and the outer surface S_2. If the outer boundary S_2 expands to infinity so as to include all space, the integrand vanishes faster than the surface area and the integral goes to zero. The integrand over the surfaces S_p, bounding the current-carrying loops, vanishes because $(\mathbf{B} - \mathbf{B}_1) \cdot \mathbf{i}_n = 0$ on S_p since the normal component of the magnetic flux density must always be zero on the surface of a perfect conductor. The only remaining non-zero term is the surface integral over S_1,

$$-\frac{1}{2}\oint_{\Sigma} (\psi + \psi_1)(\mathbf{B} - \mathbf{B}_1) \cdot \mathbf{i}_n dS = \frac{1}{2}\int_{S_1} (\psi + \psi_1)(\mathbf{B} - \mathbf{B}_1) \cdot \mathbf{i}_{n1} dS \tag{B.62}$$

where we note that $\mathbf{i}_{n1}$, the positive normal to the surface S_1, points in the opposite direction from the normal $\mathbf{i}_n$ to surface Σ.

Using the divergence theorem to write Eq. B.62 as a volume integral over V_1 leads to the expression,

$$\frac{1}{2}\int_{S_1} (\psi + \psi_1)(\mathbf{B} - \mathbf{B}_1) \cdot \mathbf{i}_{n1} dS = \frac{1}{2}\int_{V_1} \nabla \cdot \{(\psi + \psi_1)(\mathbf{B} - \mathbf{B}_1)\} dv \tag{B.63}$$

The geometric identity in Eq. B.59 can be used to rewrite the integral over V_1,

$$\tfrac{1}{2}\textstyle\int_{V_1} \nabla \cdot (\psi + \psi_1)(\mathbf{B} - \mathbf{B}_1) dv = \tfrac{1}{2}\textstyle\int_{V_1} \{(\mathbf{B} - \mathbf{B}_1) \cdot \nabla(\psi + \psi_1) + (\psi + \psi_1)\nabla \cdot (\mathbf{B} - \mathbf{B}_1)\} dv \tag{B.64}$$

The integrand of the second term in this expression $\nabla \cdot (\mathbf{B} - \mathbf{B}_1)$ is zero and $\nabla(\psi + \psi_1) = -(\mathbf{H} + \mathbf{H}_1)$. This leads to rewriting the first term in Eq. B.57 as an integral over volume V_1,

$$\frac{1}{2}\int_{V_2} (\mathbf{H} \cdot \mathbf{B} - \mathbf{H}_1 \cdot \mathbf{B}_1) dv = -\frac{1}{2}\int_{V_1} (\mathbf{B} - \mathbf{B}_1) \cdot (\mathbf{H} + \mathbf{H}_1) dv \tag{B.65}$$

Returning to the expression for the energy difference in Eq. B.57, we can use the relation in Eq. B.65 to rewrite ΔW in terms of an integral over V_1,

$$\Delta W = -\frac{1}{2}\int_{V_1}\left\{(\mathbf{B}-\mathbf{B}_1)\cdot(\mathbf{H}+\mathbf{H}_1) - \left(2\int_0^B \mathbf{H}\cdot d\mathbf{B} - \mathbf{H}_1\cdot\mathbf{B}_1\right)\right\} dv \tag{B.66}$$

The resulting expression for the energy required to introduce the magnetic substance is given by the following integral over the volume V_1,

$$\Delta W = -\frac{1}{2}\int_{V_1}\left\{\mathbf{H_1}\cdot\mathbf{B} - \mathbf{H}\cdot\mathbf{B}_1 + \mathbf{H}\cdot\mathbf{B} - 2\int_0^B \mathbf{H}\cdot d\mathbf{B}\right\} dv \tag{B.67}$$

Note that although Eq. B.67 was derived for fields excited by a configuration of perfectly-conducting, current-carrying short-circuited loops the result holds for any thermodynamically isolated magnetic system (*i.e.*, the flux at the electrical terminals is held constant). The integration in Eq. B.67 extends over a finite volume of space, unlike Eq. B.57 where the integration is over all space, which greatly facilitates the computation of energy in problems of interest, especially when studying ferrofluids in applied magnetic fields.

The derivation in this section and final expression in Eq. B.67 mirror the derivation and expression for the “Co-energy of a Magnetic body in a Magnetostatic Field” by Stratton [47]. Stratton’s expression for the co-energy change is given by,

$$\Delta W' = \frac{1}{2}\int_{V_1}\left\{\mathbf{H_1}\cdot\mathbf{B} - \mathbf{H}\cdot\mathbf{B}_1 - \mathbf{H}\cdot\mathbf{B} + 2\int_0^B \mathbf{H}\cdot d\mathbf{B}\right\} dv \tag{B.68}$$

Appendix C

Taylor-Couette flow measurement and verification of the DOP2000 ultrasound velocimeter

C.1 Theory

We used the DOP2000 ultrasound velocimeter to measure the flow of a viscous fluid between two long concentric cylinders as illustrated in Figure C-2. The fluid is driven by the rotation of the inner cylinder while the outer cylinder remains stationary. This flow is known as Taylor-Couette flow and for low Reynolds numbers it has the velocity distribution given by the analytical expression [48],

$$\mathbf{V}_\phi(r) = \Omega R_i \frac{\frac{R_o}{r} - \frac{r}{R_o}}{\frac{R_o}{R_i} - \frac{R_i}{R_o}} \mathbf{i}_\phi \tag{C.1}$$

C.2 Experimental setup

The ultrasound probe is inserted into the outer cylinder wall at an angle $\alpha = 25°$ from radial direction $\mathbf{i}_r$. The probe issues an ultrasonic beam and measures the component of fluid velocity parallel to the direction of the beam at every point along the beam. From Figure C-2 we see that the radius r at a point on the ultrasound beam path is

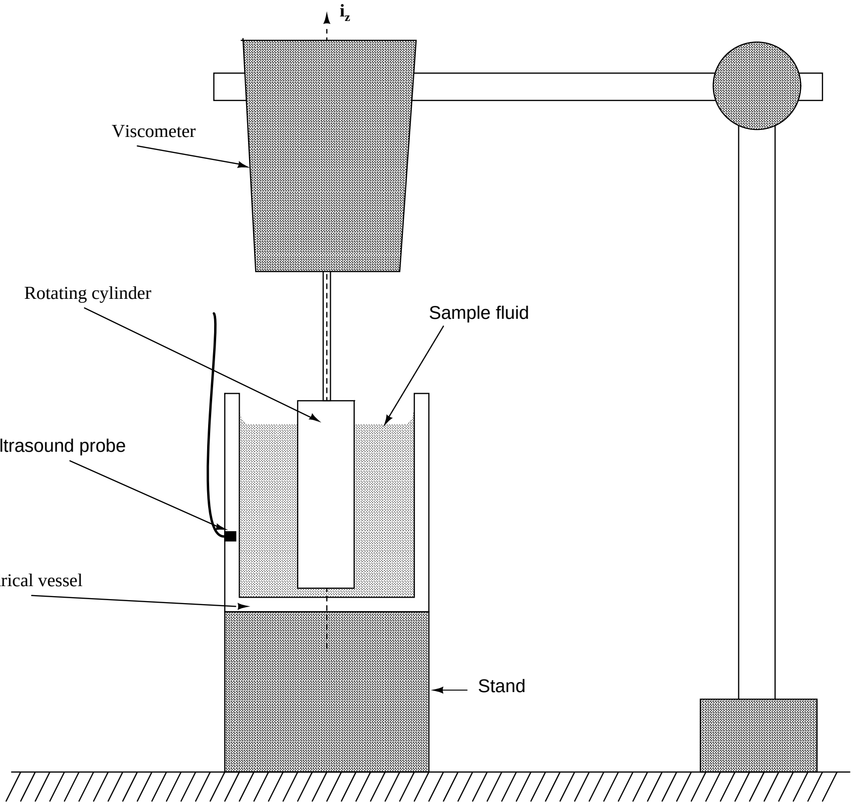

Figure C-1: Experimental apparatus for Taylor-Couette flow measurement with ultrasound velocimeter.

given by,

$$r = \sqrt{(x^2 + (R_o \sin\alpha)^2)} \tag{C.2}$$

and the direction vector $\mathbf{i}_\phi$ at a point on the ultrasound beam path is given by,

$$\mathbf{i}_\phi = \frac{-R_o \sin\alpha}{r}\mathbf{i}_x + \frac{x}{r}\mathbf{i}_y \tag{C.3}$$

To obtain the velocity component parallel to the ultrasound beam, we substitute relationships C.2 and C.3 into Eq. C.1, which leads to the expression

$$\mathbf{V}_x(x) = -\frac{\Omega R_i R_o \sin\alpha}{\frac{R_o}{R_i} - \frac{R_i}{R_o}} \left(\frac{R_o}{(x^2 + (R_o \sin\alpha)^2)} - \frac{1}{R_o} \right) \mathbf{i}_x \tag{C.4}$$

where $\mathbf{V}_x(x)$ is the component of the fluid velocity measured by the ultrasound probe.

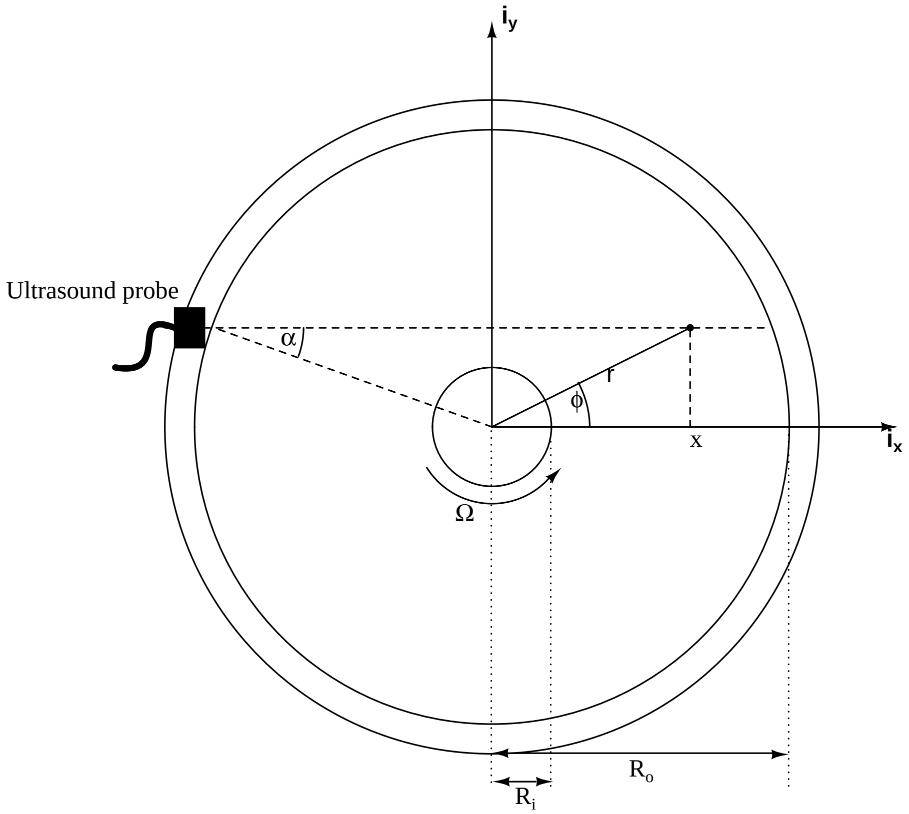

Figure C-2: Taylor-Couette geometry for flow profile measurement experiment. The inner cylinder rotates and drives the fluid flow whereas the outer cylinder remains stationary.

C.3 Experimental results

We measured Taylor Couette flows with water and transformer oil. The dimensions of the experimental apparatus and physical properties of water and oil are summarized in Table C.1 for reference.

Significant inertial effects in the water flow experiments result in the disagreement between theory and experiment in Figs. C-3 to C-5. The high calculated Reynolds numbers for these experiments ($R_E = \frac{\rho \Omega R_i^2}{\eta} = 611$, 366 and 244 respectively) explain the departure from the analytical expression for a viscous-dominated flow profile predicted by Eq. C.4. The low viscosity of the water prevents us from operating the experiment at lower Reynolds number regimes without reducing the rotation rate of the inner cylinder by a factor of a hundred.

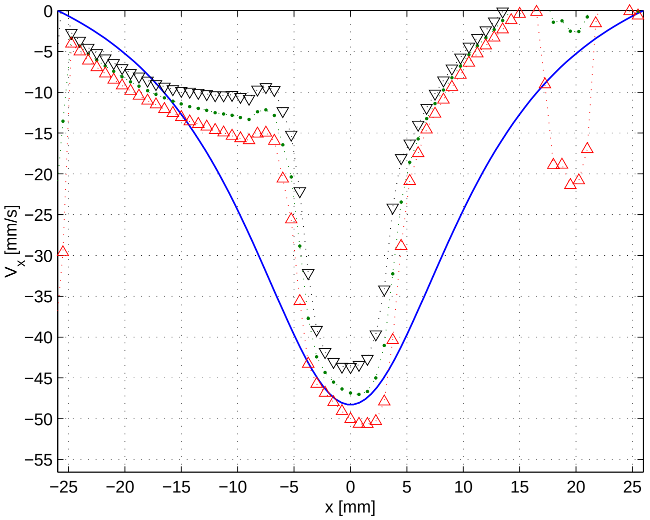

Figure C-3: Taylor-Couette flow for water between two concentric cylinders. Inner cylinder rotates at 50 rpm and outer cylinder is stationary, leading to a Reynolds number $R_E = \frac{\rho \Omega R_i^2}{\eta} = 611$. The dashed curves surrounding the time-average measured flow velocity are plus and minus one standard deviation away.

The results for the transformer oil, however, agree with the theory of Eq. C.4 better at the same rotation rates. The viscosity of the oil is 20 times that of water, which leads to lower Reynolds numbers for the same inner cylinder rotation speeds. The Reynolds numbers calculated for the velocity profiles shown in Figs C-6 to C-11

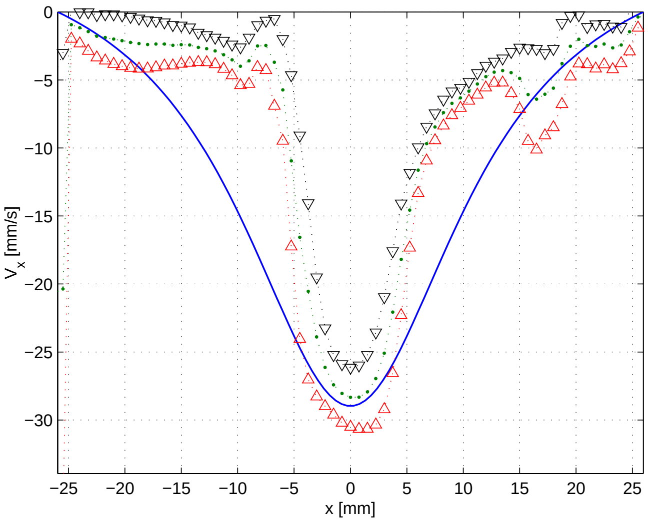

Figure C-4: Taylor-Couette flow for water between two concentric cylinders. The inner cylinder rotates at 30 rpm and the outer cylinder is stationary, leading to a Reynolds number $R_E = 366$

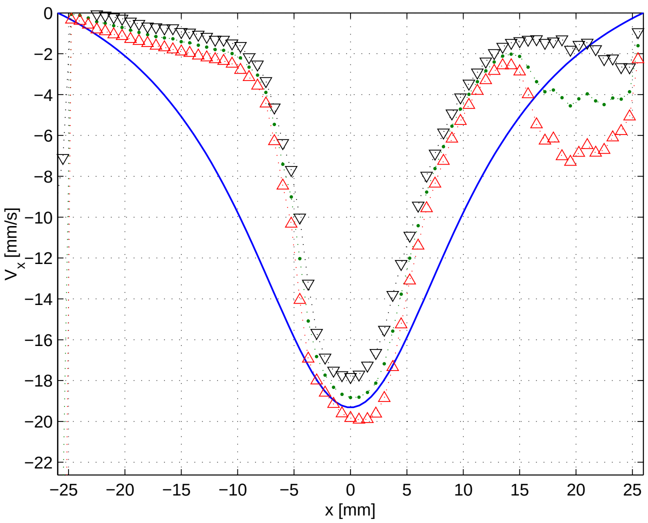

Figure C-5: Taylor-Couette flow for water between two concentric cylinders. The inner cylinder rotates at 20 rpm and the outer cylinder is stationary, leading to a Reynolds number $R_E = 244$

are $R_E = 27.5$, 16.5, 11.0, 6.60, 3.30, and 1.65 respectively. Note that the figures show that experimental data agree with theory progressively better as the Reynolds number is reduced.

Cylinder geometry		
R_i	Inner radius	10.8 [mm]
R_o	Outer radius	28.7 [mm]
α	Probe angle	25°
Water properties (room temperature)		
η	Dynamic viscosity	1.0×10^{-3} [Ns/m^2]
ρ	density	1000 [kg/m^3]
Oil properties (room temperature)		
η	Dynamic viscosity	0.020 [Ns/m^2]
ρ	density	900 [kg/m^3]

Table C.1: Summary of the dimensions of the Taylor-Couette flow experiment and material properties for water and oil at room temperature.

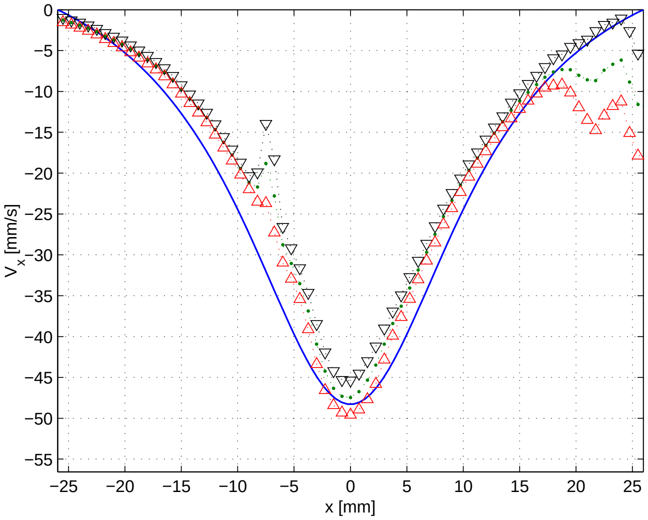

Figure C-6: Taylor-Couette flow for oil between two concentric cylinders. The inner cylinder rotates at 50 rpm and the outer cylinder is stationary, leading to a Reynolds number $R_E = 27.5$

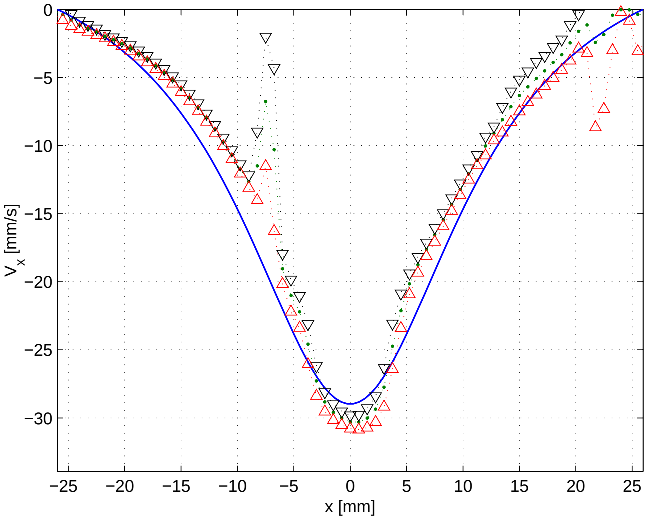

Figure C-7: Taylor-Couette flow for oil between two concentric cylinders. The inner cylinder rotates at 30 rpm and the outer cylinder is stationary, leading to a Reynolds number $R_E = 16.5$

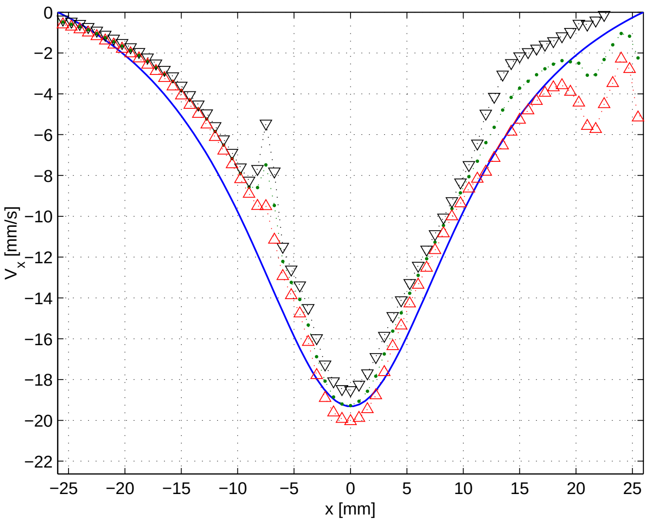

Figure C-8: Taylor-Couette flow for oil between two concentric cylinders. The inner cylinder rotates at 20 rpm and the outer cylinder is stationary, leading to a Reynolds number $R_E = 11.0$

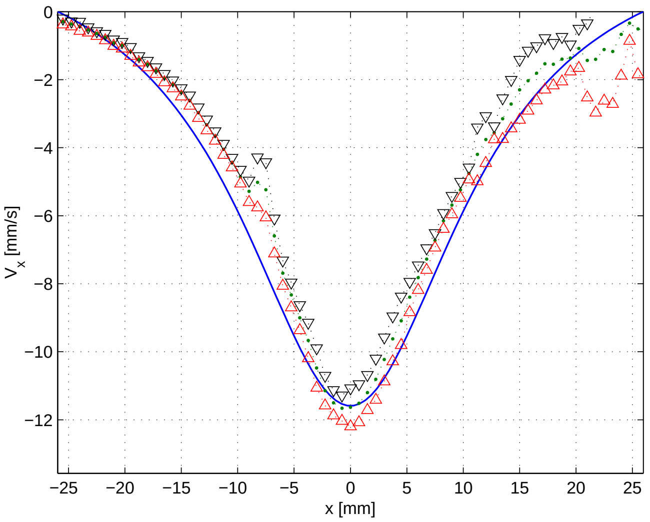

Figure C-9: Taylor-Couette flow for oil between two concentric cylinders. The inner cylinder rotates at 12 rpm and the outer cylinder is stationary, leading to a Reynolds number $R_E = 6.60$

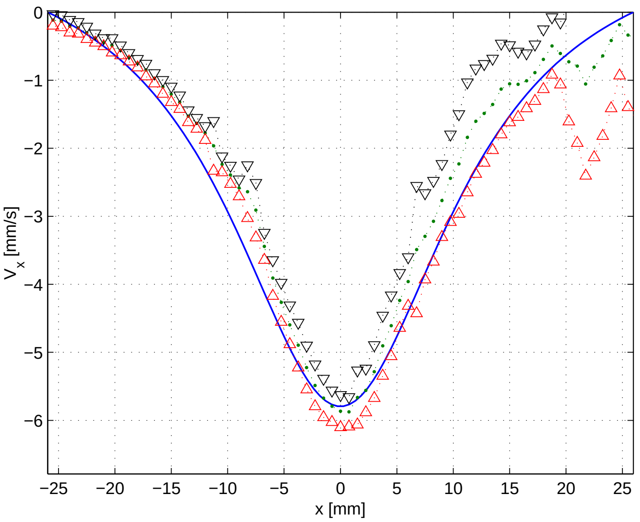

Figure C-10: Taylor-Couette flow for oil between two concentric cylinders. The inner cylinder rotates at 6 rpm and the outer cylinder is stationary, leading to a Reynolds number $R_E = 3.30$

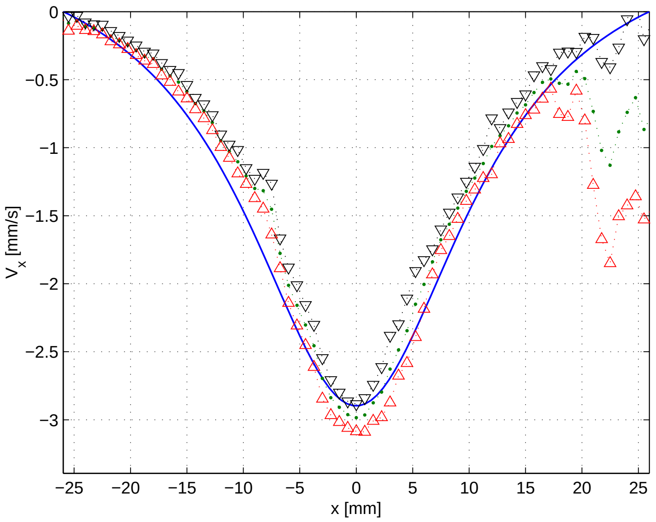

Figure C-11: Taylor-Couette flow for oil between two concentric cylinders. The inner cylinder rotates at 3 rpm and the outer cylinder is stationary, leading to a Reynolds number $R_E = 1.65$

Bibliography

[1] C. Alexiou, W. Arnold, and P. Hulin. Magnetic mitoxantrone nanoparticle detection by histology, x-ray and mri after magnetic tumor targetting. *Journal of Magnetism and Magnetic Materials*, 255:187–193, 2001.

[2] C. Alexiou, W. Arnold, and R.J. Klein. Locoregional cancer treatment with magnetic drug targetting. *Cancer Res.*, 60:6641–6648, 2000.

[3] M.S. Amin, S. Elborai, S.-H. Lee, X. He, and M. Zahn. Surface tension measurement techniques of magnetic fluids at an interface between different fluids using perpendicular field instability. *J. Appl. Phys.*, 97, 2005.

[4] J.C. Bacri, R. Perzynski, D. Salin, and A. Cebres. *Mat. Res. Soc. Symp. Proc.*, 248:241, 1992.

[5] N. Bilaniuk, S. George, and J. Wong. Speed of sound in water as a function of temperature. *Acoust. Soc. Am.*, 93:1609–1612, 1993.

[6] D. Brito, J. Aurnou, and P. Cardin. Turbulent viscosity measurements relevant to planetary core-mantle dynamics. *Physics of the Earth and Planetary Interiors*, 141:3–8, 2004.

[7] D. Brito, H.-C. Nataf, P. Cardin, J. Aubert, and J.-P. Masson. Ultrasonic doppler velocimetry in liquid gallium. *Experiments in Fluids*, 31:653–663, 2001.

[8] R. Brown and T.S. Horsnell. The wrong way round. *Electrical Review*, 183:235, 1969.

[9] A. Chaves, C. Rinaldi, S. Elborai, X. He, and M. Zahn. Bulk flow in ferrofluids in a uniform magnetic field. Accepted for publication 2006.

[10] M.D. Cowley and R.E. Rosensweig. The interfacial stability of a ferromagnetic fluid. *J. Fluid Mech.*, 80:671–688, 1967.

[11] J. Cutnell and K. Johnson. *Physics.* Wiley, New York, 1997.

[12] S. Elborai, D.-K. Kim, X. He, S.-H. Lee, S. Rhodes, and M. Zahn. Self-forming, quasi-two-dimensional, magnetic-fluid patterns with applied in-plane-rotating and dc-axial magnetic fields. *J. Appl. Phys.*, 97, 2005.

[13] T. Franklin. Ferrofluid flow phenomena. Master's thesis, MIT, 2003.

[14] H. Haus and J. Melcher. *Electromagnetic Fields and Energy.* Prentice Hall, Englewood Cliffs, NJ, 1989.

[15] X. He, S. Elborai, D.-K. Kim, S.-H. Lee, and M. Zahn. Effective magnetoviscosity of planar-couette magnetic fluid flow. *J. Appl. Phys.*, 97, 2005.

[16] I.Y. Kagan, V.G. Rykov, and E.I. Yantovskii. Flow of a dielectric ferromagnetic suspension in a rotating magnetic field. *Magnitnaya Gidrodynamika*, 9:135–137, 1973.

[17] H. Kikura, Y. Takeda, and F. Durst. Velocity profile measurement of the taylor vortex flow of a magnetic fluid using the ultrasonic doppler method. *Experiments in Fluids*, 26:208–214, 1999.

[18] D.-K. Kim, M.S. Amin, S. Elborai, S.-H. Lee, Y. Koseoglu, M. Zahn, and M. Muhammed. Energy absorption of superparamagnetic iron oxide nanoparticles by microwave irradiation. *J. Appl. Phys.*, 97, 2005.

[19] D.-K. Kim, W. Voit, W. Zapka, B. Bjelke, M. Muhammed, and K.V. Rao. Biomedical application of ferrofluids containing magnetite nanoparticles. *Mat. Res. Soc. Symp. Proc.*, 676, 2001.

[20] D.-K. Kim, Y. Zhang, J. Kehr, T. Klason, B. Bjelke, and M. Muhammed. Characterization and mri study of surfactant-coated superparamagnetic nanoparticles administered into the rat brain. *Journal of Magnetism and Magnetic Materials*, 225:256–261, 2001.

[21] D.-K. Kim, Y. Zhang, W. Voit, K.V. Rao, J. Kehr, B. Bjelke, and M. Muhammed. Superparamagnetic iron oxide nanoparticles for bio-medical applications. *Scripta mater.*, 44:1713–1717, 2001.

[22] R. Krauss, B. Reimann, R. Richter, I. Rehberg, and M. Liu. Fluid pumped by magnetic stress. *Appl. Phys. Lett.*, 86, 2005.

[23] L.D. Landau and E.M. Lifschitz. *Fluid Mechanics.* Pergamon Press, 1959.

[24] C. Lorenz and M. Zahn. Hele-shaw ferrohydrodynamics for rotating and dc axial magnetic fields. `http://pof.aip.org/pof/gallery/2003toc.jsp`.

[25] L. Mao and H. Koser. Ferrohydrodynamic pumping in spatially traveling sinusoidally time-varying magnetic fields. *Journal of Magnetism and Magnetic Materials*, 289, 2005.

[26] J. Melcher. *Continuum Electromechanics.* MIT Press, Cambridge, MA., 1981.

[27] J. Melcher and H. Haus. Field and inductance of a spherical coil. `http://ocw.mit.edu/OcwWeb/Electrical-Engineering-and-Computer-Science/6%-013Fall-2005/VideoLectures/index.htm`.

[28] S. Odenbach. Ferrofluids–magnetically controlled suspensions. *Colloids and Surfaces A: Physicochem. Eng. Aspects*, 217:171–178, 2003.

[29] J.A. Osborn. Demagnetizing factors of the general ellipsoid. *Phys. Rev.*, 67:351–357, 1945.

[30] D.T. Paris and F.K. Hurd. *Basic Electromagnetic Theory.* McGraw-Hill Book Company, Inc., 1969.

[31] A.F. Pshenichnikov and A.V. Lebedev. Tangential stresses on the magnetic fluid boundary and the rotational effect. *Magnetohydrodynamics*, 36:254–262, 2000.

[32] A.F. Pshenichnikov, A.V. Lebedev, and M.I. Shliomis. On the rotational effect in nonuniform magnetic fluids. *Magnetohydrodynamics*, 36:275–281, 2000.

[33] S. Rhodes. Magnetic fluid flow phenomena in dc and rotating magnetic fields. Master's thesis, MIT, 2004.

[34] S. Rhodes, J. Perez, S. Elborai, S.-H. Lee, and M. Zahn. Ferrofluid spiral formations and continuous-to-discrete phase transitions under simultaneously applied dc axial and ac in-plane rotating magnetic fields. *Journal of Magnetism and Magnetic Materials*, 298:353–355, 2005.

[35] C. Rinaldi. *Continuum modeling of polarizable systems*. PhD thesis, MIT, 2002.

[36] C. Rinaldi, A. Chaves, S. Elborai, X. He, and M. Zahn. Magnetic fluid rheology and flows. *Current Opinion in Colloid and Interface Science*, 10:141–157, 2005.

[37] C. Rinaldi, J.-H. Lee, A. Rosenthal, T. Franklin, and M. Zahn. Ferrohydrodynamics in time-varying magnetic fields. *Proceedings of the International Mechanical Engineering Conference and Exposition*, 126:198–205, 2002.

[38] C. Rinaldi and M. Zahn. Effects of spin viscosity on ferrofluid flow profiles in alternating and rotating magnetic fields. *Physics of Fluids*, 14:2847–2870, 2002.

[39] R. Rosensweig, J. Popplewell, and R.J. Johnston. Magnetic fluid motion in rotating field. *Journal of Magnetism and Magnetic Materials*, 85:171, 1990.

[40] R.E. Rosensweig. *Ferrohydrodynamics*. Dover Publications, 1997.

[41] R.E. Rosensweig, J. Browaeys, J.-C. Bacri, A. Zebib, and R. Perzynski. Laboratory study of spherical convection in simulated central gravity. *Phys. Rev. Lett.*, 83:4904–4907, 1999.

[42] R.E. Rosensweig, S. Elborai, S.-H. Lee, and M. Zahn. Ferrofluid meniscus in a horizontal or vertical magnetic field. *Journal of Magnetism and Magnetic Materials*, 298:192–195, 2005.

[43] R.E. Rosensweig and J.R. Johnston. Aspects of magnetic fluid flow with nonequilibrium magnetization. *Continuum mechanics and its applications*, pages 707–730, 1989.

[44] R.E. Rosensweig, M. Zahn, and R. Shumovich. Labrinthine instability in magnetic and dielectric fluids. *Journal of Magnetism and Magnetic Materials*, 39:127–132, 1983.

[45] A. Rosenthal, C. Rinaldi, T. Franklin, and M. Zahn. Torque measurement in spin-up flow of ferrofluids. *Journal of Fluids Engineering*, 126:198–205, 2004.

[46] T. Sawada, H. Kikura, and T. Tanahashi. Kinematic characteristics of magnetic fluid sloshing in a rectangular container subject to non-uniform magnetic fields. *Experiments in Fluids*, 26:215–221, 1999.

[47] J. Stratton. *Electromagnetic Theory*. McGraw-Hill Book Company, Inc., New York, NY., 1941.

[48] F. White. *Fluid Mechanics*. McGraw-Hill Book Company, Inc., New York, NY., 2003.

[49] M. Zahn. Magnetic fluid and nanoparticle applications to nanotechnology. *Journal of Nanoparticle Research*, 3:73–78, 2001.

[50] M. Zahn. *Electromagnetic Field Theory: A Problem Solving Approach*. Krieger Publishing Company, Inc., Florida, 2003.

[51] M. Zahn and D.R. Greer. Ferrohydrodynamic pumping in spatially uniform sinusoidally time-varying magnetic fields. *Journal of Magnetism and Magnetic Materials*, 149:165, 1995.

[52] V.M. Zaitsev and M.I. Shliomis. The hydrodynamics of a ferromagnetic fluid. *Zhurnal Prikladnoi Mekhaniki i Tekhnicheskoi Fiziki*, 9:41–44, 1968.

[53] V.M. Zaitsev and M.I. Shliomis. Entrainment of ferromagnetic suspension by a rotating field. *Zhurnal Prikladnoi Mekhaniki i Tekhnicheskoi Fiziki*, 10:11–16, 1969.

[54] W. Zimmerman. *Process Modelling and Simulation With Finite Element Methods*. World Scientific Publishing, Singapore, 2004.